

Design-oriented constitutive model for steel fiber reinforced concrete

Doctoral Thesis by:
Filipe Laranjeira de Oliveira

Directed by:
Antonio Aguado de Cea
Climent Molins Borrell

Barcelona, March 2010

Universitat Politècnica de Catalunya
Departament d'Enginyeria de la Construcció

TESIS DOCTORAL



Design-oriented constitutive model for steel fiber reinforced concrete

Dissertation

to obtain the degree of Doctor with European mention
by the Universitat Politècnica de Catalunya
with open defense on

Friday, 26th March 2010
12:00

Presented by

Filipe Laranjeira de Oliveira

Civil Engineer by the Faculty of Engineering
University of Oporto (Portugal)

Directed by:

Prof. Dr. Antonio Aguado de Cea Universitat Politècnica de Catalunya
Prof. Dr. Climent Molins Borrell Universitat Politècnica de Catalunya

Co-supervision by:

Prof. Dr. Joost Walraven Delft University of Technology, The Netherlands

Thesis Committee:

Prof. Dr. Antonio Marí Universitat Politècnica de Catalunya
Prof. Dr. Pedro Serna University of Valencia
Prof. Dr. Steffen Grünewald Delft University of Technology, The Netherlands
Prof. Dr. Liberato Ferrara Polytechnic of Milan, Italy
Prof. Dr. Joaquim Barros University of Minho, Portugal
Prof. Dr. Luis Agulló Universitat Politècnica de Catalunya
Dr. Bryan Barragán BASF Construction Chemicals, Italy

External referees:

Prof. Dr. Lucie Vandewalle Catholic University of Leuven, Belgium
Prof. Dr. Giovanni Plizzari University of Brescia, Italy

Universitat Politècnica de Catalunya
Department of Construction Engineering
C. Jordi Girona 1-3, Building C1
08034 Barcelona, Spain

Summary

Design-oriented constitutive model for steel fiber reinforced concrete

In the last years, the industry has been demanding for the use of steel fiber reinforced concrete (SFRC) in structural applications. Because the post-cracking strength of this material is not negligible, the crack-bridging capacity provided by fibers may replace, partial or completely, conventional steel reinforcement. Therefore, an appropriate characterization of the SFRC uniaxial tensile behavior is of paramount interest. However, in spite of the extensive research and standards recently advanced, there is no agreement on the constitutive model to be used for the design of SFRC.

The crack-bridging capacity provided by steel fibers improves both the toughness and the durability of concrete. Conventional SFRC is a material which presents softening response under uniaxial tension, but may develop hardening behavior in bending due to its ability to redistribute stresses within the cross-section. These evidences have been contributing to an increasing interest and growing number of applications of this material.

In this doctoral thesis, a direct and rationale approach to predict the tensile response of SFRC for structural design calculations is developed. While insight on the material behavior is firstly gained through an experimental investigation, the formulation of the new constitutive model follows a bottom-up approach: it fragments the material's behavior into levels of smaller complexity and then models each of them until the overall behavior can be explained.

The dissertation is subdivided into five main parts: I) The motivations for this research project are pointed out. II) Uniaxial tensile test results are obtained to understand the major mechanisms governing the post-cracking strength. III) Two models predicting the pullout responses of inclined steel fibers are developed, covering straight and hooked fibers. IV) The orientation of fibers is investigated in detail at the single fiber level through statistical analyses. Then, practical aspects associated to the manufacturing process are integrated within a novel framework to predict fiber orientation. V) Based on Parts III-IV, the new constitutive model is formulated and validated with experimental results from Part II. Further insight on the tensile behavior is gained through a parametric study and Engineered Expressions for Design and Optimization (EEDO) are proposed.

The proposed design-oriented constitutive model differentiates itself from previous studies in multiple aspects and defines a new philosophy for the design of SFRC elements. This model provides a direct and practical procedure to obtain the material's tensile behavior by means of parameters with physical meaning and based on clear concepts: fiber pullouts and orientations.

One of the major contributions of this work is the ability to predict the stress-crack width curves that reflect the specific combination of the properties of the matrix and fibers applied. Furthermore, it introduces a novel philosophy for the material design regarding that the influences of the production process, fresh-state properties and the element to be built are taken into account to define the constitutive diagram.

Filipe Laranjeira

Resumen

Modelo constitutivo orientado al diseño del hormigón reforzado con fibras de acero

En los últimos años la industria viene exigiendo el empleo del hormigón reforzado con fibras de acero (HRFA) en aplicaciones estructurales. Debido al hecho de que la resistencia pos-fisuración del material es relevante, la capacidad de coser fisuras concedida por las fibras puede permitir la sustitución, parcial o total, de la armadura de acero convencional. Por consiguiente, una adecuada caracterización del comportamiento a tracción uniaxial del HRFA es de gran interés. Sin embargo, a pesar de la amplitud de trabajo de investigación y de la reciente elaboración de normativas, no existe un consenso respecto al modelo constitutivo a ser empleado en el diseño del HRFA.

El cosido de las fibras de acero en las fisuras mejora la tenacidad y la durabilidad del hormigón. El HRFA es un material que, generalmente, presenta una resistencia residual a tracción en régimen fisurado. Sin embargo, en algunas situaciones, el HRFA puede desarrollar endurecimiento en flexotracción debido a su aptitud en redistribuir esfuerzos en la sección de fisura. Estas características vienen contribuyendo para un interés creciente así como un incremento del número de aplicaciones de este material.

En esta tesis doctoral se desarrolla un método directo y lógico para predecir la respuesta a tracción del HRFA para el diseño estructural. Mientras que la comprensión del comportamiento del material se consigue por medio de una investigación experimental, la formulación del nuevo modelo constitutivo se obtiene con un estudio segmentado del comportamiento del material en niveles de menor complejidad y, en seguida, con la caracterización de cada uno de ellos hasta conseguir explicar la respuesta a tracción del HRFA.

Esta tesis está dividida en cinco partes principales: I) Identificación de las motivaciones. II) Obtención de resultados a tracción uniaxial para comprender los principales mecanismos que controlan la resistencia pos-fisuración. III) Desarrollo de dos modelos para predecir la respuesta al arrancamiento de fibras de acero inclinadas, que cubren fibras rectas y con ganchos. IV) Investigación detallada de la orientación de las fibras al nivel individual mediante análisis estadísticos. Luego, aspectos prácticos asociados al proceso de producción son integrados en una metodología innovadora para predecir la orientación de las fibras. V) Formulación y validación del nuevo modelo constitutivo, con base en las Partes III y IV, con los resultados experimentales de la Parte II. El comportamiento a tracción se evalúa mediante un estudio paramétrico y se proponen expresiones ingenieriles para el diseño y optimización (EEDO).

El modelo constitutivo propuesto se distingue de estudios anteriores en varios aspectos y define una nueva filosofía para el diseño de elementos de HRFA. Este modelo es un método directo y práctico para obtener el comportamiento a tracción del material mediante parámetros con sentido físico y basado en conceptos claros: arrancamiento y orientación de las fibras.

Una de las principales aportaciones de este trabajo es la capacidad de predecir curvas tensión-apertura de fisura que reflejan una combinación específica de las propiedades de la matriz y de las fibras empleadas. Además, se introduce una filosofía innovadora en el diseño debido a la incorporación del proceso de producción, las propiedades en estado fresco y el elemento a construir en la definición del diagrama constitutivo.

Resumo

Modelo constitutivo orientado ao dimensionamento do betão reforçado com fibras de aço

Nos últimos anos, a indústria tem vindo a exigir a utilização do betão reforçado com fibras de aço (BRFA) em aplicações estruturais. Devido ao facto de a resistência pós-fissuração deste material ser relevante, a capacidade de coser fissuras concedida pelas fibras pode permitir a substituição, parcial ou total, da armadura de aço convencional. Por conseguinte, uma adequada caracterização do comportamento à tracção uniaxial do BRFA é do maior interesse. No entanto, apesar da existência de inúmeros trabalhos de investigação e da recente elaboração de normativas, não existe um consenso em relação ao modelo constitutivo a ser utilizado para o dimensionamento do BRFA.

A capacidade de coser fissuras conferida pelas fibras de aço melhora a tenacidade e a durabilidade do betão. O BRFA é um material que, geralmente, apresenta uma resistência residual à tracção em regime fissurado. No entanto, em algumas situações, o BRFA pode desenvolver endurecimento em flexão devido à sua aptidão para redistribuir esforços na secção de fissura. Estas características têm contribuído para um interesse crescente e um aumento do número de aplicações deste material.

Na presente tese de doutoramento desenvolve-se um método directo e lógico para prever a resposta à tracção do BRFA para o dimensionamento estrutural. Ao passo que a compreensão do comportamento do material é conseguida através de uma investigação experimental, a formulação do novo modelo constitutivo é obtida com um estudo segmentado do comportamento do material em níveis de menor complexidade e, posteriormente, com a caracterização de cada um deles até conseguir explicar a resposta à tracção do BRFA.

A dissertação está subdividida em cinco partes principais: I) Identificação das motivações. II) Obtenção de resultados à tracção uniaxial para compreender os principais mecanismos que controlam a resistência pós-fissuração. III) Desenvolvimento de dois modelos para prever a resposta ao arrancamento de fibras de aço inclinadas, que cobrem fibras rectas e com ganchos. IV) Investigação detalhada da orientação das fibras ao nível individual através de análises estatísticas. Posteriormente, aspectos práticos associados ao processo de produção são integrados numa metodologia inovadora para prever a orientação das fibras. V) Formulação e validação do novo modelo constitutivo, a partir das Partes III e IV, com os resultados experimentais da Parte II. O comportamento à tracção do BRFA é avaliado através de um estudo paramétrico e são propostas expressões engenhosas para o seu dimensionamento e optimização (EEDO).

O modelo constitutivo proposto diferencia-se de estudos anteriores em vários aspectos e define uma nova filosofia para o dimensionamento de elementos de BRFA. Este modelo é um método directo e prático para obter o comportamento à tracção do material através de parâmetros com sentido físico e baseado em conceitos claros: arrancamento e orientação das fibras.

Um dos principais contributos deste trabalho é a capacidade de prever curvas de tensão-abertura de fissura que reflectem uma combinação específica das propriedades da matriz e das fibras aplicadas. Além disso, introduz uma filosofia inovadora no dimensionamento do material tendo em conta que a influência do processo de produção, as propriedades em estado fresco e o elemento a ser construído são considerados na definição do diagrama constitutivo.

Acknowledgments

Agradecimientos

Agradecimientos

Finishing this doctoral thesis brings me a mix of satisfaction and nostalgia difficult to describe. Looking back in time, I quickly realize that these three and half years of research were a memorable stage in my life. Thereby, I want to express my gratitude to those who have contributed the most for my academic, professional and personal growth. For convenience, I will express my thanks in *Spanish*, English and Portuguese.

En primero lugar quiero agradecer a mis tutores Antonio Aguado y Climent Molins. Ellos me dieron la oportunidad de hacer el doctorado y siempre me apoyaron al máximo dentro de todas sus posibilidades. Fue un gran privilegio trabajar, convivir y aprender con los dos. Les agradezco profundamente su dedicación, contribuciones y enseñanzas a todos los niveles.

En el departamento de Ingeniería de la Construcción de la UPC tuve todas las condiciones materiales y humanas para desarrollar esta tesis de la forma más agradable posible. Agradezco al director del Laboratorio de Tecnología de Estructuras, Tomàs García, bien como a las demás personas que ahí me ayudaron, en particular a Camilo Bernad, Jordi Lafuente y Jaume Guàrdia.

Quiero agradecer también a mis compañeros y amigos del doctorado, a los que me más me apoyaron en momentos de menor motivación y me acompañaron en tantos otros buenos: Albert de la Fuente, Ana Blanco, Ana Carolina dos Santos, Bernat Viñolas, Betty de los Ríos, Francesc Pardo, Izelman Oliveira, Miguel Lobato, Noé Villegas, Oriol Arnau, Pablo Pujadas, Sandra Manso y Sergio Cavalaro, entre otros. Agradezco también a Marc Vandewalle por su apoyo e incentivo y a Luis Agulló por su amistad y por su habilidad en crear un entorno familiar en el departamento.

I gratefully acknowledge the financial support given by the Portuguese Foundation for Science and Technology (FCT) in the scope of the Research Grant SFRH/BD/36248/2007. I also thank to my directors of thesis, who provided me the financial means during the first year of research.

I would like to thank to Prof. Joost Walraven and Dr. Kees Blom for giving me the chance to work at the Delft University of Technology for six months. A special thanks to Dr. Steffen Grünewald for his conveying knowledge, constant support and friendship. Their interest and suggestions gave me motivation to develop an important part of this dissertation. I acknowledge the kindness of Dr. Lena Lappa and Dr. Petra Schumacher for the data provided and address my sincere thanks to Mrs. Luz Ton-Estrada, Bas Lottman, Yuguang Yang and to other colleagues from the Department of Structural and Building Engineering who contributed for a pleasant stay in The Netherlands.

I thank to my friends, whom without I would not have managed to achieve many things. I owe special thanks to my flatmates for their patience and support and to all those with whom I shared great experiences in Barcelona and Delft. I also thank to my friends living in Portugal and worldwide who assure me that time and distance are not barriers for true friendship.

Por fim, quero agradecer à minha família por todo o apoio que sempre recebi e dedicar este trabalho ao meu Avô, porque sei que estaria muito orgulhoso de mim neste momento. Um obrigado especial ao meu Pai e à minha Mãe por todo o carinho, compreensão e partilha constante dos meus sonhos. Eles são o exemplo de tudo o que eu mais quero ser um dia.

Muito obrigado a todos...

Filipe Laranjeira

Table of contents

Summary

Resumen

Resumo

Acknowledgments / Agradecimientos / Agradecimentos

Chapter 1: Introduction

1.1	Scope of the research	1
1.2	Research objective	3
1.3	Research strategy	3
1.4	Outline of the thesis.....	4

Part I: Motivations

Chapter 2: State of the art

2.1	Introduction.....	7
2.2	Evaluation of existing constitutive models for SFRC	8
2.2.1	Criteria and characteristics	8
2.2.2	Constitutive models advanced in literature	11
2.2.3	Constitutive models proposed by European Standards and guidelines	14
2.2.4	Demands for an improved modeling method	16
2.3	Experimental research on the tensile behavior of SFRC.....	19
2.3.1	Overview of existing test methods.....	19
2.3.2	Uniaxial tensile tests	20
2.4	Pullout behavior of steel fibers.....	21
2.4.1	Straight fibers	21
2.4.2	Hooked fibers.....	23
2.5	The orientation of fibers in SFRC.....	25
2.5.1	Methods to measure the orientation of steel fibers.....	25
2.5.2	Identification of causes for anisotropic orientations.....	27
2.5.3	Current approach to determine the orientation of fibers	27
2.6	Concluding remarks.....	28

Part II: Experimental research

Chapter 3: Uniaxial tensile tests

3.1	Introduction.....	31
3.2	Experimental program	32
3.2.1	Research parameters.....	32
3.2.2	Properties of the materials	32

3.2.3	Preparation of the specimens.....	33
3.2.4	Setup and testing procedures.....	34
3.3	Characterization of the SCSFRC	36
3.3.1	Fresh state properties.....	36
3.3.2	Hardened state properties	40
3.4	Uniaxial tensile test results	41
3.4.1	Stress-crack width curves	41
3.4.2	Fracture energy	45
3.4.3	Number of fibers at the cracked sections.....	46
3.4.4	Analysis of fiber distribution	48
3.5	Concluding remarks.....	51

Part III: Single fiber pullouts

Chapter 4: Predicting the pullout response of inclined straight steel fibers

4.1	Introduction.....	53
4.2	Research significance	54
4.3	Pullout behavior of aligned fibers.....	54
4.3.1	Qualitative description.....	54
4.3.2	Pullout response	54
4.4	Pullout behavior of inclined fibers.....	55
4.4.1	Qualitative description.....	55
4.4.2	Pullout response	57
4.5	Pullout model.....	58
4.5.1	General methodology	58
4.5.2	Extraction of interface properties from experimental data	59
4.5.3	Detailed description of the pullout model.....	60
4.5.4	Parameter identification	66
4.6	Model discussion	68
4.6.1	Experimental validation	68
4.6.2	Parametric study.....	72
4.6.3	Applying the model to optimize material properties	74
4.7	Concluding remarks.....	76

Chapter 5: Predicting the pullout response of inclined hooked steel fibers

5.1	Introduction.....	77
5.2	Research significance	78
5.3	Pullout behavior.....	78
5.3.1	Main concepts	78
5.3.2	Correlation between geometry of the hook and pullout response.....	78
5.3.3	Aligned fibers.....	80
5.3.4	Inclined fibers	81
5.4	Pullout model.....	83

5.4.1	General methodology	83
5.4.2	Extracting the contribution of the hook from experimental data.....	84
5.4.3	Detailed description of the pullout model	85
5.4.4	Parameter identification	90
5.5	Model validation.....	93
5.5.1	Robins et al. (2002).....	94
5.5.2	van Gysel (2000)	99
5.6	Concluding remarks.....	102

Part IV: Fiber orientation

Chapter 6: Characterization of the orientation profile of SFRC

6.1	Introduction.....	105
6.2	The concept of orientation profile	106
6.3	Statistical orientation law	106
6.3.1	Selection of experimental data.....	106
6.3.2	Statistical hypotheses	107
6.3.3	Statistical analyses	109
6.3.4	Selection of the orientation law.....	111
6.4	Average orientation angle	112
6.5	Dispersion of orientations	113
6.5.1	Theoretical basis.....	113
6.5.2	Experimental investigation	114
6.5.3	Evaluation of the dispersion.....	116
6.6	Applying the orientation profile	117
6.7	Concluding remarks.....	119

Chapter 7: Framework to predict the orientation of fibers in FRC: A novel philosophy

7.1	Introduction.....	121
7.2	Framework outline.....	122
7.3	Fiber orientation from a 3-D perspective	123
7.3.1	Theoretical and probabilistic envelop curves	123
7.3.2	Experimental verification.....	126
7.4	Approach to estimate generalized wall-effects.....	127
7.4.1	Analysis of the wall-effects in isotropic conditions	128
7.4.2	Approaching the wall-effects in anisotropic conditions	129
7.5	Framework analysis: step-by-step.....	130
7.5.1	Influence of fresh-state properties after mixing.....	131
7.5.2	Influence of the casting method.....	132
7.5.3	Influence of dynamic effects.....	134
7.5.4	Influence of the formwork geometry	136
7.5.5	Summary.....	136
7.6	Application of the framework to prismatic beams	137

7.6.1	Experimental data	137
7.6.2	Applying the framework: step-by-step	138
7.6.3	Overall results	139
7.8	Concluding remarks	140

Part V: Predicting the tensile behavior of SFRC

Chapter 8: New constitutive model

8.1	Introduction.....	141
8.2	Philosophy of the approach	142
8.2.1	Conceptual basis	142
8.2.2	Strategy	143
8.3	Formulation.....	144
8.3.1	Plain concrete	144
8.3.2	Steel fibers	145
8.3.3	Overview of the new constitutive model	150
8.4	Experimental validation	152
8.4.1	Identification of input parameters.....	152
8.4.2	Results and discussion.....	154
8.5	Parametric study of the SFRC tensile behavior	157
8.5.1	Focus of the constitutive model.....	158
8.5.2	Case studies.....	159
8.5.3	Comparative analysis between straight and hooked fibers	160
8.5.4	Analysis for straight fibers.....	161
8.5.5	Analysis for hooked fibers	163
8.6	Engineered expressions for design of SFRC	166
8.6.1	Basic concepts and equations.....	166
8.6.2	Analysis of the parameters	167
8.6.3	Methodology	169
8.6.4	Straight fibers	171
8.6.5	Hooked fibers.....	173
8.7	Design-oriented constitutive model: A practical example	176
8.7.1	Problem statement	176
8.7.2	Resolution based on the analytical formulation	176
8.7.3	Resolution based on the engineered expressions	180
8.8	Concluding remarks.....	181

Part VI: Concluding remarks

Chapter 9: Conclusions and future perspectives

9.1	Conclusions	183
9.2	Future perspectives	187

Bibliography	189
Appendices: overview	199
<u>Appendix 1</u> Uniaxial tensile test reports	
A1.1 Introduction.....	201
A1.2 Serie A0.....	202
A1.3 Serie A20	209
A1.4 Serie A40	217
A1.5 Serie A60	225
A1.6 Serie B0.....	233
A1.7 Serie B20	240
A1.8 Serie B40	248
A1.9 Serie B60	256
<u>Appendix 2</u> Definition of the matrix spalled lengths	
A2.1 Introduction.....	265
A2.2 Definition of L_{SP1}	266
A2.3 Definition of L_{SP2}	268
<u>Appendix 3</u> Inclined tensile strength and data for validation of the pullout model	
A3.1 Introduction.....	271
A3.2 Predicting $f_u(\theta)$	272
A3.3 Input values used for model validation.....	274
<u>Appendix 4</u> Statistical analyses of the orientation profile	
A4.1 Introduction.....	275
A4.2 Features of the experimental data.....	276
A4.3 Results from the non-parametric tests	277
A4.4 Coefficients of determination (R^2)	278
A4.5 Statistical orientation laws ($\Delta\theta=10^\circ$).....	279
<u>Appendix 5</u> Wall-effects on fiber orientation	
A5.1 Introduction.....	283
A5.2 Wall-effects under isotropic conditions	284
A5.2.1 Orientation number of a fiber with one boundary condition	284
A5.2.2 Orientation number of a fiber with two boundary conditions.....	285
A5.3 Generalized wall-effects for common cross-section geometries	289
A5.3.1 Rectangular cross-section.....	289
A5.3.2 Circular cross-section.....	290
A5.3.3 Hollow-circular cross-section.....	291
A5.3.4 Summary.....	293

Appendix 6	Experimental validation of the framework to predict fiber orientation	
A6.1	Introduction.....	295
A6.2	Input data for experimental validation	296
A6.3	Results from experimental validation	297
Appendix 7	Literature survey on pullout test results of aligned fibers	
A7.1	Introduction.....	299
A7.2	Straight steel fibers	300
A7.3	Hooked steel fibers.....	302
Appendix 8	Application of the engineered expressions on several case-studies	
A8.1	Introduction.....	305
A8.2	Straight steel fibers	306
A8.3	Hooked steel fibers.....	309
	Notations and symbols.....	313
	Publications related to this research	
	Curriculum vitae	

Chapter 1

Introduction

1.1 SCOPE OF THE RESEARCH

Reinforced concrete structures began in the nineteenth century and rapidly became a building technology which is indispensable in our modern society. Because plain concrete is a material characterized by low tensile strength and brittle behavior, the idea of adding reinforcing steel bars was brilliant, as they take over tensile forces and provide ductility to the concrete members. A variant of this principle was advanced in the 1960s, with the development of the steel fiber reinforced concretes (SFRC). In this case, the reinforcing action of steel takes place through a large number of small fibers, randomly distributed in the mixture, which bridge cracks in concrete and increase its toughness and durability.

Fiber reinforced concretes have emerged into a subject of major interest among researchers and civil engineers. Recent developments led to the appearance of high performance fiber reinforced cementitious composites (HPFRCC), a material which possesses the ability to generate multiple cracks due to its increase of resistance after cracking. In this dissertation the focus is on conventional SFRC, a material which presents softening response under uniaxial tension

(reduction of resistance after cracking). Although the latter may be seen as the weaker gender of fiber reinforced concretes, there are several reasons that justify the interest on this material.

The crack-bridging capacity provided by fibers (Fig.1.1a) improves durability and, because minimum covers are no longer required in SFRC elements, their thicknesses can be significantly reduced. Fiber reinforcement can replace, partially or totally, conventional reinforcement (rebars or welded mesh), thus providing freedom to create daring aesthetics with curved shapes (Fig.1.1b). Fibers can also be very effective on structures subjected to concentrated static or dynamic loads, applied at various places and in various directions. Despite the softening behavior observed under uniaxial tension, SFRC subjected to bending stresses may provide hardening type behavior (increasing of load-carrying capacity after cracking) due to its ability to redistribute stresses within the cross-section.

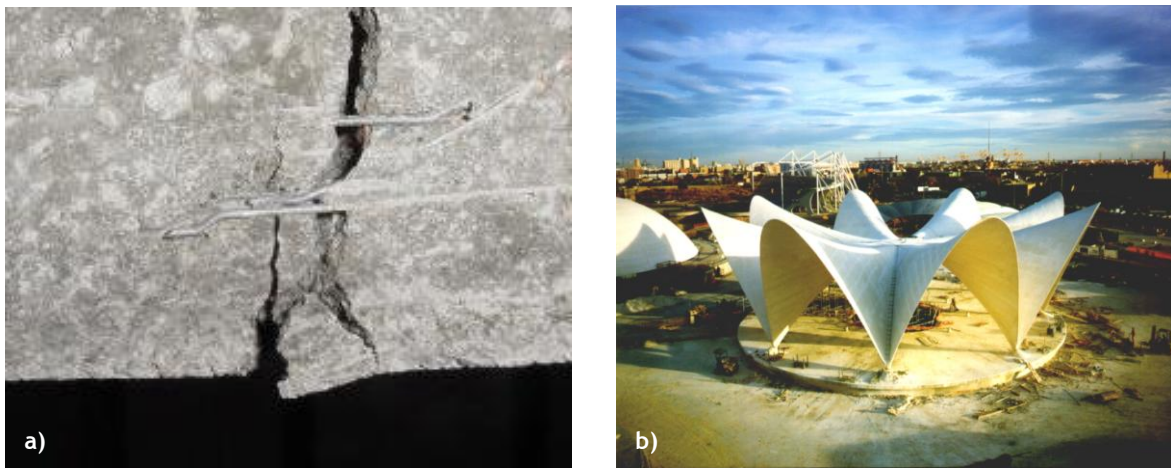


Fig. 1.1 - a) Crack-bridging effect of fibers (Aguado, 2007); b) Example of SFRC application: Oceanographic Museum in Valencia (Serna et al., 2009).

In the past years there has been a significant increase of SFRC applications, not only in quantity but also in variety. Few years ago, industrial floors and segments for tunnel linings were responsible for the majority of applications in most countries. However, the interest on SFRC has been growing due to the increasing costs of conventional steel reinforcement and the appearance of new constructive systems. Because the use of SFRC allows the industrialization of the production processes, both the handling labor and the speed rate of construction can be significantly reduced. Consequently, the material has been proving to be competitive also from an economical point of view.

Despite the remarkable advances that have been attained in the field of fiber reinforced concretes, there are still some aspects hindering its widespread use. Given that industry is demanding for SFRC with increasing structural responsibilities, the methods for characterization and quality control of the material properties in the hardened state have to be improved. As a consequence, understanding and predicting appropriately the mechanisms governing the tensile behavior of SFRC is of paramount importance in order to conceive innovative, reliable and economical structural applications.

So far, the main inhibitor for the application of SFRC in engineering practice has been the lack of appropriate standards and suitable certification. Recently, international guidelines and several national standards have been advanced in response to this limitation and the next FIB Model Code, to be published soon, will provide design recommendations for SFRC for the first time. However, in spite of these relevant advances, there has been no general agreement on the uniaxial constitutive model to be used to design of SFRC structural members. Discussions on this subject have turned out into methods that do not allow a direct definition of the material's constitutive model.

1.2 RESEARCH OBJECTIVE

The main objective of this research project is the development of a direct and rationale approach to predict the tensile response of SFRC for structural designing.

Current practice for the design of SFRC presents many disadvantages, namely: requires previous experimental work in order to characterize the material's post-cracking behavior; lacks comprehension of the physical phenomena governing its tensile response; inoperability for tailoring and optimizing concrete mixtures and fiber characteristics; inappropriate characterization of the material properties due to dissimilar orientation of fibers in testing specimens and real applications; time-consumption; costs; etc. Therefore, a material model based on a new design philosophy that could overcome these limitations would be of paramount relevance.

A new constitutive model for SFRC should provide a practical and comprehensive tool to be used by structural designers. For that purpose, the major physical aspects controlling the tensile response of SFRC (fiber pullout, distribution and orientation) should be explained and integrated within a unique approach that could account for the properties of its components, the production processes and the structure to be built. If such constitutive model could be defined, the structural design of SFRC would become much more efficient, reliable and economic.

1.3 RESEARCH STRATEGY

To achieve the objective of this research project the following strategy was developed:

First, an experimental investigation of the tensile behavior of SFRC was carried out. For that purpose, uniaxial tension tests were performed to evaluate the influence of fiber contents and concrete strengths on the stress-crack width responses.

Second, an extensive literature survey on the pullout responses of steel fibers was performed. Based on the phenomenological interpretation of the pullout behavior, the load-crack width responses of straight and hooked fibers at any inclination angle were predicted.

Third, the orientation of fibers was investigated at two different levels. In the first study, the average orientation of fibers in a cross-section was correlated with the statistical distributions of the orientation angles of the single fibers. In the second study, the average orientation of fibers in the cross-section is predicted through an innovative framework that integrates materials properties, production processes and the structure to be built within a unique approach.

Finally, based on the studies of fiber pullout responses and fiber orientation, the new constitutive model is formulated and compared to the uniaxial tension test results. A parametric study of the major parameters affecting the tensile behavior is presented and simplified expressions for design of SFRC with straight and hooked steel fibers are advanced.

1.4 OUTLINE OF THE THESIS

This thesis is subdivided into six parts, such as shown in Fig.1.2. Part I points out the motivations of the thesis. Part II presents the experimental investigation on the uniaxial tensile behavior. Part III deals with the modeling of single fiber pullout responses. Part IV focus on predicting the orientation of fibers. Part V presents, validates and analyses the new constitutive model. Part VI ends this thesis with final conclusions and future perspectives.

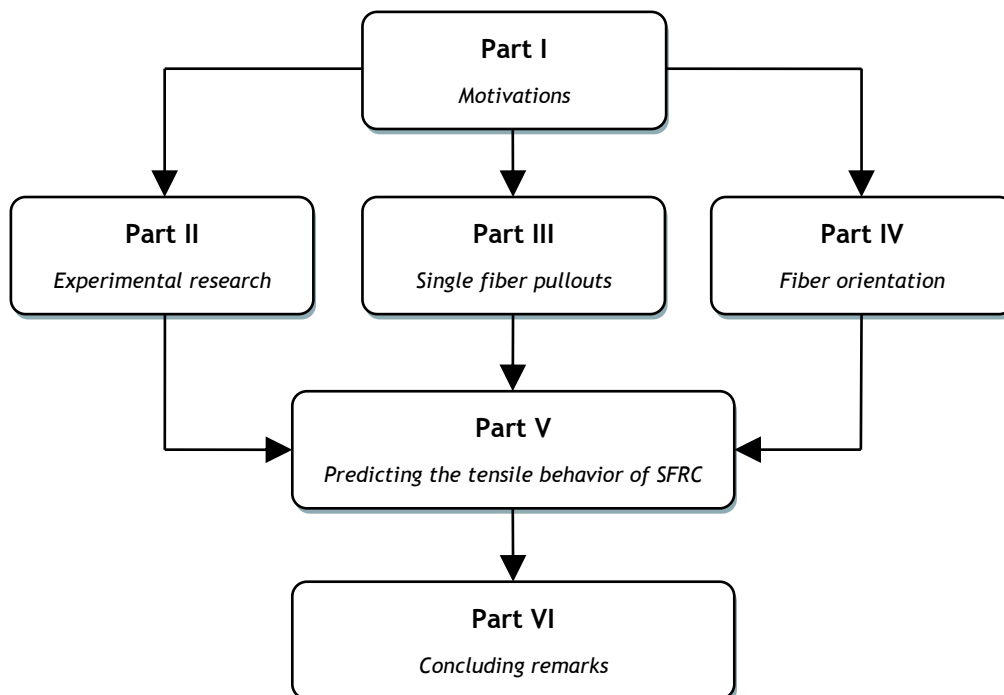


Fig.1.2 - New constitutive model for SFRC: overview of the six parts of this thesis.

Part I provides a state of the art of the subjects addressed in this thesis. Chapter 2 presents a literature survey on existing constitutive models, identifies their major characteristics and advances criteria and demands for improved material modeling. Chapter 2 also reviews previous

works regarding uniaxial tensile tests, experiments and modeling of single fiber pullout responses as well as methods and procedures to investigate the orientation of steel fibers.

Part II of this thesis describes the research on the uniaxial tensile behavior of SFRC. Chapter 3 presents the experimental program which aimed at evaluating the influence of steel fiber contents and concrete strengths on the material stress-crack width responses. This chapter summarizes and discusses the relevant results that were obtained.

Part III deals with the single fiber pullouts of steel fibers and consists of two chapters. Chapter 4 advances a model to predict the pullout responses of straight fibers at any orientation with respect to loading direction. Based on experimental data from aligned fibers, the model provides a comprehensive and straightforward procedure which is validated with test results from literature. In Chapter 5, an extension of the model to cover the pullout responses of hooked fibers is advanced. Once more, the pullout mechanisms are evaluated from a conceptual point of view, validated with experimental data and used to gain insight for tailoring the material properties.

Part IV focus on the orientation of steel fibers and is divided into two chapters. In Chapter 6, results from image analysis and computer tomographies were used to investigate the individual orientation of fibers and to correlate them with their average orientation in a cross-section. Based on an extensive statistical analysis, a procedure is advanced to predict the distribution of inclination angles in terms of the orientation number. Following, Chapter 7 introduces a new framework to predict such orientation number. For that purpose, fiber orientation is evaluated in 3-D conditions and the wall-effects are quantified under anisotropic scenarios. With these two concepts, the orientation number is approached through a step-by-step procedure which embraces material properties, production processes and the geometry of the structure.

Part V presents the new constitutive model for SFRC. Chapter 8 shows how to combine the approaches advanced in parts III and IV in order to obtain a design-oriented procedure. After the description of the new design philosophy, the analytical formulation of the constitutive model is described and validated with experimental data from part II. Then, Chapter 8 provides insight into the tensile behavior of SFRC through a parametric study. Following, the results of a study that aimed at obtaining straightforward expressions that could reproduce the stress-crack width responses provided by the new constitutive model are presented. Finally, a practical example of application of the new design philosophy is solved in detail with the two alternative approaches presented.

Part VI (Chapter 9) presents final conclusions and provides recommendations for future research concerning the design and characterization of SFRC.

Finally, in order to provide additional support to the content of the several parts of this thesis, eight appendices are included. These cover experimental features and test results, modeling of specific phenomena and respective validations. Although some of the appendices contain information of great relevance in the scope of this dissertation, they are included in the end so that the reader can easily follow the main ideas from each chapter.

Chapter 2

State of the art

2.1 INTRODUCTION

A wide research has been performed on material properties of FRC during the last four decades, both at fresh and hardened state. Research on structural response of FRC elements was mainly developed during the last fifteen years, but the continuous growth of FRC structural applications is still limited with respect to its potentials, mainly due to the lack of International Building Codes for FRC structural elements (di Prisco et al., 2009). To answer this demand extensive studies have been carried out on the mechanical property most influenced by fiber reinforcement: the post-cracking tensile strength of FRC.

This chapter aims at reviewing relevant literature concerning the post-cracking behavior of SFRC. This state of the art embraces two major parts which pursue two distinct goals: 1) to identify the motivations for this thesis; 2) to briefly cover literature concerning several subjects that will be addressed for the development of the new constitutive model presented in this dissertation.

The first part of this chapter identifies the main characteristics and criteria of the existing modeling procedures. Then, a description of the constitutive laws from literature and European Standards is advanced. Finally, the limitations of the existing methods are discussed and the demands for a more suitable and reliable modeling method are advanced.

The second part of this chapter reviews different research lines that are of paramount importance to characterize the tensile behavior of SFRC. First, reliable experimental test results are required to understand the material behavior. For that purpose, a survey of experimental researches on the uniaxial tensile behavior of SFRC is presented. Second, the fundamental strengthening mechanisms provided by fiber reinforcement need to be understood. With regard to this subject, previous studies on the pullout behavior of straight and hooked steel fibers are discussed. The crack-bridging effect provided by fibers depends on their orientation respect to the crack. Consequently, the third research line presented addresses the advances that have been achieved on the identification of preferential fiber alignments.

2.2 EVALUATION OF EXISTING CONSTITUTIVE MODELS FOR SFRC

2.2.1 Criteria and characteristics

The large variety of parameters and phenomena affecting the tensile response of SFRC make material modeling a particularly intricate task. Because of such complex behavior, there is not a unique constitutive law for its post-cracking response but rather several different methodologies. The identification of the constitutive law in uniaxial tension represents the critical ring in the design of SFRC structures (di Prisco et al., 2004). The most important step, still in progress, is the effort to propose the most reliable equations for structure design both for service and ultimate limit states (di Prisco, 2009).

Prior to the description of the existing constitutive laws in literature and standards, it may be worth to identify their main characteristics and criteria associated to modeling methodologies. Among the several proposals, four main differential aspects may be distinguished:

- Stress-crack width law (σ - w) and stress-strain law (σ - ϵ)
- Inverse approach and direct approach
- Micro-scale and macro-scale research levels
- Continuously differentiable and continuous non-differentiable diagrams

Stress-crack width law vs. Stress-strain law

The softening behavior of SFRC may be modeled either through a stress-crack width relation (σ - w) or a stress-strain one (σ - ϵ). The σ - w method is based on the fictitious crack model (Hillerborg et al., 1976). This model assumes the existence of a so-called cohesive zone on the fracture process of plain concrete in which stresses can be transferred over the crack. Latter this approach has been taken by numerous authors in attempts to describe the crack bridging ability

of fibers (Kullaa, 1994; Lange-Kombak and Karihaloo, 1998; Li, 1992; Li et al., 2003). The fictitious crack model in SFRC represents the process zone, aggregate interlock as well as fiber bridging, such as exemplified in Fig.2.1.

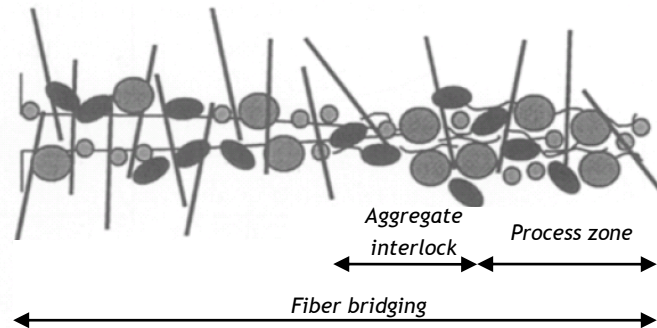


Fig. 2.1 - Essential features of a crack in SFRC (RILEM TC 162-TDF, 2002).

The σ - ε method may also be used to describe the softening behavior of SFRC. In this case, the definition of the stress-strain law is based on the identification of a crack width and its corresponding structural characteristic length (l_{cs}) of the structural element (RILEM TC 162-TDF, 2002). This concept was firstly advanced by Bazant and Oh (1983), with the designation of crack band width. This way, with the use of l_{cs} , smeared crack models and discrete crack models can be translated into each other. Such correspondence can be seen in Fig.2.2, which shows a schematic representation of a SFRC constitutive diagram using both the σ - ε and the σ - w relationships to describe the post-cracking branch.

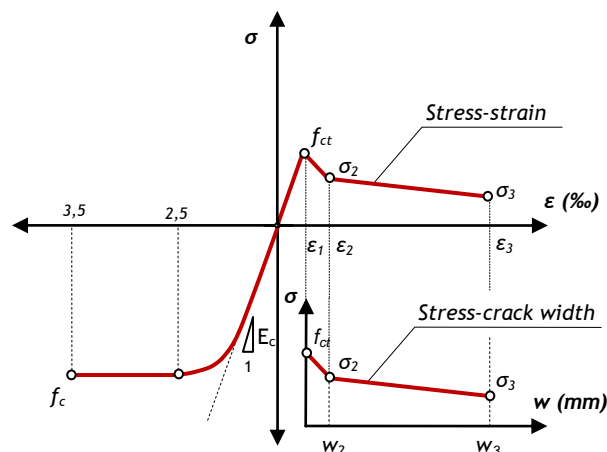


Fig. 2.2 - Scheme of the SFRC constitutive law in terms of σ - w and σ - ε .

Inverse approach vs. direct approach

The characterization of the tensile behavior of SFRC may be done both through inverse or direct approaches, similarly to what is common practice in the characterization of other material properties such as the bond strength of steel rebars or fibers embedded in concrete matrices

(Banholzer et al., 2005; Banholzer et al., 2006). The modeling procedure associated to each of these approaches is summarized in Fig.2.3.

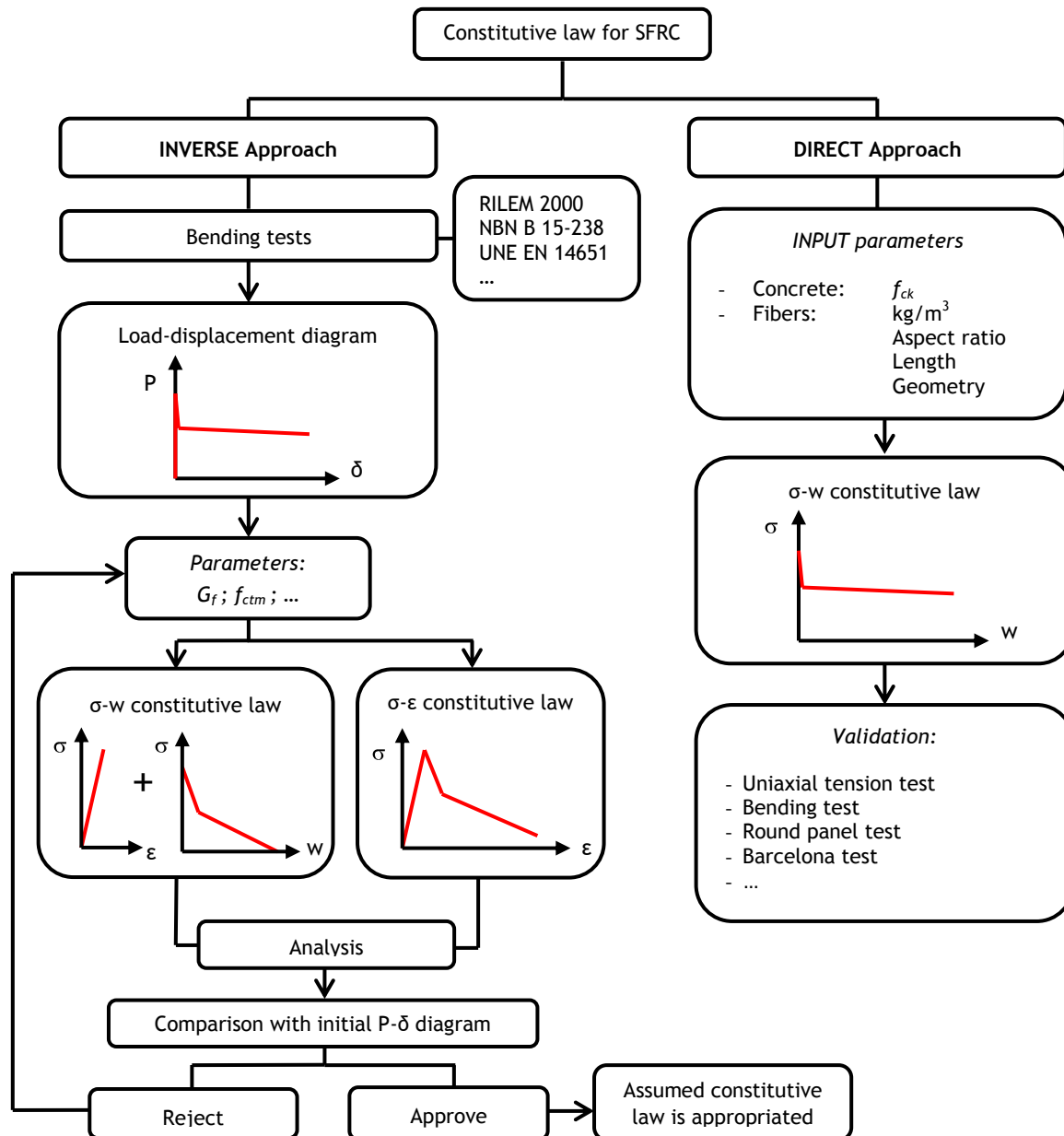


Fig. 2.3 - Schematic procedures associated to inverse and direct approaches (Laranjeira et al., 2007)

The inverse approach consists on an iterative procedure which fits experimental data in order to obtain the parameters that define an assumed shape for the constitutive diagram. This approach represents the softening response either through a smeared crack or a discrete crack method, i.e., σ - ϵ or σ - w relationships (Fig.2.3).

In the direct approach the parameters that characterize the shape of the constitutive diagram are defined through experimental values (such as occurs in the existing standards presented in the following) or, ideally, through the properties of its constituent materials (Fig.2.3).

Micro-scale vs. macro-scale research level

The stress-crack width relationship of SFRC has been investigated at different research levels. The significant advances in the field of fracture mechanics that took place during the 1980s boosted the studies of the microstructural mechanics (Bentur, 1985; Wei et al., 1986; Li et al., 1993; Shah and Li, 1995; Karihaloo and Wang, 1997) which significantly improved the understanding of the cracking processes in SFRC. Concurrently, the inverse analysis procedure applied to modeling the tensile behavior of plain concrete (Roelfstra and Wittman, 1986) was extended to SFRC (Barros and Figueiras, 1999; Sousa and Gettu, 2006). This method, which focus on fitting the experimental material behavior at a macro-scale behavior, rapidly evolved into a “new branch of science” (van Mier and van Vliet, 2002) and became the most popular method to approach the behavior of SFRC due to its practicability.

More recently it has been developed a new research line, the so-called meso-scale models. These approaches are within an intermediate scale between micro and macroscopic properties of the material, focusing at the level of the particle structure of concrete. In this research level the bridging of the crack is based on the number and orientation of the fibers and on their individual pullout responses during crack opening. In the last years, the flexural post-cracking response of SFRC has been approached through analytical meso-scale models by several researchers (Armelin and Banthia, 1997; Van Gysel, 2000; Markovic, 2006; Jones et al., 2008).

Continuously differentiable diagram vs. Continuous non-differentiable diagram

An idealized constitutive model for SFRC faces the tricky task of describing appropriately the material’s uniaxial behavior within a simple diagram to be used for design purposes. Regarding the paramount interest of the identification of SFRC constitutive law, most of the existing proposals are based on simplified continuous non-differentiable diagrams, such as shown in Section 2.2.2. Nonetheless, giving that the complex behavior of SFRC may lead to significantly different responses, more complicated mathematical functions have also been used to characterize the post-cracking behavior in terms of continuously differentiable relationships (Li et al., 1993; Lee and Barr, 2004).

2.2.2 Constitutive models advanced in literature

The quantification of the post-cracking strength provided by fibers has been largely investigated, particularly during the last two decades, where the interest for SFRC structural applications became more evident. So far, despite the large number of proposals in literature, it has not yet been found a constitutive law that gathers an overall consensus among researchers and engineers.

Most of the models that have been advanced in literature share some common characteristics: they propose simple and continuous non-differentiable constitutive diagrams that are characterized through macroscopic properties by means of inverse analysis procedures. These approaches focus either on stress-strain (σ - ϵ) or stress-crack width relationships (σ - w).

One of the first studies based on σ - ϵ diagrams was performed by Lim et al. (1987) who proposed an analytical constitutive law (Fig.2.4a) based on easily quantifiable material and mix properties. The authors considered small fiber contents and assumed that under such conditions the influence of the fibers was negligible on the pre-peak behavior and conducted to a constant post-peak branch. An alternative approach was suggested by Lok and Xiao (1998), such as shown in Fig.2.4b. They introduced a non linear relationship in the pre-peak zone and included an intermediate branch in order to improve the estimation of the residual strength. Another work of great relevance was the one carried out by Dupont and Vandewalle (2002), depicted in Fig.2.4c. They proposed a two-level stress-strain relation which, although based on the same assumptions of the tri-linear models suggested in European Standards and guidelines (described in the following), has the particularity of making the post-cracking part of the stress-strain curve completely independent of the matrix tensile strength.

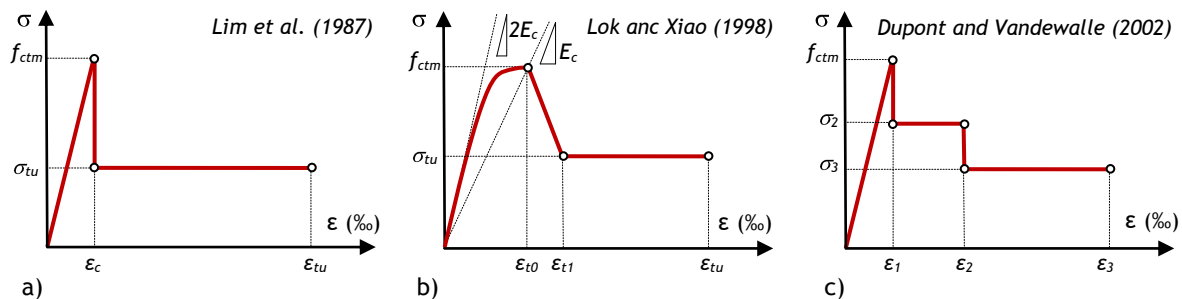


Fig. 2.4 - Examples of stress-strain (σ - ϵ) diagrams proposed in literature.

Regarding the characterization of the post-cracking behavior in terms of stress-crack width relationships (σ - w), Kooiman (2000) advanced a bi-linear diagram for the softening response of SFRC (Fig.2.5a) whose parameters were obtained through inverse analysis procedures. Following a rather different approach, Barragán (2002) proposed a tri-linear model to describe the σ - w based on test results from uniaxial tensile tests (Fig.2.5b). Contrarily to most diagrams obtained from inverse analyses, his proposal does not include a monotonically decreasing function but rather an increment of the residual strength with crack growth up to 2.0mm crack width. Similarly to previous researchers, di Prisco et al. (2004) suggested a bi-linear σ - w curve (Fig.2.5c). The first softening branch is related to matrix cracking and it is taken equal to that proposed by the Model Code (CEB-FIP, 1991) whereas the second branch is related to fiber pullout and accounts for two average stresses at two different crack widths. More recently, Dozio (2008) found out in his research that the position of the break point advanced by di Prisco et al. (2004) was partially overestimated and, consequently, proposed a modified tri-linear diagram (Fig.2.5c) that conducted to improved fitting on his inverse analysis calculations.

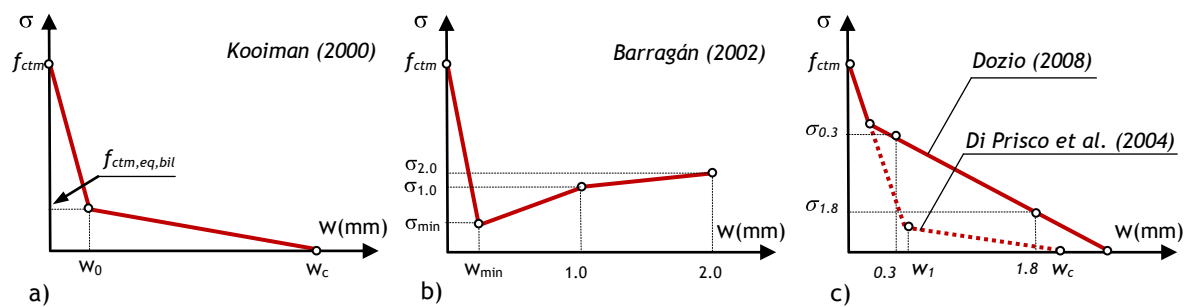


Fig. 2.5 - Examples of stress-crack width (σ - w) diagrams proposed in literature.

Most of the existing constitutive laws in literature simplify the complex behavior of SFRC by adopting continuous non-differentiable diagrams to describe the post-cracking behavior. In opposition to this trend, Lee and Barr (2004) advanced a four-exponential model that characterizes the entire load-deformation response (P - δ) of SFRC with one continuously differentiable function. Because of the complex nature of the SFRC behavior, the authors considered two types of material responses (types A and B, such as shown in Fig.2.6) that can be defined in terms of six input parameters. Despite the non-physical sense of the variables involved in this model, their procedure is very interesting to be implemented provided that differentiation and integration calculations can be readily applied.

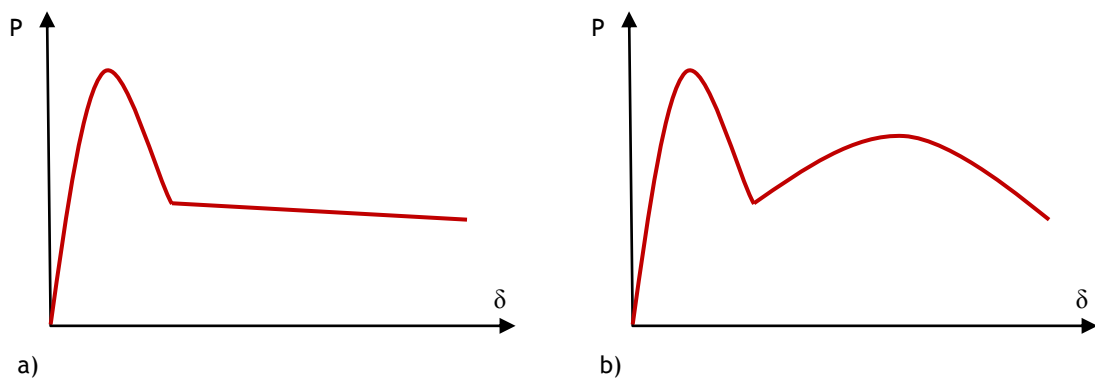


Fig. 2.6 - Four-exponential model by Lee and Barr (2004): a) Response type A; b) Response type B.

In opposition to most of the models that tend to approach the intricate behavior of SFRC through inverse analysis procedures, Li et al. (1993) derived an analytical micromechanical approach to predict the σ - w curve through a direct method. Their model provided significant insight on the physical mechanisms governing the cracking processes of SFRC by means of clear conceptual basis (Fig.2.7a). For that purpose, important concepts such as the softening relation for the plain concrete behavior, the number of fibers crossing a crack, the single fiber pullout behavior, the orientation and distribution of fibers as well as efficiency length factors were taken into account. However, despite the great relevance of this work, its applicability is limited due to the large number of parameters involved and by the fact that its range of application is limited to crack widths up to 0.3mm (Fig.2.7b).

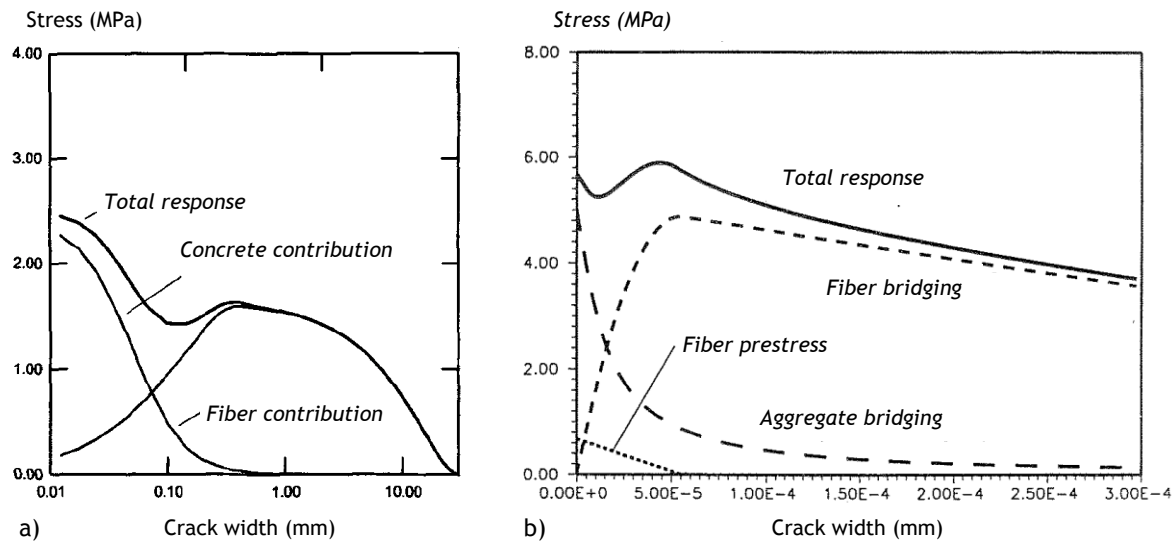


Fig. 2.7 - Micromechanical model by Li et al. (1993): a) Conceptual basis; b) Example of σ - w diagram.

2.2.3 Constitutive models proposed by European Standards and guidelines

Despite the large amount of literature on the specific topic, some basic still open questions feed doubts on the methods proposed by various Technical Committees (di Prisco et al., 2004). Because there is no constitutive law widely assumed for structural design, the existing proposals in European Standards and guidelines should be analyzed and discussed.

In a recent paper by Blanco et al. (2009) an interesting comparative analysis of constitutive models for fiber reinforced concrete was advanced. The authors covered the main features of the most relevant works in Europe, namely: German standards (DBV, 2001), the Italian standards (CNR-DT 204, 2006) and the Spanish standards (EHE, 2008) as well as the guidelines advanced by the RILEM Committee (RILEM TC 162-TDF, 2003). From that work, the shape and the parameters defining the proposed constitutive laws as well as their respective test methods could be summarized (Table 2.1). Other differences concerning relevant aspects for design were also pointed out (Table 2.2).

From Tables 2.1-2.2 it turns out evident that existing standards are based on simplified and continuous non-differentiable diagrams whose parameters are defined through inverse analysis procedures. They approach SFRC tensile behavior from a macroscopic perspective (i.e., irrespectively of the properties of its components) and both σ - w and σ - ϵ diagrams are proposed.

Despite the limitations that can be pointed out to these proposals, it is worth to mention their great relevance as they provide an important basis for the continuous growth of SFRC structural applications.

Table 2.1 - Constitutive models proposed by different European Standards (Blanco et al., 2009).

Diagram	Parameters	Test configuration	Ref.
	$\sigma_1 = f_{ctRd} = 0,33f_{R,3,d}$ $\epsilon_1 = \epsilon_u = [20\% \text{ bending; } 10\% \text{ tension}]$	3-point bending test UNE EN 14651 	EHE
	$\sigma_1 = f_{Ftu} = f_{eq2} / 3$ $\epsilon_1 = \epsilon_u = [20\% \text{ softening; } 10\% \text{ hardening}]$	4-point bending test UNI 11039 	CNR-DT 204
	$\sigma_1 = f_{eq,ctd,II} = f_{eq,ctk,I} \cdot \alpha_c^f \cdot \alpha_{sys} / \gamma_{ct}^f \leq f_{eq,ctd,I}$ $\epsilon_1 = \epsilon_u = 10\%$	4-point bending test NBN B 15-238 	DBV
	$\sigma_1 = f_{eq,ctd,I} = f_{eq,ctk,I} \cdot \alpha_c^f \cdot \alpha_{sys} / \gamma_{ct}^f$ $\sigma_2 = f_{eq,ctd,II} = f_{eq,ctk,II} \cdot \alpha_c^f \cdot \alpha_{sys} / \gamma_{ct}^f \leq f_{eq,ctd,I}$ $\epsilon_2 = \epsilon_u = 10\%$	4-point bending test NBN B 15-238 	DBV
	$\sigma_1 = f_{Fts} = 0,45f_{eq1}$ $\sigma_2 = f_{Ftu} = k[f_{Fts} - (w_u/w_{iz})(f_{Fts} - 0,5f_{eq2} + 0,2f_{eq1})]$ $k = [0,7 \text{ pure tension; } 1 \text{ remaining cases}]$ $\epsilon_2 = \epsilon_u = [20\% \text{ softening; } 10\% \text{ hardening}]$	4-point bending test UNI 11039 	CNR-DT 204
	$\sigma_1 = f_{ctd}^f = \alpha_c^f \cdot f_{ctk,fl} / \gamma_{ct}^f$ $\sigma_2 = f_{eq,ctd,I} = f_{eq,ctk,I} \cdot \alpha_c^f \cdot \alpha_{sys} / \gamma_{ct}^f$ $\sigma_3 = f_{eq,ctd,II} = f_{eq,ctk,II} \cdot \alpha_c^f \cdot \alpha_{sys} / \gamma_{ct}^f \leq f_{eq,ctd,I}$ $\epsilon_1 = \sigma_1 / E_{HRF}$ $\epsilon_2 = \epsilon_1 + 0,1\%$ $\epsilon_3 = \epsilon_u = 10\%$	4-point bending test NBN B 15-238 	DBV
	$\sigma_1 = 0,7 f_{ctm,fl} (1,6-d)$ $\sigma_2 = 0,45 \cdot \kappa_h \cdot f_{R,1}$ $\sigma_3 = 0,37 \cdot \kappa_h \cdot f_{R,4}$ $\epsilon_1 = \sigma_1 / E_{HRF}$ $\epsilon_2 = \epsilon_1 + 0,1\%$ $\epsilon_3 = \epsilon_u = 25\%$	3-point bending test RILEM TEST 	RILEM
	$\sigma_1 = f_{ct,d} = 0,6 f_{ct,fl,d}$ $\sigma_2 = f_{ctR1,d} = 0,45f_{R,1,d}$ $\sigma_3 = f_{ctR3,d} = k_1(0,5f_{R,3,d} - 0,2 f_{R,1,d})$ $\epsilon_2 = 0,1 + 1000 \cdot f_{ct,d} / E_{c,0}$ $\epsilon_3 = 2,5 / l_{cs} (l_{cs}: \text{critical length})$ $\epsilon_u = [20\% \text{ bending; } 10\% \text{ tension}]$	3-point bending test UNE EN 14651 	EHE

* The constitutive model from the FIB Model Code (2007) is equivalent to the Italian Standard (CNR-DT-204).

Table 2.2 - Summary of the main features of the different constitutive models (Blanco et al., 2009).

	DBV	RILEM	CNR-DT 204	FIB MODEL CODE	EHE
Stress-strain (σ - ϵ) / Stress-crack width (σ - w)	σ - ϵ	σ - ϵ	σ - ϵ / σ - w	σ - ϵ / σ - w	σ - ϵ
Indirect approach (IA) / Direct approach (DA)	IA	IA	IA	IA	IA
Continuously differentiable diagram (CD) / Continuous non-differentiable diagram (CND)	CND	CND	CND	CND	CND
Residual strengths (RS) / Equivalent strengths (ES)	ES	RS	ES	ES	RS
Distinction of the ultimate strain, ϵ_u			●	●	●
Value of the ultimate strain, ϵ_u (‰)	10	25	20/10	20/10	20/10
Reduction respect to linear-elastic stress distribution	●	●			●
Application of the characteristic length to obtain strains			●	●	●
Accounts for Safety Factors	●		●	●	●
Accounts for size effects	●	●			
Accounts for long-term loading factor	●				
Accounts for fiber content					
Specific of steel fibers	●	●			
Accounts for fiber contribution in crack spacing		●	●	●	

2.2.4 Demands for an improved modeling method

Ideally, the design of SFRC should be based on a simple and comprehensive method that could reproduce accurately the material's uniaxial behavior. However, because this behavior is very complex and not-uniform, obtaining such method is hard to please. From one hand, the complex nature of the SFRC post-cracking behavior needs to be both well understood and characterized so that designers acquire the confidence to work with this material. From the other hand, clear and simple design rules from Building Codes are strongly required for designers, who hardly accept to voluntarily assume responsibilities by adopting guidelines (di Prisco et al., 2009)

Because there is no constitutive law widely assumed for SFRC structural design, the main characteristics and criteria that are on the basis of the existing proposals in literature, standards and guidelines previously advanced are discussed in the following.

Stress-crack width law (σ - w) and stress-strain law (σ - ϵ)

The use of stress-crack width or stress-strain diagrams to describe the tensile behavior of SFRC has been a subject of major discussion among researchers. Because both approaches have their own advantages and limitations, there has been a tendency to accept these two alternative approaches in recent standards (CNR-DT 204, 2006; FIB Model Code, 2007).

The great benefit from the use of stress-crack width relations is the fact that they provide an actual physical insight of the strengthening mechanisms occurring in SFRC. Moreover, they can be directly compared with experimental results at a material level, such as the ones that can be extracted from uniaxial tensile tests.

Applying a stress-strain relationship for the tensile behavior of SFRC presents two main advantages: 1) because the compressive behavior is also defined this way, σ - ε diagrams provide the chance of using a unique relation to characterize the whole material both in tension and compression; 2) because the strain concept is compatible in design with all other types of materials and resembles the design procedure of traditional reinforced concrete, it can be easily introduced in structural design applications.

From the previous, the author shares the opinion that a σ - ε diagram is more convenient for practical purposes. However, it is also his conviction that modeling and characterization of a material to be used in structural applications requires an overall comprehension of the physical mechanisms involved as well as direct and clear validations with experimental data. Consequently, a σ - w relationship is preferable in what concerns the fundamentals required for the development of the material constitutive model. The link between these two approaches, the characteristic structural length, shall then be investigated in detail in order to attain more robust and reliable stress-strain diagrams for design.

Indirect approach and direct approach

Inverse modeling has traditionally been a popular approach to obtain “equivalent” softening diagrams for SFRC. Although the structural response of SFRC elements can be reasonably fitted through such approach, there are several drawbacks from its use: 1) it requires experimental characterization for each combination of fibers and concrete properties; 2) SFRC properties from experiments is likely to differ from the ones in practical applications due to different production processes (casting, flow, vibration, etc.) that influence fiber distribution and orientation; 3) it does not provide understanding of the material’s post-cracking behavior. Insight can only be gained by trial and error; 4) the suitability of the experimental fitting depends on the convenience of the assumed shape for the constitutive diagram and the prescribed deviation tolerance; 5) because the numerical approach returns the parameters that best fit a predefined shape for the diagram, the procedure provides ambiguous constitutive models regarded that several different diagrams return valid solutions for the fitting problem.

The direct approach requires the definition of the shape of the constitutive relation in order to simulate the material’s uniaxial behavior. The parameters defining the constitutive law may be obtained either from experimental data, such as occurs in standards and guidelines (DBV, EHE, RILEM, etc.), or from specific material properties (Li et al, 1993).

From the author’s point of view, an improved constitutive diagram should be based on a direct methodology that takes advantage of the growing knowledge on the SFRC properties in order to provide a more straightforward method than the inverse analysis one.

Micro-scale and macro-scale research levels

Regarding the complex and non-uniform nature of the SFRC tensile behavior researchers have been approached this topic from different perspectives. Typically, micromechanical approaches cover a wide range of aspects influencing the material behavior and investigate in detail the major governing phenomena. Nonetheless, despite the valuable insight provided by this research line, these approaches tend to be very complex, to involve a large number of parameters and, because concrete microstructure is hardly reproducible in practice, conclusions derived from these studies are hardly extrapolated for general design.

The research carried out at a macro-scale is commonly associated to the inverse analysis procedures. Obviously, fracture properties cannot be defined at the macroscopic level (van Mier and van Vliet, 2002). Although this research line is able to provide information of the material behavior, conclusions are limited to the particular features of the experiments analyzes since no physical understanding can be provided.

According to experts from the fracture mechanics (van Mier and van Vliet, 2002) meso-scale models are the most suitable approach to analyze softening mechanisms such the ones occurring in conventional SFRC. This way, the number and the orientation of fibers across the crack as well as their pullout responses are the fundamental aspects for the material constitutive relationship. Meso-scale models provide a commitment between the physical understanding given by microscopic studies and the practical approach typical of macro-scale levels.

Continuously differentiable and continuous non-differentiable diagrams

An idealized constitutive model for SFRC should be capable of reproducing either the stress-crack width or the stress-strain relationship with large accuracy. However, a commitment between the complexity of the constitutive law and its applicability for design purposes should also be guaranteed.

When deciding which type of diagram is the most convenient, the natural shape of the material tensile behavior has to be considered. Most of the existing constitutive diagrams privilege simplified continuous non-differentiable diagrams. However, because of the non-uniformity of the tensile behavior, a realistic and general constitutive model requires a flexible shape. Consequently, continuous non-differentiable functions are not suitable since a flexible shape would require too many input parameters. In order to overcome this limitation, recent standards (CNR-DT 204, EHE) are proposing alternative continuous non-differentiable diagrams with increasing number of degrees of freedom in order to obtain less conservative results.

Regarding the previous considerations, it becomes evident that a continuously differentiable diagram to describe the post-cracking behavior of SFRC is preferable. Ideally, the major contributions for the tensile behavior (plain concrete and fiber pullouts) should also be identified and characterized by continuously differentiable functions.

2.3 EXPERIMENTAL RESEARCH ON THE TENSILE BEHAVIOR OF SFRC

2.3.1 Overview of existing test methods

Several test methods may be used to determine, direct or indirectly, the tensile behavior of SFRC. Typically, bending tests of prismatic beam specimens are the most currently used to characterize the post-cracking material's response. These can be either based on 3-point tests (EN 14651, 2005; RILEM TC 162-TDF, 2003) or 4-point tests (NBN B 15-238, 1992). Other standard methods have also been used for the material characterization, namely: round determinate panel tests (Bernard, 2000; ASTM C-1550, 2003), splitting tensile tests (Tschegg and Linsbauer, 1986) or uniaxial tensile tests (RILEM TC 162-TDF, 2001). More recently, a method for the quality control of SFRC tensile behavior (Barcelona test) has also been advanced (Molins et al., 2009).

When deciding which test method should be used to characterize the post-cracking behavior of SFRC there are several criteria to be considered (Kooiman, 2000), namely:

- Complexity (test configuration, preparation of the specimens, execution, etc.).
- Complexity of processing test results into a uniaxial material relation.
- Reproducibility of the tests, costs and applicability in practice.
- Reliability and scattering of the test results.

Among these criteria, emphasis has been given on the scattering of the test results due to its implications on the design of SFRC elements. While scattering in bending tests is frequently of 20%, other methods such as the round determinate panel test tend to present lower variations (Molins et al., 2009). When adopting a testing procedure to characterize SFRC, particular care should be given to guarantee that the geometry of the cracked section(s) resembles the application for what it is aimed for, otherwise mechanical properties may differ due to dissimilar orientation of the fibers in both cases.

This brief overview does not intend to analyze in detail the specific limitations presented by each of the aforementioned test methods, but rather to point out their implications for modeling and applications. Most of these testing procedures (bending tests, round determinate panel tests, splitting tests) are quite straightforward for engineering practice but require the use of inverse analysis techniques, which are directly related to the application of numerical models and to the inability of researchers to find true properties of the materials under consideration (van Mier and van Vliet, 2002).

The uniaxial tensile test is the most fundamental test to determine the fracture properties of a material. Despite the complexity and costs associated to this testing procedure, its application is imperative to understand and characterize the actual tensile behavior of SFRC. In fact, when some difficulties are experienced in the uniaxial tensile test, it does not imply that one should revert to an apparently easier experiment to be performed, but more difficult to be interpreted (van Mier and van Vliet, 2002).

2.3.2 Uniaxial tensile tests

A number of technical problems must be solved before a reliable and reproducible uniaxial tensile test has been obtained. Hordijk (1991) carried out an extensive research of the influence of specimen size, geometry and boundary conditions on the uniaxial fracture of plain concrete. He concluded that the uniaxial tensile test is the only test that yields directly all the relevant fracture parameters, even though care must be taken to minimize effects of structural behavior of the test specimen on the measured results. Among these technical problems are the (perfect) alignment of the specimen in the complete loading “chain”, the (perfect) manufacturing of the concrete specimen, the suitability of the test control system, avoiding secondary flexure and solving the attachment of the specimen to the loading platens (van Mier and van Vliet, 2002).

Despite the difficulties inherent to the execution of the uniaxial tensile test, this method is considered to be a robust procedure. This way, although it is not a good method to determine concrete’s tensile strength, the test can be used to directly derive the stress-crack width relation of fiber reinforced concretes (Dupont, 2003).

To the author’s best knowledge, there are few SFRC uniaxial tensile test results reported in technical literature. One of the most relevant works was performed by Barragán (2002) who carried out a large experimental campaign on molded and cored notched specimens and advanced recommendations in terms of specimen’s geometry, measuring systems and the overall test setup. Taking this work as reference, other investigations assumed different testing procedures, either in terms of the specimen’s geometry (Markovic, 2006) or with regard to the attachment of the specimen to the loading machine (Stälhi, 2008).

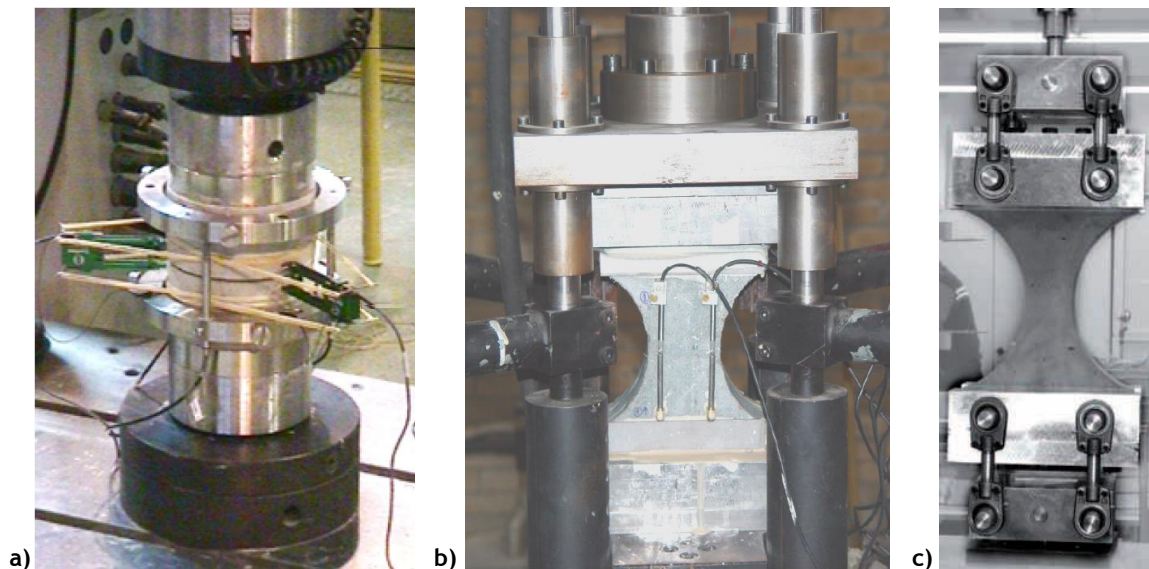


Fig. 2.8 - Different uniaxial tensile tests configurations: a) Barragán (2002); Markovic (2006); Stälhi (2008).

So far, although there is not a standardized uniaxial tensile test, a significant contribution has been advanced by RILEM TC 162-TDF (2001) which provides useful recommendations for testing SFRC with softening behavior.

2.4 PULLOUT BEHAVIOR OF STEEL FIBERS

Adding steel fibers to cementitious matrices reduces concrete brittleness and enhances crack width control. Such beneficial effects arise from the crack bridging capacity provided by fibers which is achieved through the development of bond-slip mechanisms with the surrounding matrix. Bond is recognized as a major factor in composite action (Naaman and Najm, 1991) and thereby the study of the fiber/matrix interface is important both for the predictive capability and tailoring procedures of fiber reinforced composites (Li and Stang, 1997). However, despite the intensive research that has been carried out, there is no standard method to measure bond in fiber-reinforced cementitious composites (Guerrero and Naaman, 2000). An indirect method which has been shown to produce reasonable accurate results is the single fiber pullout test. The latter has been performed by means of several test configurations, such as shown in Fig.2.9.

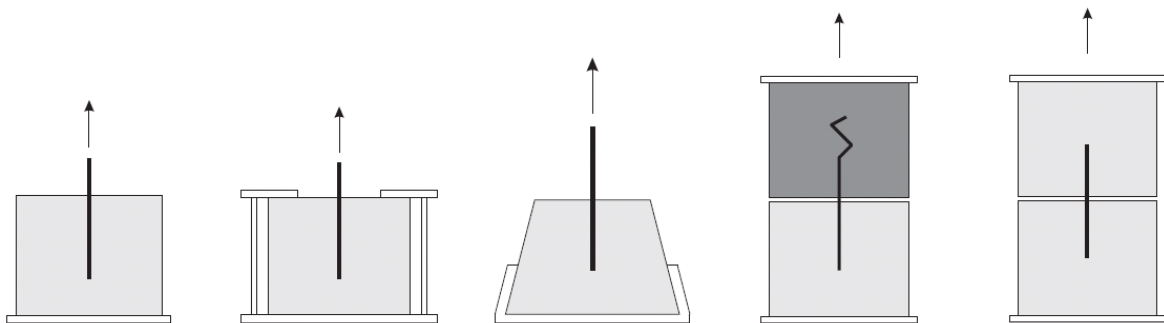


Fig.2.9 - Examples of pullout test configurations (Cunha et al., 2007).

2.4.1 Straight fibers

Numerous experimental pullout tests in straight steel fibers have been carried out in the past (Naaman and Shah, 1976; Shannag et al., 1997; Guerrero and Naaman, 2000). Concurrently many researchers developed analytical and numerical models both for solving the direct problem, whereby the pullout curve is predicted from an assumed bond-slip relationship (Naaman et al., 1991; Banholzer et al., 2005) and the inverse problem, in which the bond-slip relationship is obtained from an experimental pullout curve (Naaman et al., 1991; Banholzer et al., 2006; Cunha et al., 2007). Nonetheless, both pullout and bond-slip relations are sensitive to fiber orientation. Thereby regarding the randomly orientation of fibers in steel fiber reinforced concrete the pullout responses of fibers aligned with load direction (orthogonal to crack surface) become somehow misleading for modeling the composite tensile behavior. Predicting the pullout response of inclined fibers is therefore of paramount importance.

In the first tests performed by Naaman and Shah (1976) it was observed that the peak pullout load of an inclined fiber was almost as high as that of an aligned one. Moreover they found out that the work required to completely remove an inclined fiber was higher than that of the aligned case. Subsequently several investigations reported similar tendencies (Leung and Shapiro, 1999; Van Gysel, 2000; Cunha et al., 2007) and most authors concluded the existence of an optimal angle for which load and energy absorption capacity are maximal.

Mechanisms governing pullout response of inclined fibers are different from those verified on the aligned ones. Indeed, besides fiber debonding and friction along the interface, additional phenomena are introduced such as fiber bending, matrix spalling and local friction effects (Fig.2.10). Furthermore, the contributions of these micromechanisms depend on fiber inclination angle and on several material properties which need to be considered for modeling purposes.

Several proposals can be found in the literature to model pullout behavior of inclined steel fibers. Classical approaches assume that the condition of perfect bond persists until a failure criterion on the interface of fiber and matrix is attained. Models based on energy failure criteria (Shah and Ouyang, 1991) are very rare because of difficulties on measuring the critical interface debonding energy. Cohesive interface models, in which bond stresses are only due to slip between steel and cement-based matrix, perform an alternative procedure. However regarding that bond properties cannot be generalized and have to be measured in each single case (Shah and Ouyang, 1991) these models do not carry out analytical formulation and therefore heavy numerical iterative procedures are required (Fantilli and Vallini, 2007). Hence the evaluation of bond properties using a classical approach based on stress criterion turns out to be the most widely reported in the literature.

The first attempt to model the bridging force accounting for bending of the fiber was advanced by Morton and Groves (1974) who predicted the maximum force required to produce a given deflection of an elastic or perfectly plastic fiber in epoxy matrix. However debonding and friction on pullout of straight fibers are neglected and the assumption of yielding matrix renders it inapplicable to brittle composites such as the cementitious ones. Some years later Li et al. (1990) simulated fiber pullout as a beam bending on an elastic matrix. In such model fibers were so flexible that all the deformation was assumed to occur around the exit point of the fiber and therefore it could be idealized as string passing through a frictional pulley. Despite the good agreement with experimental results only the maximum pullout load could be obtained and none approach for the pullout load-displacement relationship was advanced. Furthermore, although spalling of the matrix and fiber bending were widely observed in the experiments they were disregarded in the model. Therefore its applicability at large inclination angles is questionable (Leung and Ybanez, 1997).

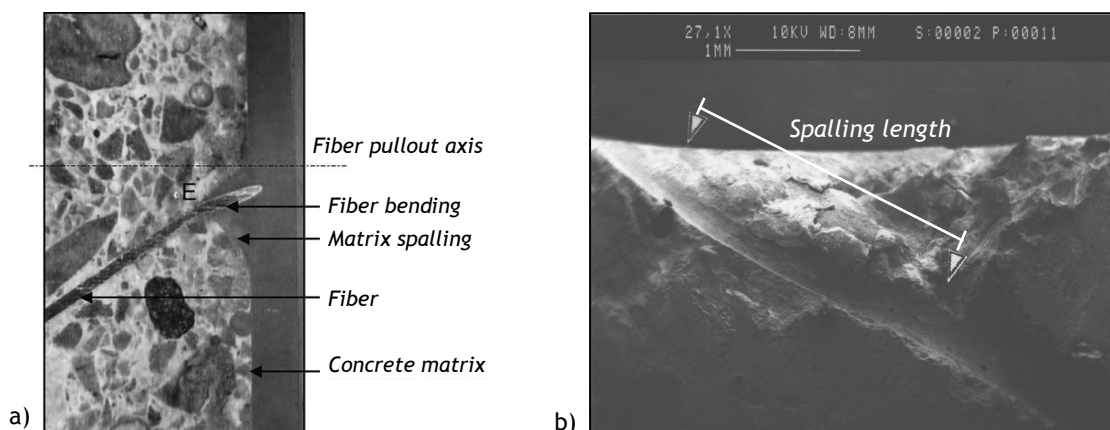


Fig.2.10 - Micromechanisms in the pullout of inclined fibers: a) Photography by Cailleux et al. (2005); b) Identification of the spalling length with scanning electron microscopy (Leung and Shapiro, 1999)

To overcome such limitations Leung and Li (1992) treated the embedded part of the fiber as a beam resting on an elastic and heterogeneous foundation whose stiffness and failure criterion were obtained by means of a finite-element model. Despite the good predictions with experimental data, the accuracy of the spalling effect was sensitive to the mesh used and the concentration of frictional load at fiber exit point was disregarded. Following the concepts advanced in this model, Katz and Li (1995) developed a numerical approach to account for the coupled effect of fiber debonding and bending mechanism of carbon fibers in cementitious composites. They found out that the superposition of the axial loading and bending effects separately (uncoupled approach), although valid for small crack widths (less than half diameter of the fiber), may lead to severe underestimation of the contribution of bending to the total bridging load for large crack widths. However their approach is somewhat limitative since it requires several empirical parameters based on pullout tests at different inclination angles in order to identify the model constants (Cailleux et al., 2005). Recently Cailleux et al. (2005) developed an analytical pullout model of inclined fibers based on strength of materials theory, taking into account fiber bending, matrix spalling and concentrated friction load at matrix exit point which provides a comprehensive physical understanding of the pullout process. However, likewise previous models, the procedure embodies considerable amount of parameters which can only be obtained through pullout tests on aligned and inclined fibers.

Regarding the aforementioned drawbacks on existing approaches, modeling the pullout response of inclined fibers seems to remain a topic open to discussion. Indeed existing procedures tend to introduce significant amount of empirical and experimental parameters which do not allow straightforward approaches for design and tailoring purposes. Furthermore, in most cases, their limitations do not arise uniquely from these aspects. Validation of existing models has been performed over experimental data obtained through several types of pullout test configurations which suitability on representing realistic pullout mechanisms, such as the ones occurring in SFRC, are highly questionable. Likewise, it is not surprising that a considerable number of experimental researches report results that are not always in agreement (Shannag et al., 1997).

2.4.2 Hooked fibers

Among the various attempts to improve bond-slip characteristics between fibers and the cement matrix, the most effective is mechanical deforming. Thereby it is not surprising that almost all commercially available fibers at present are mechanically deformed (Banthia and Trottier, 1994) and that they have been conceived and introduced in the market over thirty years ago (Naaman, 2003). However, most of bond-slip investigations focused primarily on fibers without deformations (straight fibers) and therefore scarce knowledge on behavior of deformed fibers led to commercial geometries which were only “intuitive” (Banthia and Trottier, 1994).

To understand the effects of fiber geometry on the mechanical behavior of SFRC pullout tests on aligned fibers have been extensively carried out during the years (Naaman and Najm, 1991). Nonetheless mechanisms associated with pullout behavior of deformed fibers are not well understood (Robins et al., 2002) and, apart from experimental observations, few models attempted to account for the mechanical deformation (Van Gysel, 2000; Chanvillard, 1999; Alwan et al., 1999; Sujivorakul et al., 2000).

Modeling the effect of the hook on steel fibers was advanced by Van Gysel (2000) by assuming that hook geometry is a sum of straight and curved segments. Using the principle of energy conservation advanced by Chanvillard (1999) the procedure is based both on theoretical and experimental considerations and accounts for fiber debonding, plastic deformations and additional frictional forces due to incomplete straightening of the hook. An alternative approach was proposed by Alwan et al. (1999) using the concept of a frictional pulley along with two plastic hinges to simulate the hook action. The model consists of a two-step procedure and considers the contribution of two hinges at the first stage and one hinge superposition accounting for frictional and mechanical components. Subsequently a new model based on the concept of nonlinear springs to resemble the effect of the hook was advanced by Sujivorakul et al. (2000). Applying an iterative procedure over the geometry of the mechanical anchorage, the approach superposes the effect of the spring on previous pullout models for straight fibers (Naaman et al. 1991).

Despite the valuable understanding provided by the aforementioned models, their focus relies on the strengthening contribution provided by the hook on the pullout of aligned fibers. Nonetheless further complications arise when fibers lay under a certain inclination angle respect to load direction and the stress field in the vicinity of fiber becomes highly complex, as occur in actual composite (Banthia and Trottier, 1994).

Research on the pullout response of inclined fibers with hooked ends has been performed mostly on experimental basis. Likewise, extensive works investigated the influence of fiber inclination angle (Banthia and Trottier, 1994; Armelin and Banthia, 1997; Van Gysel, 2000; Robins et al., 2002; Cunha et al., 2007) and embedded length (Van Gysel 2000; Robins et al., 2002; Cunha et al., 2007) on the pullout behavior. In some experiments different strengths of cementitious matrices (Banthia and Trottier, 1994; van Gysel, 2000; Robins et al., 2002) and fiber yield strengths were applied (Van Gysel, 2000) and the influence of the hook was evaluated by comparing pullout responses with the ones of straight fibers (Naaman and Najm, 1991; Cunha et al., 2007). The dramatic influence of the inclination angle on the load-crack width contribution of hooked steel fibers is exemplified in Fig.2.11.

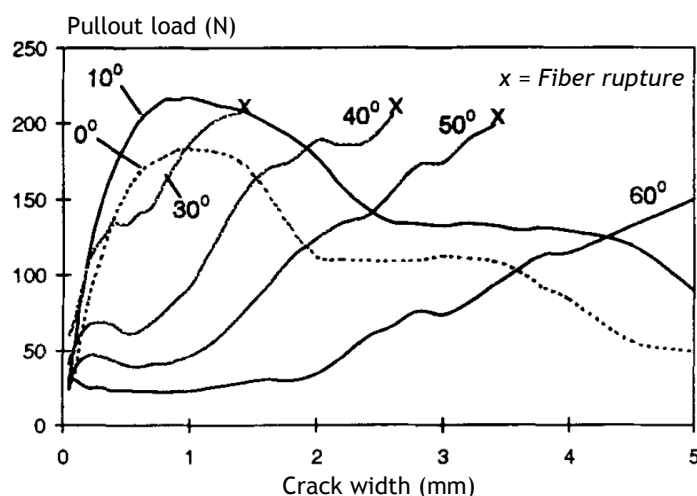


Fig.2.11 - Pullout responses of hooked steel fibers at different inclination angles (Robins et al., 2002).

Although the foregoing works allow an effective quantification of differences on pullout behavior with varying parameters, they are restricted to a set of experimental boundary conditions and material properties. Their capacity on providing an effective understanding of the pullout mechanisms is very limited and justifies why none model has been able to fully explain what actually happens at the critical cracked section in terms of fiber-matrix interactions (Prudencio et al., 2006).

Regarding that fiber pullout is the major mechanism contributing to toughness of SFRC (Taerwe and Van Gysel, 1996) a proper prediction on the pullout behavior of inclined fibers is of the utmost importance for composite design and tailoring. So far, reliable and suitable predictions for the pullout responses of inclined hooked steel fibers are still required.

2.5 THE ORIENTATION OF FIBERS IN SFRC

Substantial increase in the tensile strength and toughness are the most acknowledged features of fiber reinforced concrete (Shah, 1991). Such enhanced properties arise from fiber effectiveness on crack-width control, which depends on the individual performance of all fibers crossing a crack. Modeling the overall fiber bridging force thus requires the actual amount of fibers under each inclination angle and their respective pullout responses.

Predicting the tensile response of FRC through the superposition of single fiber pullout responses has been investigated by several researchers (Van Gysel, 2000; Markovic et al., 2004). However, most of the existent approaches are hindered by use of the concept of orientation number. In fact, considering that an average orientation can be obtained through several combinations of individual values and that pullout responses of fibers under different inclination angles are rather distinct (Banthia and Trottier, 1994; Armelin and Banthia, 1997; Van Gysel, 2000; Robins et al., 2002; Cunha et al., 2007), it is not surprising why significant scattering on mechanical properties of FRC is frequently observed. Thereby, although the orientation number is a very simple and intuitive parameter, a more robust and detailed data of fiber orientation is required.

In order to overcome the drawbacks introduced by the orientation number on the superposition approach, fiber orientation should be characterized through the complete distribution of orientation angles occurring at the crack-bridging zone. Seeking to develop such a rationale method to describe the composite behavior, this concept has actually been adopted by other researchers (Jones et al., 2008) thanks to the use of X-ray equipment (Robins et al., 2003). Indeed, given that the development of improved techniques to measure fiber orientation has been of particular relevance, the superposition approach performed in such form makes possible the development of more comprehensive constitutive models.

2.5.1 Methods to measure the orientation of steel fibers

The existing techniques to characterize the orientation of steel fibers may be categorized in destructive or non-destructive methods and based in direct or indirect measurements.

A popular example of a destructive and indirect measurement of fiber orientation is manual counting (Soroushian and Lee, 1990; Gettu et al., 2005; Dupont and Vandewalle, 2005), a method which relates the number of fibers in a cross-section with the average orientation of fibers by means of a theoretical expression (Krenchel, 1975). Because the average fiber orientation has been found to be proportional to the post-cracking strength of SFRC many investigations have also been evaluating indirectly fiber orientation through mechanical testing (Kooiman, 2000; Barragán, 2002; Grünewald, 2004).

Direct measurements of single fiber orientation can be obtained through techniques such as the image analysis (Grünewald, 2004; Lappa, 2007), X-Ray method (Van Gysel, 2000; Robins et al., 2003; Vandewalle et al., 2008) or computerized tomography (CT-scans) (Molins et al., 2008; Stälhi and van Mier, 2007). An example of the results that can be extracted from these two last techniques is shown in Fig.2.12. Because of limitations in the size of the specimens, these techniques are mostly restricted to laboratory specimens. Moreover, regarding the complexity, time-consumption and cost of these techniques, they have been mostly limited to research purposes. Hence, a major challenge consists on obtaining the orientation of fibers in great detail, such as provided by these refined methods, but using non-destructive techniques.

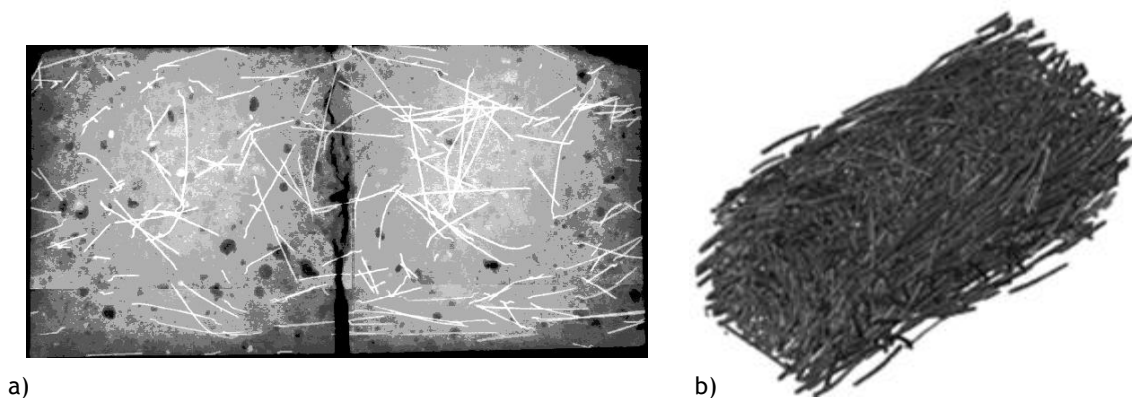


Fig.2.12 - Measurements of fiber orientation by means of: a) X-Ray images (Vandewalle et al., 2008); b) 3-D reconstruction of fiber orientation obtained through CT-scans (Stälhi et al., 2008).

Recently, there have been significant advances in the development of non-destructive methods to determine the orientation of steel fibers in large-scale elements. Examples of these methods are the alternating current-impedance spectroscopy (AC-IS) (Ozyurt et al., 2006; Ferrara et al., 2008), the open coaxial transmission line (Torrents et al., 2007), the dielectric waveguide antennas (Roqueta et al., 2009) and methods based on electrical resistivity (Lataste et al., 2008). These methods allow simple and economical measurements of fiber orientation and have the great advantage that uncertainties that tend to exist between small and large-scale elements can be avoided.

So far, a complete characterization of both fiber distribution and orientation requires destructive (and expensive) methods. A synergy between destructive and non-destructive methods may provide a reasonable approach for future structural applications.

2.5.2 Identification of causes for anisotropic orientations

Among the major aspects influencing fiber orientation (Fig.2.13), the wall-effects introduced by the formwork (Romualdi and Mandel, 1964; Kameswara, 1979; Krenchel, 1975; Soroushian and Lee, 1990; Hoy, 1998; Stroeven, 1999; Kooiman, 2000; Van Gysel, 2000; Dupont and Vandewalle, 2005) and the fresh-state properties of SFRC (Grünewald, 2004; Stälhi and van Mier, 2007; Ferrara et al., 2008; Martinie et al., 2009) are most affecting.

The way concrete is poured into the mould has also been recognized to have a major impact on fiber orientation, both due to the casting direction and due to preferential fiber alignment induced by the casting element itself (Toujanji and Bayasi, 1998; Markovic, 2006; Torrijos et al., 2008). The effects of vibration on causing fibers to rotate into planar orientations have been reported in literature (Eddington and Hannant, 1972; Gettu et al., 2005) and, in case of self-consolidating concrete, the flow of the fresh concrete has also been identified to play a major role on fiber alignment (Grünewald, 2004; Ferrara et al., 2007; Lappa, 2007).

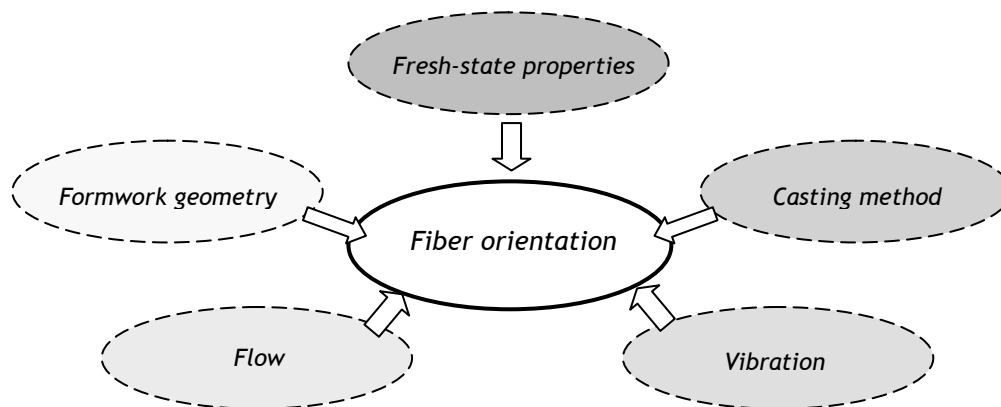


Fig.2.13 - Major aspects influencing the orientation of steel fibers.

Research on fiber orientation has been carried out mostly from an experimental perspective and the few advanced theoretical approaches refer uniquely to the quantification of wall-effects on idealized isotropic FRC (Dupont and Vandewalle, 2005). How to quantify the combined influence of all the aforementioned aspects on fiber orientation is therefore a big question mark.

2.5.3 Current approach to determine the orientation of fibers

The average fiber orientation in a certain direction is generally considered through the so-called orientation number (n). This parameter is frequently applied on experimental investigations to quantify the influence of one of the aforementioned aspects on fiber orientation by isolating it from the others. For instance, the effect of the casting direction has been quantified by considering elements poured in different positions while keeping all the remaining aspects constant (Toujanji and Bayasi, 1998; Torrijos et al., 2008). Another example consists on inferring

the effects of compaction by subtracting from the measured η the theoretical values of idealized isotropic FRC affected by the wall-effects (Soroushian and Lee, 1990).

Both procedures are straightforward and allow gaining insight on the magnitude of the influence that each aspect has on fiber alignment. Hence, up to the present, the parameters governing fiber orientation are approached independently from each other, i.e., from an isolated perspective, such as shown in previous Fig.2.13. However, considering the nature of these aspects, its determination through such isolated perspective is arguable.

Can preferential fiber alignment induced by the casting direction be quantified by disregarding the type of casting element applied?

Is it reasonable to account for the wall-effects of the mould under an isotropic fiber orientation assumption when anisotropy due to fresh-state properties, casting and compaction processes is likely to occur?

The answer to these questions seems to be obvious. By making use of an isolated procedure, fiber orientation can only be quantified for the very specific characteristics of materials and production processes applied and for the geometry of the element produced. Conclusions extracted with such a procedure are therefore limited and hardly possible to be extrapolated for different scenarios.

2.6 CONCLUDING REMARKS

The first part of this chapter reviewed the main criteria and characteristics of the existing constitutive models in literature, standards and guidelines. At this time, no single constitutive law is widely assumed to characterize the tensile behavior of SFRC. The advantages and limitations of the current procedures were discussed and the demands for an improved constitutive law were advanced. Ideally, the material's behavior should be defined in terms of a stress-strain law by means of a continuously differentiable diagram, applying physical concepts from a meso-scale level and calculated through a direct approach. Because the experimental validation of the constitutive law should be performed at a material level, the stress-strain curve should be firstly defined by means of a coherent stress-crack width relationship and then linked through an appropriated characteristic structural length.

Having identified the motivations and the target goal of this research work, the second part of this chapter covered the state of the art of the subjects addressed in this thesis. Firstly, a brief review of the existing methods to determine the tensile strength of fiber reinforced concretes was performed. Because the uniaxial tensile test was identified as the most suitable method to evaluate the post-cracking behavior of SFRC for modeling purposes, previous experimental works using this method were analyzed. The major aspects governing the tensile behavior were then reviewed: First, the pullout behavior of straight and hooked steel fibers was discussed. It was concluded that a simple and conceptual method to predict the load-crack width curves of these fibers for any inclination angle was missing out. Second, the methods to measure and determine

the orientation of steel fibers were evaluated. With respect to the measuring techniques it was concluded that a synergy between destructive and non-destructive methods might be promising for future structural applications. Regarding the current approach used to determine the orientation of fibers it was concluded that the causes for anisotropic fiber alignments cannot be evaluated independently due to their coupled nature.

Chapter 3

Uniaxial tensile tests

3.1 INTRODUCTION

Modeling the tensile response of SFRC requires reliable and extensive experimental test results both for the analysis of the material behavior and for validation purposes. In this way, the uniaxial tensile test was identified in the previous chapter as the most suitable test method but, at the same time, the one presenting the largest scarcity of available data. For modeling purposes, the uniaxial tensile tests are particularly convenient regarding that the test results directly provide the stress-crack width relation of the material.

With the aim of identifying the shape of the stress-crack width responses at different combinations of fiber contents and concrete strengths, an extensive experimental campaign of uniaxial tensile tests in self-compacting steel fiber reinforced concrete (SCSFRC) was carried out. This chapter describes the main features of the experimental program and discusses the most relevant results obtained.

3.2 EXPERIMENTAL PROGRAM

3.2.1 Research parameters

Regarding that the post-cracking response of SFRC is significantly influenced by the main characteristics of its components, different combinations of matrix properties and fiber contents should be analyzed in order to quantify in what extent the material's tensile response is affected. This work investigated two different concrete matrices, one of normal strength (type A) and the other one of high-strength (type B), and several typical fiber contents were considered (0, 20, 40 and 60 Kg/m³). A total of 8 series were performed (Table 3.1), each one comprising 6 specimens (total of 48 tests).

Table 3.1 - Notation and characteristics of the series produced.

Mixture composition	A	A	A	A	B	B	B	B
Fiber content (kg/m ³)	0	20	40	60	0	20	40	60
Notation	A0	A20	A40	A60	B0	B20	B40	B60

3.2.2 Properties of the materials

Several researchers have shown that the performance of steel fibers in the hardened-state can be improved in self-compacting concrete matrices (Grünwald, 2004; Ozyurt et al., 2007). Thereby, it was decided to investigate the uniaxial tensile behavior of self-compacting SFRC. Two mixtures of reference were adopted (Table 3.2). The water contents were adjusted for each serie to account for the absorption and humidity of the aggregates at the instant of production.

Table 3.2 - Composition of the SCSFRC mixtures (in kg/m³).

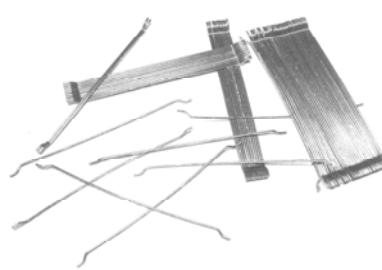
	A		B	
	Characteristics	Quantities	Characteristics	Quantities
Gravel (12/20mm)	Limestone	328.1		
Gravel (5/12mm)	Limestone	447.6	Limestone	834.8
Sand (0/5mm)	Limestone	337.3	Limestone	791.4
Sand (0/2mm)	Limestone	602.6		
Cement	CEM I 52.5 N	334.0	CEM I 52.5 R	432.0
Filler	Limestone	100.0	Limestone	130.0
Silica fume				43.2
Water		181.4		195.8
Superplasticizer	Sika Viscocrete 5920®	6.35	Sika Viscocrete TSG®	12.31

In order to avoid significant loses of workability due to the addition of the fibers, compositions shown in Table 3.2 were modified. This way, the amount of the coarser aggregate was reduced by a quantity equal to the weight of the fibers and by adjusting the superplasticizer content.

Concrete was produced in a 200 liter vertical axis mixer with the following mixing process: 1) dried components were mixed during 1 minute; 2) Addition of water; 3) after total water addition, paste was mixed for two minutes; 4) Addition of the superplasticizer and steel fibers; 5) concrete was mixed for two additional minutes.

Steel fibers were of Dramix® RC 80/60 BP with circular cross-section and hooked ends. Fibers were made of high carbon steel and were gathered into bundles by water-soluble glue. The main properties of the fibers are summarized in Table 3.3.

Table 3.3 - Characteristics of the steel fibers.

Length (L)	[mm]	60.0	
Diameter (d)	[mm]	0.75	
Aspect ratio (L/d)	[-]	80	
Tensile yield strength (f _y)	[Mpa]	2000	

3.2.3 Preparation of the specimens

From each of the eight aforementioned series six cylindrical moulds of 150 × 300 mm were cast by following the RILEM recommendations (2001). The casting process was performed by means of plastic pails and filling of the entire mould was done continuously in all specimens. After casting the steel moulds the top surfaces were smoothly leveled and covered by a plastic sheet for 24 hours. After this time, the elements were demoulded and placed in a curing chamber until the instant of testing at 20 ± 2 Celsius degrees and 95% of relative humidity.

The geometry of the specimens to be tested also followed the RILEM recommendations (2001). This way, both the nominal diameter and length of the specimen would have to be equal to 150 mm. In order to accomplish the last requirement specimens were sawed twice along the height of the original volume, such as depicted in Fig.3.1. With this procedure the orientation of fibers in the specimens to be tested were free from the top and bottom wall-effects.

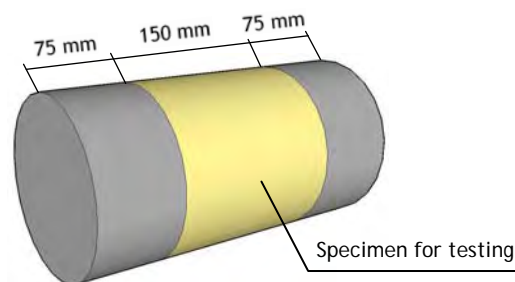


Fig.3.1 - Identification of the specimen to be tested in the original volume.

During the sawing procedure (Fig.3.2a) particular care was given in order to guarantee smooth end surfaces and as much perpendicular to the cylinder axis as possible. After this operation a circumferential notch was created at mid-height of the specimen in order to guarantee crack localization during the tests. The notch had 2 mm width and 15 ± 1 mm depth, thus reducing the nominal diameter of the central section to 120 mm. This operation was executed such as shown in Fig.3.2b. Both of these operations were performed at a minimum age of 7 days.

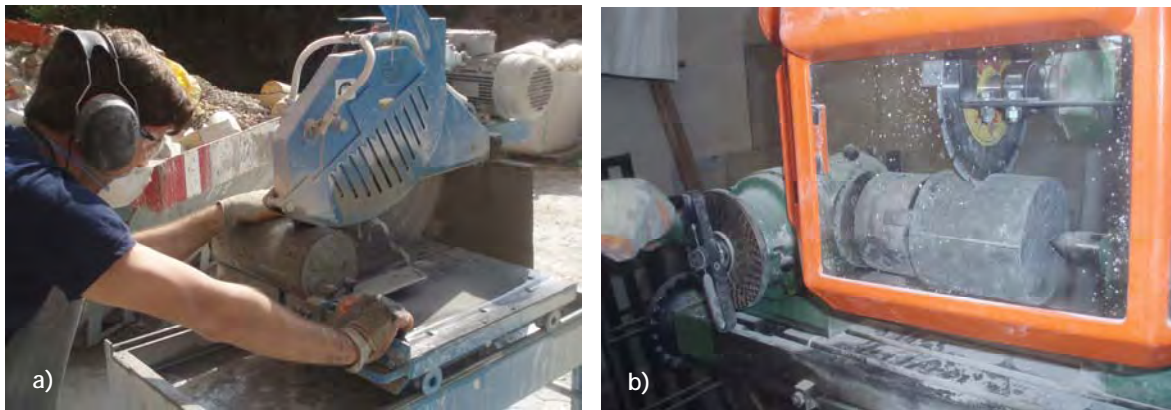


Fig. 3.2 - Preparation of the specimens: a) Sawing procedure; b) Creation of the notch.

3.2.4 Setup and testing procedures

This experimental campaign was carried out in the laboratory of structure's technology at the *Universitat Politècnica de Catalunya* in Barcelona. This facility provided an Instron 8500 servo-hydraulic testing system with stiff frame and closed-loop control which was used to perform the uniaxial tensile tests.

The testing procedures were based on the RILEM recommendations (2001) and on previous experiences carried out in this laboratory by Barragán (2002). Five main steps were followed:

1. Calibrations of the load cell and the measuring instruments.
2. Glue the specimen to the upper steel plate of the testing machine.
3. Glue the specimen to the lower steel plate of the testing machine.
4. Placement of the extensometers around the notched section.
5. Run the test under displacement control, recording the load and the individual measurements and controlling the test through the average signal of the extensometers.

In steps 2 and 3, steel plates were clamped to the testing machine in order to avoid rotations during the test. Fixing the specimen to the steel plates was performed using fast-setting two-component adhesive (X60-NP Schnellklebstoff, HBM®). Particular care was required when mixing the two components (powder and solvent) in order to guarantee an appropriate consistency for the glue. Small percentages of powder lead to a fluid and poor glue mixture that may compromise a rigid connection of the specimen to the steel plates. On the other hand, large

portions of powder return glue mixtures with excessive viscosity, which may lead to two problems: 1) introduction of axial stresses in the specimen due to hardening of the glue. Specimens had to be subjected to a minimum of 5.0 kN compressive load in order to avoid this from happening; 2) uniform spreading of the adhesive may not be attained within the entire surface of contact with the steel plate. This could induce crack initiation at the specimen/steel plate interface rather than at the notched section during the tests.

Fig.3.3a shows the aspect of an appropriate glue mixture. This was placed either in the center of the specimen (step 2) or in the center of the steel plate (step 3), such as shown in Fig.3.3b. Uniform spreading of the glue within the entire surface of contact was guaranteed whenever it reached the entire perimeter of the specimen's cross-section (Fig.3.3c).

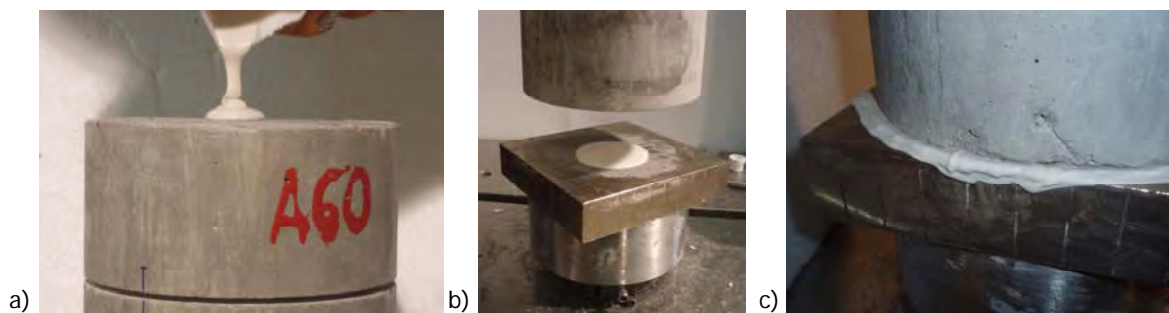


Fig.3.3 - Fixing the specimen to the testing machine: a) Placement of the adhesive in the top surface; b) Aspect of the glue when fixing the lower steel plate; c) Detail of the specimen after glue's hardening.

Step 4 of the testing procedure consisted in placing three extensometers around the notch at 120° between each other, such as shown in Fig.3.4. Then, the uniaxial tensile tests could finally be performed. Two measuring equipments were available, namely: the average signal of the extensometers (ASE) and the linear variable displacement transducer (LVDT) of the testing machine. The three extensometers had 25.0 mm gage length and 5.0 mm span. Regarding that the individual measurements of the extensometers may be slightly different from the average value (Barragán, 2002) the range of accuracy for the ASE readings was considered up to 4.0mm. This way, six main stages were defined in order to accomplish a commitment between results accuracy and the time consumed per test (Table 3.4).

Table 3.4 - Stages of the uniaxial tensile test.

		Stage					
		1	2	3	4	5	6
Displacement rate	[mm/min]	0.005	0.050	0.100	1.0	1.0	5.0
Displacement upper bound	[mm]	0.05	0.20	0.50	4.0	6.0	60.0
Control		ASE	ASE	LVDT	LVDT	LVDT	LVDT
Readings		ASE	ASE	ASE	ASE	LVDT	LVDT

ASE = Average Signal of the Extensometers; LVDT = Linear Variable displacement transducer

Stage 1 is very sensitive due to concrete failure and the respective change on the specimen's stiffness. At this stage, the uniaxial tensile response is mostly dependent on the matrix composition. In stage 2, however, steel fibers play the major role as they start absorbing the tensile stresses. In both of these stages the test control is performed through the average signal of the extensometers. Then, in order to prevent any instability during the test, the control of the subsequent stages was done through the LVDT of the testing machine.

As the post-cracking behavior becomes governed uniquely by fiber pullout mechanisms the crack opening rate can be increased. Increments were introduced progressively to avoid instability of the measurements. At a crack width of 4.0 mm (end of stage 4) test were suspended for a couple of minutes to extract the extensometers around the notch. Afterwards, both the readings and control of the test were done through the LVDT of the testing machine. The same displacement rate of stage 4 was kept until a maximum crack width of 6.0 mm in order to guarantee that the hooked end of the removed part of the fiber was fully deformed. Then, the test proceeded at a larger displacement rate until the physical separation of both parts of the specimen.

The duration of the test itself was about 35 minutes for each specimen. Data acquisition was performed with a frequency of 2.0 Hz.

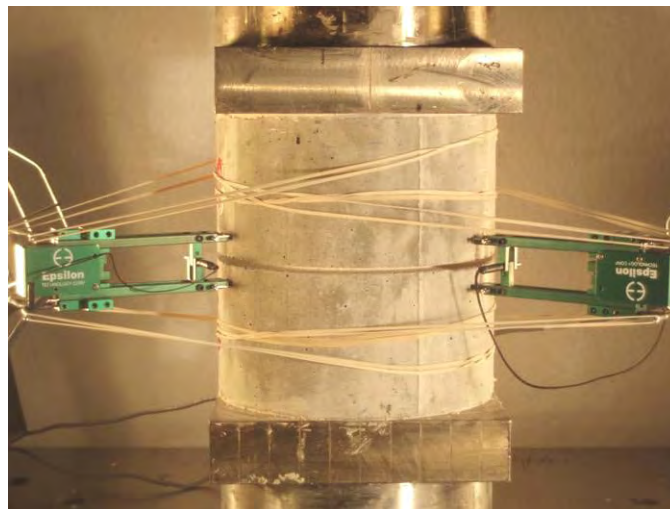


Fig.3.4 - Configuration of the uniaxial tensile test.

3.3 CHARACTERIZATION OF THE SCSFRC

3.3.1 Fresh state properties

The main requirements of fresh self-compacting concrete (SCC) are filling ability, passing ability and resistance to segregation (RILEM TC 188-CSC, 2006). In order to verify whether these requirements could be satisfied in the eight manufactured series, the rheological properties of the SCSFRC were analyzed. With these results, the effect of fiber additions on the fresh-state properties could also be investigated.

The fresh-state properties of the SCSFRC were evaluated by means of slump flow tests (Fig.3.5a), J-ring tests and through a viscosimeter (Fig.3.5b). In the slump flow test the filling ability of the mixture is assessed through the average of two perpendicular diameters of spread concrete (D_f) and the time taken by the mixture to spread up to a diameter of 500 mm (T_{50}). The test also allows a qualitative evaluation of the material stability by analyzing signs of segregation such as irregular distribution of coarse aggregates, existence of coarse aggregates without mortar or separation of the paste around the perimeter. In order to quantify the passing ability, the J-ring test measures the average spread diameter (D_j) as well as the average difference of concrete heights inside and outside the ring (H_j). The viscosimeter is an alternative method to measure the most relevant rheological properties, namely the yield strength (τ_{00}) and the plastic viscosity (μ_{pl}). A BMB-Viscosimeter 3 was used for the material characterization, but the equipment was only available for series A0, A20 and A40.

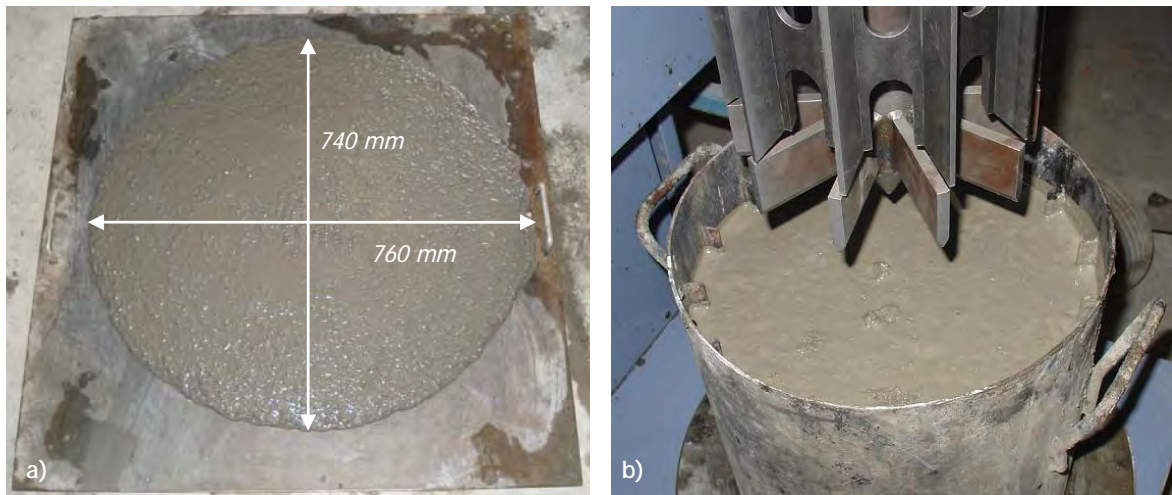


Fig.3.5 - Characterization of the fresh-state properties:
a) Slump flow test of serie B20; b) Serie A0 in the viscosimeter.

The outcome from the characterization of the fresh-state of the eight manufactured series with these three methods is summarized in Table 3.5.

Table 3.5 - Results from the characterization of the fresh-state properties.

			A0	A20	A40	A60	B0	B20	B40	B60
Slump flow	D_f	[mm]	620	745	745	715	695	750	720	660
	T_{50}	[sec]	1.3	1.9	1.7	1.8	1.9	1.7	3.2	2.4
J-ring	D_j	[mm]	645	---	715	600	640	640	580	505
	H_f	[mm]	3	---	25	36	8	28	26	45
Viscosimeter	τ_0	[Pa]	25.5	7.0	12.7	*	*	*	*	*
	μ	[Pa.sec]	38.0	42.2	53.5	*	*	*	*	*

* Inoperability of the equipment

Analysis of the slump flow tests

The effect of different types and contents of steel fibers in the slump flow is quantified through the fiber factor (Groth and Nemegeer, 1999), a parameter that accounts for the volume fraction of fibers (V_f) and their aspect ratio (L/d). In theory, the slump flow should decrease at increasing fiber factors because of the larger specific surface of the fibers with respect to the coarse aggregates that were substituted in these mixtures. Such tendency can be observed in Fig.3.6 for the series having fiber additions.

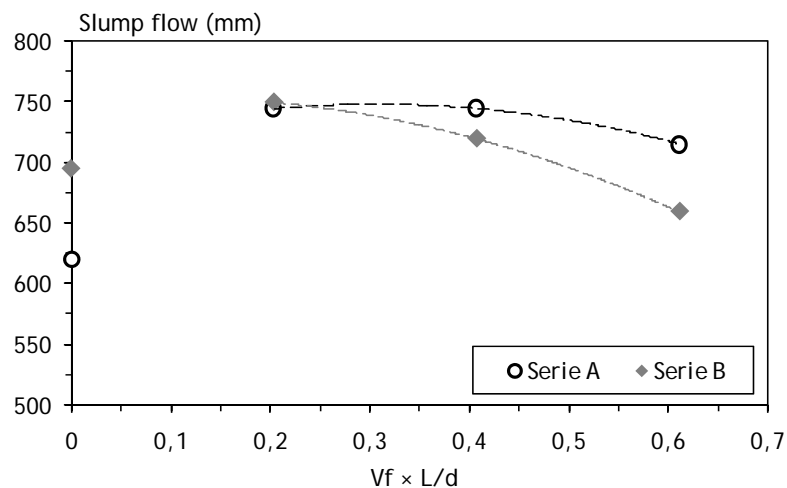


Fig.3.6 - Effect of the fiber factor ($V_f \cdot L/d$) on the slump flow.

Unexpectedly, the slump flows from the plain self-compacting mixtures were smaller than most of the respective mixtures with fibers. The reason for the small slump flows observed in the plain mixtures was an inadequate content of the superplasticizer (Table 3.2) which was subsequently adjusted for each serie, according to the amount of steel fibers added. Despite the small values obtained, the minimum slump flow of reference for self-compacting admixtures (600 mm) was guaranteed in all the mixtures.

Analysis of the J-ring tests

The J-ring test was performed to evaluate the passing ability of the mixtures. Theoretically, the J-ring increases the rate at which the slump flow decreases for larger fiber factors. Such occurs due blockage effects that take into account the difference of the heights of concrete at the inner and outer part of the ring. Despite the unavailability of data for series B0 and B20, both of these tendencies could be observed in the material characterization for types A and B (Fig.3.7).

The large slump flow reductions and blockage effects denoted in Fig.3.7 are justified by the fact that an inappropriate spacing between the vertical bars of the ring was chosen. The latter was only 42 mm, a value much smaller than the length of the fibers (60 mm). In order to avoid blocking in SCSFRC with this type of fibers ($L/d=80$) Groth (2000) suggested a bar spacing equal to three times the fiber length (180 mm) and a maximum amount of fibers of 30 kg/m^3 .

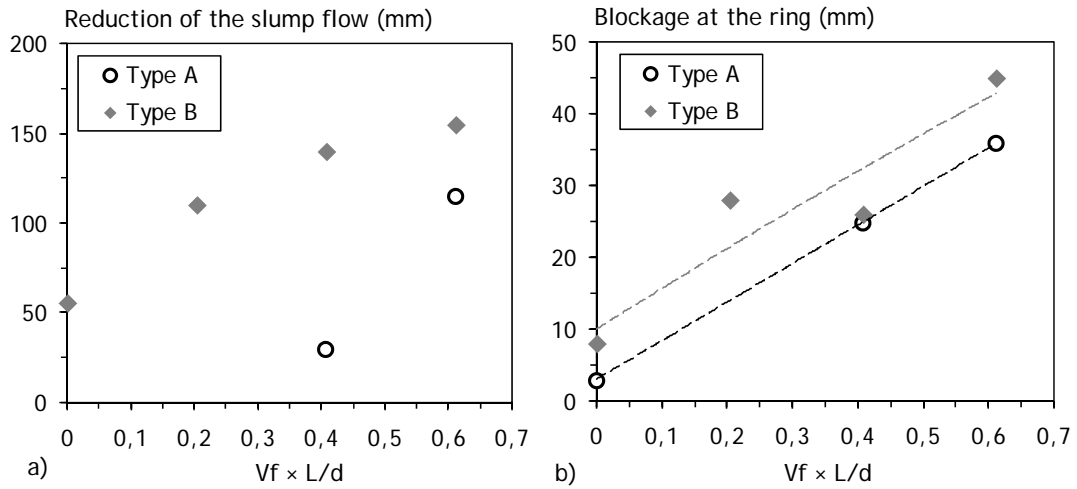


Fig.3.7 - Effect of the fiber factor ($V_f \cdot L/d$) on: a) Reduction of the slump flow; b) Blockage at the J-ring.

Analysis of the viscosimeter tests

Although few measurements could be obtained with the viscosimeter it is worth to evaluate whether it provides an agreement with the results from the slump flow tests. For this purpose, the expressions suggested by Gomes (2002) for the yield stress (Eq.3.1) and by Sedran and de Larrard (1999) for the plastic viscosity (Eq.3.2) will be considered:

$$\tau_{00} = \frac{\rho}{11740} \times (808 - D_f) \tag{3.1}$$

$$\mu_{PL} = \frac{\rho \times 9.81}{10000} \times (0.026 \times D_f - 2.39) \times T_{50} \tag{3.2}$$

where ρ is the material density in kg/m^3 . The correlations between the values proposed by these expressions with the measurements are presented in Fig.3.8.

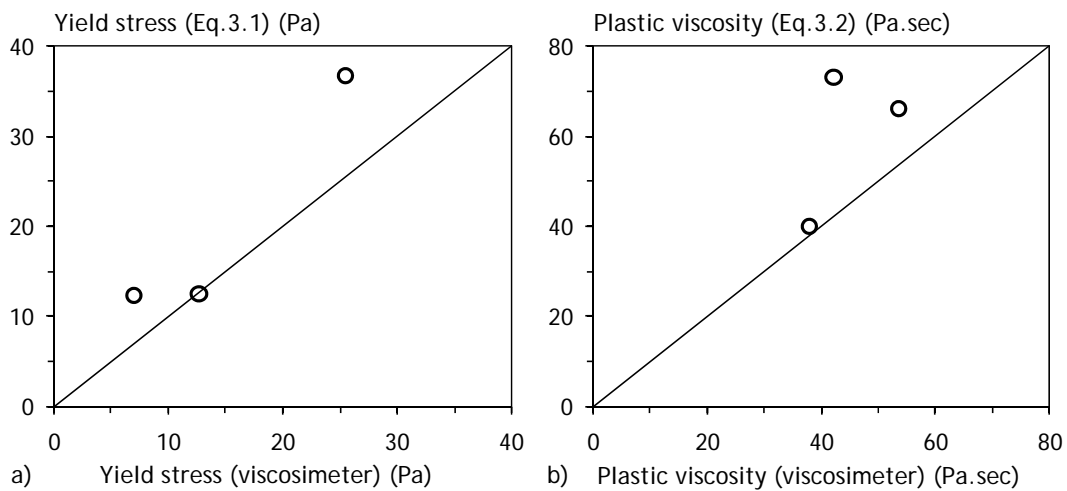


Fig.3.8 - Correlation of measurements and expressions in literature for: a) Yield stress; b) Plastic viscosity.

In theory, the yield stress (minimum shear stress that needs to be surpassed to initiate flow) should tend to zero for SCC without fibers. However, such was not observed in mixture A0, which have already reported an unexpected small slump flow. Despite this value, the increasing yield stresses at decreasing slump flows was consistently observed.

The correlation of the viscosimeter measurements with Eq.3.2 did not provide a reasonable agreement for mixtures A20 and A40. However, such as expected, the plastic viscosity (the slope of the Bingham model) increased at increasing fiber factors.

3.3.2 Hardened state properties

The characterization of the eight mixtures in the hardened state consisted on the evaluation of the average compressive strength at 7 days ($f_{cm,7}$) and 28 days (f_{cm}) as well as the average elastic modulus at 28 days (E_{cm}). The average values for these properties (Table 3.6) were obtained by means of three specimens per mixture. Test methods followed the specifications advanced by UNE 83507 (2004) for the compression tests and by UNE 83316 (1996) for the elastic modulus.

Table 3.6 - SCSFRC average compressive strengths and elastic modulus.

Age		A0	A20	A40	A60	Average(A)	B0	B20	B40	B60	Average(B)
7 days	$f_{cm,7}$ [MPa]	31.2	31.4	30.1	32.0	31.2	58.3	60.7	54.1	56.8	57.5
	C.V. %	20.7	11.9	11.6	3.6	13.5	1.2	1.3	9.6	6.8	7.1
28 days	f_{cm} [MPa]	50.5	46.5	45.7	49.9	48.5	74.8	80.6	76.1	78.5	77.1
	C.V. %	3.0	5.4	0.7	0.7	5.3	2.7	0.7	2.2	3.3	3.8
	E_{cm} [GPa]	35.5	35.8	32.3	32.9	34.0	37.6	37.0	36.3	36.4	37.0
	C.V. %	1.7	2.4	2.5	1.3	4.9	1.7	0.2	1.1	1.1	1.8

The results from Table 3.6 corroborate the findings from other researchers (Maidl, 1995; König and Kützing, 1999; Sato et al., 2000; Grünwald, 2004) that the addition of the steel fibers has hardly any effect on the compressive strength. The average evolution of this property with the age, measured in terms of the ratio between $f_{cm,7}$ and f_{cm} , is smaller in serie A (64%) than in serie B (75%). This occurs because mixtures B have smaller average particle sizes and a different type of cement, both of these aspects contributing to speed up the hydration process and the respective strength evolution. In most cases the scatter of results decreased with time and remained within acceptable values for all mixtures.

For the same compressive strength, the elastic modulus of self-compacting mixtures is expected to be smaller than the one of traditional vibrated concrete. This occurs because mixtures with larger strengths have larger contents of hydrated paste which present lower modulus than the aggregates. This way, the existing building codes, which focus on traditional vibrated concrete, (CEB-FIP, 1993; EN 1992-1-1, 2004) tend to slightly overestimate the elastic modulus of SCSFRC, (Fig.3.9).

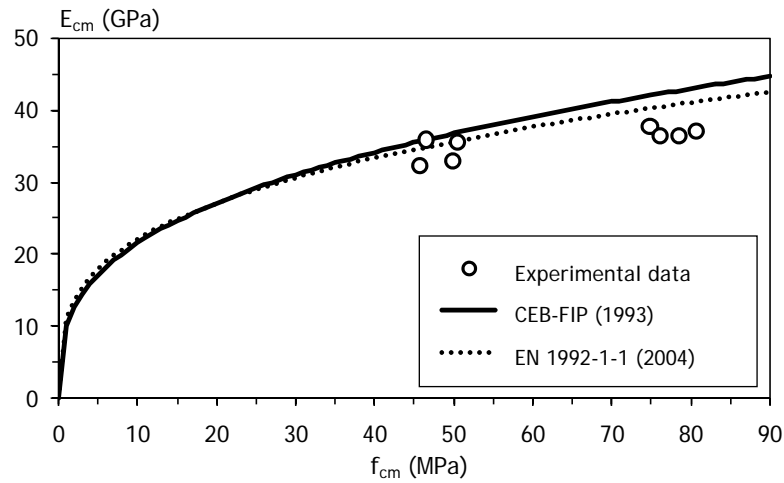


Fig.3.9 - Relationship between the SCSFRC elastic modulus (E_{cm}) and its average compressive strength (f_{cm}).

3.4 UNIAXIAL TENSILE TEST RESULTS

3.4.1 Stress-crack width curves

In the analysis of the uniaxial tensile responses of SFRC three relevant stages were identified: 1) the instant of matrix cracking; 2) the maximum residual strength; 3) the final crack width (when the residual strength becomes zero). The average values for each group of specimens at each of these stages are summarized in Table 3.7.

Table 3.7 - Average displacements/crack widths and stresses at relevant stages of the tensile responses.

			A0	A20	A40	A60	B0	B20	B40	B60
Matrix cracking	δ	[μm]	6.4	5.4	5.8	5.9	5.1	5.2	4.1	4.3
	C.V. (δ)	[%]	3.3	7.3	15.9	14.8	17.3	23.5	11.4	43.5
	σ	[MPa]	2.70	2.35	2.36	1.59	2.60	2.74	1.67	1.56
	C.V. (σ)	[%]	28.6	15.9	13.9	34.6	17.1	30.5	18.9	24.0
Maximum residual strength	w	[mm]	---	2.86	2.20	1.98	---	2.55	2.35	1.69
	C.V. (w)	[%]	---	25.7	25.9	42.7	---	21.2	22.9	45.6
	σ	[MPa]	---	0.92	1.14	1.77	---	0.80	1.27	0.70
	C.V. (σ)	[%]	---	23.8	23.2	17.1	---	52.1	22.0	35.3
Final crack width	w	[mm]	---	33.7	30.9	34.2	---	27.1	30.1	28.9
	C.V. (w)	[%]	---	10.8	9.0	14.5	---	18.0	11.3	20.4

Results from Table 3.7 indicate that stress at which matrix cracking occurs does not increase with the fiber content, but rather tends to decrease with it. The reason for these results might be the increasing porosity of the matrices due to inappropriate modification of the mixture

compositions due to fibers addition. If a correct granular skeleton would have been chosen, the stresses at matrix cracking of all series would have been more similar. Note, however, that the latter tend always to be smaller than the actual tensile strength of the matrices due to the limitations of the uniaxial tensile test method in measuring this property.

The displacement (δ) at which matrix cracking occurs presents a limited range of variation (0.004 to 0.007 mm). However, it is noticeable that matrices with smaller compressive strength (type A) present smaller coefficients of variation at the instant of cracking comparatively to matrices of type B. This occurs because crack growth takes place in a different manner: in normal strength matrices (type A) the major crack propagates within the weakest link in the matrix (cement paste) whereas in high strength matrices (type B) it expands by crossing the aggregates as well. Consequently, matrices of type A present a more stable and ductile behavior than the ones of type B, whose post-peak strengths tend to be very small (Fig.3.10). In specimens from serie B, because a sudden loss of stiffness occurs just after cracking, controlling of the test is difficult to guarantee. Thereby, results from Fig.3.10 should be analyzed carefully. Extended information of all the results obtained and difficulties experienced on testing each of the 48 specimens is provided in Appendix 1.

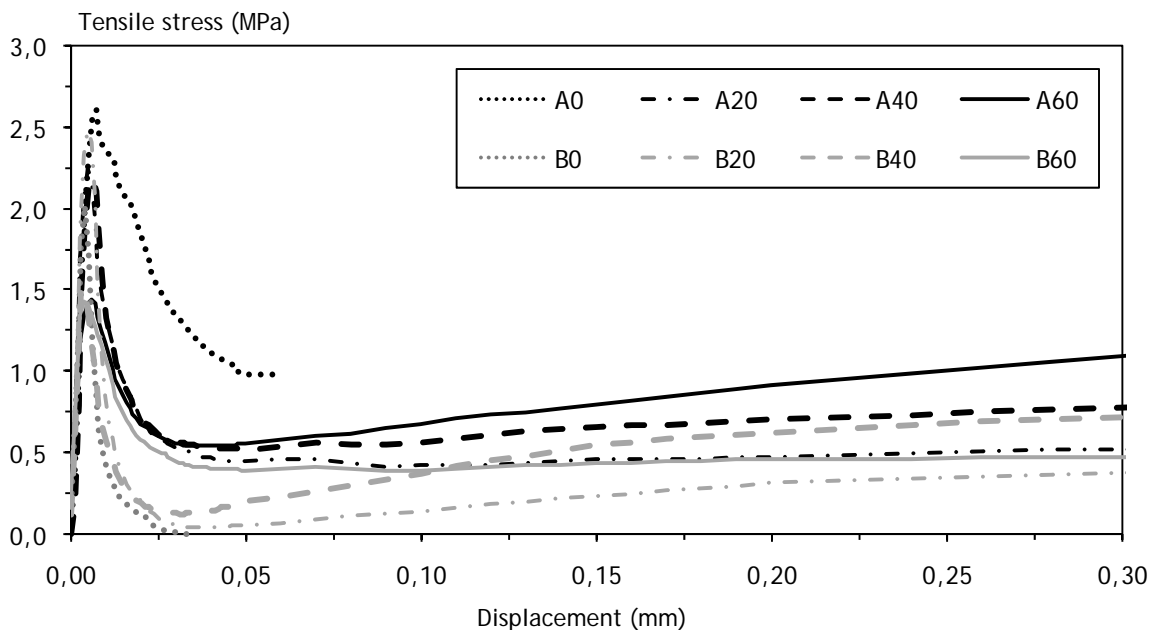


Fig.3.10 - Average tensile responses up to 0.30mm displacement.

Despite the instability of the test just after matrix cracking, the uniaxial tensile tests were found to be an appropriate test method to measure the post-cracking strength. The crack-bridging effects provided by fibers are noticeable for displacements smaller than 0.050 mm, the range at which fibers start acting due to interfacial shear stresses taking place during their debonding process (Fig.3.10). Following, the pullout mechanisms of steel fibers become the unique phenomena governing the material's tensile behavior. The post-cracking strength increased progressively up to a maximum residual strength and then decreased progressively at increasing

crack widths due to slippage of the fibers (Fig.3.11). Visual inspection of the cracked surfaces of all the specimens showed that rupture of the fibers did not occur in any case.

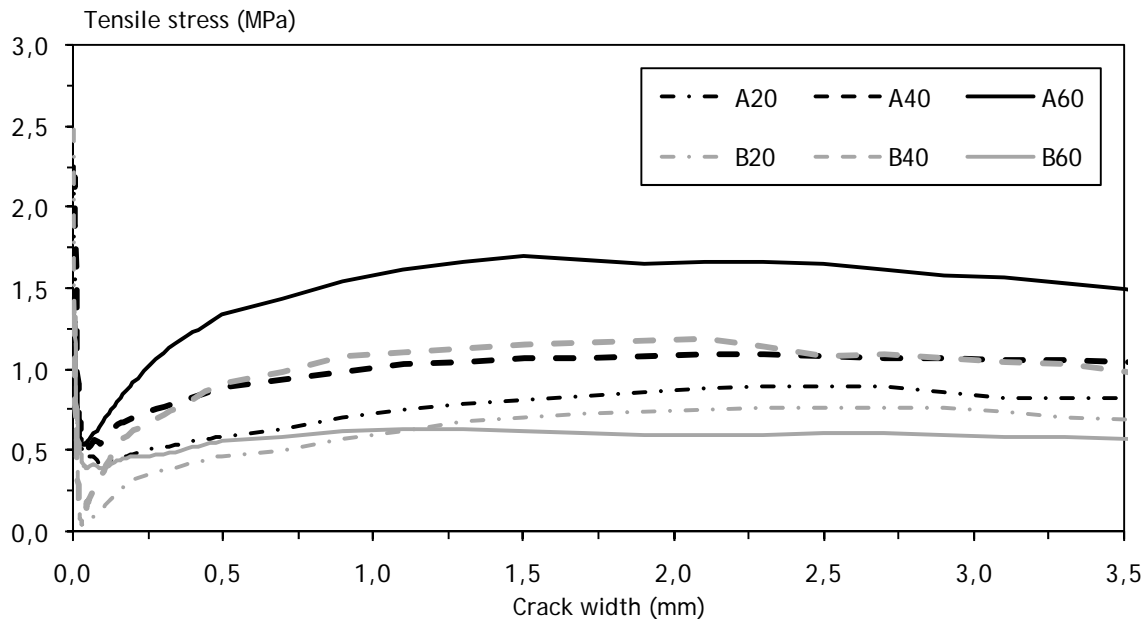


Fig.3.11 - Average tensile responses up to 3.5mm crack widths.

As it was expected, the maximum residual strengths of all the series with fibers increased with the fiber content, with the exception of serie B60 (Table 3.7). However, the average increment of the residual tensile strength was not proportional to the steel fiber content. Indeed, the greatest relative benefit arises from the addition of 20 kg/m³ of fibers in the specimens (Fig.3.11). The differences on the type of matrix did not play a clear influence on the stress-crack width curves in the cases of 20 and 40 kg/m³ reinforcement (Fig.3.11).

The average crack widths at which the maximum residual strengths took place were within a range of 1.69 to 2.86 mm and they tended to be decrease at increasing maximum residual strengths. Nonetheless, because the post-cracking curves were approximately constant in the crack width range of 1.0 to 3.5mm, their coefficient of variation was rather large (always above 20%).

In order to evaluate the entire stress-crack width curves of SFRC up to the physical separation of the two parts of the specimen, the uniaxial tensile tests proceeded after the extraction of the extensometers (stages 5 and 6 in Table 3.4) by measuring the crack width through the LVDT of the testing machine. The new test configuration is shown in Fig.3.12

Although the results for large crack widths are not of interest for structural applications, they are useful to understand the mechanisms governing the pullout responses of fibers. Contrarily to straight fibers, hooked fibers do not necessarily slip within the concrete at the side of the crack with smaller embedded length. Thereby, the final crack width at which the load-carrying capacity of the specimens becomes zero (w_u) is a relevant result (Table 3.7).



Fig. 3.12 - Final stage of the uniaxial tension test in a specimen from serie A60.

The stress-crack width curves up to the final crack width are shown in Fig.3.13, where it can be seen that, in some cases, the load load-carrying capacity of fibers could be extended almost up to 40mm. Nonetheless, the average values of w_u for all the series is about half the fiber length (30 mm) and for crack widths above this value the residual strength of the composite is almost negligible.

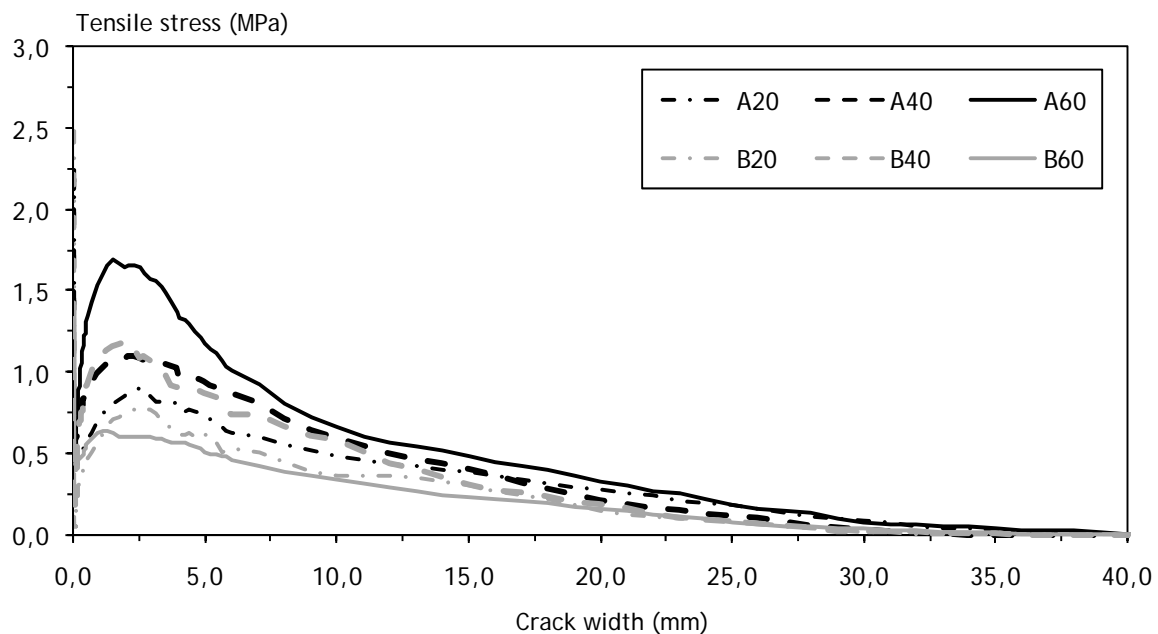


Fig. 3.13 - Average tensile responses up to the final crack width (w_u).

3.4.2 Fracture energy

The area below the σ - w curve represents an energy absorbed within the damage zone, usually denoted by G_f , which represents the fracture energy per unit area of the fracture surface (Hillberborg, 1985). This is a property which is commonly used to evaluate the beneficial effects of fibers in SFRC. While G_f of plain concrete in uniaxial tension are always smaller than 0.2 N/mm (Appendix 1), G_f of SFRC tends to be significantly larger. Fig.3.14 shows the average values of this parameter in uniaxial tension for the six series with fiber reinforcement.

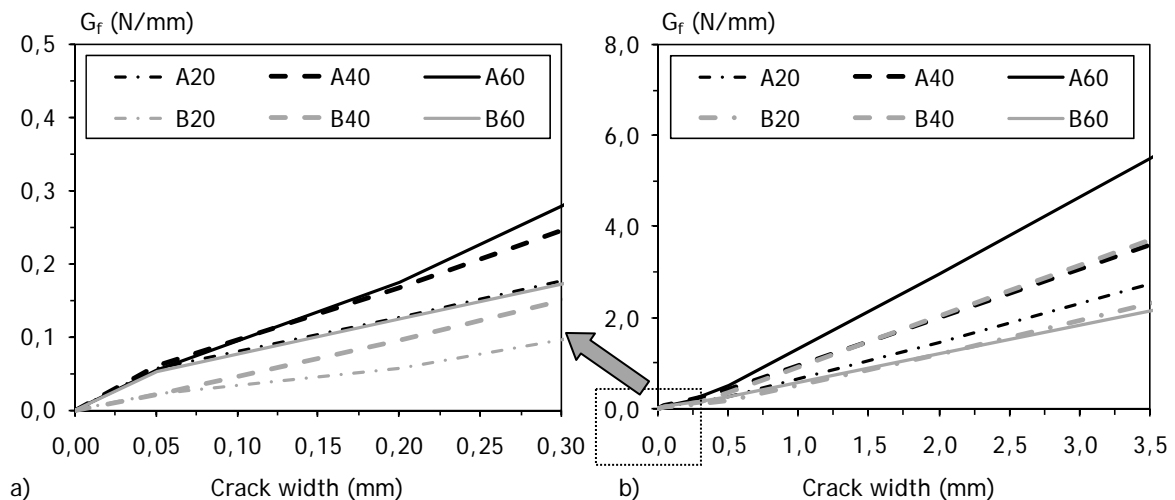


Fig. 3.14 - Average fracture energies per unit area of cracked surface (G_f) at: a) $w=0.30$ mm; b) $w=3.5$ mm.

From Fig.3.14a it can be seen that, due to the brittle behavior of high strength matrices (series B20, B40 and B60), the average fracture energies of these series denote a rather poor performance than the ones with normal strength concrete (type A). At this stage, the crack-bridging effect provided by fibers is still limited and, consequently, the values for this property are mostly governed by the matrix properties. However, for larger crack widths (Fig.3.14b) the average fracture energies per area of cracked increase substantially.

The relative performance of the series in Fig.3.14b is in accordance with the stress-crack width curves shown in Fig.3.11. Nonetheless, for the cases with 20 and 40 kg/m³ of fibers, series from type B tend to present values slightly smaller. This occurs due to the unstable post-cracking responses consistently observed in the uniaxial tests of specimens from type B (Appendix 1). The reason for this behavior might be the fact that the large brittleness of high strength matrices tends to induce sudden local spalling of the matrix during the pullout of inclined fibers. The effect of this phenomenon is even more noticeable when calculating the average fracture energy per unit area for the entire uniaxial tensile test (Fig.3.15).

Fig.3.15 clearly shows that the rate at which the fracture energy increases the most is within in the crack width range associated to the straightening process of the hook (approx. up to 5.0 mm, such as shown in Fig.3.13). For larger crack widths, the slope of the fracture energy is much more similar in all series regarding that fiber pullouts are governed by frictional mechanisms.

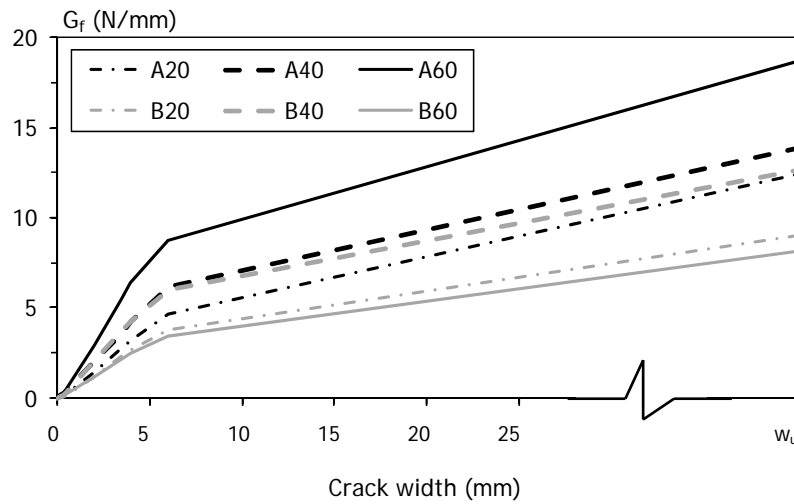


Fig.3.15 - Average fracture energies per unit area of cracked surface (G_f) of the thorough σ - w curves.

3.4.3 Number of fibers at the cracked sections

In order to understand the reasons for the different stress-crack width curves obtained, the average number of fibers at the two cracked sections generated after testing in each specimen were calculated and compared to their maximum residual strengths (Table 3.8).

Table 3.8 - Average number of fibers at the cracked sections (N_f).

		A20	A40	A60	B20	B40	B60
N_f	[--]	32	57	95	26	55	62
C.V. (N_f)	[%]	13.3	11.1	17.0	25.0	16.6	34.8
$\sigma_{res,max}$	[MPa]	0.92	1.14	1.77	0.80	1.27	0.70
C.V. ($\sigma_{res,max}$)	[%]	23.8	23.2	17.1	52.1	22.0	35.3

Table 3.8 shows that the increment of the number of fibers at the cracked sections is proportional to the increment of the fiber content in the mixture. For the same fiber content, the average number of fibers was similar in both types of concrete, with exception of serie B60 which provided an unexpected small number of fibers at the cracked surfaces.

The number of fibers may influence the post-cracking strength in two ways: 1) less fibers imply less crack-bridging elements; 2) less fibers indicate that, in the assumption of constant fiber distribution, the average orientation of the fibers in the direction perpendicular to the cross-section is rather poor. Consequently, the pullout performance of these fibers is also smaller.

Generally, the coefficients of variation for the number of fibers in Table 3.8 are always smaller than the ones observed for the maximum residual strengths. Moreover, they also denote an agreement with the latter regarding that the largest coefficients of variation in the number of fibers on series B20 and B60 support the large scattering observed in the maximum residual strengths observed for these series (Table 3.8). In the case of serie B20, a C.V. of 25.0% in the

number of fibers implied a variation on the maximum residual strength of more than 50%. However, in serie B60, a C.V. of 34.8% in the number of fibers conducted to a smaller variation (C.V. of 35.3%). The causes for this discrepancy needed to be investigated.

Fig.3.16 shows the correlation between N_f and the maximum residual strengths for all specimens, with exception of the ones from serie B60. It can be seen that, in accordance to the findings of other researchers (Barragán, 2002; Markovic, 2006) an almost linear correlation can be traced between these two parameters.

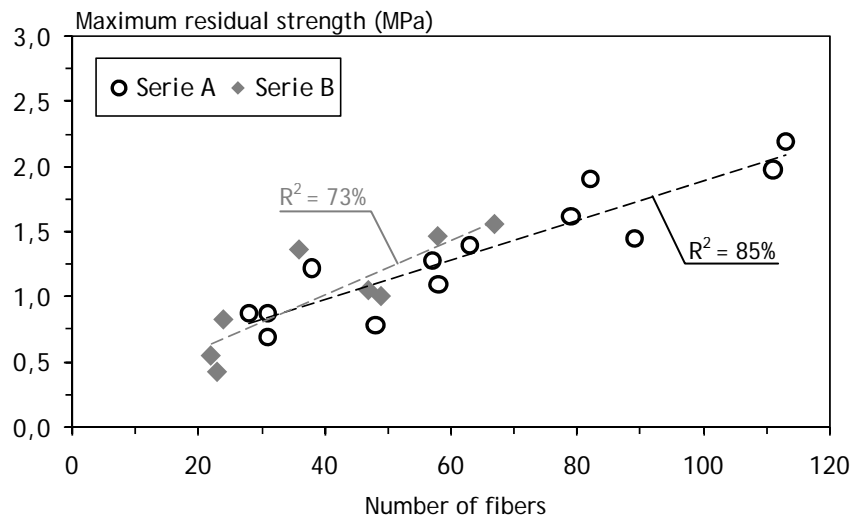


Fig. 3.16 - Number of fibers at the cracked section and respective maximum residual strengths.

The larger slope of the linear correlation for serie B (Fig.3.16) indicates that, for a constant number of fibers, its maximum residual strengths tend to be somewhat larger than in matrix A. Such conclusion derives from the bond strength between fibers and the matrix, which tend to be larger for higher strength concretes under similar orientation patterns. The average pullout loads of all the fibers in the cracked section at the instant of maximum residual strength are shown in Fig.3.17.

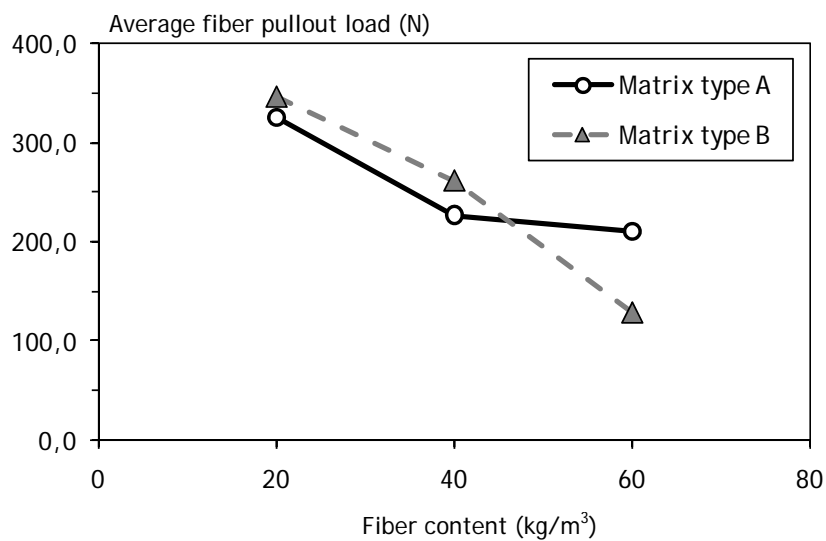


Fig.3.17 - Fiber content and respective average pullout load of fibers at the maximum residual strength.

Fig.3.17 shows that the poor performance denoted by serie B60 is not uniquely due to the small number of fibers at the cracked section (relatively to what was expected) but also because the average contribution from each single fiber is much smaller than in the other series, which might be related with an average unfavorable preferential orientation of the fibers.

3.4.4 Analysis of fiber distribution

In order to understand whether the reason for the unexpected stress-crack width curves of serie B60 was a preferential orientation of fibers, a previous inspection was carried out on the fiber distribution.

The first assumption that needed to be validated was the uniform distribution of the fiber content within the specimens. For that purpose, the number of fibers was counted in greater detail on four specimens of this serie. These specimens were sawed along their height in two other cross-sections (Fig.3.18a) where fiber counting was performed into five different domains (Fig.3.18b) whose diameters differed 30 mm.

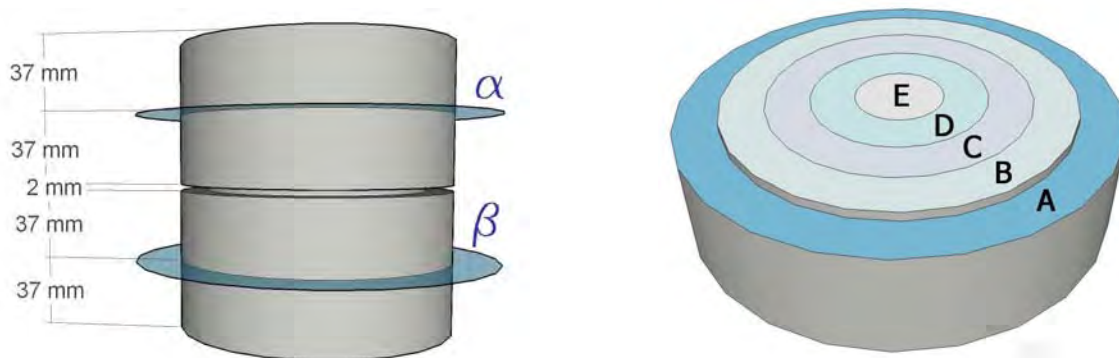


Fig. 3.18 - Fiber counting: a) Location of the sawed sections; b) Domains of the cross-sectional surface.

When comparing the total number of fibers at the cracked section and at the sawed sections (excluding the outer domain in order to simulate the notch effect) it was observed in most cases a relatively homogeneous distribution along the height of the specimens, with an average coefficient of variation between the three sections of about 21.0%, such as shown in Table 3.9.

Table 3.9 - Number of fibers in different cross-sections (according to Fig.3.18a).

Cross-section	Specimen				Average
	B60-3	B60-4	B60-5	B60-6	
α	45	48	38	35	42
Notch	40	79	58	30	52
β	41	113	49	41	61
Average	42	80	48	35	51
C.V.	6%	41%	21%	16%	21%

With respect to the radial distribution within the sections, the average number of fibers in each domain (Fig3.18b) was very similar to their relative areas (Table 3.10). Consequently, a uniform volumetric distribution of fibers in serie B60 could be concluded.

Table 3.10 - Relative distribution of fibers per domain in each specimen.

Domain	Specimen				Average N_f	Relative area
	B60-3	B60-4	B60-5	B60-6		
A	43%	32%	28%	46%	37%	36%
B	27%	26%	28%	31%	28%	28%
C	19%	27%	27%	12%	21%	20%
D	8%	11%	12%	9%	10%	12%
E	3%	4%	5%	2%	4%	4%

The second assumption that required verification regards the steel fiber contents. Each steel mould used to produce the uniaxial tensile specimens had 5.3 liters, which means a total volume of 31.8 liters per batch of concrete produced. Regarding that an extensive characterization of this material with other test methods was intended (Guardià, 2007) each batch had about 200 liters. Consequently, because only 16% of the volume produced was being used for these specimens, it would be worth to verify that the actual steel fiber contents within the specimens were in accordance with the expected quantities (60 kg/m^3).

For this purpose, two specimens from serie B60 were weighted and then crushed into small fragments (Fig.3.19a). Afterwards, all the steel portions of the mixture were isolated through a magnet (Fig.3.19b) and weighted (Fig.3.19c). The latter step showed that the weight of the steel portions with respect to the original volumes guaranteed the existence of a minimum reinforcement larger than 60 kg/m^3 in both specimens.

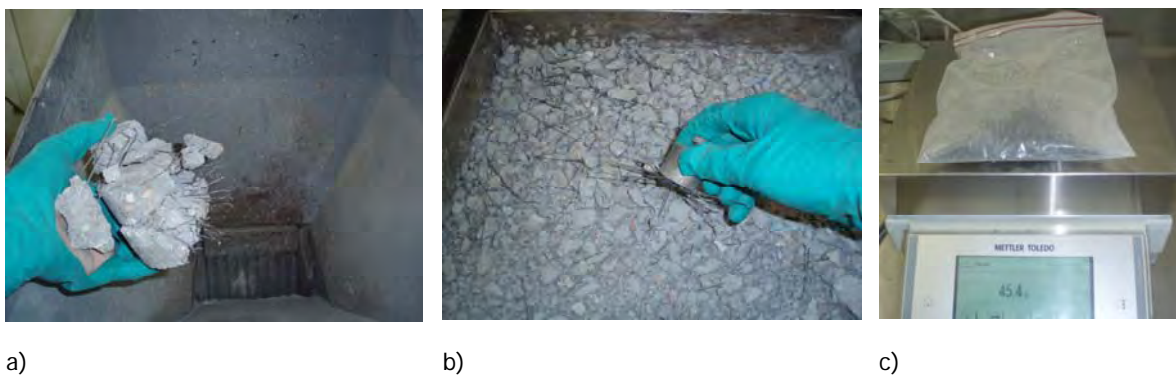


Fig.3.19 - Steps for the determination of the fiber content in specimens of serie B60: a) Crushing each specimen; b) Separation of the steel fibers through a magnet; c) Weighting the fibers.

Despite the homogenous volumetric distribution of the fibers and the guarantee of a minimum steel fiber content of 60 kg/m³, the average number of fibers in the cracked sections of serie B60 was much lower than expected. The reason for this fact was the existence of a very small orientation number (i.e., average orientation of fibers tended to be parallel to the plane of the cracked section). Such can be seen on a representative specimen from serie B60 (Fig.3.20).



*Fig.3.20 - Preferential alignment of fibers at the two cracked surfaces of specimen B60-4:
a) Perspective of the out-of-plane; b) Perspective of the in-plane.*

One of the reasons for the preferential orientations observed in Fig.3.20 was the fresh-state properties of this mixture, which presented the smallest slump flow among the series having fibers (Table 3.5). Because the workability of the mixtures decreased with time after mixing, at the instant of casting the fresh-properties of serie B60 were no longer fluid, but rather tending to resemble a dry conventional concrete. Consequently, when filling a mould, fibers tended to rotate into horizontal planes due the weight of dry concrete casted above, performing the horizontal orientation shown in Fig.3.20a.

Another reason for the observed preferential orientation of the fibers in serie B60 was the casting method applied. Regarding the extra effort required to cast a dry concrete into the mould, the tip of the plastic pails used to cast the specimens were narrowed (Fig.3.21). This procedure forced fibers to be guided into a V-funnel which induced the planar preferential orientation shown in Fig.3.20b.

These observations point out the need of applying appropriate techniques to adjust the granular skeleton of SCSFRC due to fiber additions and to consider the influence of the casting methods when studying the orientation of fibers.



Fig.3.21 - Casting method applied on the manufacturing of the specimens.

3.5 CONCLUDING REMARKS

This chapter described a large experimental campaign of uniaxial tensile tests in SCSFRC. The study herein presented corroborates the suitability of this test method on characterizing the uniaxial post-cracking responses of fiber reinforced concretes.

The greatest relevance of this work arises from the identification of the actual stress-crack width curves from a significant variety of fiber contents on normal and high strength self-compacting concretes. From the analysis of the results obtained a significant insight could be gained in terms of the two most important mechanisms governing the tensile response of the material, namely: 1) the pullout responses of individual fibers; 2) the orientation of the fibers.

The studies presented in the following parts of this thesis focus on predicting the individual pullout response of steel fibers (Chapters 4 and 5) and their respective orientation (Chapters 6 and 7).

Chapter 4

Predicting the pullout response of inclined straight steel fibers

4.1 INTRODUCTION

The experimental research presented in the previous chapter emphasized the dependency of the residual strength of SFRC on the number of fibers and their respective orientations at the cracked section. In some cases, despite the similar number of fibers observed, the post-cracking behavior of the material was rather different. Thereby, evaluating the load-crack width responses of individual fibers at different inclination angles may be of great interest to understand the different performances of this material.

The main objective of this study is to propose a comprehensive and straightforward analytical model to predict the pullout response of inclined straight steel fibers in cementitious matrices.

A qualitative discussion of fiber pullout mechanisms is firstly introduced in order to identify the major phenomena governing the pullout response of steel fibers, setting the basis for the subsequent description of the new pullout model. Experimental validation is performed against single fiber pullout tests carried out on initially straight steel fibers and a parametric study to

evaluate the influence of fiber orientation on the pullout response is then presented. Finally, the model is applied on a design procedure to optimize the use of SFRC for structural applications. The content of this chapter has been published by Laranjeira et al. (2009).

4.2 RESEARCH SIGNIFICANCE

Extensive research has been carried out to understand the governing pullout mechanisms of inclined steel fibers in cementitious matrices. So far, existing predictive models are complex, involve significant experimental data and empirical parameters and their suitability on describing realistic pullout conditions is sometimes questionable due to unreasonable testing configurations. This chapter presents a model to predict the pullout response of inclined fibers superposing the effects derived from the inclination angle over the experimental pullout performance of aligned fibers. The procedure takes into account the debonding process, the different friction mechanisms involved and matrix spalling, providing a comprehensive and straightforward approach which can be used to design SFRC applications.

4.3 PULLOUT BEHAVIOR OF ALIGNED FIBERS

4.3.1 Qualitative description

The crack bridging capacity provided by fibers in brittle cementitious matrices is commonly evaluated by means of single fiber pullout tests. However, the bulk of the research has been focused on the peak pullout load and post-peak behavior, neglecting the important crack deflection and debonding processes which occur prior to the peak load (Easley et al. 1999).

The load-displacement diagram derived from a standard pullout test typically presents an initial linear branch with zero ordinate in which the fiber-matrix interface is bonded. At this stage the stress field in the matrix may be negligible and thereby such response derives uniquely from the straining of the protruded fiber portion (Kerans and Parthasarathy 1991). The failure at the fiber-matrix interface starts at the cracked surface in the region of maximum stress concentration and may induce two types of debonding mechanisms, either a progressive and stable process, or alternatively, a catastrophic one. In the first case a non linear concave downward pullout curve occurs whereas in the latter the diagram is expected to be linear up to peak and then drop to the friction load. Due to abrasion on the interface the post-peak drop sometimes smoothly curves and friction decays into a lower and approximately constant value. Upon this stage the rating of load decrease is approximately linear with fiber slippage up to complete removal. The latter turns out to occur at crack widths of about the shorter fiber embedded length.

4.3.2 Pullout response

Despite the consistent qualitative observations on the pullout behavior, the responsiveness of the debonding mechanisms with such variety of parameters leads quite frequently to significant

differences on the load-displacement diagrams. In fact tremendous variations on the interfacial fracture energy (2.5-22 J/m²) and interfacial shear stresses (1-20 MPa) can be found on literature (Easley et al. 1999). To overcome this concerning sensitiveness some authors support that microstructure of the interfacial transition zone, in which debonding takes place, should be always quantified experimentally (Shah and Ouyang 1991; Bentur and Alexander 2000; Fantilli and Vallini 2007).

Scattering on the shape of the pullout response at the debonding stage may occur due to different balances between initiation and propagation loads. In fact, peak and initial friction loads, which are the most prominent and easily measurable features of the pullout response, cannot be rigorously translated to interface properties (Kerans and Parthasarathy 1991). To overcome such limitation bond strength in fiber reinforced concretes should be evaluated through the parameters affecting debonding initiation and propagation. For such purpose a critical perspective regarding pullout testing configurations should be pointed out.

The activation of toughening mechanisms in fiber reinforced concrete requires a growing matrix crack to be deflected at the fiber-matrix interface. Standard pullout test configurations represent the matrix crack by a free surface and therefore an additional barrier to debonding is introduced since crack initiation rather than main crack deflection occurs (Easley et al. 1999). In the actual composite when the main crack front has passed the fiber some debonding will likely have already occurred (Kerans and Parthasarathy 1991). Thereby standard pullout configurations may lead to unstable debonding conditions (Easley et al. 1999) due to the artificially increment of initiation load introduced. The initiation load may also be influenced by the testing procedure itself. Recent experimental tests (Bindiganavile and Banthia 2005) showed that under higher loading rates both stiffening in the fiber-matrix bond and increasing bond strength may occur, irrespectively of the inclination angle. An increment on the initiation load increases the magnitude of stored energy and thereby some details of the post-peak load drop are also test dependent (Kerans and Parthasarathy 1991).

It can then be concluded that interface properties shall be always quantified experimentally by means of single fiber pullout tests on aligned fibers, but those shall be obtained from representative and reliable testing procedures, such as the one proposed by Mumm and Faber (1995).

4.4 PULLOUT BEHAVIOR OF INCLINED FIBERS

4.4.1 Qualitative description

The previous description of the pullout response covers the most significant phenomena with which crack bridging of SFRC can be explained. Nonetheless pullout mechanisms on inclined fibers such as debonding and relative slippage between fiber and the matrix turn out to be substantially different (Naaman and Shah 1976). Moreover bending of the fiber and matrix spalling introduce additional complexities to the pullout behavior (Ouyang et al. 1994).

When a crack intersects an inclined fiber it propagates in the path of least resistance. Therefore crack tends to change direction and run parallel to the inclined fiber for a significant distance along its length rather than crossing it (Bentur and Mindess 1985). The asymmetric stresses induced by inclined fibers on the matrix spread the crack pattern either by fragmentation, offset or ramification, leading to a more curved shape of the main crack (Bentur and Mindess 1985). Such microcracks and crack deflection affect the debonding mechanisms and therefore also the early stage of the pullout response. Indeed experiments have shown that the pullout load at which debonding starts decreases at increasing inclination angles (Van Gysel 2000; Cunha et al. 2007).

Once the first segments of the inclined fiber get debonded crack width increases. In order to guarantee geometric compatibility during crack opening those debonded segments tend to reorient into a smaller inclination angle, but the process is counteracted by the reaction provided by the surrounding matrix. Hence increasing crack widths imply higher deviation forces in order to progressively bend the fiber. The curvature which arises from fiber bending depends on its shape and flexibility. Due to moderate maximum pullout loads and weak anchorage of straight steel fibers, curvature is not critical for these fibers and thereby no experimental tests are found in the literature in which fiber rupture occurs (Naaman and Shah, 1976; Ouyang et al., 1994; Leung and Shapiro, 1999; Van Gysel, 2000; Cailleux et al., 2005; Cunha et al., 2007). However increasing curvatures on fiber do influence the distribution of pressures against the surrounding matrix wedge. Since cementitious matrices are brittle in nature, whenever the pressures imposed by the fiber exceed a certain critical value, local failure tends to occur. Due to the non homogeneous microstructure of the matrix, spalling tends to occur alternatively at both sides of the crack. Whenever small pieces of matrix spall off a load drop is observed on the pullout curve. Hence several load drops can be observed on the pullout curve of inclined fibers, being the number and amplitude of these drops proportional to the inclination angle (Cailleux et al. 2005). Experimental observations shown that spalling mechanisms occur perpendicularly to the embedded fiber axis (Cailleux et al. 2005) and that the free fiber length increment generated moves the initial fiber exit point from the initial pullout axis towards inner sections of the fiber (Fig.4.1).

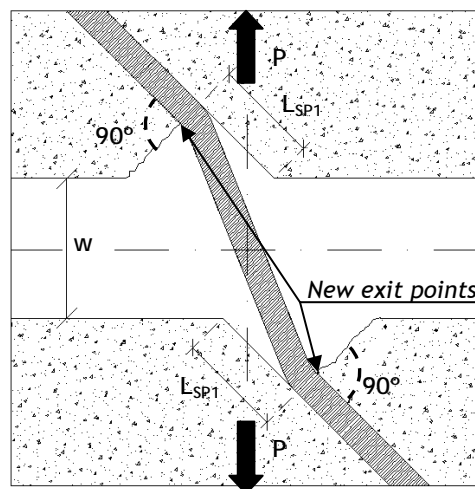


Fig.4.1 - Fiber pullout with similar spalling of the cement matrix at both sides of the crack.

The volume of the matrix wedge spalled off depends on the external load, fiber shape and inclination angle as well as matrix properties such as the tensile strength and maximum aggregate size. Spalling mechanisms cease when the bearing force induced on the matrix is lower than a critical resistant value. Upon this stage the additional friction to sliding provided by the matrix remains constant almost until the end of the pullout process regarding that curvature of the fiber is unchanged.

The bridging capacity of inclined steel fibers can then be considered as the sum of two components, one aligned and the other one perpendicular to fiber main axis (Leung and Li 1992), decreasing and increasing with the inclination angle, respectively (Naaman and Shah 1976). Regarding that the aligned component decreases with fiber slippage and that a stable deviation force is only provided by the matrix at the end of matrix spalling process, the crack width at which maximum pullout load occurs is strongly dependent on the magnitude of spalled matrix and on fiber embedded length.

As a result of this combined resisting mechanism, scattering on pullout response increases with the inclination angle (Naaman and Shah 1976; Li et al. 1990; Ouyang et al. 1994) and the peak loads are as much as high as those of aligned fibers (Naaman and Shah 1976) and occur under larger crack widths (Markovic et al. 2003; Ouyang et al. 1994).

The additional friction provided by the deviation force at fiber exit point avoids steep load drops on the post-peak range and pullout develops under a more stable fashion. The higher the inclination angle, the more pronounced is this effect and the smaller becomes the load drop. After this point the pullout load decreases at increasing crack widths under an approximately constant slope, resembling the behavior of aligned fibers. At the later stage of the pullout process the load carried out by the fiber is mainly dependent on the local friction at fiber exit point. However, contrarily to the aligned case, when the remaining fiber embedded length approaches a short value, an increase on the final pullout load is sometimes observed. Such fact occurs due to improved shear stresses imposed by the shorter fiber embedded length (Fantilli and Vallini 2007) which may also lead to some additional spalling of the matrix. Following this final pullout load there is a sharp drop on the pullout diagram towards a zero load value (Fantilli and Vallini 2007). The crack width at which this stage occurs is no longer the initial fiber embedded length but a reduced value due to matrix spalling.

4.4.2 Pullout response

Regarding the above described conceptual pullout behavior it is not surprising that the inclination angle has been shown to have a significant effect on composite properties (Katz and Li 1995). The pullout responses of inclined and aligned fibers shall then be compared to explain such influence on a comprehensive manner.

Taking into account the foregoing concepts it is now possible to point out the effects introduced by the inclination angle and sketch expected general pullout relationships for inclined fibers. A typical pullout response for inclined steel fibers is shown in Fig.4.2 in which the initial range is enlarged at the left hand-side for clarity. The initial elastic portion of the pullout curve will rise

almost linearly until the beginning of the debonding process, such in the case of aligned fibers (S_1 in Fig.4.2).

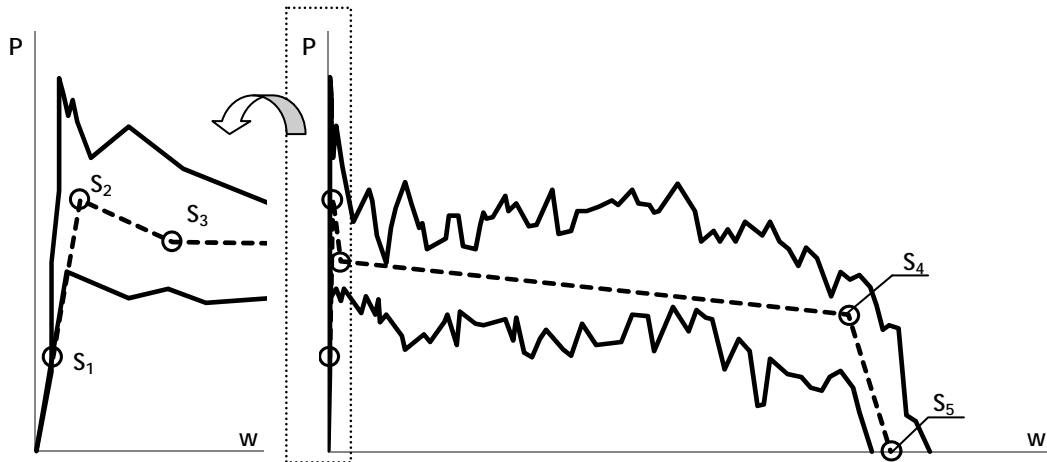


Fig.4.2 - Identification of the key-points on the range of experimental pullout responses of inclined steel fibers obtained from (Van Gysel 2000).

Upon initiation the debonded segments of the fiber nearby its exit point are now submitted to increasing friction caused by the supporting matrix. These coupled phenomena lead to an unstable load-crack width branch in which successive relative peaks and load drops are observed due to local failure of the matrix. As a consequence of this complex fiber-matrix interaction the average load carried out by the fiber increases progressively. The additional free fiber lengths generated by matrix spalling increase significantly the crack width and thereby the pullout diagram increases at a slower rate than previously, until a peak value is reached (S_2 in Fig.4.2). The drop on the post-peak range turns out to occur smoothly than in the case of aligned fibers because the local friction introduced by the matrix counteracts the unstable slippage associated to the completion of debonding process. Therefore the beginning of the purely friction stage (S_3 in Fig.4.2) occurs always at higher loads and crack widths than in the aligned case. Then the load carried out by the fiber decreases proportionally to the increment on crack width until a very short fiber length remains embedded (S_4 in Fig.4.2) in which the final pullout load is mostly provided by the local friction. Once this critical embedded length is attained the fiber is removed and a fast load drop is observed (S_5 in Fig.4.2). The zero load is always attained at smaller crack widths than in the aligned case since spalling mechanism reduce the available embedded lengths.

4.5 PULLOUT MODEL

4.5.1 General methodology

The developed model centers on predicting the pullout behavior of inclined straight steel fibers embedded on cementitious matrices. If the shape and magnitude of the load-crack width response of a single inclined fiber can be ascertained then it can be incorporated on improved

constitutive models to predict the thorough tensile behavior of the composite material. Furthermore, if such model bases itself on a reduced number of physical parameters, a straightforward and intuitive procedure can thus be used for design purposes.

This model primarily focuses on the conceptual description of the pullout behavior and then incorporates the several phenomena identified within a predictive load-crack width relationship. For such purpose the schematic pullout response previously described in Fig.4.2 is taken into account.

The procedure consists on defining a group of key-points which are able control the global shape of the diagram (S_1 , S_2 , S_3 , S_4 and S_5 in Fig.4.2) by attributing to each of them a physical meaning and identifying the phenomena in which they play a major role. The key-points are specified through experimental data obtained from experimental pullout tests on aligned fibers in which the main interface properties under specific testing conditions are characterized. Subsequently the effect of the inclination angle is introduced in each of the key-points by means of geometrical concepts and mechanical properties of the fibers and matrix involved. Once the key-points are completely defined they perform the basis to trace the multi-linear diagram which predicts the pullout response of inclined fibers.

4.5.2 Extraction of interface properties from experimental data

Unlikely the tensile behavior of SFRC the pullout response of a single fiber aligned with the load direction presents a well-defined shape and its physical behavior is vastly described in the literature. The major challenge centers on extracting material properties from the results of the tests which can then be used for modeling the composite behavior (Kerans and Parthasarathy 1991). For that purpose a suitable and reliable experimental quantification of the aligned component of the pullout response is demanded in order to integrate it within more complex mechanisms such as the ones occurring on inclined fibers.

For practical purposes the narrow extension of the non linear stage of debonding process can be neglected and, consequently, the load-crack width relationship can be roughly approximated by a tri-linear relationship. This simplified diagram is shown in Fig.4.3, in which an amplification of the initial stage is provided for clarity. Since the pullout response of aligned fibers starts at the origin and ceases at a crack width of about the shorter fiber embedded length (S_{03} in Fig.4.3), two additional key-points are required for a complete definition: the peak value (S_{01} in Fig.4.3) and the initial friction value (S_{02} in Fig.4.3). While the former is easily detected, the initial friction value may be doubtful because of the sometimes observed curvature at the final stage of the load drop. To avoid such uncertainties it is proposed to define S_{02} as the intersection of the two linear segments which best fit the post-peak branch, one starting from the peak value (S_{01}) and the other from the last recorded value (S_{03}), as shown in Fig.4.3. Hence a simplified pullout diagram becomes defined (discontinuous line in Fig.4.3) whose reasonableness can be checked by comparing its pullout work with the experimental one.

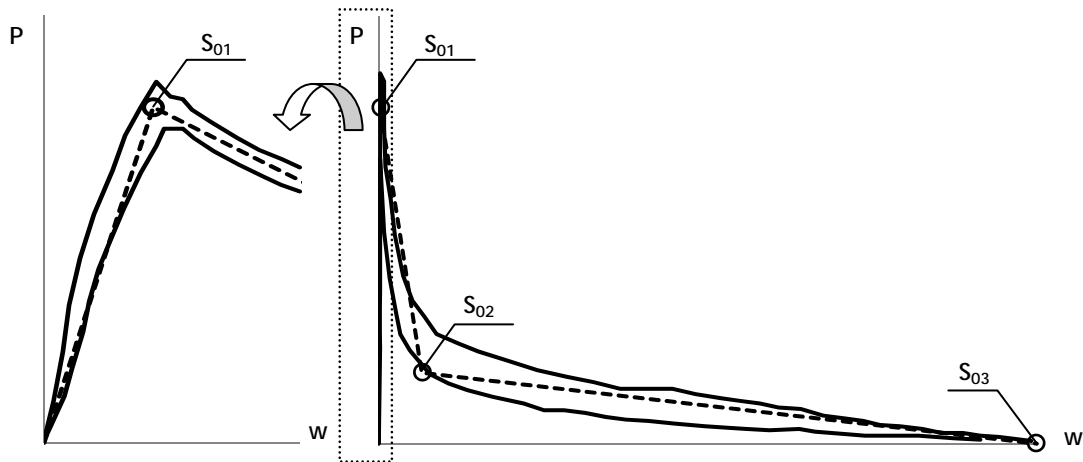


Fig.4.3 - Identification of key-points on the range of experimental results of aligned steel fibers obtained from (Van Gysel 2000).

4.5.3 Detailed description of the pullout model

Point S_1 : Debonding process

According to experimental observations debonding on steel fibers with embedded lengths (L_e) of 30mm and 0.70mm diameter (d) finishes at fiber slips up to 0.080mm (Van Gysel 2000). Hence even if some debonding occurs at the non-pulled out side of the fibers, crack widths at the end of the debonding process will likely be lower than 0.200mm for the common steel fibers used on structural applications (30-60mm length and 0.50-1.00mm diameter). Since the present pullout model focus on this type of fiber geometries, it turns out evident that the geometric idealization for crack bridging of inclined fibers based on the simple beam theory (Morton and Groves 1974) might not be reasonable because the moment arm for bending within such range of crack widths is negligible and therefore double curvature cannot occur. Thus the geometric configuration of fiber free length during the thorough debonding process of inclined fibers is assumed to be straight (Fig.4.4) and uniquely governed by the aligned component of the pullout mechanism.

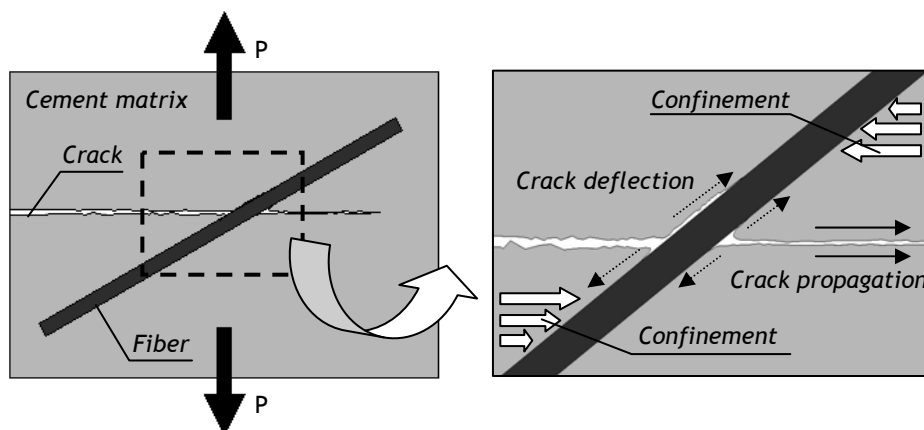


Fig.4.4 - Schematic configuration of the pullout process within the debonding stage.

Regarding the sensitiveness of the debonding process the experimental data obtained from the pullout tests of aligned fibers will be at this point extremely valuable. Given that interface properties are test-dependent the shear stress distribution $\tau(s)$ along fiber embedded length is unknown. Thereby an averaging and straightforward procedure will be applied, rather than an attempt to find the maximum interfacial shear stress which generates debonding (τ_{\max}) or the friction shear stress on the debonded segments of the fiber (τ_{fric}).

As aforementioned the maximum value of the pullout response in the aligned case (S_{01} in Fig.4.3) is the stage which immediately precedes full debonding of the fiber and, at this point, equilibrium between the external and the resisting aligned components can be applied, such as defined in Eq.4.1:

$$P_{S_{01}} = \tau^* \pi d L_e \quad (4.1)$$

where τ^* is an apparent interfacial shear stress which depends on the interfacial shear stress distribution $\tau(s)$ along the fiber embedded length as following:

$$\tau^* = \frac{\int_0^{L_e} \tau(s) ds}{L_e} \quad (4.2)$$

In this model debonding is assumed to be progressive and therefore slippage of the fiber at the peak value is almost negligible due to its remaining bonded end tip and the depreciable stretching of the fiber. Propagation load for debonding is assumed to be only slightly higher than the one required for initiation. Hence the increase on crack width due to the non linear debonding will be negligible and a linear relationship can then be applied from the beginning of the test up to this stage.

When the pullout load along fiber main axis is lower than the one required to initiate debonding elastic bond conditions prevail and, consequently, a certain confinement is provided by the surrounding matrix, orthogonally to the load direction (Fig.4.4). Since the initiation load for debonding is assumed to be closer to the aligned peak load such effect can be extended into this later stage and therefore, regarding the geometric configuration shown in Fig.4.4, the external pullout load (P_{S_1}) which leads to the maximum contribution of the aligned component ($P_{S_{A1}}$) depends on the inclination angle (θ), such as shown in Eq.4.3:

$$P_{S_1} = P_{S_{A1}} = P_{S_{01}} \cos\theta \quad (4.3)$$

Regarding that up to point S_1 no significant slippage of the fiber occurs, the crack width at this stage of the pullout process (w_{S_1}) is assumed to be approximately the same as the one observed in the aligned case ($w_{S_{01}}$):

$$w_{S_1} = w_{S_{01}} \quad (4.4)$$

Point S₂: Effects of matrix spalling

When the external pullout load (P_{S1}) induces the maximum contribution along the fiber main axis (P_{SA1}) debonding has already been extended up to almost the entire fiber embedded length but the remaining fiber end tip. During this stage the debonded segments of the fiber tend to bend and align with the direction of external loading due to the progressively increasing in crack growth. Then it becomes obvious that an important part of fiber debonding and spalling of the matrix occur simultaneously. However, while the former itself is usually extended to crack widths less than few hundredths of millimeter, the coupled mechanism may occur on crack widths up to several millimeters. In this model it will be assumed that debonding and spalling of the matrix are coupled phenomena. Hence spalling is considered to take place just after the beginning of fiber debonding but prior to its full accomplishment.

During crack growth increasing bending of the debonded segments of the fiber occurs and the most superficial pieces of matrix wedge tend to spall off. In order to account for the local failure of the matrix the volume of concrete removed from the cracked surface has to be quantified. Such is performed by defining the matrix spalled length (L_{SP1}) which is a measure of the amount of superficial matrix removed along fiber main axis, as described in Appendix 2.2.

When L_{SP1} is removed a stiffer and stable concrete wedge supports the new fiber exit point. The reaction provided by the matrix may be then idealized as a deviation force (D_{F1}) applied at the fiber exit point and laying in the direction of the angle bisector between the embedded length and the protruded segments of the fiber. While the inclination of the embedded length remains constant along the entire pullout process, the protruded segments are likely under lower inclination angles. However due to crack growth the average inclination angle of the latter is constantly changing and so also the deviation force (D_{F1}) does. Hypothetically, in the absence of matrix spalling the free fiber length would tend to approach the direction of external loading, thus leading to a severe deviation force at fiber exit point. This idealization is obviously unreasonable due to the occurrence of matrix spalling, which is commonly assumed to take place evenly at both sides of the crack. Although this assumption seems wise to account for an average increment of the crack width, due to the sensitiveness of matrix microstructure, spalling occurs differently at both sides of the crack and therefore critical deviation angles may arise at small crack widths (Fig.4.5).

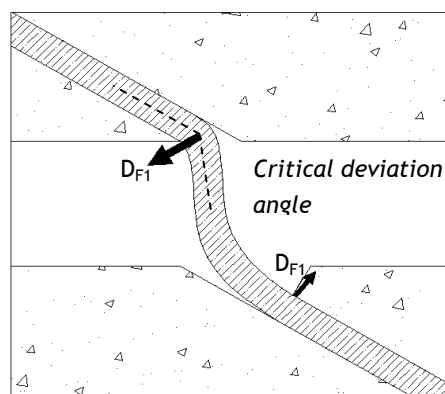


Fig.4.5 - Intermediate stage of matrix spalling process.

In this model it will be assumed that deviation force at the fiber exit point is critical and therefore fiber protruded length is parallel to the load direction (Fig.4.6). Hence the deviation force provided by the matrix introduces an additional friction resistance, the so-called non-aligned component of the pullout mechanism (P_{SN}), depicted in Fig.4.6 and defined in Eq.4.5 such as:

$$P_{SN} = \mu D_{F1} = \mu P_{S01} \sin\theta \cos\frac{\theta}{2} \tag{4.5}$$

Where μ is the friction coefficient between the steel fiber and the matrix which enables an assessment of the average shear stress, activated in the fiber-matrix interface, according to the intensity of the normal average stress. Based on experimental results Chanvillard (1999) found out a maximum value of μ equal to 0.60 with a standard deviation of 7%, irrespectively of matrix variables, fiber diameter and curvature radius. Such will be taken into account in the present work as a constant value for the entire pullout process.

The load of the second key-point of the pullout diagram (P_{S2}) is then defined by the synergy between a contribution along fiber main axis (P_{SA}) and the stable non-aligned component (P_{SN}) provided by the matrix at the cracked surface, as shown in Fig.4.6 and defined in Eq.4.6:

$$P_{S2} = P_{SA2} + P_{SN} \tag{4.6}$$

The aligned contribution at the end of matrix spalling (P_{SA2}) has to account for the reduction of the initial fiber embedded length due to matrix spalling, which will be considered by means of the effective length factor ($L_{eff(S2)}$) defined in Eq.4.7:

$$L_{eff(S2)} = \frac{L_e - L_{SP1}}{L_e} \tag{4.7}$$

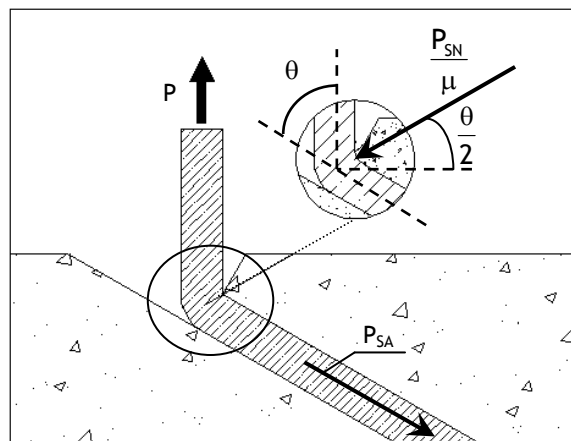


Fig.4.6 - Schematic representation of the aligned (P_{SA}) and non-aligned (P_{SN}) components of the pullout mechanism after matrix spalling.

Besides the reduction of the available embedded length the contribution of the aligned component to the pullout load also depends upon the ratio between the lengths of bonded and debonded segments on the fiber, in which P_{S01} and P_{S02} should apply, respectively. The difference between these values corresponds to the deterioration of the load carrying capacity along fiber main axis which is obtained from the experimental data, as shown in Fig.4.3.

The extension of the debonded length comprehends the segments of the fiber in which elastic bond conditions no longer exist at the interface. Such elastic conditions prevail until a critical relative strain between fiber and the matrix at the interface occurs, whose value is related with their elastic modulus. Therefore, for an intermediate stage of the debonding process, the extension of the debonded length (L_d) will be approximated by Eq.4.8, whose upper bound is the lower embedded length of the fiber.

$$L_d = \frac{E_f}{E_m} L_{SP1} \approx 6 L_{SP1} \quad (4.8)$$

The aligned component of the pullout mechanism after matrix spalling (P_{SA2}) can then be defined into a general expression such as presented in Eq.4.9, in which P_{S1} turns out to be a particular case without any matrix spalled length.

$$P_{SA2} = P_{S1} \cdot L_{eff(S2)} \left(\frac{L_e - L_d}{L_e} + \frac{P_{S02}}{P_{S01}} \frac{L_d}{L_e} \right) \quad (4.9)$$

The respective crack width at this stage (w_{S2}) should take into account both the increments due to slippage of the fiber along its embedded axis (w_{SA2}) and due to reorientation of the protruded length of the fiber during matrix spalling process (Δw_{SP1}). Fiber elastic strain is disregarded and therefore w_{S2} becomes defined as:

$$w_{S2} = w_{SA2} + \Delta w_{SP1} \quad (4.10)$$

The aligned component of the crack width (w_{SA2}) might be proportional to the extension of the debonded length (L_d) and to the total increment of crack width observed in the aligned case during the thorough debonding process:

$$w_{SA2} = w_{S1} + \frac{L_d}{L_e} (w_{S02} - w_{S01}) \cos\theta \quad (4.11)$$

The increment of crack width due to spalling (Δw_{SP1}) regards the geometric configuration depicted in Fig.4.6 and can then be defined as following:

$$\Delta w_{SP1} = N L_{SP1} (1 - \cos\theta) \quad (4.12)$$

Where N is the number of sides of the crack where spalling occurs (N=1 or N=2).

Point S₃: Friction mechanisms

Such as in the case of aligned fibers the maximum pullout load of inclined fibers occurs prior to full debonding of the fiber. However, when the end tip of an inclined fiber gets debonded, the drop on the load within the post-peak range is increasingly smoothed at larger fiber inclination angles due to the presence of growing deviation forces. Hence the pullout load at the beginning of the frictional stage (P_{S3}) is obtained by gathering both aligned and inclined components, such as depicted in Fig.4.6 and defined in Eq.4.13:

$$P_{S3} = P_{SA3} + P_{SN} \quad (4.13)$$

Regarding the crack bridging geometry adopted in this model (Fig.4.6) both fiber deviation angle and its curvature at the exit point from the matrix remain constant under further crack growth. Therefore the non-aligned component (P_{SN}) is assumed to also remain constant. On the other hand, at the beginning of the pure frictional stage fiber is already fully-debonded and, consequently, the respective aligned component of the pullout mechanism (P_{SA3}) is a particular case of Eq.4.9 with a debonded length (L_d) equal to the shorter embedded length of the fiber (L_e):

$$P_{SA3} = P_{S02} \cos\theta L_{eff(S2)} \quad (4.14)$$

The respective crack width (w_{S3}) introduces a small increment of fiber slippage due to debonding of the remaining length of the fiber and can then be defined by Eq.4.15:

$$w_{S3} = w_{S02} \cos\theta + \Delta w_{SP1} \quad (4.15)$$

Point S₄: Pre-removal stage

Within the friction stage of the pullout process the shorter embedded length of the fiber slips progressively along the matrix duct walls and passes through the exit point from the matrix under a constant deviation force, likely the idealization of a string sliding over a pulley. Upon full debonding the contribution of the aligned component decreases almost linearly at decreasing available fiber embedded length. Therefore prior to complete removal of the fiber the pullout load can then be approximately defined as uniquely dependent on the non-aligned component:

$$P_{S4} = P_{SN} \quad (4.16)$$

When the remaining embedded length of the pulled out part of the fiber approaches a critical embedded length ($L_{S,crit}$) the pullout mechanism enters into a new unstable stage. At this point bending of the fiber is increasingly more difficult and therefore fiber tends to rotate and cut into the matrix (Leung and Shapiro 1999). Although this effect has been observed to increase the final pullout load, its influence occurs at a crack width (w_{S4}) with no interest for structural applications and thereby it will not be taken into consideration within this model. Hence w_{S4} can be defined as following:

$$W_{S4} = L_e - (L_{SP1} + L_{S,crit}) \quad (4.17)$$

$L_{S,crit}$ depends on fiber curvature at the exit point and therefore its magnitude is somewhat dependent on fiber diameter (d). In this approach it will be roughly as:

$$L_{S,crit} = d \quad (4.18)$$

Point S₅: Removal from the matrix

Once the remaining embedded length of the fiber attains L_{crit} the deviation force provided by the matrix disappears and a sharp load drop occurs up to the end of the pullout process, defined by Eqs.19-20.

$$P_{S5} = 0 \quad (4.19)$$

$$W_{S5} = L_e - L_{SP1} \quad (4.20)$$

4.5.4 Parameter identification

This model is based on the following input parameters: fiber diameter (d), shorter fiber embedded length (L_e), average tensile strength of the cement matrix (f_{ctm}) and the experimental key-points from the pullout of aligned fibers at peak (W_{S01}, P_{S01}) and at friction (W_{S02}, P_{S02}). A schematic predictive multi-linear pullout diagram for inclined fibers is shown in Fig.4.7, whose shape is governed by the five-key points previously described and summarized in Tab.4.1. The several stages of the pullout process associated to each key-point are depicted in Fig.4.8 to provide a better understanding on the physical mechanisms involved. The pullout response of inclined steel fibers may differ from the one shown in Fig.4.8 whenever any of the following conditions is observed.

Fiber rupture condition

Due to their limited bond strength, straight steel fibers start slipping at small crack-widths under relatively moderate pullout loads. Thereby, geometric compatibility at the crack zone is achieved through small curvature of the fibers at their exit points from the matrix and no plastic deformations tend to occur due to this effect. That is the reason why, as previously mentioned, no rupture of straight steel fibers in cementitious matrices are reported in literature. Indeed, for the range of fiber geometries considered in this model, the maximum pullout loads of inclined fibers observed in experiments are, commonly, less than half of their respective ultimate loads. Consequently, fiber yield strength can be disregarded in the present model since fiber rupture is not prone to occur.

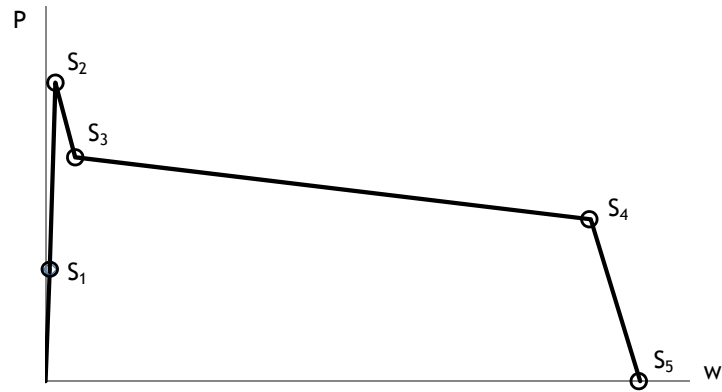


Fig.4.7 - Schematic diagram of the pullout model for inclined straight fibers.

Table 4.1 - Summary of expressions which define the pullout model.

Point	Formulation
S_1	$P_{S1} = P_{S01} \cos \theta$ $w_{S1} = w_{S01}$
S_2	$P_{S2} = P_{S01} \cos \theta L_{\text{eff}(S2)} \left(\frac{L_e - L_d}{L_e} + \frac{P_{S02} L_d}{P_{S01} L_e} \right) + \mu D_{F1}$ $w_{S2} = w_{S01} \cos \theta + \frac{L_d}{L_e} (w_{S02} - w_{S01}) \cos \theta + \Delta w_{SP1}$
S_3	$P_{S3} = P_{S02} \cos \theta L_{\text{eff}(S2)} + \mu \cdot D_{F1}$ $w_{S3} = w_{S02} \cos \theta + \Delta w_{SP1}$
S_4	$P_{S4} = \mu D_{F1}$ $w_{S4} = L_e - (L_{SP1} + L_{S,\text{crit}})$
S_5	$P_{S5} = 0$ $w_{S5} = L_e - L_{SP1}$

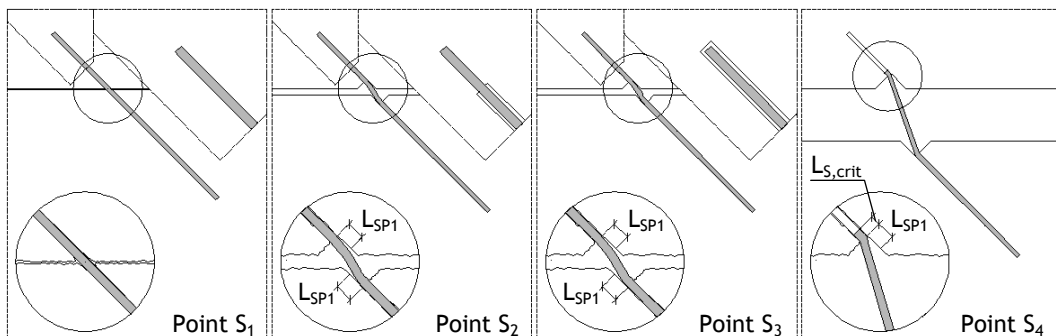


Fig.4.8 - Main stages of the pullout process of inclined fibers and associated model key-points.

Available embedded length condition

Fiber with short embedded lengths and significantly inclined relatively to load direction may not develop the entire load-crack width response such as previously described. That occurs due to the reduction of available embedded length imposed by matrix spalling which may induce earlier fiber removal. Therefore model predictions are based on the key-points defined in Tab.4.1 whenever Eq.4.21 is verified for all j between 1 and 3.

$$w_{S_4} > w_{S_j} \quad (4.21)$$

In case that one or more key-points do not obey Eq.4.21 earlier removal of the fiber will tend to occur and a simplified version of the pullout model has to be used. Such takes into account the points which verify Eq.4.21 and the ones corresponding to the stage of fiber removal (S_4 and S_5) which starts at crack width w_{S_4} with a respective pullout load defined as shown in Eq.4.22:

$$P_{S_4} = P_{S_j} + (P_{S_{(j+1)}} - P_{S_j}) \frac{w_{S_4} - w_{S_j}}{w_{S_{(j+1)}} - w_{S_j}} \quad (4.22)$$

Where j corresponds to the higher numbered key-point at which Eq.4.21 is verified.

4.6 MODEL DISCUSSION

4.6.1 Experimental validation

In order to ascertain the reliability of the proposed approach, pullout diagrams are compared with those experimentally obtained by Leung and Shapiro (1999). The specimens adopted by these authors consisted of two blocks, one made of plexiglass and the other of cement mortar (Fig.4.9). The former had a hole drilled at the center of the block in which fiber was partially inserted at different inclination angles (0° , 30° and 60°), remaining with a fixed protruded length which was then involved by mortar at the instant of casting the matching mould. Steel fibers had 0.50mm diameter and 10.0mm embedded length on a cement matrix with 36.5MPa mean compressive strength.

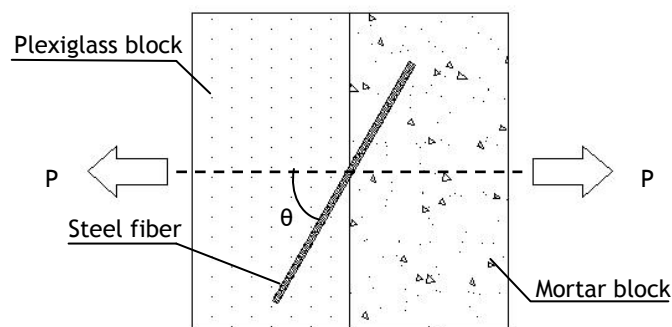


Fig.4.9 - Pullout test setup used by (Leung and Shapiro 1999).

Applying the present model requires a previous characterization of the interface properties between fiber and the matrix. To extract such information the pullout diagrams of aligned fibers ($\theta=0^\circ$) were analyzed and the ranges of experimental results were extracted. Then the graphical procedure described in section 4.2 was applied in each case (Fig.4.10). Cases A, B, C and D refer to fiber yield strengths of 275 MPa, 469 MPa, 635 MPa and 1171 MPa, respectively.

Such simplified tri-linear diagrams start in the origin and increase up to peak loads (P_{S01}) whose mean values were fixed accordingly with the published results (Leung and Shapiro 1999). Since the crack widths at which peak values occur (w_{S01}) were not reported they had to be approximated. Based on values observed in other experimental works (Naaman and Najm 1991; Van Gysel 2000; Markovic et al. 2003) w_{S01} was assumed to be equal to 0.050mm in all the cases.

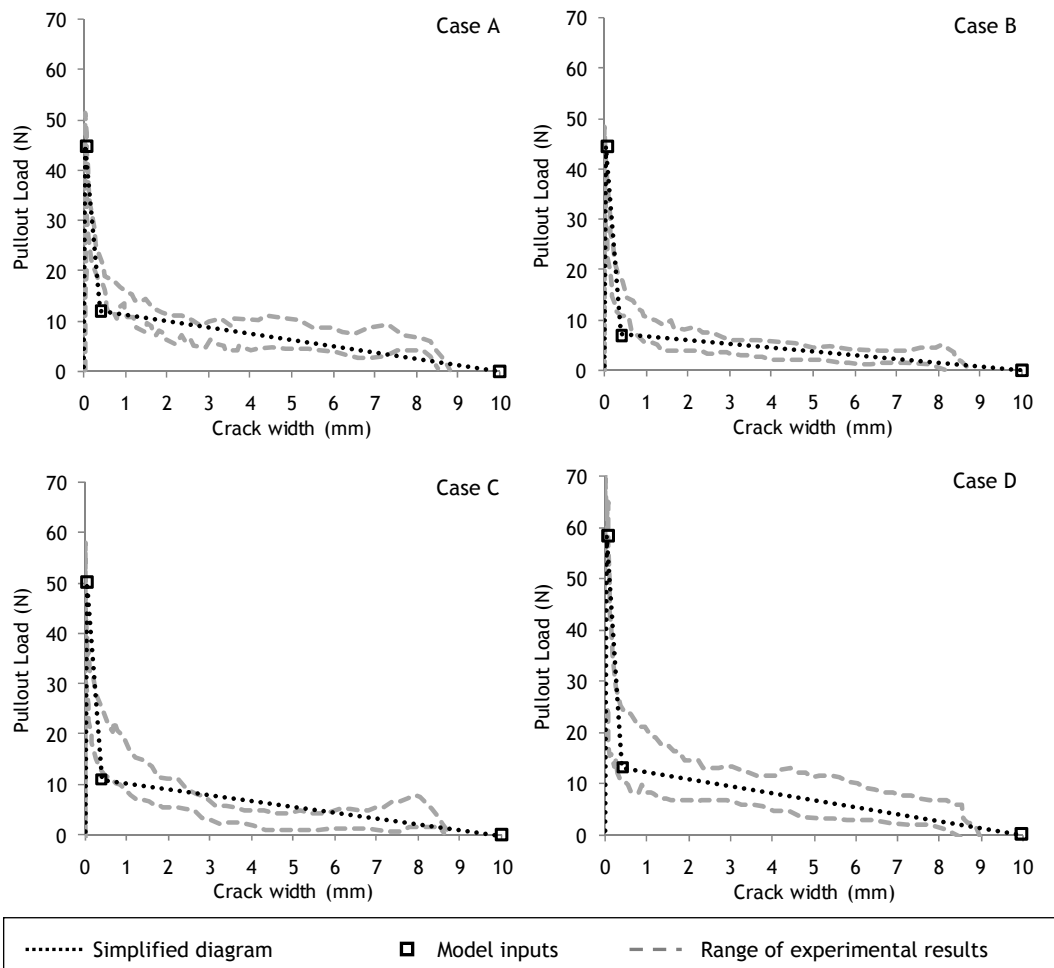


Fig.4.10 - Graphical extraction of simplified pullout diagrams of aligned fibers ($\theta=0^\circ$) for each case-study based on experimental results obtained from (Leung and Shapiro 1999).

Regarding the post-peak key-point (S_{02}), a constant crack width (w_{S02}) of 0.400mm was assumed whereas the respective loads (P_{S02}) were fixed in order to better fit the experimental results of each case-study. The average tensile strength of the matrix (f_{ctm}) was calculated based on the expressions from (ENV 1992-1-1 1992). The thorough set of parameters used in the model is summarized in Tab.4.2.

Table 4.2 - Input values used on the pullout model.

Case	P_{S01} [N]	P_{S02} [N]	w_{S01} [mm]	w_{S02} [mm]	d [mm]	L_e [mm]	f_{ctm} [MPa]	μ [-]	N [-]
A	44.9	12.0							
B	44.4	7.0	0.050	0.400	0.50	10.0	2.80	0.60	1
C	50.2	11.0							
D	58.2	13.0							

Fig.4.11 shows how model predictions accomplish to depict different pullout shapes for the different case-studies and orientations. Fibers inclined 30° denote high performance at small crack widths (few tenths of mm) and a relatively weak load carrying capacity for larger crack openings whereas in the case of fibers under 60° inclination the load-crack width relationship becomes smoother along the entire post-peak branch. Such dissimilar trends derive mainly from the different magnitude of deviation forces which occur at fiber exit point and on the relative weight presented by the aligned component of the pullout mechanism on the overall response. For such reason, despite the rough procedure used to extract material properties (Fig.4.3), the underestimations introduced tend to disappear with the increase on the inclination angle. The procedure thus proves to be worthwhile regarding the required commitment between model straightforwardness and accuracy.

The increment of pullout load prior to complete removal of the fiber is not considered in the model because the crack width range which is influenced by this effect (about 1.0mm) is most of the times out of interest for SFRC structural applications. Therefore modeling efforts focused on the main parameters which affect the initial stage of pullout process such as matrix spalling. In Fig.4.12a it can be seen that the magnitude of the experimental matrix spalled lengths does not changes significantly with fiber yield strengths, presenting coefficients of variation of about 10 and 15% for inclination angles of 30° and 60° , respectively.

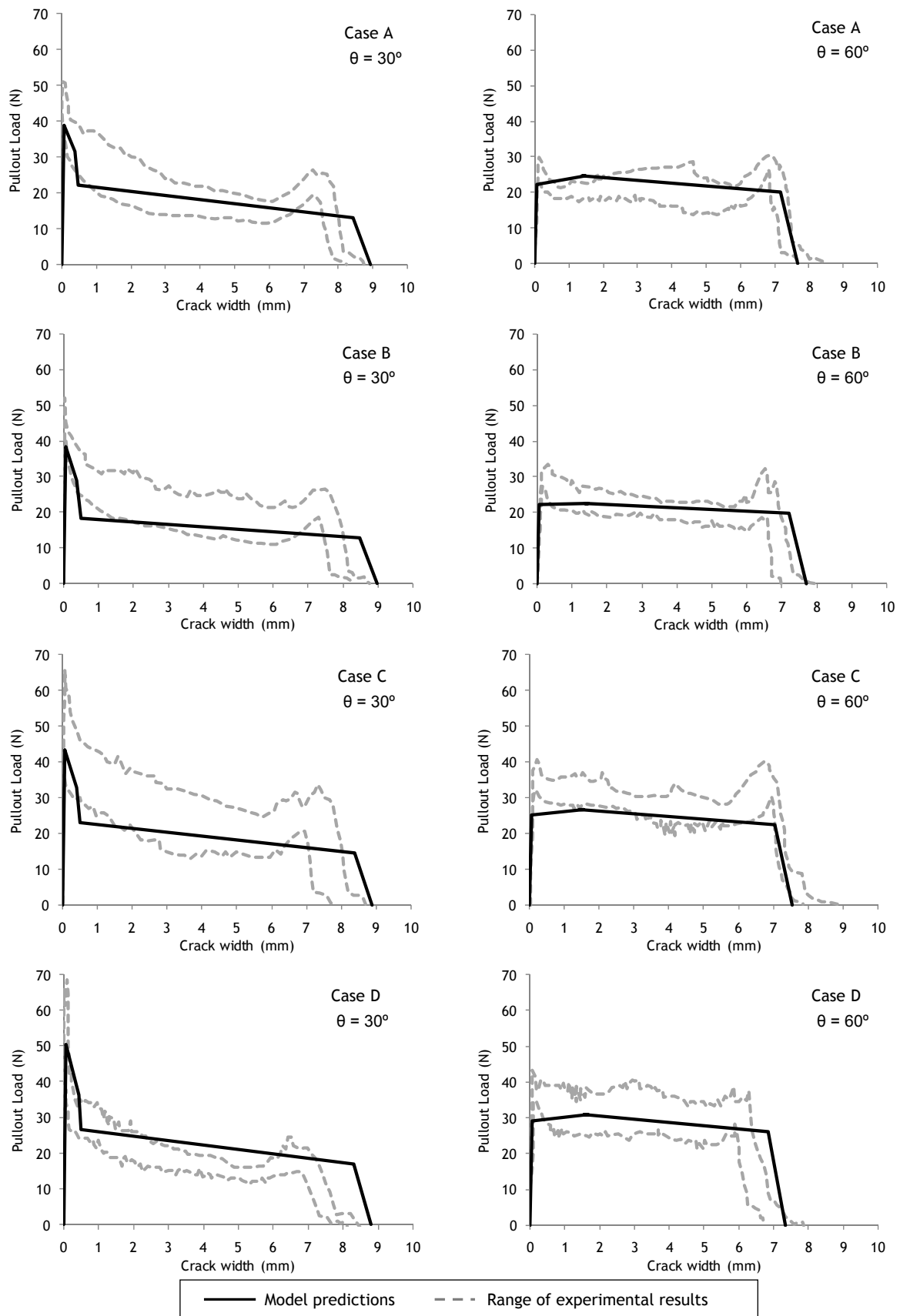


Fig.4.11 - Comparison between model predictions and experimental data from Leung and Shapiro (1999) for inclination angles of 30° and 60° and several case-studies.

Regarding such scattering the predictions of matrix spalled lengths (L_{SP1}) provided by the model are acceptable and within the limit range of experimental results in most cases.

In order to quantify the good agreement between the load-crack width responses presented in Fig.4.11 the pullout works of the entire process were calculated (Fig.4.12b). A good correlation on pullout works is observed in Fig.4.12b for all cases, i.e. irrespectively of fiber yield strength, supporting that the simplified diagrams adopted for aligned fibers perform a reasonable assumption.

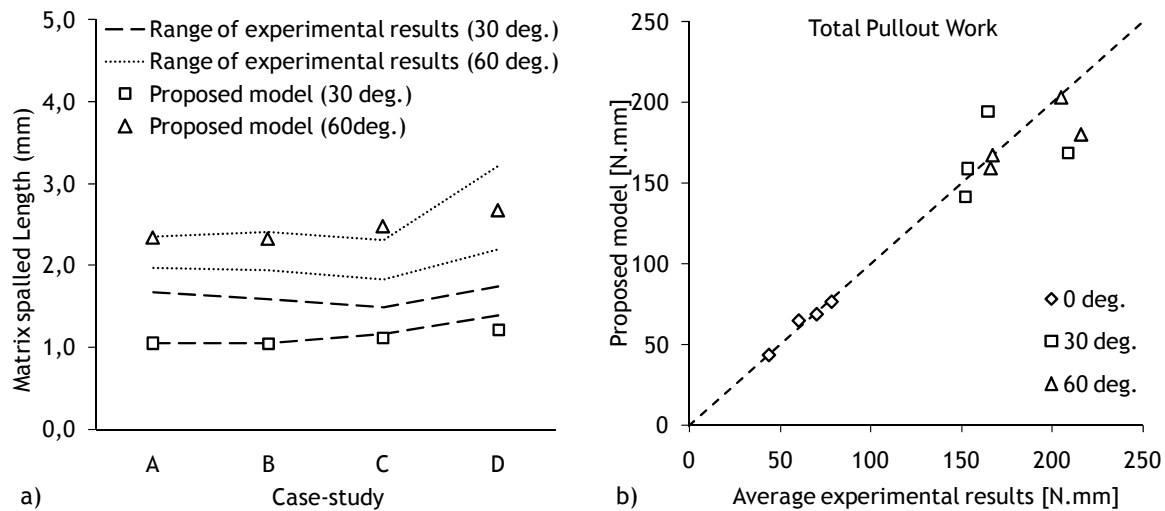


Fig.4.12 - Comparison between model predictions and experimental data from (Leung and Shapiro 1999):
a) Matrix spalled lengths; b) Total pullout work.

4.6.2 Parametric study

In this study the influence of the inclination angle (θ) on the shape of the pullout diagram is firstly evaluated. Then θ is related with the increments of crack width due to matrix spalling, with the pullout work of the entire diagram and with the maximum pullout loads. Finally an optimum range of inclination angles concerning the pullout work up to 0.2mm is identified. All the calculations are based on the aforementioned case D, whose parameters are shown in Tab.4.2.

The effect of the inclination angle on the shape of the load-crack width relationship is shown in Fig.4.13. Increasing inclination angles not only reduce the pullout load at small crack openings but also decrease the extent of the crack width in which fiber contributes for strengthening. Both of these effects occur due to increasing magnification of matrix spalling which postpones the contribution of the deviation force and reduces the available fiber embedded length.

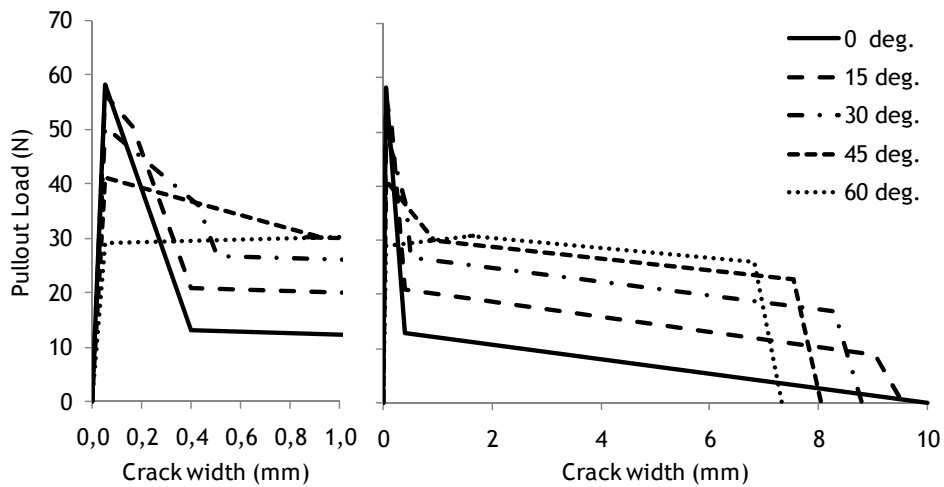


Fig.4.13 - Influence of the inclination angle on the shape of the pullout response.

Matrix spalling plays a major role on the initial stage of the pullout diagram due to the increments of crack width generated by reorientation of fiber protruded length. Fig.4.14 shows the relation between the increments of crack width due to matrix spalling and fiber inclination angle.

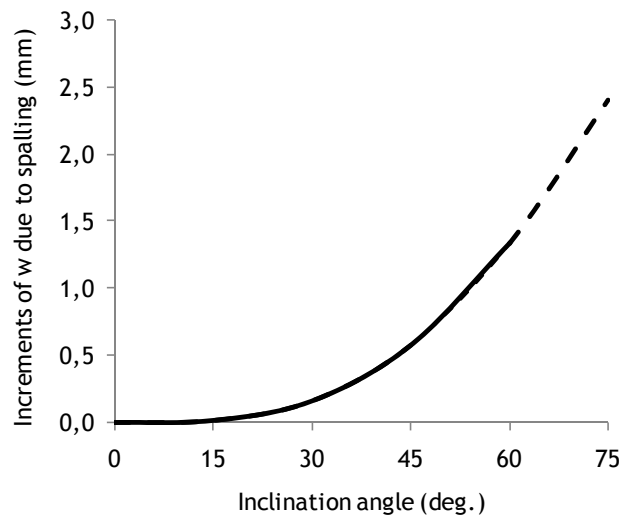


Fig.4.14 - Increment of crack width due to matrix spalling (Δw_{SP1}) at different fiber inclination angles.

Pullout loads strongly depend on the balance between the contributions provided by the interface properties and the magnitude of the deviation force around fiber exit point. The latter is absent on aligned fibers and increases progressively with fiber inclination angle, enhancing local friction and therefore the work required to completely remove the fiber. The low quality of the cement matrix in this case-study implies a rather poor contribution from the aligned component of the pullout mechanism and therefore it is not surprising that inclined fibers require much higher pullout works (Fig.4.15a).

The small fiber embedded length of these fibers led to premature fiber debonding. Consequently the beneficial effect provided by the deviation force in terms of maximum pullout load only acts concurrently with partial bonded fibers up to an inclination angle of 2° (Fig.4.15b). Therefore the peak loads progressively decreases at larger inclination angles. Regarding the pullout work up 0.2mm a much lower performance is also denoted by fibers under large inclination angles (Fig.4.15b). In the present case-study such is even more noticeable due to the moderate tensile strength of the matrix which leads to an optimum inclination angle of 18° and pullout work performances higher than the aligned one up to 38° .

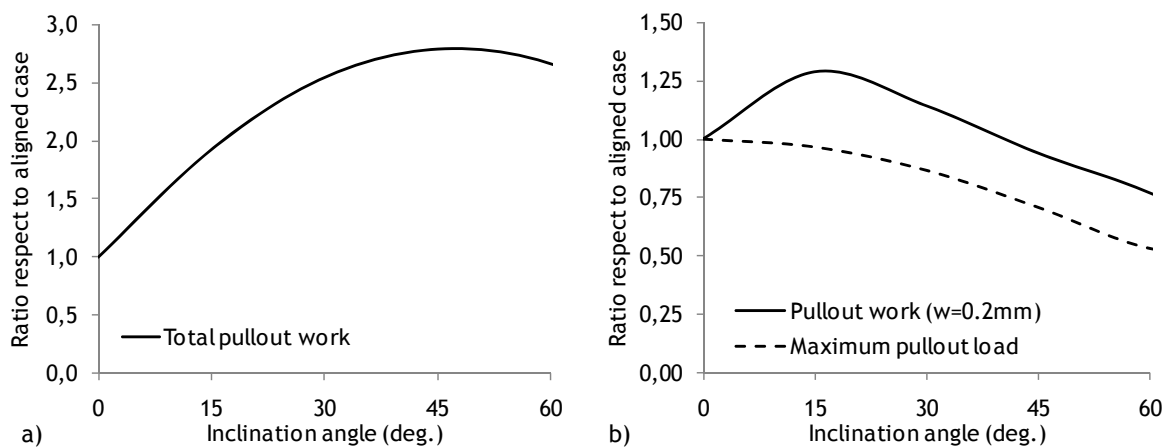


Fig.4.15 - Effect of fiber inclination angle on: (a) the total pullout work; (b) the maximum pullout load and pullout work up to 0.2mm.

4.6.3 Applying the model to optimize material properties

Given the suitability of the current approach on describing the pullout behavior of inclined fibers a major step towards optimization of SFRC can be performed. In order to exemplify how this model accomplishes such purpose a practical example of design tailoring is advanced.

Consider the design of SFRC for structural applications in which high performance of the material is required up to a crack width of 0.5mm. Now assume that the reference material is the one previously presented in case D (see Tab.4.2) and that no preferential orientation of the fibers exists within the material. What is the most convenient combination of fiber geometry and matrix strength?

To answer the question two different design possibilities will be discussed. The first one comprehends an improvement of the matrix strength by doubling its average compressive strength up to 73.0MPa. The second case evaluates the effect of increasing the ratio between fiber embedded length and fiber diameter. For such purpose the embedded lateral surface of the fiber was kept constant and a 0.25mm fiber diameter with 20mm was chosen. The input parameters of the model for each case are summarized in Tab.4.3.

Table 4.3 - Input values used on different design cases.

Case	P _{S01} [N]	P _{S02} [N]	w _{S01} [mm]	w _{S02} [mm]	d [mm]	L _e [mm]	f _{ctm} [MPa]	μ [-]
Reference							2.80	
1	58.2	13.0	0.050	0.400	0.50	10.0	4.50	0.60
2					0.25	20.0	2.80	

The pullout responses of inclined fibers with 15°, 30°, 45° and 60° were calculated for different cases and the matrix spalled lengths, maximum pullout loads, pullout works of the entire diagram and up to crack widths of 0.5mm were obtained (Fig.4.16).

From Fig.4.16 it becomes evident that the improvement on the matrix strength (case 1) reduces the matrix spalled lengths but does not enhances significantly the performance of the material, neither in terms of maximum pullout loads nor pullout works. Such occurs mainly due to the low value of the pullout load which was kept constant relatively to the case of reference. Indeed, the increase on the matrix strength might increase as well the interfacial bond and therefore also the deviation force at fiber exit point, from which the effect of the matrix strength would magnify the benefic effect on maximum load and pullout work.

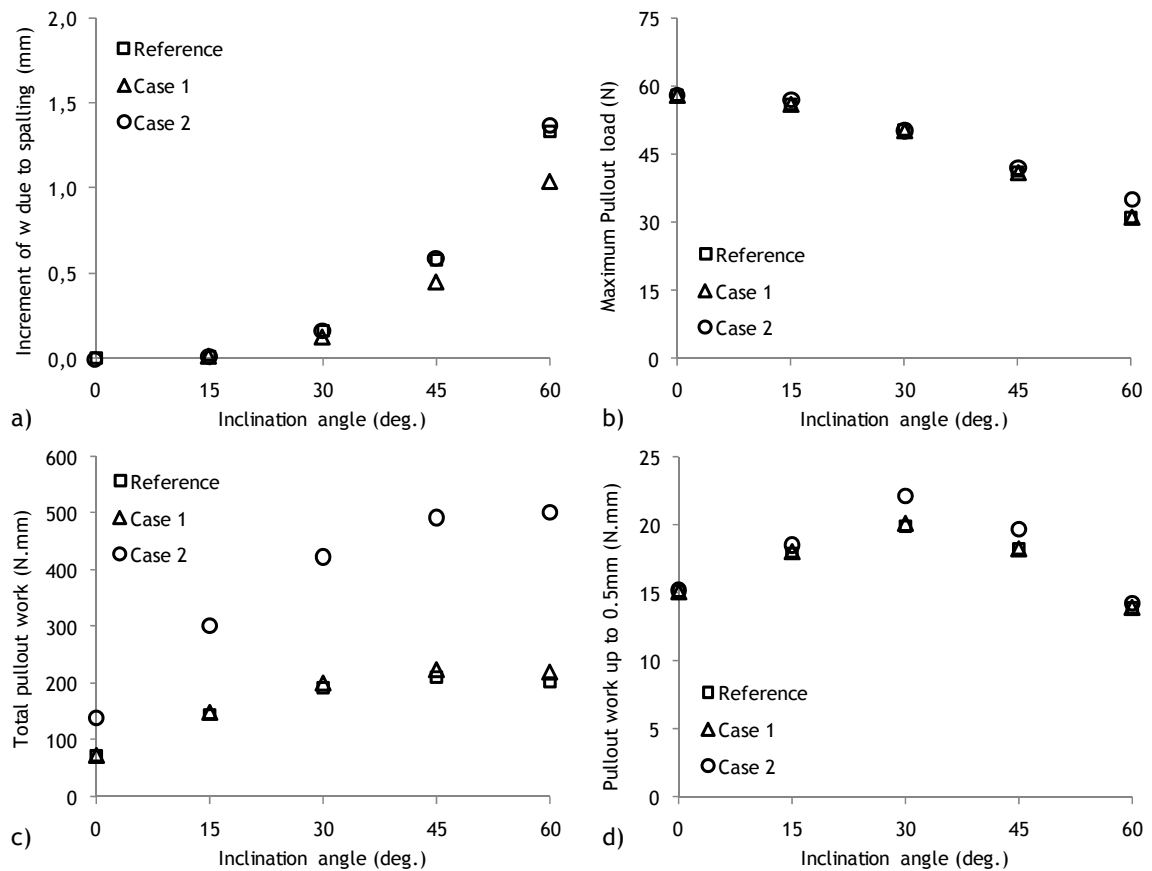


Fig.4.16 - Comparison between the results of three design cases in terms of (a) matrix spalled lengths; (b) maximum pullout loads; (c) total pullout work; (d) pullout work up to 0.5mm crack width.

The increase on fibers aspect ratio (case 2) improves dramatically the total pullout work due to the higher embedded length and, at small extent, also the maximum pullout loads and pullout work up to 0.5mm. Moreover the improvement of aspect ratio reduces to 50% the embedded fiber volume on the matrix and therefore keeping the same dosage of fibers in the matrix would double its beneficial effect.

With the aim of maximizing the structural contribution provided by the material up to a certain limit crack width, the choice of the most appropriate design solution shall be conducted by the values of maximum pullout work up to that limit. The energy required to open the crack is the sum of the pullout contributions of all the individual fibers in the cracked section. Under the assumption of material isotropy and regarding a simplified case in which fibers would have the same embedded length respect to the crack, the best design solution would be the one leading to the larger pullout work up to a limit crack width, 0.5mm in this particular case. Therefore, for the present case-study, changing fiber geometry (case 2) would provide a better structural performance and, most likely, also a better economic solution. Although these conclusions apply for this particular case of materials and boundary conditions, the procedure highlights the capacity of the approach on providing a straightforward and comprehensive method to evaluate different design solutions.

4.7 CONCLUDING REMARKS

The several phenomena involved within the pullout response of inclined straight steel fibers embedded in cement matrices were considered in this chapter. The input parameters of the model are related to material properties (fiber and matrix tensile strengths and fiber geometry), boundary conditions (fiber inclination angle and embedded length) and experimental pullout responses of fibers aligned with loading direction.

The approach predicts multi-linear diagrams which result from assembling a set of five key-points, each of them with clear and well defined conceptual background. Each key-point refers to a specific stage of the pullout process in which the magnitude of the load-crack width relationship is quantified by means of physical and geometrical properties. Model predictions were compared against experimental results on fibers with different tensile strengths and inclination angles. The results show that the model is able to reproduce the main features of pullout behavior and to reasonably predict the entire load-crack width response.

Physical insight on the parameters which play major influence at each stage of pullout response is provided through a very simple and straightforward diagram. Thereby this model supplies relevant guidelines to understand how the shape of the pullout response of inclined straight fibers can be manipulated by merely changing any fiber or matrix property independently.

With this new predictive tool an important step towards a new concept of comprehensive design and optimization of SFRC for structural applications is therefore being advanced. To greatly accomplish such purpose the model shall also be able to predict the pullout behavior of more common geometries, such as fibers with hooked-ends, which are covered in the next Chapter 5.

Chapter 5

Predicting the pullout response of inclined hooked steel fibers

5.1 INTRODUCTION

Nowadays, fibers with hooked-ends are the most common type of steel fibers used in concrete reinforcement. Thereby, understanding the mechanisms governing the crack-bridging effect of these fibers at any inclination angle is very important. In the previous chapter, a model for the pullout response of inclined straight steel fibers was advanced. Such model is herein extended to fibers with hooked-ends.

This chapter aims at providing a straightforward method to predict the effect of the inclination angle on the load-crack width response of hooked steel fibers.

A description of the pullout response of this type of fibers is firstly presented. Then, a new conceptual approach to predict their pullout behavior is introduced on a comparative manner with the one previously advanced for straight fibers. Finally, the model is validated against several experimental pullout test results from literature.

5.2 RESEARCH SIGNIFICANCE

Mechanical deformation of fibers introduces additional complexity on the pullout response of inclined fibers. Although fibers with hooked-ends have been largely investigated, predicting their load-crack width relationships under any inclination angle has not yet been solved. This chapter proposes a new analytical model to predict such pullout response within a straightforward method, taking as input parameters properties of constituent materials and pullout tests of fibers aligned with load direction. Model validation is performed through published experimental data in which large variety of fibers and matrices were used within different boundary conditions. Results show that this approach provides a powerful tool to develop a conceptual, comprehensive and design-oriented constitutive model for the tensile behavior of SFRC.

5.3 PULLOUT BEHAVIOR

5.3.1 Main concepts

The pullout behavior of hooked fibers comprises all the phenomena described for inclined straight fibers such as fiber debonding, matrix spalling, frictional sliding and fiber removal. Nonetheless hooked ends imply plastic deformations which increase the force required to pullout the fiber, thus magnifying the matrix spalling effects of inclined fibers.

To account for the contribution provided by the hook along fiber slippage, a clear physical comprehension of its straightening process is required. Correlations between fiber pullout and respective load-crack width responses were advanced by Pompo et al. (1996) through video photography techniques. From that research a typical pullout response of inclined fibers was suggested, consisting of four distinct regions: (1) elastic response followed by debonding; (2) fiber pullout and straightening processes; (3) frictional sliding within the straight matrix duct; (4) fiber removal from the matrix. Such trend resembles the typical pullout behavior considered for straight fibers (Chapter 4) with exception of stage concerning fiber straightening (region 2) which was absent in straight fibers and, consequently, will be discussed with detail.

5.3.2 Correlation between geometry of the hook and pullout response

The correlation between fiber pullout responses and the several deformation phases of the hook requires accurate measurements of its geometry. According to investigations on steel fibers with diameters of 0.50 and 0.80mm (Van Gysel 2000), the hook's geometry was found to be composed of straight and arc segments (Fig.5.1). Considering the reported magnitude for the radius of curvature (about 1.20mm) each arc-length was approximately 1.05mm whereas intermediate straight segments were about 1.45 and 1.20mm (total hook length of 4.75mm).

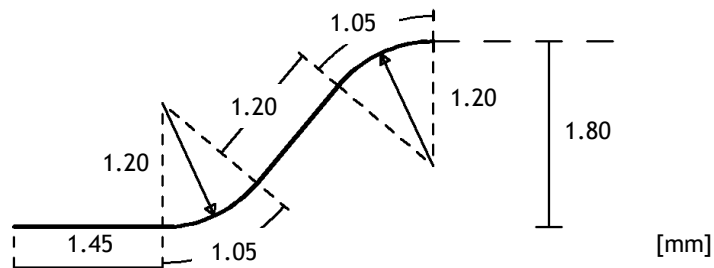


Fig.5.1 - Geometry of fiber hooked-end according to dimensions reported by (Van Gysel 2000).

The region of pullout response concerning fiber straightening comprises four main stages (Fig.5.2). The crack widths (w) and the increments of crack width (Δw) at each of these stages are suggested in Fig.5.2 according to the hook's geometry advanced in Fig.5.1.

At the beginning of the pullout process fiber has just been fully debonded and therefore its end section (G_1 in Fig.5.2a) as well as the intermediate sections of the arc lengths (G_2 and G_3 in Fig.5.2a) coincide with the initial print of the hook. Then both curved sections are progressively subjected to bending and plastic deformations, leading to a substantial increase on the pullout load. The maximum force required to pullout the fiber arises when G_2 and G_3 enter the straight segments of the matrix duct walls, which occurs for fiber slippages of about half of the arcs length (Fig.5.2b). Afterwards pullout load decreases given that G_2 and G_3 do not undergo significant plastic deformations while slipping along the straight ducts. However, once G_1 passes through the original print of section G_2 , the latter is already at the next curved length of the hook print where it is forced to bend contrarily to its original shape. Considering the relative slippages at which G_1 and G_2 experiment maximum plastic deformations (1.48 and 1.72, respectively), pullout load may stabilize for an increment of crack width of about 1.60mm (Fig.5.2c).

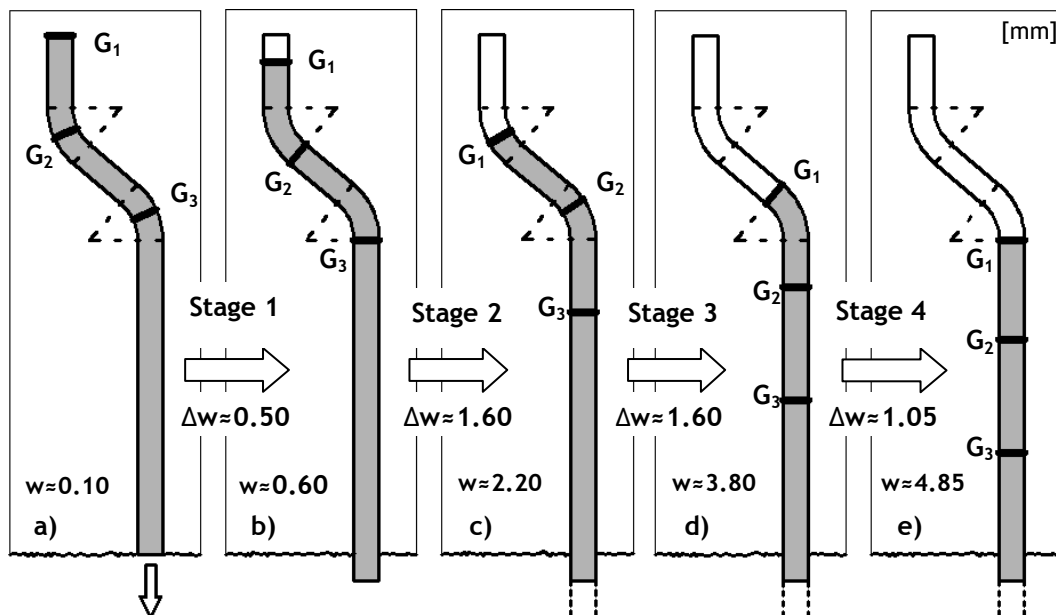


Fig.5.2 - Main stages of the straightening process of the hooked-end within the cement matrix.

At the third stage of hook deformation a moderate decrease in pullout load occurs due to the entrance of G_2 on the last straight segment of the duct. The pullout load is now mainly governed by the local friction effects imposed by G_1 and G_3 along the duct walls, thus keeping the pullout load nearly stable. When G_1 enters the second curved segment, abrasion against the duct walls increases due to incomplete straightening of the last straight portion (Fig.5.2d). The final stage of the straightening process occurs when G_1 enters the straight duct (Fig.5.2e). At this instant, although no further plastic deformations occur on the fiber, a residual resistance is prone to remain due to incomplete straightening of the hook. Likewise the hook slips along the ducts with a three-point contact mechanism (Pompo et al. 1996) which can be clearly identified by comparing the hook's geometries before and after testing (Fig.5.3), as also pointed out by other researchers (Naaman and Najm 1991).

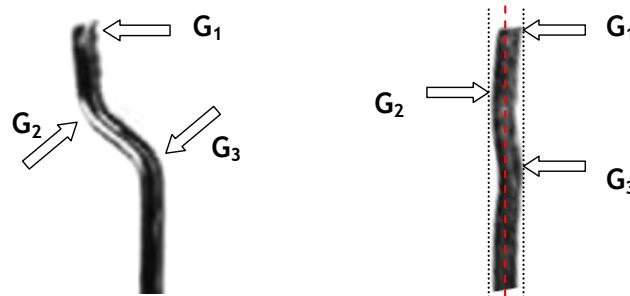


Fig.5.3 - Detail of hook geometry before testing (left) and after pullout (right).

5.3.3 Aligned fibers

The magnitude of the contribution provided by the mechanical anchorage depends upon several material properties. The larger the fiber diameter, the more energy has to be invested to deform the fiber due to its increasing bending stiffness (Van Gysel 2000). Pullout tests on aligned fibers reported that maximum loads increase less than proportionally with fiber squared diameter, under similar pullout conditions and geometry of the hooked ends (Van Gysel 2000).

Similarly to straight fibers, the pullout performance has also been shown to be enhanced by improving the properties of the matrix in which fibers are embedded (Naaman and Najm 1991; Van Gysel 2000). Experiments on steel fibers with 1200MPa tensile yield strength reported 25% increment on maximum loads when testing fibers from normal to high strength matrices ($f_{cm}=47\text{MPa}$ and $f_{cm}=76\text{MPa}$) whereas larger increments (about 65%) were observed when using fibers with 2100MPa tensile yield strength (Van Gysel 2000).

Since the peak load is controlled by the plastic deformations of the hooks, an alternative and more effective method to improve pullout performance consists on increasing fibers tensile strength. The investigation performed by Van Gysel (2000) denoted an increment of 100% on the peak load when improving the tensile yield strength of fibers from approximately 1200 to 2100MPa on high strength matrices ($f_{cm}=76\text{MPa}$). A smaller increment was found (50%) when such improvement was performed on normal strength matrices ($f_{cm}=47\text{MPa}$), inducing that lower bond strength conditions might not have allowed full straightening of the hooked ends.

A commitment between matrix composition and fiber tensile strength shall be pursued in order to extract the maximum performance while avoiding brittle failure of the fibers. How to optimize these material properties will be further addressed in Section 5.5.1.

5.3.4 Inclined fibers

Experimental observations

Tests on inclined fibers showed that crack widths at peak increase with the inclination angles (Banthia and Trottier 1994; Armelin and Banthia 1997; Van Gysel 2000; Robins et al. 2002; Cunha et al. 2007) and those were found to be generally independent of fiber embedded length providing that the hook end was fully mobilized (Robins et al. 2002). These increments of crack width are most likely a combination of fiber straightening with crushing and spalling of the concrete that take place at the corner where fiber enters the matrix (Bartos and Duris 1994; Banthia and Trottier 1994; Robins et al. 2002; Cunha et al. 2007) (Fig.5.4). At large inclination angles the pullout response becomes progressively less influenced by the matrix strength and increasingly governed by the mechanical properties of the fiber as it attempts to straighten in line with the loading direction (Robins et al. 2002).

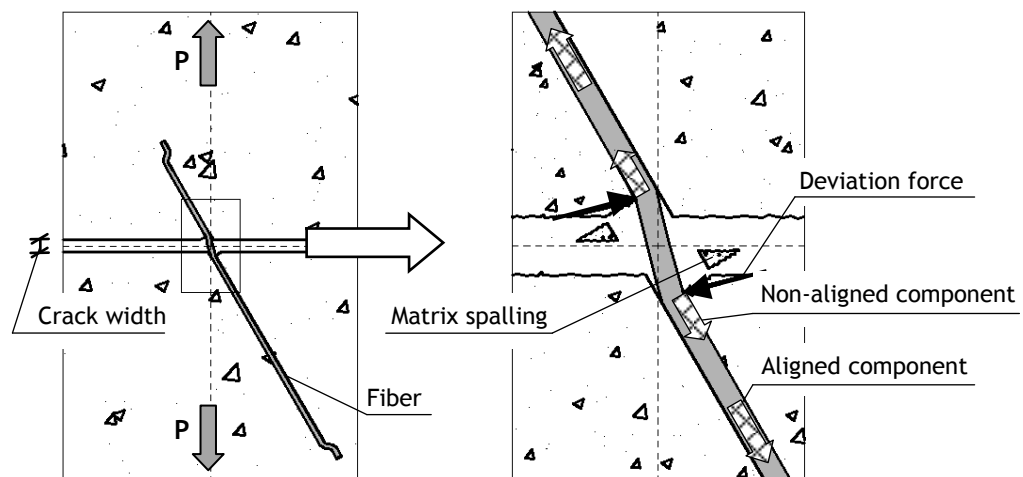


Fig.5.4 - Pullout of an inclined fiber with matrix spalling at both sides of the cracked surface.

Optimum peak loads of hooked fibers occur under non-zero inclination angles due to the increasing friction that occur at fiber exit point. Experiments indicate that optimal fiber inclinations angles may be within 10° - 30° (Banthia and Trottier 1994; Armelin and Banthia 1997; Robins et al. 2002) with increments at peak load with respect to aligned fibers up to 20% (Robins et al. 2002). The latter are sometimes limited by fiber rupture, which introduces a brittle and undesirable failure mode. Hence two major pullout failure modes may occur, either by straightening and removal of the fiber or, alternatively, by fiber rupture (Banthia and Trottier 1994; Van Gysel 2000; Robins et al. 2002; Markovic et al. 2003; Cunha et al. 2007).

Experimental works (Bartos and Duris 1994; Banthia and Trottier 1994; Armelin and Banthia 1997; Van Gysel 2000; Robins et al. 2002; Cunha et al. 2007) showed that the load at which fibers fail

decreases at increasing inclination angles. The reduction in the ultimate load may be best explained by Bartos and Duris (1994) who introduced a new fiber characteristic, the so-called inclined tensile strength, which accounts for the coupled nature of axial, bending and shear stresses that occur at the fiber exit point.

Fiber rupture takes place during the early stage of the pullout process where relative slippage is still being greatly counteracted by the hook. Therefore the maximum curvature nearby fiber exit point is limited to a short extent of the fiber that can be idealized as a single plastic hinge. For fibers under large inclination angles the axial component of the pullout mechanism is not dominant and rupture tends to occur due to attainment of the ultimate strain capacity of the steel at the exit point from the matrix. Although this is the most commonly observed location for fiber rupture (Banthia and Trottier 1994; Van Gysel 2000; Cunha et al. 2007), fracture at the hook portion has also been observed (Robins et al. 2002). This may occur due to the small distance between the actual fiber exit point and the portion where the hook is located, typically when matrix spalling produces small fiber embedded lengths. In those cases bending stresses generated by local curvature extend towards inner sections of the fiber on a degree dependent upon fiber flexibility. Hence rupture at the hook portion occurs as result of the superposition of bending stresses with the ones existing from the straightening process.

Regarding the severe decrease of the total pullout energy caused by fiber rupture, the consideration of an inclined tensile strength rather than the co-axial one is fundamental to evaluate pullout of inclined fibers appropriately (Bartos and Duris 1994).

Pullout response

Taking into account the aforementioned concepts and the trends of experimental results reported in literature, a general shape for the pullout diagram of inclined steel fibers with hooked ends can be observed (Fig.5.5).

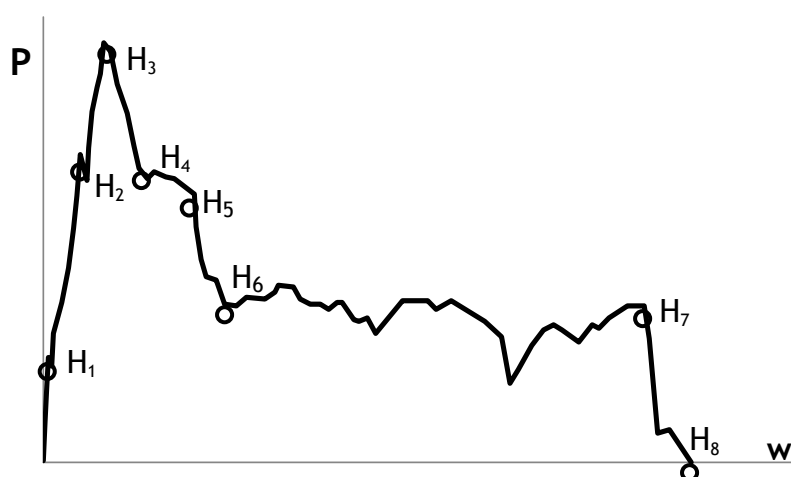


Fig.5.5 - Identification of the key-points on the experimental pullout response of inclined steel fibers with hooked ends obtained from (Van Gysel 2000).

The initial branch of the pullout response is similar to the one denoted by inclined straight fibers. When fiber debonding occurs (H_1 in Fig.5.5) the pullout response enters into an unstable phase in which bending of the debonded segments of the fiber tends to impose failure of the matrix at the cracked surface. Depending on the flexibility of the fiber different distribution of pressures and volumes of matrix wedge may be mobilized. Since the respective equivalent force depends upon the fiber axial stress, matrix spalling can then be conceptually divided in two stages: (1) due to the axial stress developed along the straight portion of the fiber; (2) due to the increment of axial stress provided by the hook.

Contrarily to straight fibers, at the end of the first stage of matrix spalling (H_2 in Fig.5.5) equilibrium at fiber exit point is no longer guaranteed since the hook has already been partially activated. The larger the inclination angle, the larger are the matrix spalling effects and the smaller is the contribution provided by the straightening process of the hook at point H_2 .

Matrix spalling moves fiber exit point from the initial pullout axis into sections whose depth respect to cracked surface is progressively higher. Thereby matrix stability increases with the amount of spalling. When the maximum contribution provided by the hook is attained (H_3 in Fig.5.5) no further spalling occurs and pullout develops under a more stable mechanism. The post-peak branch is then characterized by three key-points (H_4 , H_5 and H_6 in Fig.5.5) whose relative slippages are associated to the geometry of the hook.

When the end tip of the fiber enters the initially straight segment of the duct (H_6 in Fig.5.5) no further plastic deformations occur. Then friction becomes the dominant mechanism and the load carrying capacity decreases proportionally to the available embedded length at an almost constant rate. When the remaining embedded length tends to zero the pullout load depends mainly on the deviation force at fiber exit point. Thus when a critical embedded length is reached (H_7 in Fig.5.5) the load sharply decreases to zero (H_8 in Fig.5.5). The latter tends to occur at crack widths of about the initial embedded length deducted by the total length of spalled matrix measured along fiber main axis.

5.4 PULLOUT MODEL

5.4.1 General methodology

The pullout response of fibers aligned with the load direction is firstly evaluated and the contribution of the hook along the load-crack width diagram is taken into account through four key-points. Then this contribution is superposed over the pullout response of inclined straight fibers, thus clearly providing the effect of the anchoring mechanism on the pullout diagram. The latter is composed by eight key-points (Fig.5.5), each of them related to a different stage of the pullout process. These key-points are then used to trace the predictive pullout responses of inclined fibers.

5.4.2 Extracting the contribution of the hook from experimental data

An experimental evaluation of the contribution provided by the hook is an irrevocable procedure. One of the main reasons for this requirement regards the dissimilar performances exhibited by different types of commercial fibers, which differ both in the quality of the steel and on the geometry of the hook itself. The other major cause is related to the need of testing fibers embedded in representative matrices that reflect the actual characteristics affecting fiber pullout (ex: aggregate grading and maximum grain size, presence of microfibers in the pullout medium, matrix shrinkage, etc.).

In order to evaluate the effect of the hook some authors (Naaman and Najm 1991; Cunha et al. 2007) adopted a procedure which consists of subtracting the pullout curve of aligned straight fibers to the respective diagram of fibers with hooked ends. Such an approach is considered in this model by quantifying the contribution of the hook through four key-points (Fig.5.6).

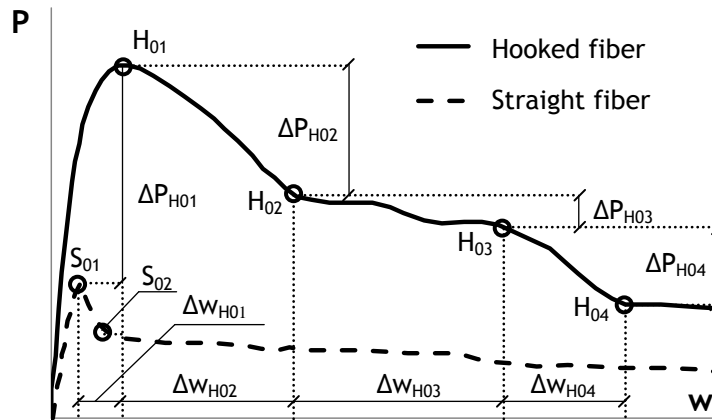


Fig.5.6 - Identification of the key-points on experimental data of aligned fibers obtained from (Cunha et al. 2007).

The initial strengthening provided by the hook is assessed through the increments of pullout load (ΔP_{H01}) and slip at peak (ΔW_{H01}) according to Eqs.1-2, respectively (Fig.5.6).

$$\Delta P_{H01} = P_{H01} - P_{S01} \quad (5.1)$$

$$\Delta W_{H01} = W_{H01} - W_{S01} \quad (5.2)$$

The identification of the post-peak key-points (H_{02} , H_{03} and H_{04}) is performed through their relative pullout loads and respective crack widths, such as defined in Eq.5.3-5.4 (Fig.5.6):

$$\Delta P_{H0(i+1)} = P_{H0(i+1)} - P_{H0i} \quad (5.3)$$

$$\Delta W_{H0(i+1)} = W_{H0(i+1)} - W_{H0i} \quad (5.4)$$

With i ranging from 1-3. The relative crack widths (Eq.5.2 and Eq.5.4) are related to the geometry of the hook and therefore no significant differences respect to values advanced in Fig.5.2 should exist.

5.4.3 Detailed description of the pullout model

Using the experimental data (H_{01} , H_{02} , H_{03} and H_{04} in Fig.5.6) the pullout model becomes defined by eight key-points (Fig.5.5). In cases where post-peak accuracy is not fundamental, a simplistic variant of the model can be applied by taking into account uniquely H_{01} and H_{04} . In such case, the pullout model only comprises six key-points (H_4 and H_5 are neglected).

Point H_1 : Debonding process

The first pullout stage evolves from crack propagation and subsequent fiber activation. Whenever crack passes through the fiber at any of its straight segments (excluding hooked segments) the pullout performance of hooked fibers prior to the beginning of debonding process does not differ from the one of straight fibers. Hence the first key-point (H_1) is defined just like in the case of straight fibers (Chapter 4) by Eqs.5-6:

$$P_{H1} = P_{S1} = P_{S01} \cos\theta \quad (5.5)$$

$$W_{H1} = W_{S1} = W_{S01} \quad (5.6)$$

Point H_2 : Effects of matrix spalling (stage 1)

In the model advanced for straight steel fibers (Chapter 4), the length of spalled matrix (L_{SP1}) was calculated through a failure criterion which considered, on one side, the tensile strength and the geometric configuration of the matrix wedge at the cracked surface and, on the other side, a spalling force (F_{SP1}) dependent on the deviation force at fiber exit point. A similar phenomenon is observed in the pullout of hooked fibers. Matrix spalling extends under increasing pullout loads such that when the contribution along the fiber main axis equalizes the one observed in straight fibers (P_{S01}) the length of the spalled matrix might be suchlike (L_{SP1}). However, at the end of the first stage of matrix spalling process (point H_2) the anchorage effect provided by the hook might have introduced some resistance against fiber slippage. Accordingly, it will be assumed that the hook is activated just after fiber debonding (point H_1) and its contribution increases progressively until a maximum value along fiber main axis (P_{H01}) is observed (point H_3).

In the case of fibers under large inclination angles, local friction at the fiber exit point governs the pullout process, thus postponing the anchoring effect provided by the hook. According to the model advanced for straight fibers (Chapter 4) the balance between the aligned and non-aligned components of the pullout mechanism at the end of the first stage of matrix spalling is proportional to the spalling length (L_{SP1}). Thereby the aligned component of the pullout load (P_{HA2}) becomes defined as following:

$$P_{HA2} = \left(P_{S01} L_{\text{eff}(H2)} + \Delta P_{H01} \frac{L_e - 6 \times L_{SP1}}{L_e} \right) \cos\theta \quad (5.7)$$

Where $L_{\text{eff}(H2)}$ is the effective length factor taking into account the reduction of available embedded length (Eq.5.8):

$$L_{\text{eff}(H2)} = L_{\text{eff}(S2)} = \left(\frac{L_e - L_{SP1}}{L_e} \right) \quad (5.8)$$

P_{S01} applies for the straight segment of the fiber since sliding is restrained by the hook. The non-aligned component of the pullout (P_{HN2}) accounts uniquely for the deviation force (D_{F1}) which equilibrates the respective spalling force (F_{SP1}), such as defined in Eq.5.9:

$$P_{HN2} = P_{SN} = \mu D_{F1} = \mu P_{S01} \sin\theta \cos\frac{\theta}{2} \quad (5.9)$$

The pullout load at this stage is then obtained by summing Eq.5.7 and Eq.5.9:

$$P_{H2} = P_{HA2} + P_{HN2} \quad (5.10)$$

The respective crack width (w_{H2}) is defined consistently by considering the contribution derived from the aligned component (w_{HA2}) and the increment due to matrix spalling (Δw_{SP1}):

$$w_{H2} = w_{HA2} + \Delta w_{SP1} \quad (5.11)$$

The portion of the crack width which accounts for the effects occurring along the embedded fiber axis (w_{HA2}) includes the crack width associated to the debonding process (w_{H1}) and the increment of crack width due to partial deformation of the hook (Eq.5.12).

$$w_{HA2} = w_{H1} + \Delta w_{H01} \frac{L_e - 6 \times L_{SP1}}{L_e} \cos\theta \quad (5.12)$$

The increment of crack width accounting for the reorientation of the fiber due to the first stage of matrix spalling (Δw_{SP1}) is the one defined for straight fibers:

$$\Delta w_{SP1} = N L_{SP1} (1 - \cos\theta) \quad (5.13)$$

Where N is the number of sides of the crack where spalling occurs (N=1 or N=2).

Point H₃: Effects of matrix spalling (stage 2)

The anchoring effect provided by the hooks increases significantly stresses on the fiber and consequently matrix undergoes a second stage of spalling until the maximum force along fiber main axis (P_{H01}) is equilibrated at the new fiber exit point. To account for the increment of

spalled matrix along fiber main axis (L_{SP2}) a simplified failure criterion was adopted (Appendix 2.3). The pullout load at the end of the second stage of matrix spalling (P_{H3}) is then obtained by summing the respective aligned (P_{HA3}) and non-aligned (P_{HN}) components. The former takes into account the increment of strength provided by the hook such as measured on experimental data (ΔP_{H01}) as well as the contribution provided by the straight segments of the fiber, affected by the reduction of embedded length due to matrix spalling:

$$P_{HA3} = (P_{S01} L_{eff(H3)} + \Delta P_{H01}) \cos\theta \quad (5.14)$$

Where $L_{eff(H3)}$ is the effective length factor at key-point H_3 , defined as following:

$$L_{eff(H3)} = \frac{L_e - (L_{SP1} + L_{SP2})}{L_e} \quad (5.15)$$

Although full-debonding has already occurred at this stage, P_{S01} still applies in Eq.5.14 since frictional sliding is still restrained due to the presence of the hook.

The non-aligned component of the pullout mechanism (P_{HN}) stands for the local friction introduced by the new deviation force (D_{F2}) which depends upon the maximum axial force on the fiber (P_{H01}) and on the deviation angle between the embedded and protruded lengths of the fiber (Eqs.16-17).

$$P_{HN} = \mu D_{F2} \quad (5.16)$$

$$D_{F2} = P_{H01} \sin\theta \cos\frac{\theta}{2} \quad (5.17)$$

The crack width at which the peak pullout load occurs (w_{H3}) accounts for the crack width prior to debonding (w_{H1}) and for its increment due to straightening of the hook, such as measured in the experimental data (Δw_{H01}). Furthermore it also considers the increments of crack width due to both stages of matrix spalling, being the latter defined in Eq.5.18. Hence w_{H3} becomes the sum of the multiple components, such as shown in Eq.5.19.

$$\Delta w_{SP2} = N L_{SP2} (1 - \cos\theta) \quad (5.18)$$

$$w_{H3} = w_{H1} + \Delta w_{H01} \cos\theta + \Delta w_{SP1} + \Delta w_{SP2} \quad (5.19)$$

Point H_4 : Post-peak (stage 1)

Once the maximum contribution provided by the hook is attained (point H_3) the decrease on the pullout load is similar to the one observed on the post-peak branch of aligned fibers (Fig.5.6). In the absence of further matrix spalling the curvature of fiber at the exit point remains unchanged and therefore a constant non-aligned component will be assumed (P_{HN}). On the other hand, the aligned contribution (P_{HA4}) becomes defined such as shown in Eq.5.20:

$$P_{HA4} = \left(P_{S01} L_{\text{eff}(H4)} + \sum_{i=1}^2 \Delta P_{H0i} \right) \cos\theta \quad (5.20)$$

Where $L_{\text{eff}(H4)}$ is the effective length factor at key-point H_4 :

$$L_{\text{eff}(H4)} = \frac{L_e - (L_{SP1} + L_{SP2} + \Delta W_{H02})}{L_e} \quad (5.21)$$

Regarding that after peak load no further matrix spalling occurs, the crack width at this stage (w_{H4}) is obtained by adding to the previous stage the increment derived from the straightening of the hook, such as defined in Eq.5.22.

$$w_{H4} = w_{H3} + \Delta w_{H02} \cos\theta \quad (5.22)$$

Point H_5 : Post-peak (stage 2)

The second stage of the post-peak branch is defined on a comparative way relatively to point H_4 . The pullout load accounts for the deviation force at fiber exit point (P_{HN}) and for a reduced aligned contribution (P_{HA5}):

$$P_{HA5} = \left(P_{S01} L_{\text{eff}(H5)} + \sum_{i=1}^3 \Delta P_{H0i} \right) \cos\theta \quad (5.23)$$

Where $L_{\text{eff}(H5)}$ is the effective length factor at key-point H_5 :

$$L_{\text{eff}(H5)} = \frac{L_e - \left(L_{SP1} + L_{SP2} + \sum_{i=2}^3 \Delta W_{H0i} \right)}{L_e} \quad (5.24)$$

The crack width at which the second post-peak stage occurs (w_{H5}) is obtained by summing the respective slippage of the hook in that phase (Eq.5.25).

$$w_{H5} = w_{H4} + \Delta w_{H03} \cos\theta \quad (5.25)$$

Point H_6 : Post-peak (stage 3)

Analogously to previous post-peak stages, the load at point H_6 also accounts for the non-aligned component (P_{HN}) and for an aligned contribution (P_{HA6}):

$$P_{HA6} = \left(P_{S02} L_{\text{eff}(H6)} + \sum_{i=1}^4 \Delta P_{H0i} \right) \cos\theta \quad (5.26)$$

Where $L_{\text{eff}(H6)}$ is the effective length factor at key-point H_6 :

$$L_{\text{eff}(H6)} = \frac{L_e - \left(L_{\text{SP1}} + L_{\text{SP2}} + \sum_{i=2}^4 \Delta W_{H0i} \right)}{L_e} \quad (5.27)$$

The interface properties at the straight segments of the fiber are now represented by P_{S02} assuming that the fiber is subjected uniquely to frictional sliding. The load at this stage comprises the contribution provided by the deviation force at the fiber exit point, the residual friction provided by incomplete straightening of the hook and also friction along the straight segments of the fiber. The respective crack width is obtained as following:

$$W_{H6} = W_{H5} + \Delta W_{H04} \cos\theta \quad (5.28)$$

Point H₇: Pre-removal stage

At the end of the pullout process the hook portion becomes progressively closer to the cracked surface. The pullout load (P_{H7}) is then provided both by the component derived from the deviation force (P_{HN}) and by the aligned component (P_{HA7}), which depends majorly on the residual contribution of the hook (Eq.5.29).

$$P_{HA7} = \left(\sum_{i=1}^4 \Delta P_{H0i} \right) \cos\theta \quad (5.29)$$

When the hook starts being removed, the three-point mechanism turns into two single points of contact (G_1 and G_2 in Fig.5.3). Whenever the remaining embedded length equalizes the distance between these two points ($L_{H,crit}$) an unstable mechanism is generated. Fiber end tip tends then to rotate and the friction generated may increase locally the pullout load. The crack width at which this process of fiber removal begins (w_{H7}) is defined by Eq.5.30.

$$W_{H7} = L_e - (L_{\text{SP1}} + L_{\text{SP2}} + L_{H,crit}) \quad (5.30)$$

Where $L_{H,crit}$ is the distance between sections G_1 and G_2 (approx. 2.0mm in Fig.5.1).

Point H₈: Removal from the matrix

Upon the beginning of the fiber removal process, the pullout load drops sharply to a zero value within a crack width range of about the critical length ($L_{H,crit}$). Consequently, P_{H8} and w_{H8} become defined by:

$$P_{H8} = 0 \quad (5.31)$$

$$W_{H8} = L_e - (L_{\text{SP1}} + L_{\text{SP2}}) \quad (5.32)$$

5.4.4 Parameter identification

This model is based on the following input parameters:

- Fiber diameter (d), embedded length (L_e) and tensile strength (f_u)
- Average tensile strength of the cement matrix (f_{ctm})
- Experimental key-points from the pullout of aligned fibers (straight and hooked geometries)

The proposed pullout diagram for inclined fibers is shown in Fig.5.7, whose shape is governed by the eight highlighted key-points, summarized in Tab.5.1 for convenience. The several stages of the pullout process represented by each key-point are depicted in Fig.5.8 in order to provide a better understanding on the physical mechanisms involved.

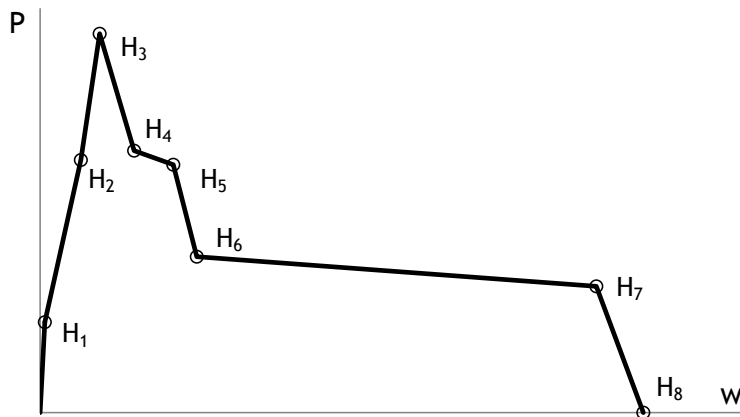


Fig.5.7 - Schematic diagram of the pullout model for inclined fibers with hooked ends.

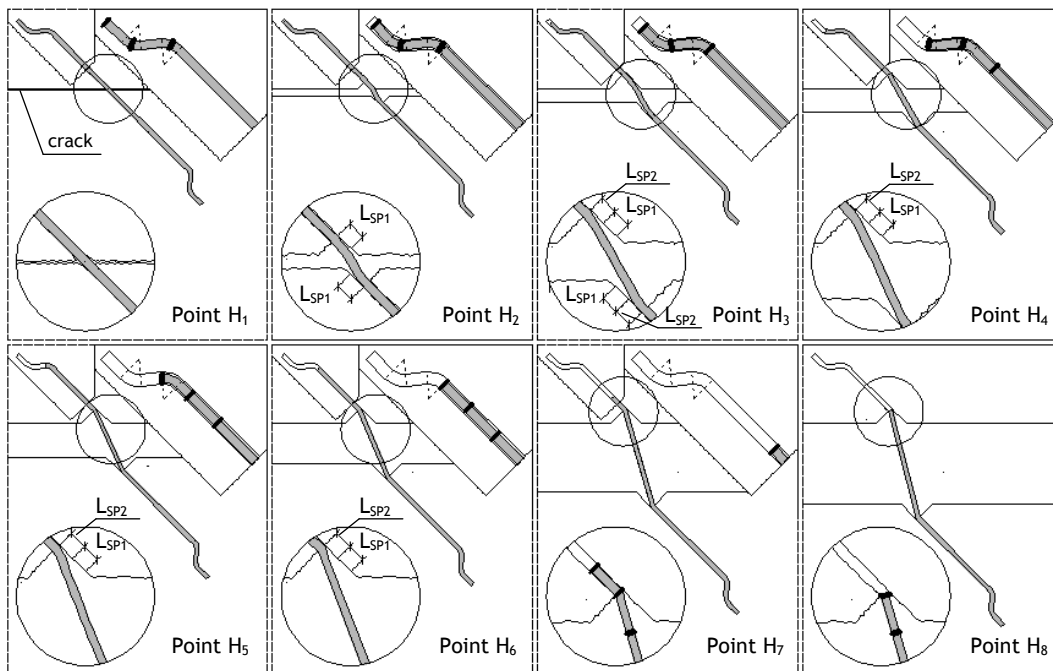


Fig.5.8 - Main stages of the pullout process of inclined fibers and associated model key-points.

Table 5.1 - Summary of expressions which define the pullout model.

Point	Formulation
H ₁	$P_{H1} = P_{S01} \cos \theta$ $W_{H1} = W_{S01}$
H ₂	$P_{H2} = \left(P_{S01} L_{\text{eff}(H2)} + \Delta P_{H01} \frac{L_e - 6 \times L_{SP1}}{L_e} \right) \cos \theta + \mu D_{F1}$ $W_{H2} = W_{H1} + \Delta W_{H01} \cos \theta \frac{L_e - 6 \times L_{SP1}}{L_e} + \Delta W_{SP1}$
H ₃	$P_{H3} = (P_{S01} L_{\text{eff}(H3)} + \Delta P_{H01}) \cos \theta + \mu D_{F2}$ $W_{H3} = W_{H1} + \Delta W_{H01} \cos \theta + \Delta W_{SP1} + \Delta W_{SP2}$
H ₄	$P_{H4} = \left(P_{S01} L_{\text{eff}(H4)} + \sum_{i=1}^2 \Delta P_{H0i} \right) \cos \theta + \mu D_{F2}$ $W_{H4} = W_{H3} + \Delta W_{H02} \cos \theta$
H ₅	$P_{H5} = \left(P_{S01} L_{\text{eff}(H5)} + \sum_{i=1}^3 \Delta P_{H0i} \right) \cos \theta + \mu D_{F2}$ $W_{H5} = W_{H4} + \Delta W_{H03} \cos \theta$
H ₆	$P_{H6} = \left(P_{S02} L_{\text{eff}(H6)} + \sum_{i=1}^4 \Delta P_{H0i} \right) \cos \theta + \mu D_{F2}$ $W_{H6} = W_{H5} + \Delta W_{H04} \cos \theta$
H ₇	$P_{H7} = \left(\sum_{i=1}^4 \Delta P_{H0i} \right) \cos \theta + \mu D_{F2}$ $W_{H7} = L_e - (L_{SP1} + L_{SP2} + L_{H,\text{crit}})$
H ₈	$P_{H8} = 0$ $W_{H8} = L_e - (L_{SP1} + L_{SP2})$

To generalize the model to any hooked fiber embedded in a cement matrix, the model has to include scenarios in which insufficient fiber embedded length induces earlier removal of the fiber and the case of rupture of a fiber due to attainment of its rupture load at a certain inclination angle ($P_u(\theta)$). Furthermore, the shape of the pullout response at the pre-peak branch may vary depending on whether it is governed by matrix spalling effects or by the straightening of the fiber hook. These three cases are considered in the model through the conditions described in the following.

Fiber rupture condition

Contrarily to straight steel fibers, in which fiber tensile strength does not play a major role, the significant anchorage effect provided by the hooked ends converts $P_u(\theta)$ into a paramount parameter to evaluate the pullout of inclined steel fibers. Regarding the intricacy of the phenomenon a simplified heuristic procedure was adopted to quantify the inclined tensile strength at any inclination angle, $f_u(\theta)$, as shown in Appendix 3.2. Thereby the key-points described in Tab.5.1 apply whenever the maximum pullout load at a certain inclination angle is lower than the correspondent ultimate pullout load:

$$P_{H3} < P_u(\theta) \quad (5.33)$$

In cases where Eq.5.33 is not verified the pullout model accounts uniquely for points H_1 , H_2 and the point at which fiber fails, defined by $P_u(\theta)$ and a respective crack width obtained by linear interpolation (Eq.5.34):

$$w_u(\theta) = w_{H2} + \frac{P_u(\theta) - P_{H2}}{P_{H3} - P_{H2}} (w_{H3} - w_{H2}) \quad (5.34)$$

Available embedded length condition

In order to provide a better understanding on the influence of each phenomenon in the pullout response, the formulation of the model key-points was performed in an additive form. Likewise, the extent of the post-peak range depends upon the available fiber embedded length after the occurrence of matrix spalling. In cases where the initial fiber embedded length is small and/or the matrix spalling lengths are significant, the post-peak range may be severely reduced or completely vanished. The latter may also compromise the complete mobilization of the hooked end and therefore the maximum pullout load has to be reduced accordingly. Hence model predictions are based on the key-points defined in Tab.5.1 whenever the Eq.5.35 is verified for all j between 1 and 6.

$$w_{H7} > w_{Hj} \quad (5.35)$$

In case that one or more points do not obey Eq.5.35 it means that earlier removal of the fiber occurs and that the hooked end is not fully mobilized. In such conditions a new and simplified pullout diagram applies taking into account only the points which verify Eq.5.35 and the ones

corresponding to the stage of fiber removal (H_7 and H_8), starting at crack width w_{H7} and with a respective pullout load such as defined in Eq.5.36:

$$P_{H7} = P_{Hj} + (P_{H(j+1)} - P_{Hj}) \frac{W_{H7} - W_{Hj}}{W_{H(j+1)} - W_{Hj}} \quad (5.36)$$

Where j corresponds to the higher numbered key-point at which Eq.5.35 is verified.

Shape of the pullout response

Once the thorough set of key-points is defined, the pullout response of inclined steel fibers can be approximated by a multi-linear diagram such as shown in Fig.5.7. Although this is a quite straightforward procedure, one should be aware of the approximations that are being introduced, particularly within the range of crack widths with interest for structural applications.

When observing the pullout of aligned fibers (Fig.5.6) it can be observed a non-linear pre-peak behavior due to the straightening of the hook. Consequently, on fibers under small inclination angles (whose pullout mechanisms are governed by the aligned component), a multi-linear assumption would underestimate the load carrying capacity of those fibers. To overcome this limitation, the pullout diagram in the pre-peak branch (from H_1 to H_3 in Fig.5.7) may be defined depending on the dominance either of the spalling mechanisms or, alternatively, of the hook's deformation on the crack width at peak. Thereby, the interpolation between key-points H_1 to H_3 should respect the following condition:

$$\begin{cases} \Delta W_{SP1} + \Delta W_{SP2} \geq \Delta W_{H01} & \Rightarrow \text{Bi-linear branch} \\ \Delta W_{SP1} + \Delta W_{SP2} < \Delta W_{H01} & \Rightarrow \text{Parabolic branch} \end{cases} \quad (5.37)$$

When the spalling effects are relatively reduced the parabolic expression may be obtained by means of the coordinates at points H_1 and H_3 and by fixing the derivate at peak (H_3) equal to zero. Note that, in this case, the use of a non-linear pre-peak branch disregards the calculation of H_2 .

5.5 MODEL VALIDATION

In order to ascertain the suitability of the proposed approach on describing the pullout response of inclined fibers, different experimental results from literature are taken into account (Robins et al. 2002; Van Gysel 2000). The experimental data herein presented considers hooked fibers with different diameters, tensile strengths and embedded lengths within different cement matrices.

5.5.1 Robins et al. (2002)

The experimental research carried out by these authors evaluates the influence of fiber inclination angle, fiber embedded length and type of matrix on the load-crack with response. In their work specimens were cast in two stages, firstly with the matrix for testing and then using a high strength mortar to guarantee that pulling out of the fiber occurred uniquely from one side of the specimen. A brass with a 10mm hole in the center was inserted to provide continuity and to form a reduced section at which matrix cracked. Fibers with 50mm length were inserted within the matrix at 5, 10, 15 and 20mm embedded lengths under inclination angles of 0° , 10° , 20° , 30° , 40° , 50° and 60° . The average results considered hereafter are the outcome of four specimens with concretes of 72MPa average compressive strength. The procedure described in Section 4.2 was applied to extract the experimental input values from the pullout of aligned fibers ($\theta=0^\circ$). A summary of the values used on this model validation is shown in Appendix 3.3.

The initiation of debonding occurs whenever crack is deflected along the fiber-matrix interface, which corresponds to the minimum post-peak value of the load-crack width response (Easley et al. 1999). According to experimental results the crack width at that minimum was between 0.020-0.050mm and the respective load between 10-40N. w_{S01} and P_{S01} will then be roughly approximated as 0.035mm and 25N, respectively. In the absence of experimental values for straight fibers, the crack width at the beginning of friction stage (w_{S02}) will be assumed as 0.3mm and the respective load (P_{S02}) as half of the peak value (P_{S01}). Comparisons between model predictions and experimental results are shown in Figs.5.9-5.12, in which good agreement of the pullout diagrams can be seen in most of the cases.

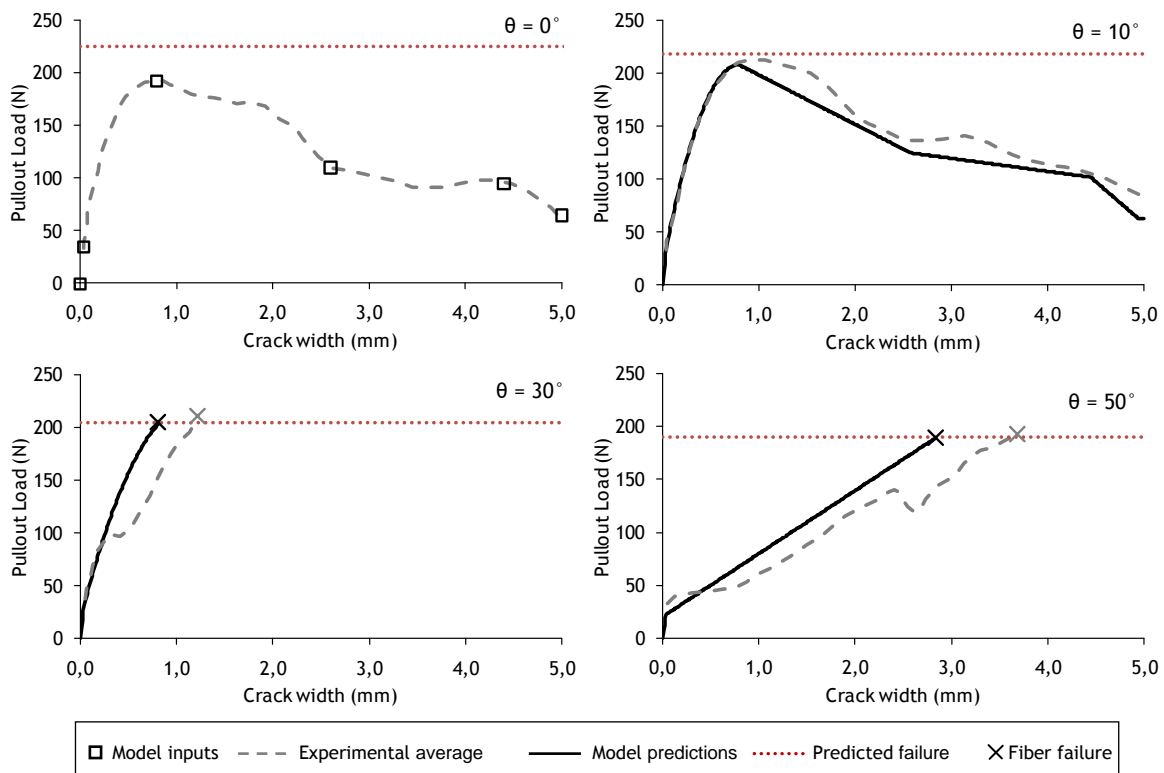


Fig.5.9 - Model validation over experimental results from (Robins et al. 2002) for L_e equal to 20mm.

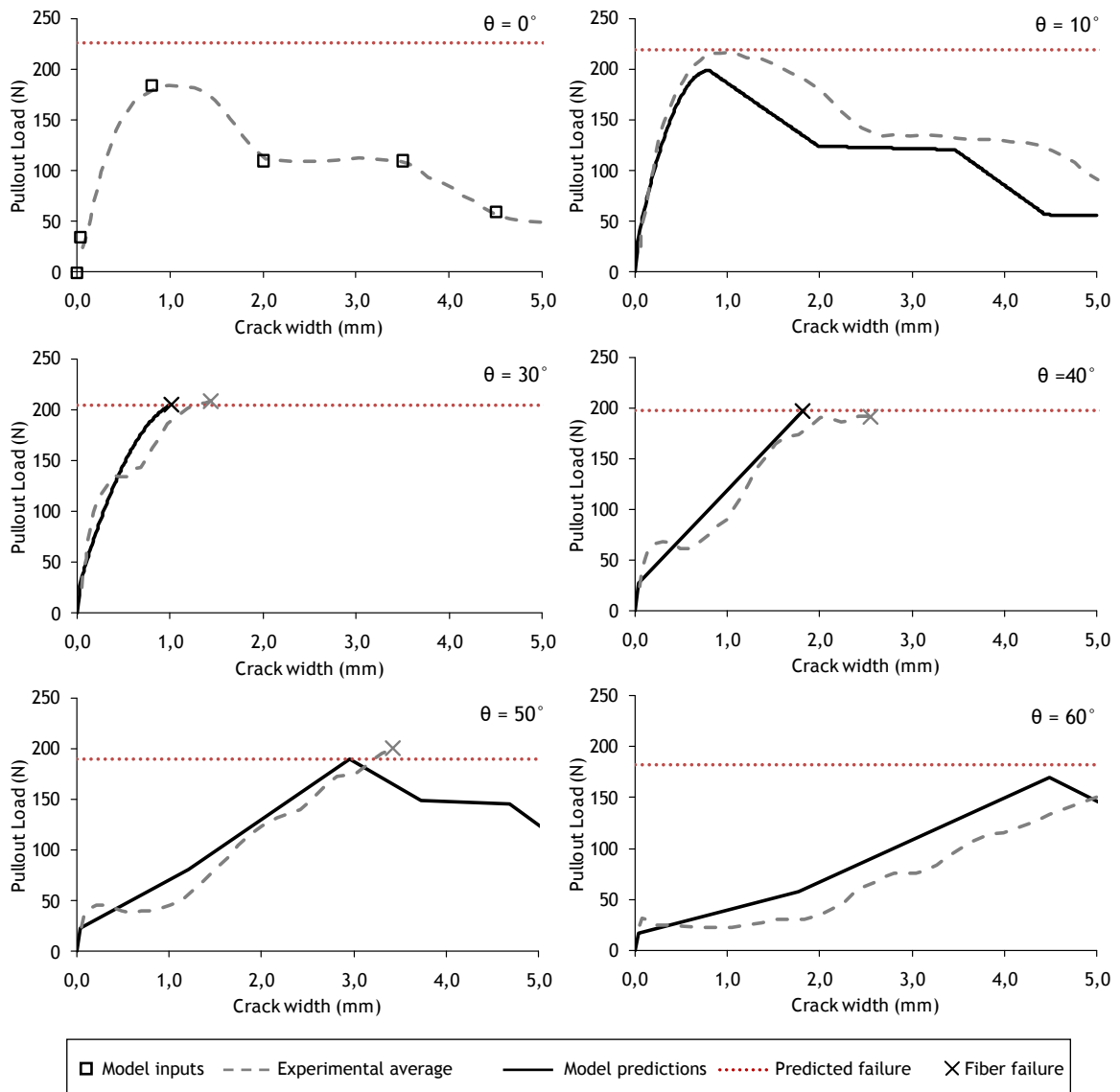


Fig.5.10 - Model validation over experimental results from (Robins et al. 2002) for L_e equal to 15mm.

The pullout model is able to reproduce the postponed activation of the mechanical anchorage at increasing inclination angles (Figs.5.9-5.11). Predicted crack widths at peak increased more than proportionally with the inclination angle as a result of the magnification of matrix spalling. In cases of fibers at 10° and 30° the spalled lengths of the matrices are not significant and, consequently, the predictions provided by the model consider a non linear pre-peak branch, such as previously suggested in Eq.5.37. With this criterion, the model approximates with good accuracy the pre-peak branch of all fibers, irrespectively of the governing pullout mechanisms.

At larger crack widths, the post-peak range up to complete straightening of the hook is reasonably well predicted for fibers with small inclination angles, at least for the available crack width range of comparison (5mm).

According to experimental values, fibers with embedded lengths greater than 5mm and inclination angles larger than 20° were likely to have their peak loads limited by fiber rupture. Such trend is also successfully reproduced, although in some cases a slight overestimation of fiber’s rupture load leads to post-peak branches on the pullout model.

The pullout response of fibers under large inclination angles seems to be significantly overestimated by the model. However it should be pointed out that the scattering of experimental results was reported to increase significantly with fiber inclination angles, reaching coefficients of variation for the pullout response between 25-50% for fibers at 60° inclination angle.

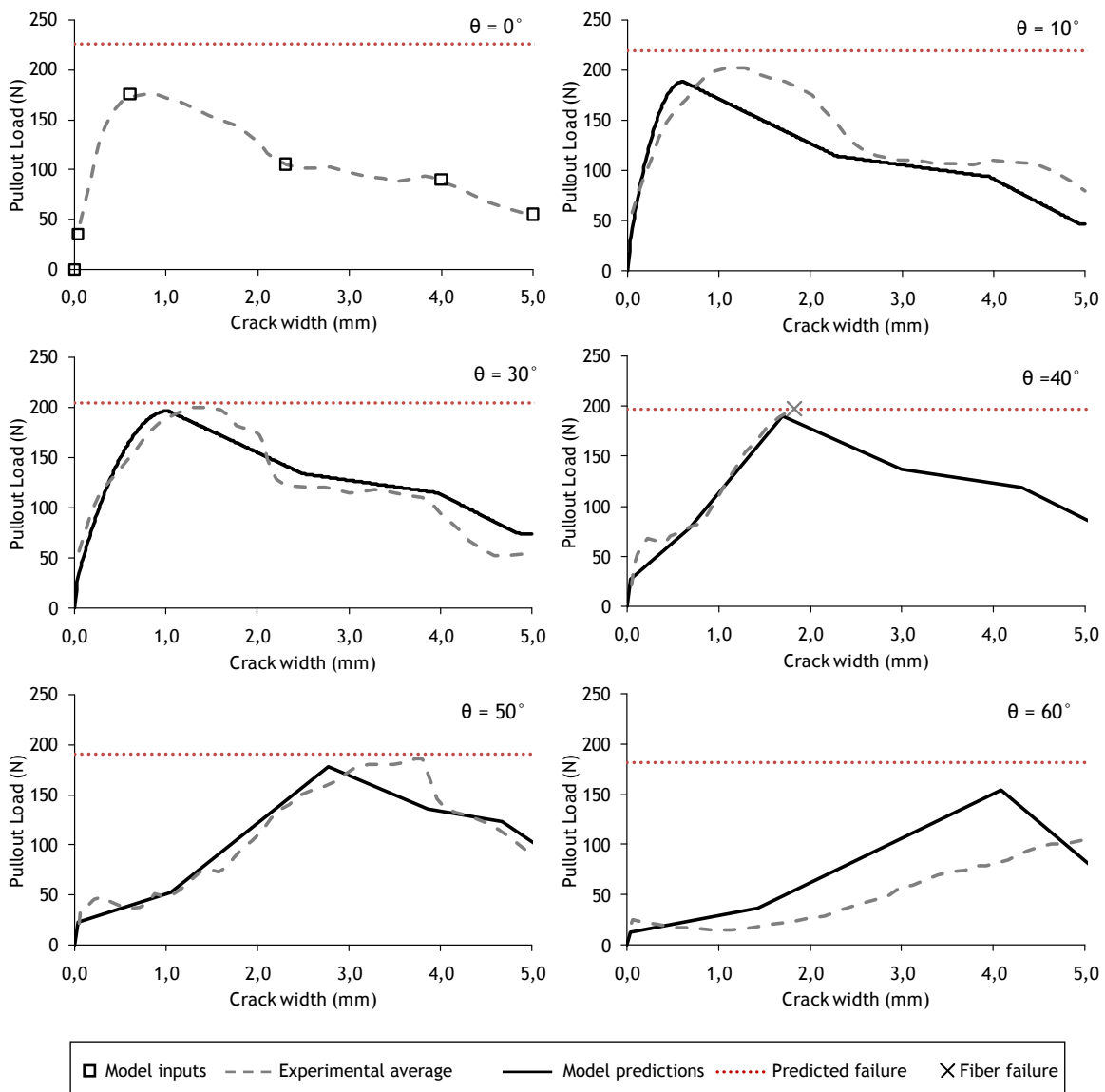


Fig.5.11 - Model validation over experimental results from (Robins et al. 2002) for L_e equal to 10mm.

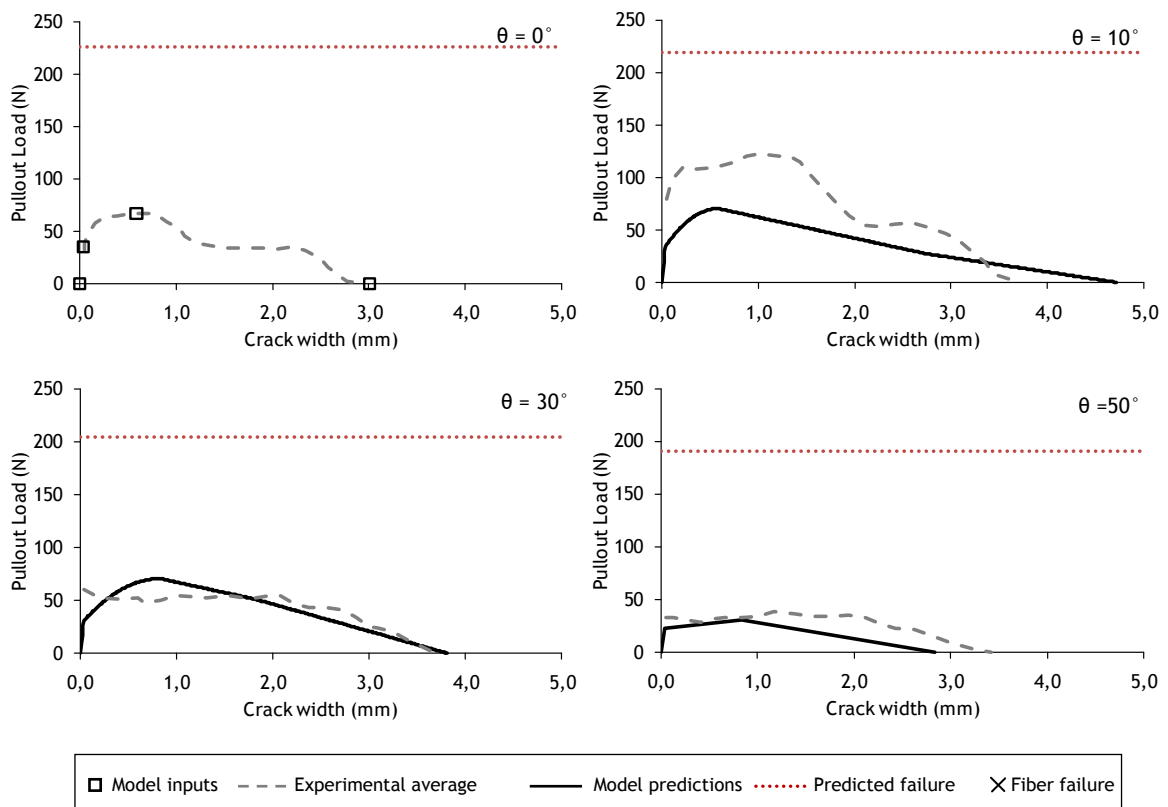


Fig.5.12 - Model validation over experimental results from (Robins et al. 2002) for L_e equal to 5mm.

To evaluate the suitability of the model in describing the main features of the pullout response, correlations between the model predictions and average experimental results for peak values and pullout work are shown in Fig.5.13. It is evident that pullout responses of fibers at different inclination angles were essentially the same whenever the hook was fully mobilized (Fig.5.9-5.11). On the other hand, with fibers with 5mm embedded length (Fig.5.12) the mechanical anchorage was not fully developed and therefore pullout performance was rather poor. Moreover uncertainties regarding accurate measurements of the actual embedded length (which in the case of aligned fibers led to complete fiber removal at only 3.0mm) might also support the significant coefficients of variations observed for this case (10 to 60%). Therefore it is not surprising the lower agreement provided by the model, which even though, is able to reasonably approximate the pullout work in such unsteady conditions (Figs.5.12-5.13).

Once analyzing Fig.5.13 one should be aware that the experimental failure mode of fibers with inclination angles larger than 20° and embedded lengths greater than 5mm was mostly by fiber rupture. Given that this is an undesirable failure mode, the pullout model can then be used to provide some valuable insights and optimize the design of SFRC.

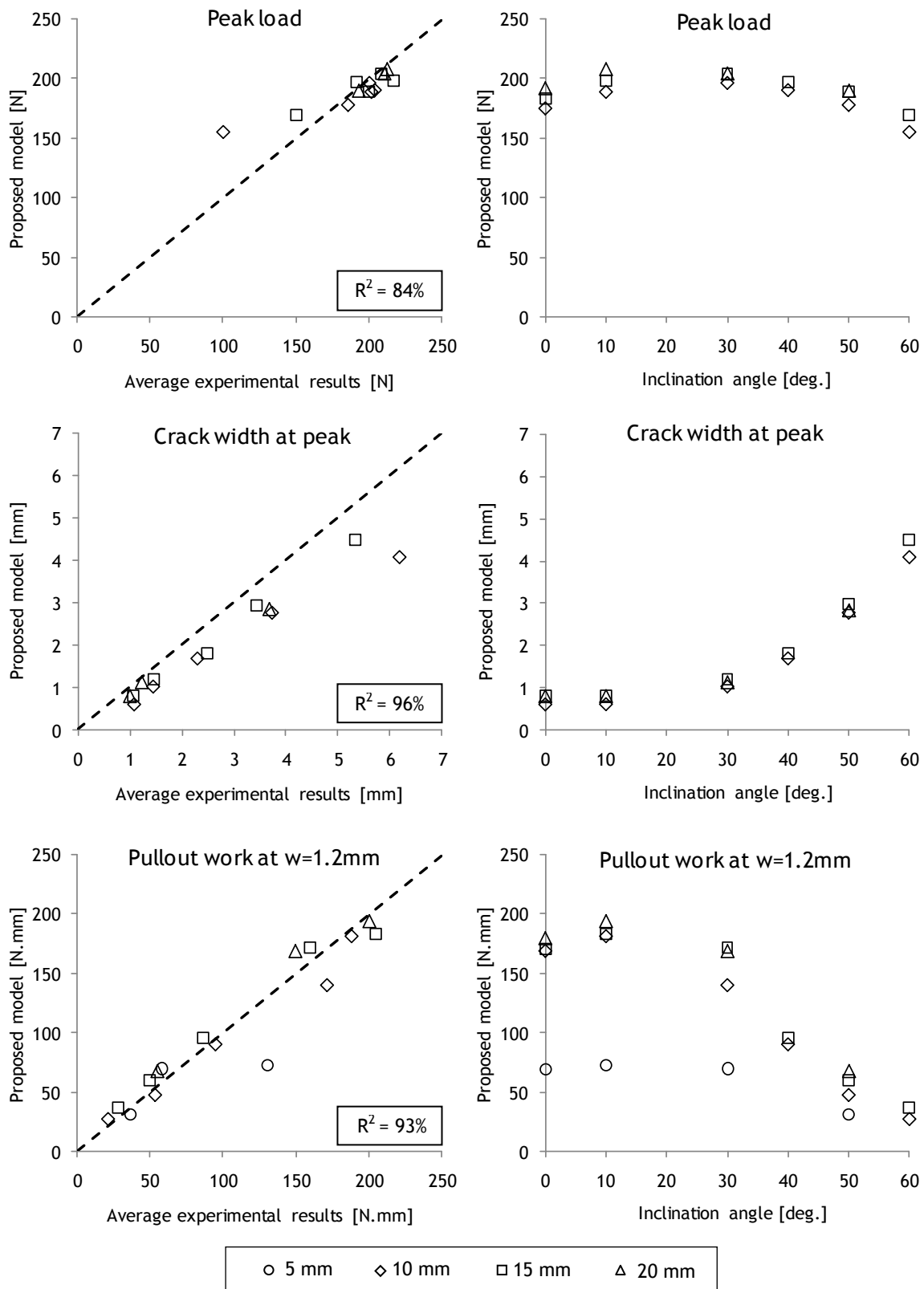


Fig.5.13 - Comparison between model predictions and experimental results obtained from (Robins et al. 2002) (left) and influence of fiber inclination angle on the pullout model (right).

According to model predictions, the critical inclination angle (θ_{crit}) above which fiber rupture occurs for fibers with 20mm embedded length is 16° . Thereby a steep decrease on the pullout work is expected for fibers at larger inclination angles. Such becomes evident in Fig.5.14a, where significantly lower pullout works are predicted for angles ranging between 16° - 35° . For angles larger than 35° the pullout work is no longer affected by fiber rupture regarding that the range of crack widths at which it takes place is larger than 1.2mm.

By performing a simple parametric study it is possible to conclude that, if fiber rupture could be avoided, pullout work at 1.2mm crack width would be maximized at 17° (199.0N.mm) and it would be at least as higher than that of aligned fibers (179.3N.mm) up to 31° (Fig.5.14a). With regard to the peak loads (Fig.5.14b), they remain larger than those of aligned fibers up to 55° and their optimum range occurs between 25° and 30° , with values about 14% higher than those of aligned fibers.

The maximum difference between peak and fiber rupture loads provides a first step to optimize the tensile strength of steel fibers. In this particular case, the range between 35° and 40° is the one providing minimum safety against fiber rupture. At this angle the peak load would exceed the respective ultimate failure load about 9% (Fig.5.14b). Therefore fiber tensile strength would have to be at least 1250MPa (9% higher) to avoid fiber rupture at any inclination angle.

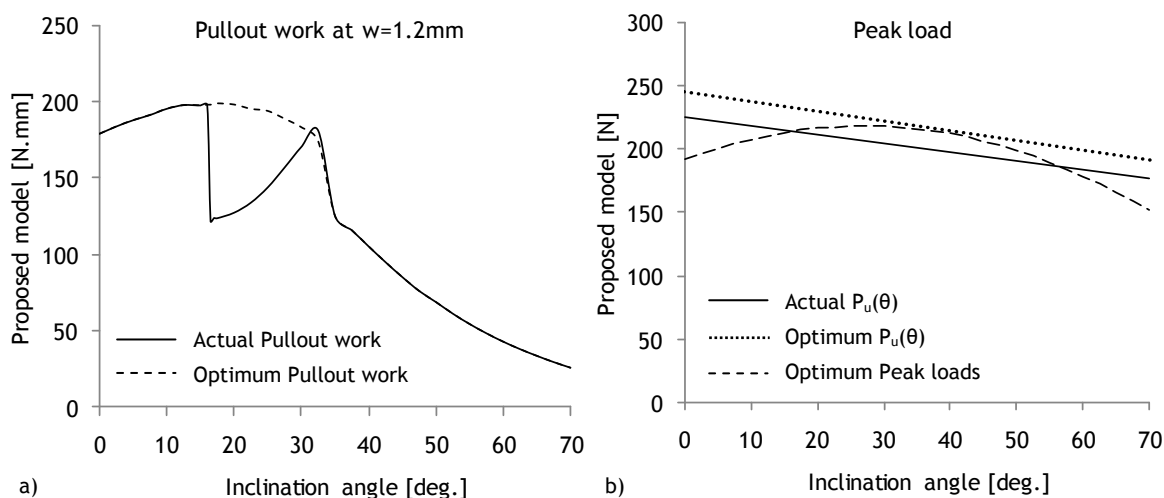


Fig.5.14 - Study on the influence of fiber tensile strength on pullout work and peak load at different θ .

5.5.2 Van Gysel (2000)

This investigation comprised an extensive experimental work in which fibers with different geometries and tensile strengths were pulled out from two types of mortar matrices. Two diameters of fibers (0.50 and 0.80mm) were tested at five different angles (0° , 15° , 30° , 45° and 60°) with 30mm fiber embedded length. Fiber ultimate tensile strengths were 2148 and 2117MPa for diameters 0.50 and 0.80mm, respectively. The mean compressive strength of the

matrix was about 76.5MPa and four specimens were tested for each set of parameters. The input values for the pullout model are summarized in Appendix 3.3.

The pullout responses of aligned fibers were available both for straight and hooked fibers. In the former the peak values reported were considered whereas the friction stage was assumed to start at a crack width of 0.3mm with 50% of the peak load. With regard to the experimental data of hooked fibers, the procedure described in Section 4.2 was applied to identify the contribution of the hook (Fig.5.15).

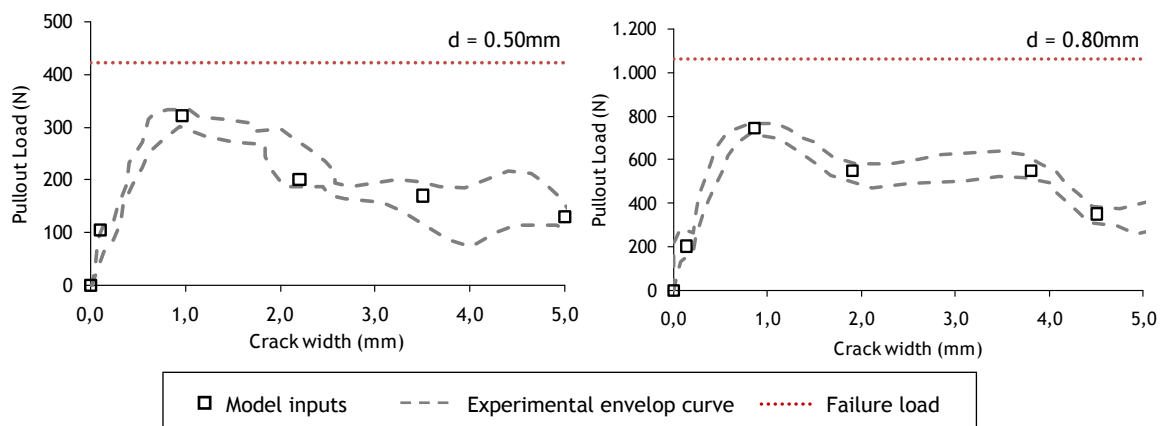


Fig.5.15 - Extraction of the hook contribution from experimental data on aligned fibers from (Van Gysel 2000).

Pullout responses of fibers with 0.50mm diameter at different angles are shown in Fig.5.16. It can be seen that model predictions fit the range of experimental results along the entire pullout diagram in most cases. Experimental results at 30° presented a mixed type of rupture, with three fibers failing and one undergoing subsequent pullout. For this case the pullout model predicted a peak value of about 99% the ultimate load of inclined fibers, thus also denoting an eminent change in the pullout failure mode. Tests on fibers at 45° and 60° present larger scattering along the load-crack width responses and fiber rupture in all situations. Fiber rupture is well predicted for 45° whereas its prominence is evident with fibers at 60°, where the peak load attains about 98% its inclined ultimate load.

Model predictions for fibers with 0.80mm diameter are also in good agreement with the experimental results (Fig.5.17). For fibers with 15° and 30° the experimental post-peak behavior is smoother than predicted by the model. This supports that the simplified version of the model (excluding points H₄ and H₅) would apply in this case with particular good results.

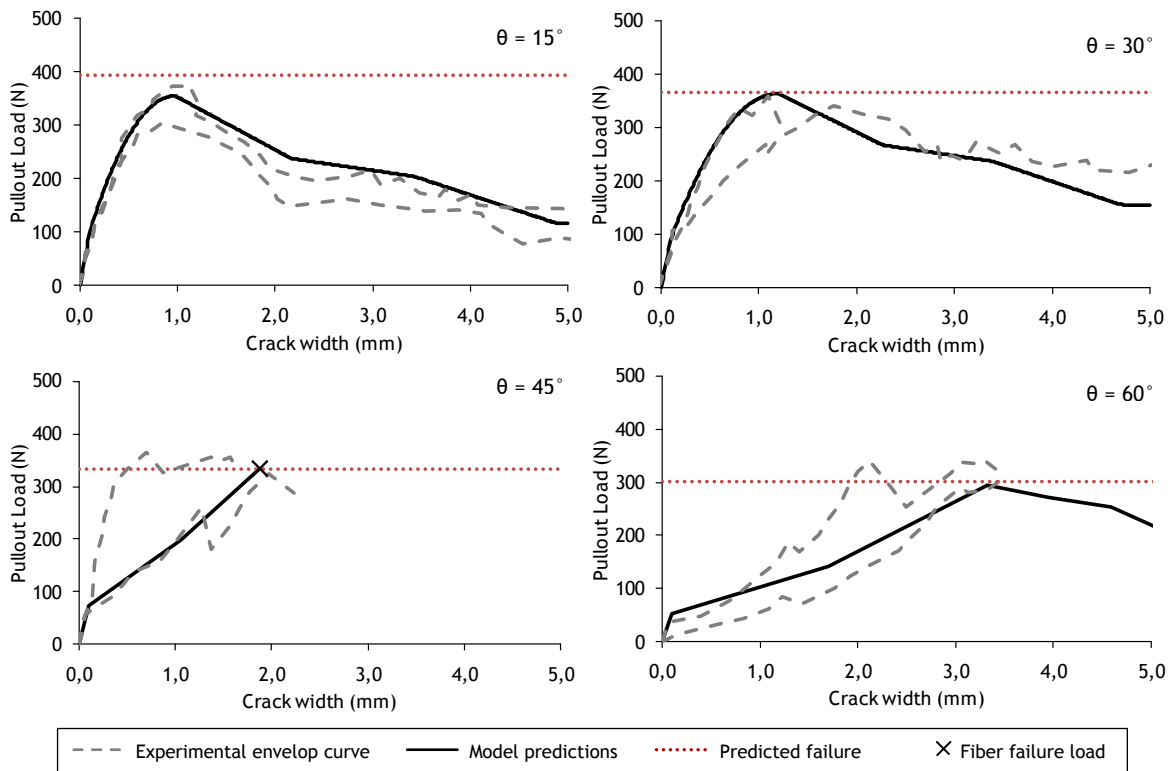


Fig.5.16 - Model validation over experimental results from (Van Gysel 2000) for fibers with $d=0.50\text{mm}$.

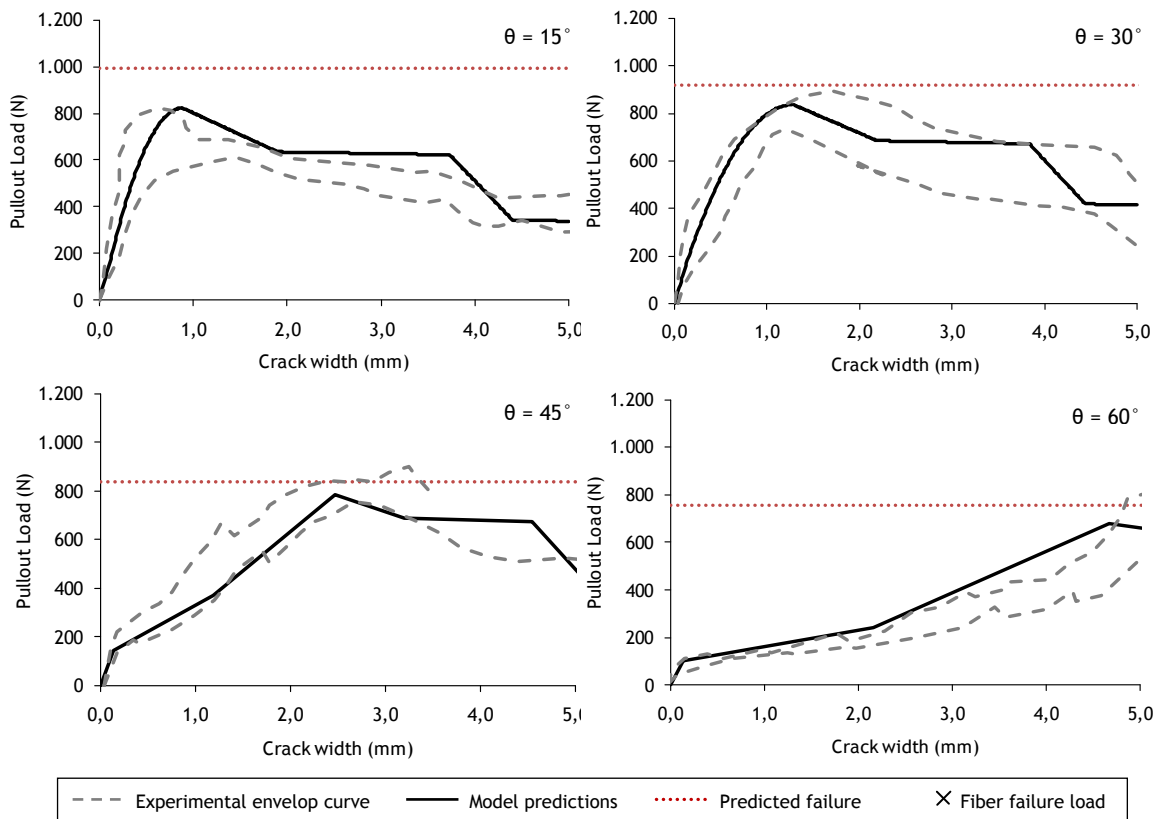


Fig.5.17 - Model validation over experimental results from (Van Gysel 2000) for fibers $d=0.80\text{mm}$.

Fig.5.16-5.17 show that tests on fibers with 15° and 30° report failure modes in which all fibers, or significant part of them, are pulled out. At least two valid experimental pullout results were reported in this situation, with the exception being fibers with 0.50mm diameter and 30° which only provided one diagram. In these cases it is possible to validate the model along the entire load-crack width response (Fig.5.18). It can be observed in Fig.5.18 a good agreement on the predicted responses also at very large crack widths, with similar performances both on magnitude and slope of the friction branch.

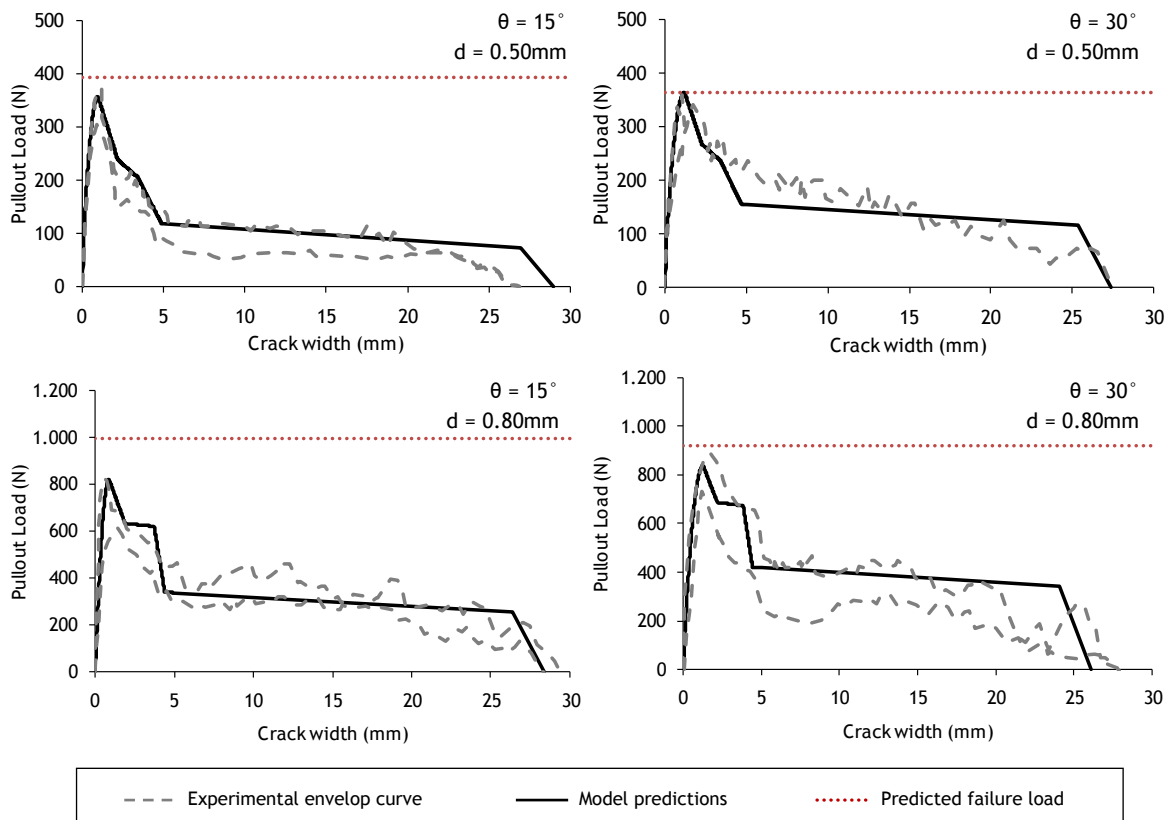


Fig.5.18 - Model validation over experimental results from (Van Gysel 2000) up to complete removal of the fiber from the matrix.

5.6 CONCLUDING REMARKS

In this work a new conceptual approach was advanced to predict the pullout response of inclined steel fibers with hooked ends. The model is based on the most representative geometric and strength properties of the constituent materials and on experimental data of fibers aligned with the load direction. From the latter the contributions provided both by hooked ends and straight segments of the fiber are evaluated. Then fiber-matrix interaction nearby the cracked surface is considered by estimating the amount of spalled matrix and by including local friction effects at the point where fiber exits the matrix. The approach embodies physical parameters and a straightforward formulation which define a set of key-points that govern the shape of the

predictive multi-linear pullout diagram. Therefore an intuitive explanation on how material properties influence the several stages of pullout process is provided.

Comprehensive validation against experimental data highlight a good agreement on the load-crack width responses of fibers with different diameters, tensile strengths, embedded lengths and inclination angles within dissimilar matrix properties.

This innovative model enables the prediction of the fundamental strengthening mechanisms existing on SFRC through an easy-manageable approach. This way, with a database of the pullout of aligned fibers, the performance of different fibers and matrices can be evaluated at any orientation. Given the random nature of fiber orientation in FRC applications, this means that material tailoring can be done in a much more realistic scenario. In fact, the implications of this study go further than this. Regarding the investigations that are currently being carried out, increasing knowledge on the way fibers distribute and orient themselves within the concrete is being attained. Consequently, if the orientation of fibers could be somehow predicted, the tensile response of SFRC could be predicted as well by means of the several pullout responses of inclined fibers.

Chapter 6

Characterization of the orientation profile of SFRC

6.1 INTRODUCTION

In Part III of this thesis, the pullout responses of steel fibers at different inclination angles were evaluated and it was shown that the inclination angle of the fibers has a major effect on their crack-bridging ability. Therefore, in order to accurately predict the load-carrying capacity for the cross-section of a SFRC member, the number of fibers at each inclination angle that exist in such cross-section would be necessary. In this regard, the individual orientations of fibers in SFRC elements need to be investigated.

This study pursued two main goals, namely: 1) to identify the statistical nature of fiber orientation; 2) to develop a procedure capable of predicting the distribution of orientation angles based uniquely on the orientation number. If fiber orientation could be extensively and unambiguously defined, phenomena often attributed to scattering of material properties could then be physically explained.

This chapter reports detailed measurements of individual fiber orientations from different experimental works. Statistical analyses are carried out to identify an appropriate statistical orientation law and the dispersion of the orientation angles is then investigated and correlated with the orientation number.

6.2 THE CONCEPT OF ORIENTATION PROFILE

The orientation profile, $P(\theta)$, is a set of values that characterizes fiber orientation through the complete distribution of orientation angles. Its definition requires as input parameters an appropriate statistical law, $f(\theta)$, as well as the average orientation (θ_m) and respective dispersion of orientation angles, $\sigma(\theta)$, such as sketched in Fig.6.1.

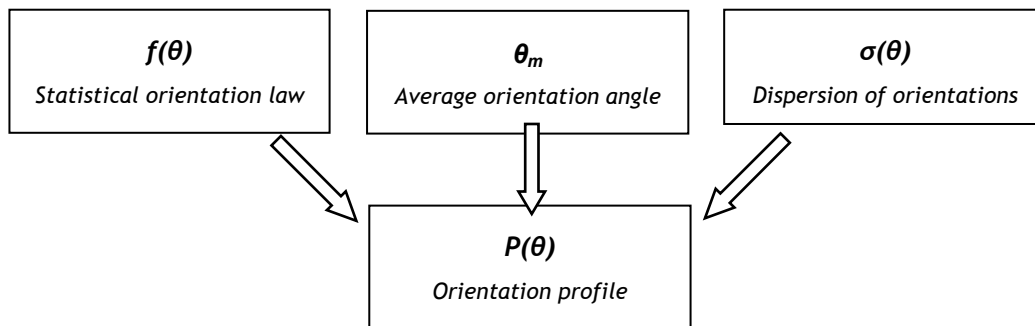


Fig.6.1 - Schematic outlook of the orientation profile.

In order to avoid misinterpretations of the following some terms commonly referred to in literature deserve clarification. Likewise, dispersion is measured as the standard deviation of orientation angles, or alternatively, by its respective coefficient of variation. Fiber orientation, such as considered in this study, accounts uniquely for data obtained through direct measurements. Indirect approaches which make use of theoretical expressions to relate fiber content with the orientation number (Krenchel, 1975) are therefore excluded. This way orientation is evaluated independently from fiber distribution, avoiding uncertainties introduced by heterogeneous fiber contents or manufacturing tolerances on fiber diameters.

6.3 STATISTICAL ORIENTATION LAW

6.3.1 Selection of experimental data

The experimental data taken into account regards the investigations performed by Grünewald and Walraven (2002) and Molins et al. (2008) on self-compacting steel fiber reinforced concretes (SCSFRC). Among the considered experimental data from both works (28 cases) a large variety of matrix compositions, fiber geometries and fiber contents were tested. A summary of the main characteristics of each case-study is provided in Appendix 4.2. For clarity, all the results were analyzed according to the referential shown in Fig.6.2.

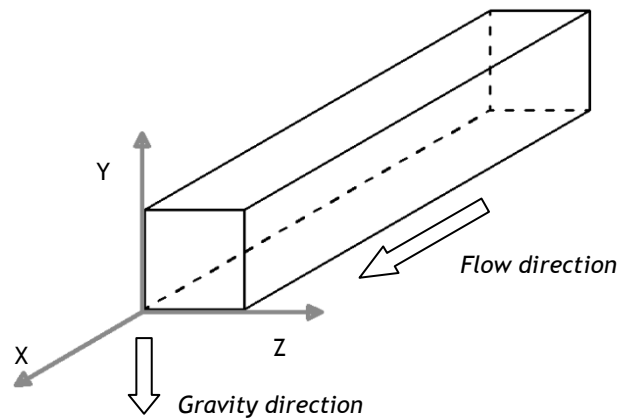


Fig.6.2 - Coordinate system adopted.

In the first experimental work (Grünewald and Walraven, 2002) the image analysis technique was applied both on small (150×150×600mm) and large beams (200×500×3700mm). With this method the angles of all fibers respect to the orthogonal axis of the analyzed cross-section could be measured. Results from 13 small beams account for images extracted at 70mm from the middle cross-sections in the direction perpendicular to the flow (X-direction). These are herein numbered as cases 1-13. From the study on large beams, the six images selected correspond to cross-sections with 200×250mm, parallel to the bottom of the mould (Y-direction). These results are numbered as cases 14-19. Further details of this investigation can be found elsewhere (Grünewald, 2004)

The second group of results considered in this study (Molins et al., 2008) refers to CT-scans of three concrete cores extracted from a small beam (150×150×600mm). Samples had 100mm diameter, 300mm length in X-direction and 150mm length in Y-and Z-directions and were analyzed through multiple axial tomographies evenly spaced by one millimeter. Assembling the thorough set of consecutive tomographies, 3D-models could be built to analyze the orientation of all fibers, either partial or completely embedded within the samples. These case-studies are numbered as 20-28.

6.3.2 Statistical hypotheses

A realistic description of fiber orientation demands detailed knowledge on the actual frequency distribution of the orientation angles of single fibers. Thereby, after an investigation on several statistical distributions, two statistical laws were selected and their suitability on describing the experimental orientation patterns was studied.

One of the statistical hypotheses considered to evaluate the frequency distribution of orientation angles was the Gaussian law. Several reasons encourage the study of this hypothesis: Firstly, its suitability on describing statistical distributions in which several small effects act additively and independently. Secondly, the fact of being the most widely used statistical distribution on many

scientific areas and, particularly, on the characterization of concrete properties such as the compressive strength. Last but not the least, some degree of similarity between measured and Gaussian curves of fiber counting has been identified by several authors (Soroushian and Lee, 1990; Lappa, 2007; Behloul, 1996; Mora, 2008). Hence, since a theoretical linear dependence exists between the number of fibers in a cross-section and the respective orientation number (Krenchel, 1975), according to the central limit theorem, it is also very probable that the orientation of fibers will follow a Gaussian distribution.

The second statistical hypothesis analyzed was the Gumbel distribution. The latter belongs to the family of statistical laws of extreme values, likely useful to represent distributions of maximum values when the underlying sample data is of Gaussian or exponential type. It is expected that this hypothesis may provide good agreement when describing cases with accentuated preferential orientations.

When analyzing the suitability of a given statistical law it must be guaranteed that its cumulative distribution reaches a unitary value (100%) within the admissible range of orientation angles (0° to 90°). However, when dispersion is large and the average value is small, this condition is unlikely to be accomplished as the amplitudes of variation of the probabilistic distributions tend to be larger than 90° . Because such statistical results have no physical sense, the frequencies of occurrence of the inclination angles should be revised. Such correction will be herein considered through a factor accounting for the range error of the statistical distribution, $F_{RE}(\theta)$, such as defined in Eq.6.1.

$$F_{RE}(\theta) = 2 - [F(90) - F(0)] \quad (6.1)$$

Where $F(90)$ and $F(0)$ are the cumulative distributions of the statistical law at the upper and lower bound of the admissible range of inclination angles, respectively. According to the dispersion of orientations presented hereafter (Section 6.5), these values can be obtained uniquely in terms of the orientation number (η_θ), leading to $F_{RE}(\theta)$ such as shown in Fig.6.3.

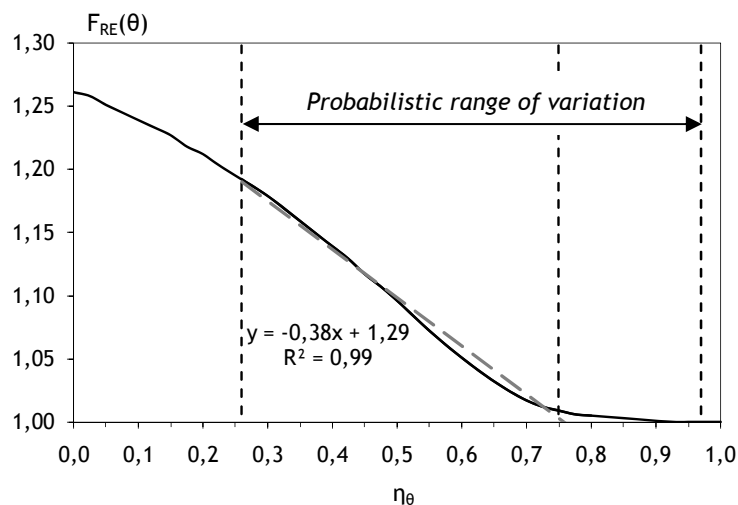


Fig.6.3 - Factor accounting for the range error of the statistical law in terms of η_θ .

The probabilistic range of variation indicated in Fig.6.3 limits the most probable range of values for η_θ and it will be further explained in Section 7.3. According with the linear regression shown in Fig.6.3, the factor accounting for the range error can be simply defined such as follows:

$$F_{RE}(\theta) = \begin{cases} 1.29 - 0.38 \times \eta_\theta & \text{if } \eta_\theta < 0.75 \\ 1 & \text{if } \eta_\theta \geq 0.75 \end{cases} \quad (6.2)$$

Once $F_{ER}(\theta)$ is obtained, the orientation profile, $p(\theta)$, will be defined in terms of the frequency of occurrence of the inclination angle θ , $f(\theta)$, according to Eq.6.3:

$$P(\theta_i) = f(\theta_i) \times F_{RE}(\theta) \quad (6.3)$$

6.3.3 Statistical analyses

To ascertain whether any of the statistical hypotheses considered is suitable to describe the frequency distribution of orientation angles, it was applied one of the most well-known types of non-parametric tests, the Kolmogorov-Smirnov test (KS-test). For that purpose the 28 cases considered were grouped into discrete intervals ($\Delta\theta=10^\circ$ and $\Delta\theta=15^\circ$) and evaluated through a significance level (α) of 5%. A summary of the main results presented in Appendix 4.3 is shown in Fig.6.4.

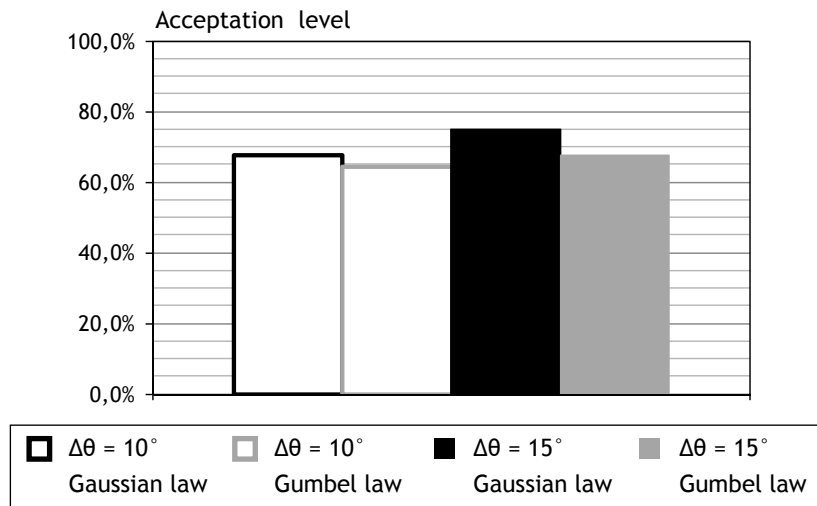


Fig.6.4 - Overall acceptance levels from the non-parametric tests

The overall acceptance levels represent the ratios of accepted cases. For instance, the acceptance level of about 75% provided by the Gaussian hypothesis when ($\Delta\theta=15^\circ$) means that it was accepted in 24 out of the 28 cases analyzed. The acceptance levels provided by Gaussian hypothesis are larger than the ones provided by the Gumbel distribution, irrespectively of the

intervals considered. Grouping data into larger intervals ($\Delta\theta=15^\circ$) smoothes the experimental frequencies of orientation angles and therefore increases the acceptance levels of both hypotheses considered (Fig.6.4).

Despite these first conclusions, results from non-parametric tests should be evaluated carefully. In fact, one should be aware that the ultimate goal of the present study consists on deciding whether these statistical hypotheses are appropriate or not to describe the frequency distribution of orientation angles. The rejection criterion of KS-tests accounts uniquely for the sample size (number of fibers) and the maximum deviation between theoretical and experimental cumulative distributions. Therefore, there may be cases where, although an overall good agreement in terms of frequency distributions could be observed for a given statistical hypothesis, the latter could be rejected if localized scattering on the experimental data would exist. Hence, to overcome such limitation, an additional measuring parameter such as the coefficient of determination (R^2) is required. Extended results on this parameter are included in Appendix 4.4. For convenience a brief summary of such results is shown in Fig.6.5.

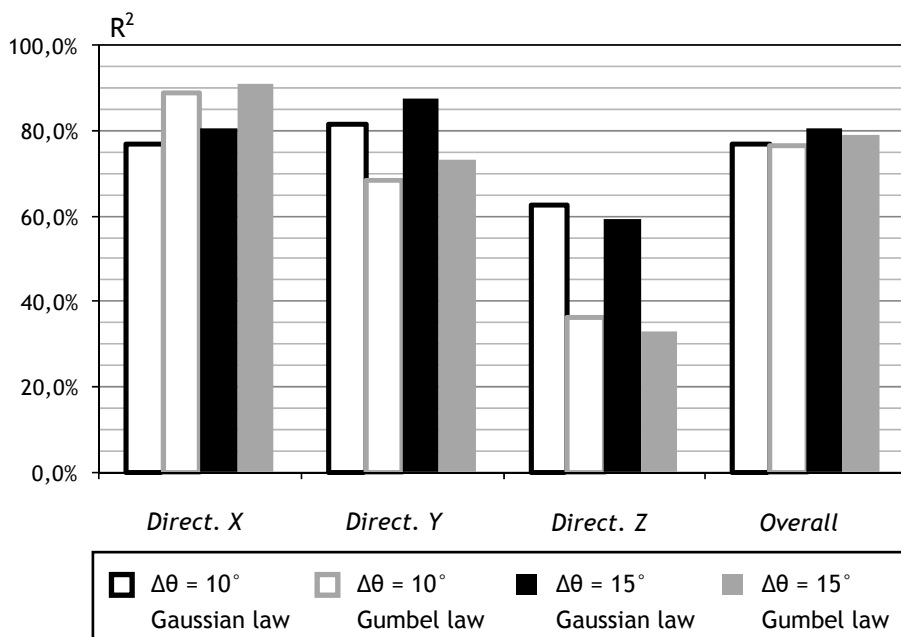


Fig.6.5 - Average coefficients of determination (R^2)

The first conclusion provided by Fig.6.5 is that coefficients of determination with $\Delta\theta$ equal to 15° are always at least as high as the ones provided by the cases with 10° for both hypotheses in all directions. Such evidence means that, similarly to KS-tests, R^2 results are also sensitive with scattering of experimental data. Observing the overall performance on the 28 cases it can be seen that Gaussian and Gumbel hypotheses provide similar fitting abilities, with values of R^2 for $\Delta\theta$ equal to 15° of about 81% and 79%, respectively. However, R^2 are rather different when partial results in each independent direction are considered (Fig.6.5). Such dissimilarities can be explained if the magnitude of the orientation number (η_θ) in each direction is taken into

account. The dependency of R^2 with η_θ for both statistical hypotheses is shown in Fig.6.6. In order to better identify the trends of each relationship, residual scattering was avoided by condensing the 28 cases analyzed into 9 averaged values. Only the cases with $\Delta\theta$ equal to 15° are considered in Fig.6.6 regarding that a similar tendency is observed when $\Delta\theta$ is equal to 10° .

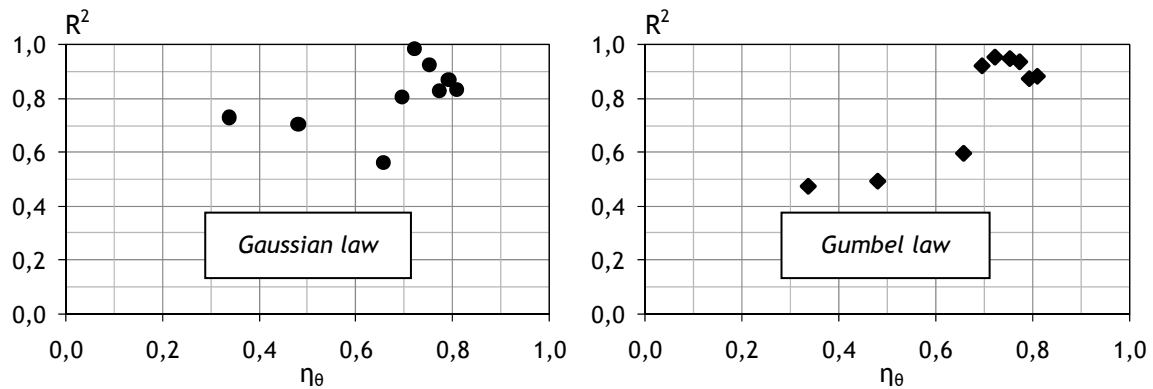


Fig.6.6 - Correlations between R^2 and η_θ ($\Delta\theta=15^\circ$)

Fig.6.6 points out that the fitting ability of both statistical laws depends on the magnitude of the orientation numbers, with better performances occurring when η_θ varies between 0.7 and 0.8. Such range of values takes place along the X-direction (section perpendicular to the flow) where performance of Gumbel law surpasses the Gaussian hypothesis (average R^2 in Fig.6.5 of 91% and 81%, respectively). On the other hand, in cases with smaller orientation numbers (Y-and Z-axes in Fig.6.5), Gaussian law is able to provide averaged steady results whereas Gumbel distribution performs quite poorly. The incongruent results provided by the latter are due to the fact that laws of extreme values are only suitable to describe distributions of maximum values (η_θ tending to 1.0), thus being inappropriate when more homogeneous orientation patterns exist.

6.3.4 Selection of the orientation law

Two criteria should be fulfilled in order to select the most appropriate statistical orientation law to be used on the characterization of FRC. The first requirement is that good agreement on the distribution of orientation angles has to be guaranteed, particularly for orientations which provide significant load carrying capacity within the crack-width ranges of interest for structural applications. According to Chapters 4 and 5, the pullout loads for small crack widths decrease significantly at large orientation angles, being somewhat meaningless on fibers with angles larger than 70° . This aspect is an important one regarding that the R^2 results in Y-and Z-axes summarized in Fig.6.5 are affected by disagreements within the range of 70° to 90° (cases 23-28 in Appendix 4.5). Therefore, if a truncated range from 0° to 70° would be selected for practical purposes, R^2 provided by both statistical hypotheses are likely to be larger than the ones herein presented.

The second major requirement that the statistical orientation law should fulfill is the ability to describe the distribution of orientation angles in any direction, so that a generalized

applicability can be guaranteed. In the statistical analysis herein presented, although the overall performance between Gaussian and Gumbel hypotheses is quite similar, the fitting ability provided by Gumbel distribution is noticeably lower for small orientation numbers. As a matter of fact, if the number of cases selected in the three directions would have been the same, rather poor overall results would have been provided by Gumbel hypothesis. Contrarily, Gaussian distribution denotes consistent agreements with experimental data irrespectively of the magnitude of the orientation numbers.

Given the previous it can then be concluded that the Gaussian law is a suitable and general hypothesis to describe the distribution of fiber orientation angles.

6.4 AVERAGE ORIENTATION ANGLE

The orientation of fibers is commonly characterized through the so-called orientation number (η_θ). The latter corresponds to the average length of all fibers in a section, after projection along the orthogonal axis of the section, divided by the total fiber length (Dupont and Vandewalle, 2005). The orientation number varies from 0.0 to 1.0, referring to fibers contained and orthogonal to the analyzed cross-section, respectively.

Assuming a fiber that rotates freely around its gravity point, when all possible orientations are considered, its end points describe the surface of a sphere with diameter equal to fiber length (L), as shown in Fig.6.7. Under isotropic conditions each point of the sphere surface has an equal probability to be the end of the fiber (Dupont and Vandewalle, 2005). This means that the probability that the fiber makes an angle θ with the orthogonal axis of the section is proportional to the area dA (Fig.6.7) and the contribution to the orientation number is equal to $\cos\theta \cdot dA$ (Dupont and Vandewalle, 2005).

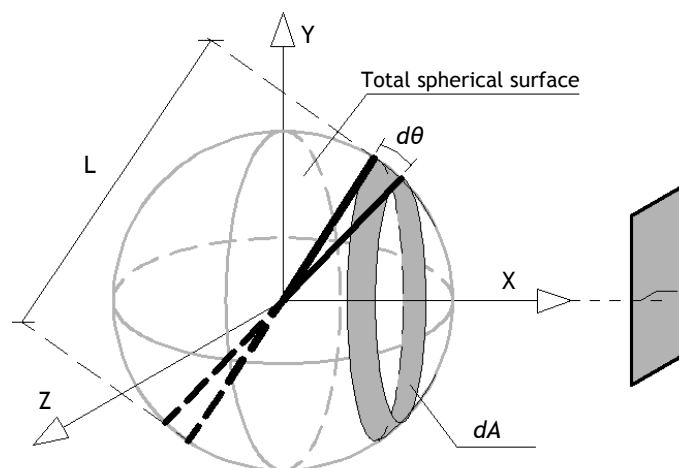


Fig.6.7 - Fiber rotating freely under isotropic conditions

The orientation number can then be calculated using Eq.6.4 (Grünewald, 2004; Schönlin, 1988), with N being the number of fibers in the cross-section and θ_i the angle of each fiber respect to the orthogonal axis of the section.

$$\eta_{\theta} = \frac{1}{N} \sum_{i=1}^N \cos \theta_i \quad (6.4)$$

From Eq.6.4 an approximated average orientation angle in degrees (θ_m) can then be proposed:

$$\theta_m = \arccos(\eta_{\theta}) \times \frac{180}{\pi} \quad (6.5)$$

6.5 DISPERSION OF ORIENTATIONS

The dispersion of fiber orientation accounts for the variability of orientation angles round its average value (θ_m) and can be quantified through the standard deviation of orientation angles, $\sigma(\theta)$. Although average and standard deviation tend to be dissociated parameters, a physical interpretation of the orientation problematic will show in the following that a logical correlation between them can be found. Experimental results will then be used to validate the theoretical assumptions and to propose an analytical expression.

6.5.1 Theoretical basis

Such as aforementioned, the probability that a fiber makes an angle θ with the orthogonal axis of the section is proportional to the area dA (Fig.6.7). When the fiber rotation capacity is restrained by boundary conditions the available spherical surface containing possible positions of fiber end-points decreases (Fig.6.8). This has two major consequences in terms of fiber orientation. On the one hand, the ratio between projected and the available spherical surface increases and therefore so does the orientation number. On the other hand, the available spherical surface becomes limited and therefore the probabilistic dispersion of orientation angles decreases. Hence, the maximum dispersion of the fiber orientation is expected to occur under isotropic conditions (free rotation) and progressively lower dispersions would tend to exist in the presence of preferential orientations. In the limit, fibers completely aligned or oriented orthogonal to the reference axis (0° and 90° , respectively) should be dispersion-free (zero standard deviation).

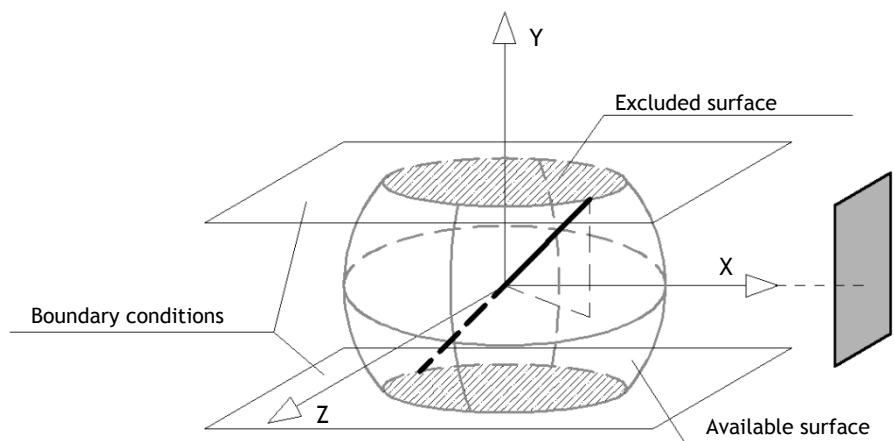


Fig.6.8 - Effect of boundary conditions on the probabilistic field

In order to quantify the maximum standard deviation occurring under isotropic conditions one should be aware that fiber orientation is only fully characterized in the spatial domain when the out-of-plane and the in-plane angles are known (φ and β in Fig.6.9, respectively). Although only the out-of-plane angle is likely to be relevant to account for crack-bridging capacity of fibers, both angles are of interest to fully understand and characterize the orientation problematic.

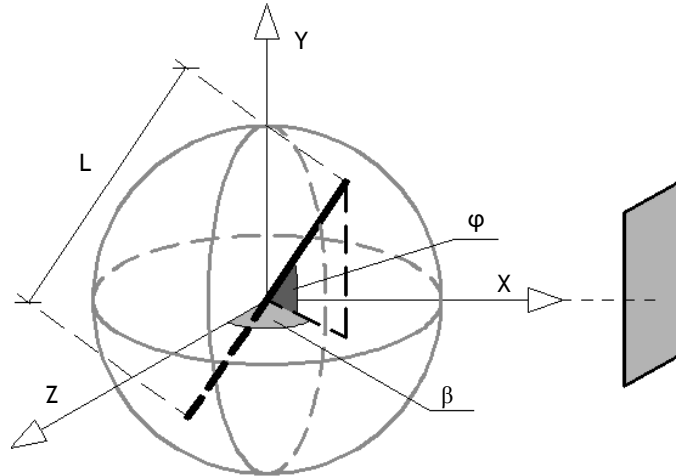


Fig.6.9 - Angles characterizing fiber orientation

The previous analyses of the statistical orientation laws were performed using two different types of experimental results. Cases 1-19 were obtained through the image analysis technique, which is only able to quantify the out-of-plane angle (φ). On the other hand, cases 20-28 refer to orientation data measured in the three independent directions of the spatial domain, thus covering both the out-of-plane and the in-plane angles. Thereby, it can be assumed that the Gaussian law appropriately describes the distribution of orientations of both types of angles.

In theory, under isotropic conditions, both the in-plane and the out-of-plane angles provide an average value of 45° in the 2-D domain whenever they are analyzed independently. From the previous analysis, it can be assumed that the distributions of both angles follow a Gaussian law. According to the properties of the Gaussian law, the amplitude of variation (90°) can be approximated by a confidence interval of about 95.4% through a quantity equal to four times the standard deviation. The maximum standard deviation of a general angle θ (irrespectively if referred to the out-of-plane or in-plane angle) occurring under isotropic conditions can therefore be proposed such as:

$$\sigma(\theta)_{\max} = \frac{90}{4} = 22.5^\circ \quad (6.6)$$

6.5.2 Experimental investigation

The dispersion of fiber orientation was investigated using the same experimental data mentioned in section 6.3.1. For that purpose the projected length of all fibers and the respective

orientation number (Eq.6.4) of each case-study were calculated. Then it was possible to analyze dispersion through the coefficient of variation of the cosine angles of single fibers, $CV(\eta_\theta)$, and correlate it with the average orientation numbers, η_θ (Fig.6.10a). A clear linear tendency between $CV(\eta_\theta)$ and η_θ can be identified in Fig.6.10a, supported by a high coefficient of determination (R^2) of 94%. Hence the following analytical expression can be proposed:

$$CV(\eta_\theta) = 1 - \eta_\theta \tag{6.7}$$

Considering Eq.6.7 and the intrinsic definition of the coefficient of variation (Eq.6.8), an analytical expression for the standard deviation of the orientation numbers, $\sigma(\eta_\theta)$, can then be advanced (Eq.6.9). The latter is compared with the respective experimental values in Fig.6.10b.

$$CV(\eta_\theta) = \frac{\sigma(\eta_\theta)}{\eta_\theta} \tag{6.8}$$

$$\sigma(\eta_\theta) = \eta_\theta \times (1 - \eta_\theta) \tag{6.9}$$

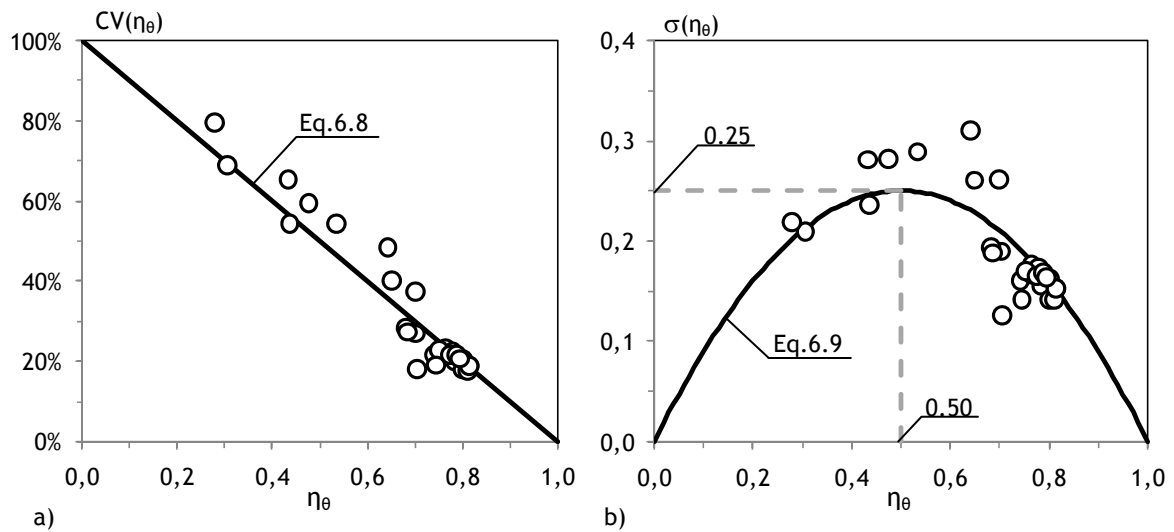


Fig.6.10 - Correlations between orientation angles and standard deviations

From Fig.6.10b it can be observed that the dispersion of fiber orientation, measured in terms of standard deviations, is in accordance with the theoretical basis previously advanced. Indeed, it is observed that maximum dispersions occur approximately for orientation numbers referring to isotropic conditions ($\eta_\theta = 0.5$) and denote a decreasing tendency when approaching extreme values ($\eta_\theta = 0.0$ or $\eta_\theta = 1.0$).

Although Fig.6.10b shows that Eq.6.9 is able to approach the observed dispersions, the analysis of fiber orientation is much more intuitive and comprehensible if performed in terms of orientation angles in degrees (θ). For that purpose η_θ should be converted into averaged orientation angles (θ_m) through Eq.6.5 and a scale factor (K) should be applied to $\sigma(\eta_\theta)$ to obtain

dispersion in terms of orientation angles in degrees, $\sigma(\theta)$. Regarding Eq.6.6 and the maximum value provided by Eq.6.9 (0.25 in Fig.6.10b), K can then be calculated through the particular case of isotropic conditions (Eq.6.10), returning a standard deviation for the orientation angles (in degrees) such as shown in Eq.6.11.

$$K = \frac{\sigma(\theta)}{\sigma(\eta_0)} = \frac{22.5}{0.25} = 90 \quad (6.10)$$

$$\sigma(\theta) = 90 \times \eta_0 \times (1 - \eta_0) \quad (6.11)$$

A comparison between dispersions provided through Eq.6.11 and the 28 experimental cases analyzed is shown in Fig.6.11. Average results from other investigation (Robins et al., 2003) concerning orientation on cast and sprayed SFRC are also included.

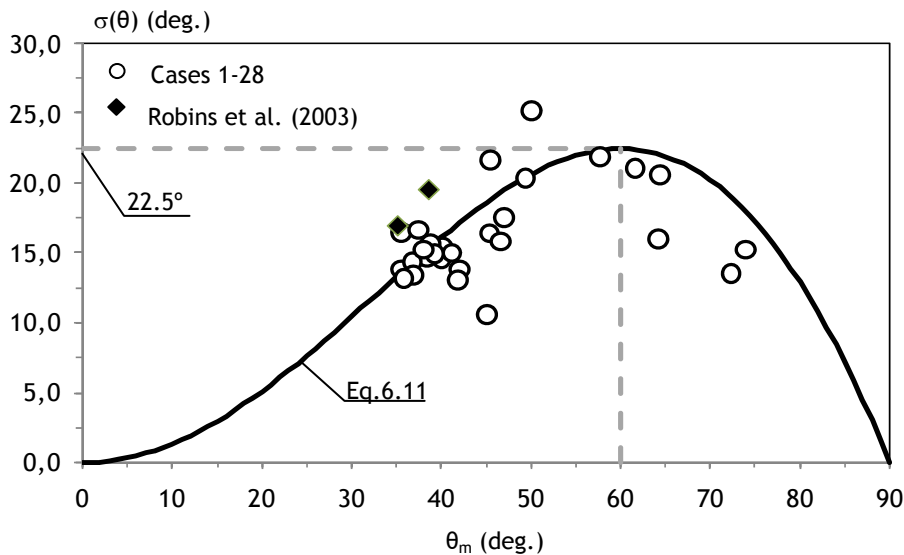


Fig.6.11 - Correlation between average orientation angles and standard deviations

6.5.3 Evaluation of the dispersion

From the previous it can be concluded that, as a matter of fact, dispersion does depend on the average orientation of fibers. The experimental investigation supports the assumptions advanced for dispersion values under isotropic and anisotropic conditions and allows the proposal of an analytical relationship between the orientation number and the standard deviation of orientation angles.

Predicted dispersions using such relationship (Eq.6.11) provide good agreement both on self-compacting, cast and sprayed steel fiber reinforced concrete.

6.6 APPLYING THE ORIENTATION PROFILE

Given the results from the previous analyses, the calculation of the orientation profile turns out to be quite a straightforward and intuitive procedure. Indeed, simply taking the orientation number, both the average value and dispersion of orientation angles can be calculated and then used as input parameters to define the respective distribution of orientation angles. Since the latter was shown to follow a Gaussian law, the respective standardized distribution can also be used to simplify even more the procedure. An example of application is herein described for convenience.

Considering that the orientation angle θ follows a Gaussian law with average θ_m and standard deviation $\sigma(\theta)$:

$$\theta \sim N(\theta_m, \sigma(\theta)) \quad (6.12)$$

The standardized Gaussian orientation angle θ_s can then be obtained through:

$$\theta_s = \frac{\theta - \theta_m}{\sigma(\theta)} \quad (6.13)$$

Adding Eq.6.5 and Eq.6.11, Eq.6.13 can then be rewritten such as:

$$\theta_s = \frac{\theta - \arccos(\eta_\theta)}{90 \times \eta_\theta \times (1 - \eta_\theta)} \quad (6.14)$$

Given that the cumulative distribution of the standardized Gaussian law is tabulated and widely acknowledged, the complete characterization of the orientation profile can then be performed without introducing any other additional variable rather than the orientation number.

To provide insight on the straightforwardness of this procedure an example is shown in Table 6.1. Five simple steps were followed:

1. Identification of the orientation number (η_θ) and selection of the amplitude of the grouping intervals, $\Delta\theta$ (i.e. 10° or 15°).
2. Calculation of the approximated average orientation angle, θ_m (Eq.6.5) and respective standard deviation of orientation angles, $\sigma(\theta)$ (Eq.6.11).
3. Determination of the standardized Gaussian orientation angle at the extreme values of the intervals considered, θ_{si} (Eq.6.13).
4. Identification of the cumulative distribution values of the standardized Gaussian law, $F(\theta_{si})$, and conversion into respective cumulative values of Gaussian distribution, $F(\theta_i)$.
5. Calculation of the relative frequency of each interval, $f(\theta_{ia})$, at the respective class marks, θ_{ia} .
6. Application of the factor accounting for the range error, $F_{ER}(\theta)$, over $f(\theta_{ia})$ in order to obtain the complete orientation profile, $P(\theta_{ia})$.

Table 6.1 - Example of application of the orientation profile

Inputs:		$\eta_{\theta} = 0.70$				
		$\Delta\theta = 15^{\circ}$				
		$F_{RE}(\theta) = 1.017$ (Eq. 6.2)				
Outputs:		$\theta_m = 45.6^{\circ}$ (Eq. 6.5)				
		$\sigma(\theta) = 18.9^{\circ}$ (Eq. 6.11)				
θ_i	θ_{Si}	$F(\theta_{Si})$	$F(\theta_i)$	θ_{ia}	$f(\theta_{ia})$	$P(\theta_{ia})$
[$^{\circ}$]	[$^{\circ}$]	[%]	[%]	[$^{\circ}$]	[%]	[%]
0	-2.41	49.2	0.8			
				7.5	4.5	4.5
15	-1.62	44.7	5.3			
				22.5	15.4	15.6
30	-0.82	29.4	20.6			
				37.5	28.2	28.7
45	-0.03	1.2	48.8			
				52.5	28.8	29.3
60	0.76	27.6	77.6			
				67.5	16.4	16.7
75	1.56	44.1	94.1			
				82.5	5.0	5.1
90	2.35	49.1	99.1			

Given the basic steps involved, a simple spreadsheet can be used to obtain the orientation profiles for any orientation number, such as exemplified in Fig.6.12 for some common values.

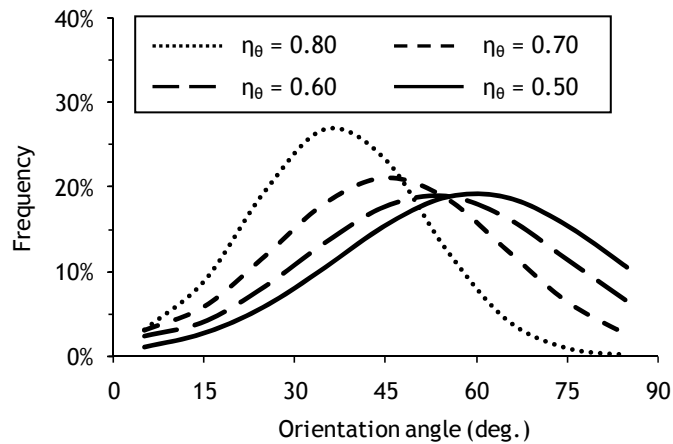


Fig.6.12 - Predicted orientation profiles for different orientation numbers

6.7 CONCLUDING REMARKS

This chapter presents a detailed analysis on the distribution of fiber orientation angles in SFRC. To provide an extended and unambiguous description of the orientation field the new concept of orientation profile was advanced. The latter demands an appropriate statistical orientation law, with the average and the standard deviation of fiber orientation angles as input values.

Making use of different experimental data sets it was possible to conclude that the Gaussian law appropriately describes the statistical distribution of fiber orientation. The overall agreement provided by this hypothesis indicates that it is a suitable approach irrespectively of the magnitude of the average orientation angles considered.

Through some brief theoretical remarks it was pointed out that dispersion of fiber orientation is likely to be related with the average orientation value. Further analysis on experimental data supported such dependency quite clearly. Hence, it was possible to apply the orientation profile in different orientation scenarios to gain insight into the realistic distributions of fiber orientation angles by means of a very simple and straightforward procedure.

Regarding the paramount effect of fiber orientation on the mechanical properties of FRC, improving their characterization through a more robust and complete concept is evidently of great interest. Moreover, regarding that no other parameter rather than the ordinary orientation number is required, improved material characterization can be achieved through current fiber orientation measuring techniques.

Chapter 7

Framework to predict the orientation of fibers in FRC: A novel philosophy

7.1 INTRODUCTION

The orientation profile proposed in Chapter 6 provides a detailed characterization of the distribution of individual fiber orientation angles in a cross-section. If this data could be obtained, comprehensive and cost-effective designs for SFRC applications could be developed. For that purpose, the orientation number of fibers in a cross-section needs to be predicted.

In this chapter, the orientation of fibers is analyzed and predicted through a novel philosophy. Firstly, the outline of the new framework is presented and its core concepts are highlighted. Then, fiber orientation is evaluated in the spatial domain through a probabilistic approach, which provides a larger insight than the 1-D analysis commonly covered in literature. Subsequently, the wall-effects are studied in detail and a new approach is advanced for its quantification both in isotropic and anisotropic conditions.

The framework herein proposed aims at evaluating fiber orientation from a wider perspective than mere particular cases, including theoretical concepts to explain some of its major aspects

and bringing together the combined influence of material properties, production processes and the structure itself. The goal of this chapter is not to present a final operational framework, but rather serves, hopefully, to provide a step towards the development of a rational and design-oriented procedure to predict fiber orientation.

7.2 FRAMEWORK OUTLINE

Fiber orientation in the hardened-state is the final result of a chain of stages that FRC passes through from mixing to hardening inside the formwork. The specific boundary conditions that characterize each phase of the production process induce many stages of interaction at which fiber orientation is modified.

The transient fiber orientation at the end of each of these stages depends on the specific type of action imposed (wall-effects, gravity, external vibration, etc.), but also on the predominant orientation existing prior to each stage. Hence, the several aspects governing fiber orientation cannot be evaluated independently but rather shall be approached from an integrated and sequential perspective of the overall production process through a step-by-step procedure. For that purpose, four transient orientation numbers prior to the final one in the hardened-state (η_θ) are defined:

- concrete fresh-state properties after mixing (η_M)
- after casting into the formwork (η_C)
- after occurrence of dynamic effects (such as vibration or flow) (η_D)
- after the wall-effects introduced by the formwork (η_F) (Fig.7.1).

In order to quantify and to establish the interdependence of the several orientation numbers occurring along the production process, two major topics need to be covered: 1) fiber orientation in the spatial domain; 2) wall-effects in anisotropic conditions. Both subjects are discussed in the following sections as a first attempt to predict fiber orientation through this new framework.

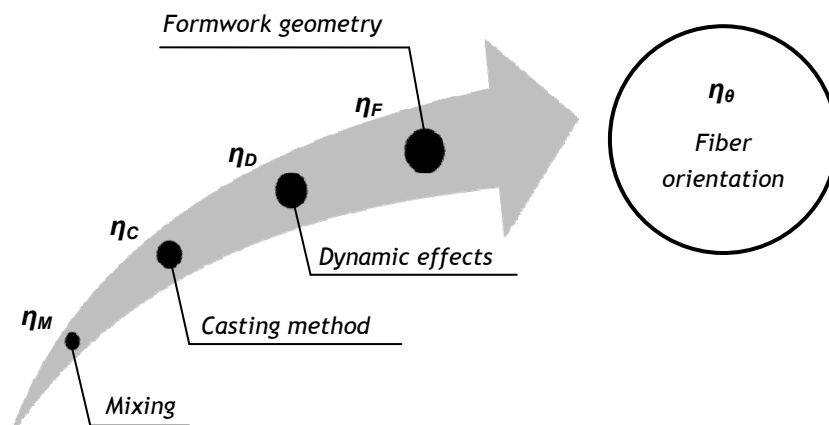


Fig.7.1 - Main stages of the production process and respective orientation numbers.

7.3 FIBER ORIENTATION FROM A 3-D PERSPECTIVE

Although FRC has been extending its field of applications, this material probably performs best when 2-D or 3-D stresses are concerned. Because fibers are everywhere and oriented in all directions they can cope with any expected and unexpected stresses, wherever in concrete (Walraven, 2007). Mechanical properties and fiber orientation of FRC shall therefore be evaluated globally, regarding not only one but several different directions.

When measuring η , the fiber orientation is evaluated along one unique axis. Its value varies from 0.0 to 1.0, referring to fibers orthogonal and parallel to the analyzed direction, respectively. If a fiber rotating in space is now considered, when preferential orientation is observed along a certain axis, the projected fiber lengths on the remaining two independent axes decrease. The orientation numbers in three independent axes are therefore evidently correlated. How they depend on each other and what is their theoretical and probabilistic ranges of variation is herein presented and compared to experimental results.

7.3.1 Theoretical and probabilistic envelop curves

The relationship between the orientation numbers in three independent axes can be analyzed by calculating the spherical coordinates of all the possible positions of fiber end-points. Fixing fiber length (L) as a unitary vector, η in x-, y- and z-directions become uniquely defined through horizontal and vertical angles (β and φ , respectively), such as shown in Fig.7.2.

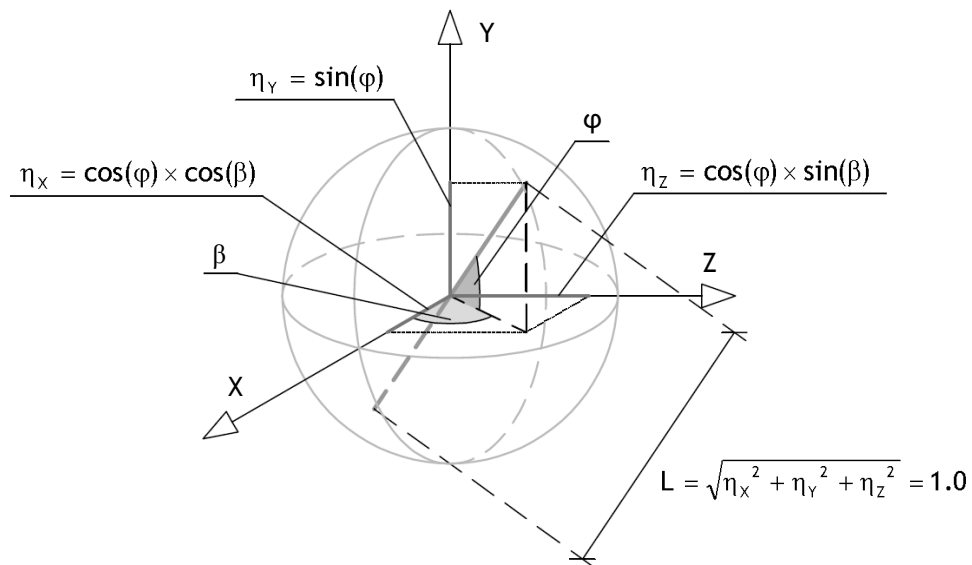


Fig.7.2 - Characterization of fiber orientation through two independent angles.

For practical purposes, more than determining the theoretical range of variation of η in the spatial domain, a probabilistic confidence interval is demanded. Thereby, the probability of occurrence of the governing angles (β and φ) has to be related with each of the orientation numbers.

Under isotropic conditions, any point of the spherical surface shown in Fig.7.2 has an equal probability of occurrence. However, the chances that a fiber is nearly aligned with any of the independent axes are quite small. To support this statement consider Fig.7.3, in which a small angle ξ around each of the independent axes is related with its respective probability of occurrence (A_ξ) in half of the sphere. The latter corresponds to the surface of a sphere cap which is defined by:

$$A_\xi = \frac{\pi \times L^2}{2} \times (1 - \cos \xi) \quad (7.1)$$

Regarding that six sphere caps can be extracted from a sphere, it is possible to define a certain significance level (SL) up to which the probability of occurrence is not representative:

$$SL = \frac{6 \times A_\xi}{A_{\text{sphere}}} = 3 \times (1 - \cos \xi_{SL}) \quad (7.2)$$

By selecting a significance level of 0.10, the respective angle around each of the axis (ξ_{SL}) returns a value of about 15° . Consequently, the 90% confidence intervals for β and φ (in degrees) can be derived:

$$\varphi_{(SL=0.10)} \in [0, 75] \quad (7.3)$$

$$\beta_{(SL=0.10)} \in \begin{cases} [0, 90] & \text{if } \varphi \geq 15^\circ \\ [0, 90 - 2 \times (15 - \varphi)] & \text{if } \varphi < 15^\circ \end{cases} \quad (7.4)$$

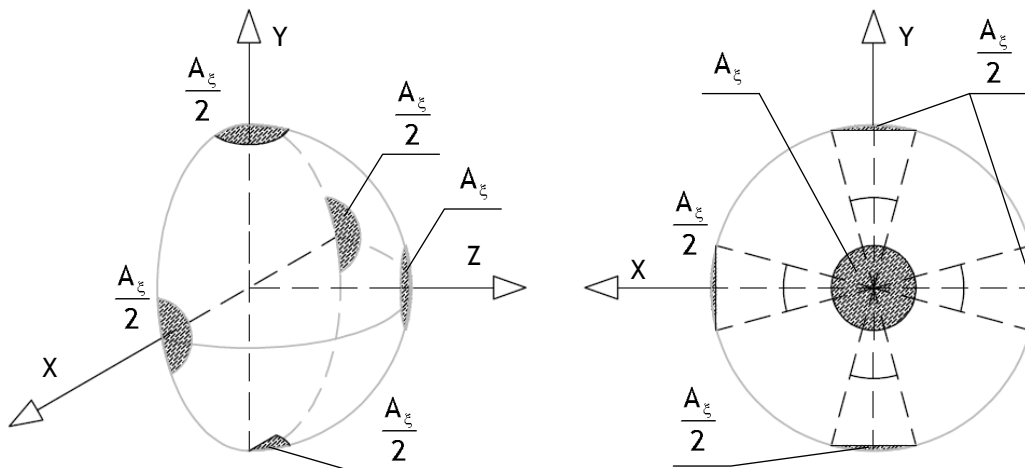


Fig.7.3 - Identification of the significance level of half of the spherical surface.

To identify the correlation between η in 3-D a parametric study was carried out by varying both β and φ along their entire ranges of variation. Then the fiber projected lengths were obtained, as shown in Fig.7.2, and the sums of the orientation numbers in the horizontal plane (η_{xz}) and in the spatial domain (η_{xyz}) were calculated, according to Eqs.7.5-7.6. The dependency of η_{xz} and

η_{xyz} with β and φ are presented in Fig.7.4, both for their theoretical and probabilistic ranges of variation.

$$\eta_{xz} = \eta_x + \eta_z \leq \sqrt{2} \tag{7.5}$$

$$\eta_{xyz} = \eta_x + \eta_y + \eta_z \leq \sqrt{3} \tag{7.6}$$

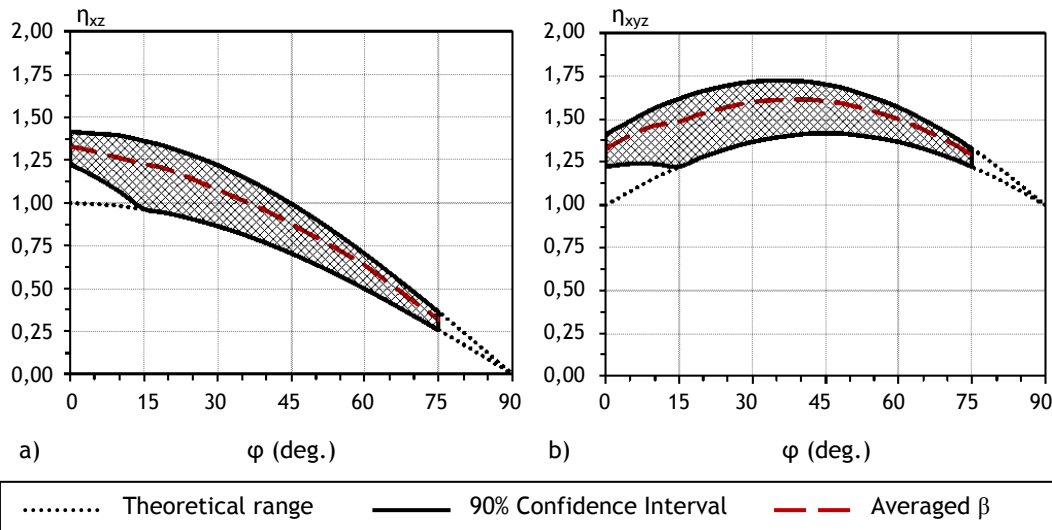


Fig.7.4 - Theoretical and probabilistic ranges of variation of: a) 2-D; b) 3-D.

Fig.7.4a shows the influence of the vertical angle (φ) on the horizontal plane for any value of β . When increasing φ , both the magnitude and the amplitude of the theoretical η_{xz} decrease progressively towards a zero value. On the other side, when accounting for the aforementioned 90% confidence interval, minimum and maximum values of 0.26 and 0.37 can be found when φ equals 75° . For vertical angles smaller than 15° , the reduced amplitude of variation of η_{xz} due to the restrained range of β is noticeable and the minimum value in this range is equal to 0.97.

By analyzing the variation of the orientation numbers in the spatial domain (Fig.7.4b) it can be observed that, although the amplitude of the theoretical η_{xyz} decreases with φ , its magnitude no longer varies monotonically. A maximum value can be observed ($\sqrt{3}$) when β is equal to 45° and φ approaches 35° . The probabilistic confidence interval applies such as in the previous case, defining a minimum value for η_{xyz} of about 1.23 that is verified when φ is equal to 0° , 15° and 75° . The upper bound of both η_{xz} and η_{xyz} occurs when β is equal to 45° whereas the lower bound refers to fibers whose projection in the horizontal plane coincides with the main axes x and z (β equal to 0° and 90°).

Results shown in Fig.7.4 are relevant as they fix the theoretical and most probable range of variation for the sum of orientation numbers in different directions through a correlation with the horizontal and vertical angles. This way, changes on preferential fiber alignments such as the ones imposed by the direction of casting can be intuitively explained.

7.3.2 Experimental verification

In order to validate the theoretical and probabilistic envelop curves, the experimental work performed by Molins et al. (2008) was taken into account. In the latter, four cylindrical samples with 100mm diameter and 150mm height were extracted in different directions from a bending test specimen and the fiber orientation was analyzed through the computerized tomography technique (CT-scans). In all the samples, axial tomographies of the cross-sections were taken with a constant spacing of 1mm along the height, thus providing the exact number and orientation of fibers in 3-D. The applied FRC was a SCC with 20kg/m^3 steel fibers (60mm length; 0.75mm diameter).

The results obtained by this experimental investigation (Molins et al., 2008) identified a total of 686 fibers, 118 of which were completely embedded in the analyzed samples. The orientation numbers of all the fibers were calculated for the three independent axes and the results of η_{2D} and η_{3D} are compared with the theoretical and probabilistic envelop curves in Fig.7.5-7.6, respectively.

The experimental average of the sum of orientation numbers in 2-D ($\eta_{xz,m}$) was approximately 1.15 with a standard deviation, $\sigma(\eta_{xz})$ of 0.19. On the other hand, the respective average of the sum of orientation numbers in 3-D ($\eta_{xyz,m}$) was 1.48 with a standard deviation ($\sigma(\eta_{xyz})$) of 0.16. According to the investigation performed in Chapter 6, the Gaussian law is capable to describe the statistical distribution of fiber orientation. According to the properties of such law, the intervals $[\eta_{xz,m}-2\cdot\sigma(\eta_{xz}), \eta_{xz,m}+2\cdot\sigma(\eta_{xz})]$ and $[\eta_{xyz,m}-2\cdot\sigma(\eta_{xyz}), \eta_{xyz,m}+2\cdot\sigma(\eta_{xyz})]$ should contain at least 95.4% of the fibers. Indeed, 97.4% and 95.3% of the fibers were observed within these limits in Fig.7.5a and Fig.7.6a, respectively.

A second conclusion derived from Figs.7.5-7.6 is that η_{xz} and η_{xyz} are always within the theoretical enveloping curves presented. Furthermore, also the suitability of the probabilistic approach could be verified, with η_{xz} and η_{xyz} providing values that support the predefined confidence interval (91.5% and 91.3%, respectively).

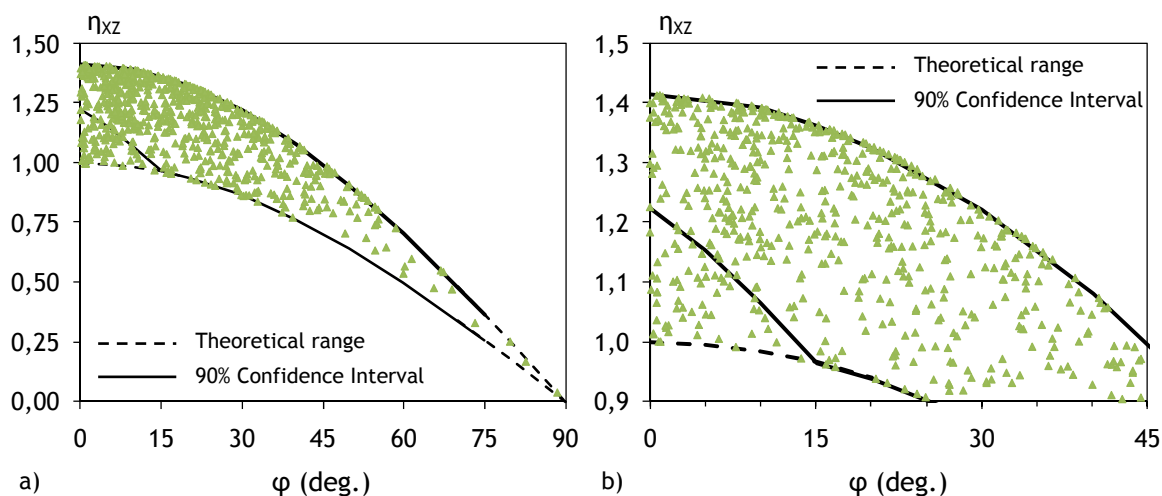


Fig.7.5 - Experimental verification of η_{xz} : a) Overall results; b) Detailed analysis.

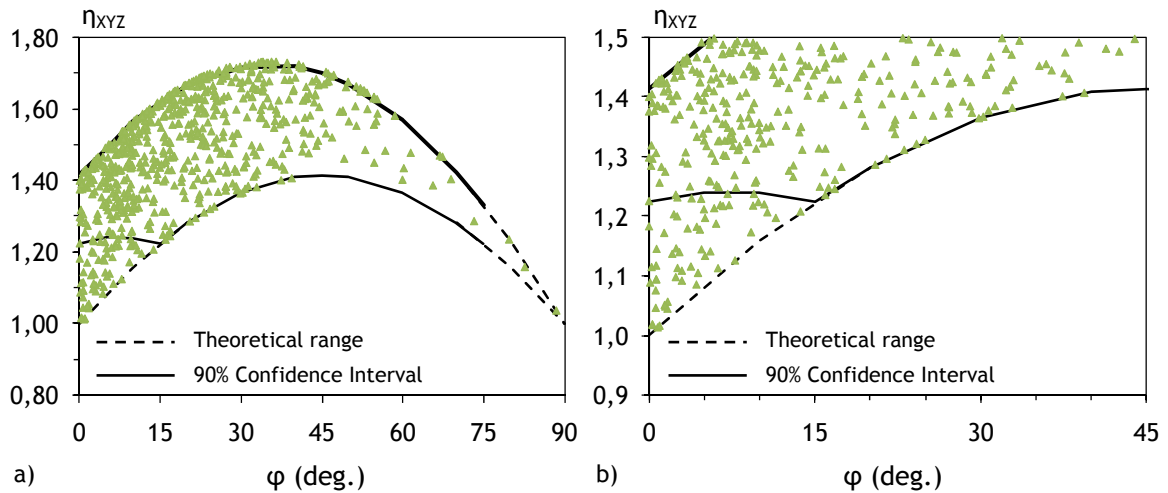


Fig.7.6 - Experimental verification of η_{XYZ} : a) Overall results; b) Detailed analysis.

7.4 APPROACH TO ESTIMATE GENERALIZED WALL-EFFECTS

The calculation of the orientation number has been of interest of many researchers (Romualdi et al., 1964; Krenchel, 1975; Kameswara, 1979; Soroushian and Lee, 1990; Hoy, 1998; Stroeven, 1999; Kooiman, 2000; Van Gysel, 2000; Grünewald, 2004; Dupont and Vandewalle, 2005). Analytical formulations proved that η in isotropic conditions for 1-D, 2-D and 3-D are equal to 1.0, $2/\pi$ and 0.5. However, despite the interest of these values, their applicability is very limited since the restraining action introduced by external boundaries on fiber rotation is not considered.

In order to take into account the influence of wall-effects on the orientation number, Dupont and Vandewalle (2005) advanced an averaging procedure by identifying the zones of the cross-section with none, one and two boundary conditions (A_0 , A_1 and A_2) and then attributing their respective average orientation numbers (η_0 , η_1 and η_2), as shown in Fig.7.7. They assumed that the location of a fiber can be characterized by its center of gravity and that each point of the cross-section has an equal probability of being the gravity point of a fiber. They considered that the top surface of the section has the same boundary condition (BC) as the sides of the mould and that no differences exist between straight and hooked-end fibers concerning the calculation of η . Through the development of a mathematical model, the average orientation numbers under the influence of one BC (η_1) and two BCs (η_2) were found to be approximately equal to 0.60 and 0.84, respectively.

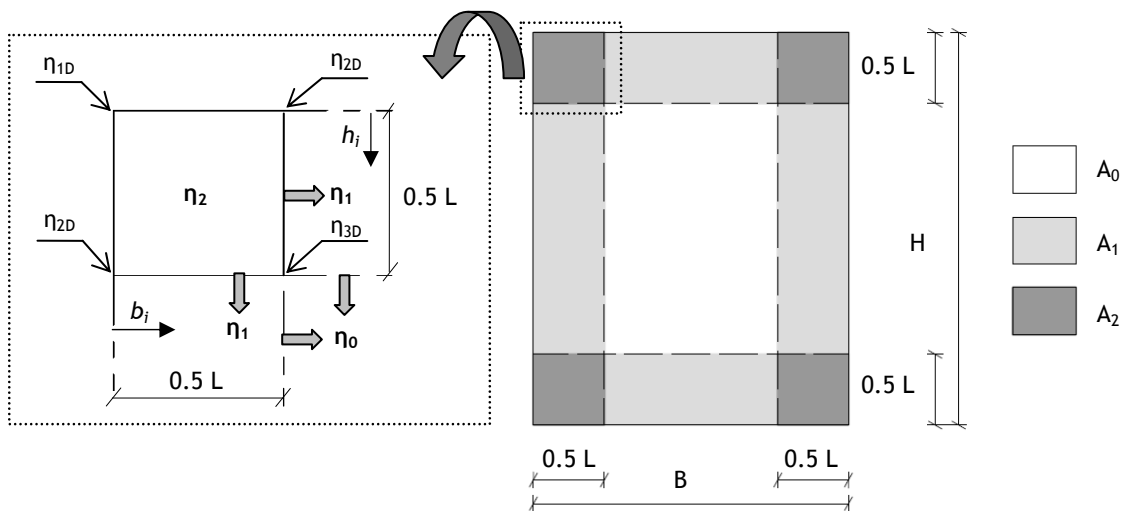


Fig.7.7 - A cross-section divided in three zones (with detail of the corner).

Despite the relevant work reported by (Dupont and Vandewalle, 2005), a major limitation is the fact that the procedure is only applicable under the assumption of isotropic conditions, i.e., that the orientation number in the bulk (η_0) coincides with the one in the spatial-random case, η_{3D} (0.50). However, the reasonability of this hypothesis is highly arguable regarding that preferential fiber orientation is likely to occur due to several aspects (casting procedures, vibration, flow, etc.). Consequently, the actual influence of wall-effects on η will differ: if fibers in bulk are mostly orthogonal to one BC, the increment of fiber alignment in the direction parallel to that BC will be much larger than in the case that fiber in bulk would have already some preferential orientation parallel to the BC. Thereby, η_1 and η_2 shall be adapted consistently to any orientation number in bulk (η_0) in order to obtain generalized wall-effects.

7.4.1 Analysis of the wall-effects in isotropic conditions

The numbers η_1 and η_2 result from an averaging process which simplifies a much more complex behavior. In fact, a realistic distribution of the orientation number nearby a wall(s) consists of a progressive transition zone that bridges η_0 to the one close to the wall(s) (2-D or 1-D cases). In order to determine the nature of such transition relationships, η has to be calculated systematically by considering the fiber gravity point at different distances from the wall(s). By using the formulations advanced in the aforementioned work (Dupont and Vandewalle, 2005), heavy and slowly-convergent numerical integrations have to be carried out. A more simple and analytical alternative approach is proposed in Appendix 5.2.

By applying the expressions included in Appendix 5.2, η can be easily calculated for different distances between fiber gravity point and both walls, such as presented in Fig.7.8. The average orientation number obtained along the influence zone of one BC for the spatial-random case (η_1) supports the value advanced in (Dupont and Vandewalle, 2005): 0.60. In the planar-random case ($h_i/L=0$) an average orientation number of 0.93 was obtained. The average of all curves along h_i provides an average orientation number at the corner of the section of about 0.84, thus confirming the value previously advanced (Dupont and Vandewalle, 2005).

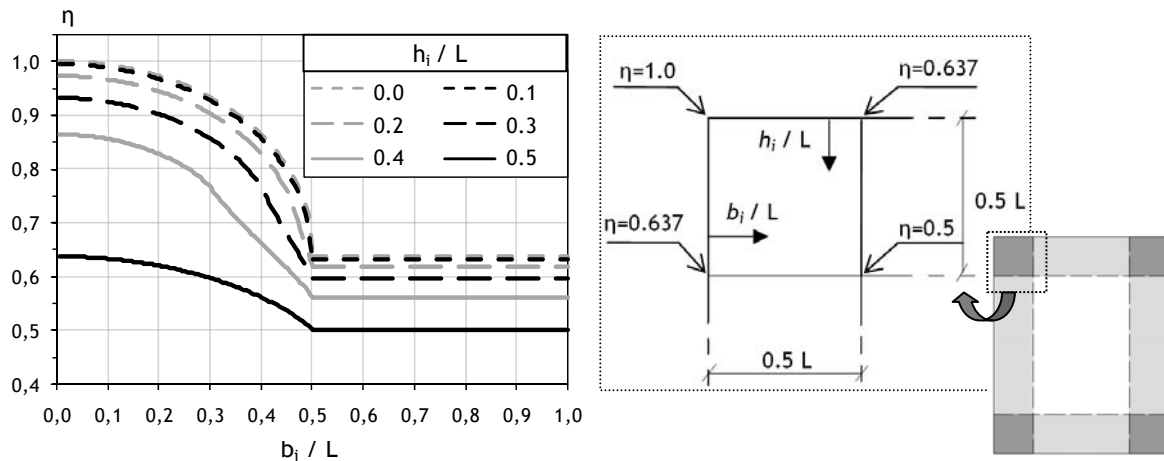


Fig.7.8 - Variation of η at different distances from both walls.

7.4.2 Approaching the wall-effects in anisotropic conditions

At a first glimpse, the results provided in Fig.7.8 may seem excessively minutia and with none practical application. However, valuable information on fiber orientation can be extracted from it. First of all, the average of the diagrams shown in Fig.7.8 support the values advanced in literature (Dupont and Vandewalle, 2005) for fibers in isotropic conditions under the influence of one and two BCs. Thereby, adjusted η_1 and η_2 can be easily obtained for any cross-section in isotropic conditions when the shorter dimension is smaller than the fiber length.

A nonlinear transition can be observed in Fig.7.8, with η barely decreasing at short distances from the wall and then denoting a less pronounced wall-effect when the fibers' gravity point approaches a distance equal to half the fiber length. Given these consistent results, a simplified bilinear diagram is hereafter proposed to approach such behavior (Fig.7.9). In the case of one BC, the fiber orientation reflects the transition between η_{2D} at the wall (≈ 0.637) and η_{3D} in bulk (≈ 0.50), providing an average value (η_1) of 0.60. Considering these values, the equivalent bilinear diagram becomes defined by fixing the intermediate point of the diagram at a distance of about 0.23 times the fiber length (Fig.7.9).

When two orthogonal BCs exist, the influence of one wall on η depends on the distance of the fibers' gravity point relative to the other orthogonal wall, thus different transition diagrams (Fig.7.8) are obtained, which provide an average η_2 equal to 0.84. This value can be interpreted as the average η between the extreme cases (h_i/L equal to 0.0 and 0.50), whose representative averages of η are 0.93 and 0.60, respectively. Thereby, when calculating the bilinear diagram with these extreme values and an average of 0.84, the intermediate point of the diagram turns out to be, again, at a distance of about 0.23 times the fiber length from the wall (Fig.7.9). Such feature of the bilinear diagrams provide ground to justify from a theoretical perspective that, up to a distance of about 0.23 times the fiber length, the fiber orientation is higher than in the remaining zone under the influence of the wall. This conclusion is supported by experimental

observations (Hoy, 1998), which found different densities of fibers within the band of influence of the wall, particularly larger values on the region closest to the mould surface.

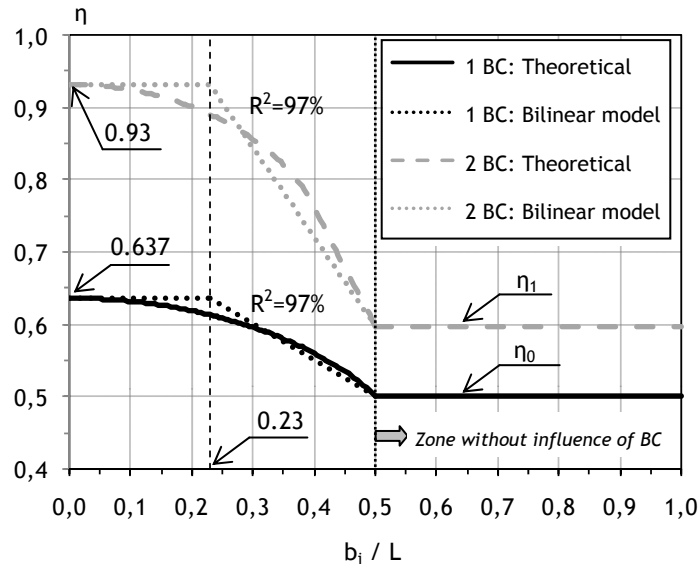


Fig.7.9 -Bilinear models to approach wall-effects under isotropic conditions.

Given the existence of a bandwidth close to the walls with approximately constant orientation numbers (0.93 and 0.637) and the fact that η at distances from the walls equal to half the fiber length are always equal to η_0 , the bilinear diagrams shown in Fig.7.9 provide a tool to define the wall-effects for any anisotropic scenario. This way, η_1 and η_2 can be generalized as a function of the orientation number in bulk (η_0), such as defined by Eqs.7.7-7.8. These expressions are valid whenever fiber alignment is affected by the walls (η_1 and η_2 equal or greater than η_0). In cases with fibers having large orientation numbers in bulk (large η_0), Eqs.7.7-7.8 may not be verified. This is typically the case of fibers which are already so oriented parallel to the walls that the latter do not play any influence. In those cases, η_1 and η_2 shall be assumed equal to η_0 .

$$\eta_1 = 0.465 + 0.270 \cdot \eta_0 \quad (\geq \eta_0) \quad (7.7)$$

$$\eta_2 = 0.677 + 0.270 \cdot \eta_1 \quad (\geq \eta_0) \quad (7.8)$$

By applying Eqs.7.7-7.8 in the averaging procedure depicted in Fig.7.7, the wall-effects can then be quantified for any anisotropic conditions ($\eta_0 \neq 0.50$). The increments of orientation number due to the wall-effects ($\Delta\eta_w$) are quantified in Appendix 5.3 for common cross-section geometries (rectangular, circular and hollow-circular).

7.5 FRAMEWORK ANALYSIS: STEP-BY-STEP

Taking into account the theoretical concepts advanced in Sections 7.3-7.4, some of the major aspects governing fiber orientation become clear and physically explained.

In this part of the chapter, the main stages of the production process influencing fiber orientation (Fig.7.1) are discussed:

1. Mixing (η_M)
2. Casting method (η_C)
3. Dynamic effects (η_D)
4. Formwork geometry (η_F)

Firstly, relevant experimental evidences and conclusions reported in literature are highlighted. Then, based both on theoretical and experimental results, a first attempt is advanced to quantify each of the four transient orientation numbers. A step-by-step methodology was adopted in order to integrate several production stages within a rational procedure. A brief summary of the main steps of the framework is shown at the end of this section.

7.5.1 Influence of fresh-state properties after mixing

One of the major aspects governing fiber orientation is the rheology of FRC. Although the latter has been subject of extensive research, standardized equipment and measuring techniques are not yet available and therefore its correlation with the orientation of fibers in fresh concrete is unknown (Ozyurt et al., 2007). Hence, given the scarce knowledge about this subject, fiber orientation will be herein approached by simply distinguishing the behavior of conventional and self-compacting FRC in the fresh-state. Conventional concrete (CC) is a granular mass requiring vibration to be compacted while self-compacting concrete (SCC) is a liquid suspension following the rules of fluid mechanics (Rilem TC 188-CSC, 2006). Thereby, fiber orientation in the three independent axes after mixing is likely to be different according to the type of concrete considered.

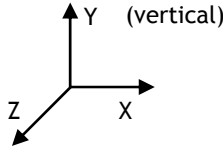
CC mixtures are homogeneous due to lack of flow-ability and therefore the orientation of fibers may be random in three dimensions when the material is discharged from the mixer (Edington and Hannant, 1972). According to the theoretical range of variation of η_{xyz} in isotropic conditions (Fig.7.4b), an average constant value within the predefined confidence interval can be obtained by averaging the two independent angles β and φ . In such conditions, η_{xyz} is equal to 1.50 with a small coefficient of variation (CV) of 7.9%. Because isotropy conditions imply the absence of preferential fiber alignment, η_M of CC can then be assumed to be equal to 0.50 in three independent axes.

In contrast, a mixture with increased flow-ability in the fresh-state shows a stronger alignment of the fibers than a material with lower flow-ability (Stälhi et al., 2008). SCC requires filling ability for horizontal and vertical flow, thus being prone to induce planar orientation of fibers. The flow can be idealized as taking place in layers that force fibers which are crossing them to align along their borderlines (Grünwald, 2004). The latter can then be idealized as virtual boundaries which restrain the rotation capacity of fibers. In this approach, the thickness of these virtual layers is assumed to be equal to the fiber length (L), which according to the expressions of the wall-effects for isotropic conditions, returns an average η of 0.60 in the two independent

directions of the horizontal plane (η_{Mx} and η_{Mz}). Consequently, according to the average value of 1.50 advanced for η_{xyz} in 3-D, η along the remaining direction (η_{My}) would be equal to 0.30. The orientation numbers after mixing of FRC considered (η_M) are summarized in Table 7.1:

Table 7.1 - Summary of considered η_M according to direction and type of concrete.

Type of concrete	η_{Mx}	η_{My}	η_{Mz}
CC: Conventional	0.50	0.50	0.50
SCC: Self-compacting	0.60	0.30	0.60



7.5.2 Influence of the casting method

Several researchers have reported remarkable influences of casting elements (Toujanji and Bayasi, 1998; Markovic, 2006; Torrijos et al., 2008) and the casting direction on fiber orientation (Torrijos et al., 2008; Stälhi et al., 2008; Dozio, 2008). Consequently, in order to be able to compare properties of different FRCs, casting methods have to be exactly the same (described and reproducible) (Stälhi et al., 2008). These facts lead to the obvious conclusion that the non-uniformity of fiber orientation due to different casting methods has to be considered in the design of structural elements (Lappa, 2007). This explains tremendous differences in structural performances sometimes observed in elements with the same FRC poured in different directions. However, its influence cannot be evaluated independently from other aspects. Indeed, the casting direction was found to have a paramount influence on the mechanical properties of fluid fibrous mixtures, but a significantly smaller effect was observed with more viscous mixtures (Toujanji and Bayasi, 1998). The link between the casting method and the rheological properties of fresh concrete is of utmost importance (Roussel, 2007).

The effect of pouring elements on fiber orientation may be somehow irrespective of the type of element applied (e.g.: skip, trolley, shovel, bucket, etc.), but rather mainly dependent on the geometry of their exit cross-sections. Therefore, the generalized expressions presented in Appendix 5.3 can be used to quantify the increment of orientation number due to wall-effects introduced by the casting element ($\Delta\eta_{CW}$). The orientation number in bulk of the casting element (η_{C0}) should account for the casting direction (previously defined in terms of φ and β in Fig.7.3) and for the fresh-state properties of the concrete after mixing (η_M), according to Eq.7.9:

$$\eta_{C0} = \sqrt{(\eta_{Mx} \times \cos \varphi \times \cos \beta)^2 + (\eta_{My} \times \sin \varphi)^2 + (\eta_{Mz} \times \cos \varphi \times \sin \beta)^2} \quad (7.9)$$

Then, η have to account for the wall-effects through a parameter referring to the misalignment between the casting element and the main axes of the formwork in direction i (C_{Di}). For that purpose, the same referential adopted for concrete properties (Fig.7.2) will be considered. In

such hypothesis, the increment of η due to casting method within any direction i ($\Delta\eta_{Ci}$) can be obtained (Eq.7.10). Consequently, η after casting FRC into the formwork along any direction i (η_{Ci}) is given by Eq.7.11.

$$\Delta\eta_{Ci} = \Delta\eta_{CW} \times C_{Di} \quad (7.10)$$

$$\eta_{Ci} = \eta_{Mi} + \Delta\eta_{Ci} \quad (7.11)$$

According to the analysis in the 3-D domain advanced in Section 3, η in the three main axes depend on the two governing angles φ and β . The introduction of a preferential orientation due to the wall-effects changes the representative angles φ and β of all fibers in the section and, consequently, η in the two remaining axes are also modified. This phenomenon will be herein defined as secondary wall-effects. The latter cannot be quantified arbitrarily, but rather have to be consistent with the nature of the BCs that generated the wall-effects. Consider, for instance, the case where the casting method accounts for a pouring element with rectangular exit cross-section and aligned along the x-axis of the formwork (Fig.7.10). Since the geometry of the cross-section implies different effects of vertical and horizontal boundaries ($B_C > H_C$) it seems reasonable to apply a criterion proportional to their respective perimeter fractions (Eqs.7.12-7.14). This way, the higher the perimeter fraction of one border of the casting element, the larger will be the reduction of η in the direction orthogonal to such border. Note that η_{xyz} is kept constant regarding that, as previously shown, it provides a reasonable approximation within the defined probabilistic confidence interval.

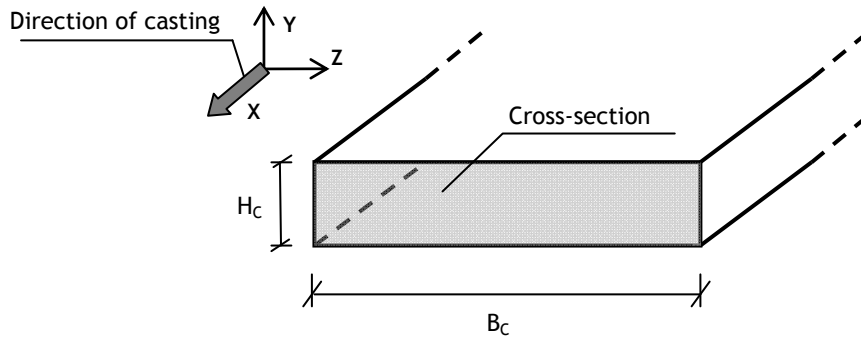


Fig.7.10 -Example of cross-section of a casting element aligned with the x-axis.

$$\Delta\eta_{Cx} = \Delta\eta_{CW} \quad (7.12)$$

$$\Delta\eta_{Cy} = -\Delta\eta_{CW} \times \frac{B_C}{B_C + H_C} \quad (7.13)$$

$$\Delta\eta_{Cz} = -\Delta\eta_{CW} \times \frac{H_C}{B_C + H_C} \quad (7.14)$$

Regarding the previous example, general expressions to quantify the parameters accounting for the misalignment between casting element and the formwork in the three main axes (η_{Cx} , η_{Cy} and η_{Cz}) can be advanced (Table 7.2). For circular geometries, B_C and H_C may be chosen equal to the diameter of the cross-section.

In the case of self-compacting FRC, the high flow ability of the material tends to decrease the orientation number of fibers in the y-axis. Thereby, once FRC is cast inside the formwork, the effects introduced by BCs orthogonal to the y-axis may be depreciable since the material will tend to denote a preferential planar-orientation. For SCC, η_{Cy} should remain equal to η_{My} . Consequently, a fictitious BC orthogonal to the gravity axis may be assumed, implying that H_C equals L. If the casting is performed with free top surface, H_C is the minimum value between L and two times the geometric H_C of the casting element.

Table 7.2 - Summary of C_{Di} in the three main axes of the formwork.

$$C_{Dx} = \cos \varphi \times \cos \beta - \sin \beta \times \frac{H_{C,eff} \times \cos \varphi}{B_C + H_{C,eff}}$$

$$C_{Dy} = \sin \varphi - \cos \varphi \times \frac{B_C}{B_C + H_{C,eff}}$$

$$C_{Dz} = \cos \varphi \times \sin \beta - \cos \beta \times \frac{H_{C,eff} \times \cos \varphi}{B_C + H_C}$$

7.5.3 Influence of dynamic effects

After casting FRC the orientation of fibers may be modified due to dynamic effects that take place in order to guarantee appropriate filling of the formwork. In the origin of these dynamic effects, the external vibration process applied on conventional FRC and the flow of self-compacting mixtures are paramount stages. Thereby, η after the occurrence of dynamic effects in direction i (η_{Di}) depends on the pre-orientation of fibers once cast into the formwork (Eq.7.15) and shall account for the respective variations due to external vibration and flow, $\Delta\eta_{DVi}$ and $\Delta\eta_{DFi}$, respectively (Eq.7.16).

$$\eta_{Di} = \eta_{Ci} + \Delta\eta_{Di} \quad (7.15)$$

$$\Delta\eta_{Di} = \Delta\eta_{DVi} + \Delta\eta_{DFi} \quad (7.16)$$

The effect of external vibration

Vibration may cause rotation and alignment of the fibers preferentially in a specific direction (Gettu et al., 2005). External vibration tends to orient fibers in a plane perpendicular to the direction of vibration (Eddington and Hannant, 1972), with the tendency towards a planar fiber

orientation (Soroushian and Lee, 1990; Kooiman, 2000; Gettu et al., 2005). Some authors reported there is essentially no difference between poured FRC subjected to external vibration and sprayed concrete in terms of fiber distribution and orientation (Robins et al., 2003). Vibration does not have a significant effect on fiber orientation if the specimen is only vibrated for 1 or 2 minutes and if the workability of the concrete is not too high, whereas excessive vibration leads to preferential orientation of fibers together with segregation (Gettu et al., 2005).

According to experimental evidences, external vibration has a direct influence on fiber orientation along the gravity axis (η_y): the more FRC is vibrated, the more fibers tend to align in the horizontal plane, thus decreasing η_y . According to the probabilistic analysis advanced in Section 3, the latter will likely vary between 0.30 and 0.95. Although the qualitative effect of external vibration is indisputable, its quantification remains unknown. Consequently, it is required to investigate the influence of the energy, frequency and duration of vibration on fiber orientation of mixtures with different properties in the fresh-state and various fiber types. If the decrease in the y-axis could be quantified ($\Delta\eta_{DVy}$), $\Delta\eta_{DVx}$ and $\Delta\eta_{DVz}$ would compensate it in the same way, providing that constant η_{xyz} holds a reasonable assumption.

The effect of the flow

Fresh cementitious materials behave as fluids with a yield stress (τ_{00}), which is the minimum stress for irreversible deformation and flow to occur. This parameter controls whether or not concrete will start or stop flowing under an applied stress, thus being the most important property for the filling ability of SCC (Roussel, 2007). However, due to the thixotropic behavior of cementitious materials, there is an evolution of the rheological properties from the end of the mixing phase until casting and hardening occurs. In thixotropic materials, flocculation and deflocculation occur at rest and under flow, respectively. For fresh plain concrete the first one is far more important regarding that, on the aspects of major practical interest (formwork pressure and multi-layer casting), concrete is indeed not flowing (Roussel, 2007). Nonetheless, in the case of fresh FRC, fiber orientation tends to be the major concern and thereby the process of deflocculation may also play an important role.

When FRC flows along the formwork a certain flow profile develops, most likely due to frictional restraint with the walls of the formwork (Stälhi et al., 2008), and fibers align with the flow of fresh concrete (Grünewald, 2004; Lappa, 2007; Stälhi et al., 2008). This effect is stronger at higher flow velocity (Lappa, 2007) and therefore it may be associated to the material plastic viscosity and casting rate. Fiber alignment also increases with the time that fibers are submitted to the flow velocity, or indirectly, with the flow-distance (Grünewald, 2004; Ferrara et al., 2008; Stälhi et al., 2008). Thereby, the influence of flow is inherently related to the casting method and to the geometry of the element itself. Moreover, dependent on the height and width of the formwork, secondary flow may also develop in zones out of the influence of the walls of the formwork (Lappa, 2007; Stälhi et al., 2008).

Until now, in spite of the recent advances on the link between rheological properties and casting processes of plain concrete (Roussel, 2007), the specific influence of the flow on fiber alignment

remains unknown. Thereby, further research is required so that the increment of orientation number due to the flow ($\Delta\eta_{DF}$) can be incorporated in the present framework.

7.5.4 Influence of the formwork geometry

The effect of the mould sides and a free surface causes fibers to orient parallel to the wall or surface. The quantification of these wall-effects has only been reported in literature by assuming the absence of preferential fiber orientations in the zones out-of-influence of BCs. In this chapter an innovative approach was proposed to quantify the increment of orientation number due to wall-effects in the three independent axes and for any η in the bulk of a section. Thereby, similarly to the previous stages of this framework, the orientation number after passing walls of the formwork in any direction i (η_{Fi}) is obtained through an additive process by:

$$\eta_{Fi} = \eta_{Di} + \Delta\eta_{FWi} \quad (7.17)$$

Given that no further stages of the production process occur that influence fiber orientation, the latter also coincides with η in the hardened-state:

$$\eta_{\theta i} = \eta_{Fi} \quad (7.18)$$

Note that, due to the tendency towards planar fiber orientation of SCC, this material was idealized as having a fictitious horizontal BC equal to a fiber length. Thereby, η under the influence of one side of the formwork (η_1) corresponds to the actual value in the bulk of the cross-section (η_b) and the increment of η only accounts for the vertical sides of the mould.

7.5.5 Summary

The proposed framework implies a stepwise calculation of several production stages that play major influence on fiber orientation. The steps required to determine $\eta_{\theta i}$ are summarized in Table 7.3.

According to the sequential procedure shown in Table 7.3, $\eta_{\theta i}$ can be predicted by:

$$\eta_{\theta i} = \eta_{Mi} + \Delta\eta_{Ci} + \Delta\eta_{Di} + \Delta\eta_{FWi} \quad (7.19)$$

Or, alternatively, in its extended form:

$$\eta_{\theta i} = \eta_{Mi} + (\Delta\eta_{CWi} \times C_{Di}) + (\Delta\eta_{DVi} + \Delta\eta_{DFi}) + \Delta\eta_{FWi} \quad (7.20)$$

Table 7.3 - Summary of the steps required to apply the proposed framework

1. Fresh-state properties after mixing (η_{Mi})
1.1. Select the type of FRC (Table 7.1)
2. Casting method ($\Delta\eta_{Ci}$)
2.1. Identify casting direction (φ and β) and determine η_{C0} (Eq.7.9)
2.2. Calculate wall-effects induced by the casting element, $\Delta\eta_{CW}$ (Table A5.1)
2.3. Determine C_{Di} (Table 7.2)
2.4. Obtain $\Delta\eta_{Ci}$ (Eq.7.10)
3. Dynamic effects ($\Delta\eta_{Di}$)
3.1. Quantify the influence of external vibration, $\Delta\eta_{DVi}$
3.2. Quantify the influence of flow, $\Delta\eta_{DFi}$
4. Formwork geometry ($\Delta\eta_{FWi}$)
4.1. Determine wall-effects introduced by the formwork, $\Delta\eta_{FWi}$ (Table A5.1)
5. Final orientation number ($\eta_{\theta i}$) (Eq.7.20)

7.6 APPLICATION OF THE FRAMEWORK TO PRISMATIC BEAMS

7.6.1 Experimental data

Among the extensive experimental research that has been done on fiber orientation there is, unfortunately, a significant part of works that do not provide information on the specific production processes applied. Procedures such as direction of casting, characteristics of casting elements or energies of vibration are commonly omitted and, consequently, results of fiber orientation cannot be used to validate the present framework.

In this section, experimental results from three doctoral thesis carried out at Delft University of Technology are taken into account (Grünewald, 2004; Markovic, 2006; Schumacher, 2006). Fiber orientation was analyzed through the image analysis technique both on small and large-scale beams made of self-compacting steel fiber reinforced concrete (SCSFRC).

On the investigation carried out by Grünewald (2004), fourteen small beams were produced with various types of fibers. Casting was performed at middle-length of the beams using a shovel. The latter had a cross-section 60mm wide (B_C) and with lateral walls (H_C) of 30mm (Fig.7.11). Casting direction was 45° with respect both to the longitudinal and vertical axes of the beam (φ and β). Results from this work are herein defined as Cases 1-14.

Schumacher (2006) analyzed two large beams of reinforced concrete with steel fibers. Each of the beams was sawed at five different cross-sections along the longitudinal axis, thus providing a

total of ten independent results (Cases 15-24). Given the small amount of conventional reinforcement, the effect of the latter on fiber orientation was considered negligible. Casting of the beams was performed with a concrete trolley which, once touching one of the lateral sides of formwork, was lifted and rotated. This way, filling was done along with the vertical of the beam (y-axis). Given the geometry of the concrete trolley (large B_c comparatively to L), no preferential orientation due to the pouring element was considered.

The work performed by Markovic (2006) embraced the production of six prismatic beams, four of which were made of hybrid SCSFRC. The later combined both macro-and micro-fibers which, for the purpose of measuring fiber orientation, were independently analyzed. This way, ten results are herein considered (Cases 25-34). The same shovel used in the first work (Grünewald, 2004) was applied to cast the concrete. Nonetheless, the casting method was rather different: concrete was poured in layers with thicknesses (H_c) “couple of times smaller than the fiber length” (Grünewald, 2004) and the direction of casting coincided with the longitudinal axis of the beam (x-axis).

Further details of the experimental data are listed in Appendix 6.2. Note that, in all Cases considered, step 3 of the proposed framework is omitted regarding that no external vibration occurred and that flow-distance was assumed to be negligible.

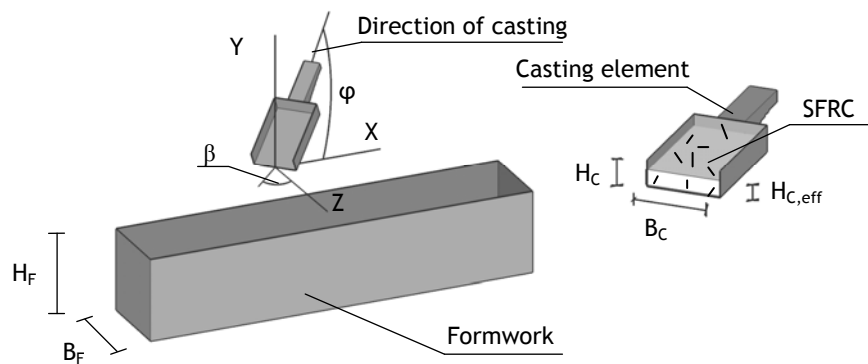


Fig.7.11 -Schematic representation of the main input parameters.

7.6.2 Applying the framework: step-by-step

For clarity, the proposed framework is applied hereafter in detail for Case 10 (Table 7.4). The main steps defined in Table 7.3 are followed to calculate the orientation number of the fibers along the longitudinal axis (x-direction). Detailed results of all the other cases considered are listed in Appendix 6.3.

Table 7.4 - Example of the application of the proposed framework (Case 10).

Main steps	Expression	Application	Result
1	Table 7.1	Self-compacting concrete	$\eta_{Mx} = \eta_{Mz} = 0.60$; $\eta_{My} = 0.30$
2.1	Eq.7.9	η_{Mx} ; η_{My} ; η_{Mz} ; $B = 45^\circ$; $\varphi = 45^\circ$	$\eta_{C0} = 0.474$
2.2	Table A5.1	$B_C = 60.0\text{mm}$; $H_{C,eff} = L = 41.2\text{mm}$; $\eta_0 = \eta_{C0}$	$\Delta\eta_{CW} = 0.286$
2.3	Table 7.2	B ; φ ; B_C ; $H_{C,eff}$	$C_{Dx} = 0.296$
2.4	Eq.7.10	$\Delta\eta_{CW}$; C_{Dx}	$\Delta\eta_{Cx} = 0.085$
3	Eq.7.16	(Not applicable)	$\Delta\eta_{Dx} = 0.0$
4	Table A5.1	$B_F = 150.0\text{mm}$; $L = 41.2\text{mm}$; $\eta_0 = \eta_{Dx} = 0.685$	$\Delta\eta_{FWx} = 0.049$
5	Eq.7.20	η_{Mx} ; $\Delta\eta_{Cx}$; $\Delta\eta_{Dx}$; $\Delta\eta_{FWx}$	$\eta_{\theta x} = 0.734$

7.6.3 Overall results

The comparisons between experimental and predicted orientation numbers in the hardened-state (η_θ) for the 34 cases considered are summarized in Fig.7.12 (detailed values are presented by Appendix 6.3). Fig.7.12 shows that the proposed framework is able to provide good predictions of the average fiber orientation for a large number of cases, irrespectively of fiber geometry, casting method and formwork geometry. It should be noticed that, in spite of the complexity involved on predicting fiber orientation through such a rational approach, the deviations between predicted and experimental η are not significant. As a matter of fact, the average deviation of the 34 cases was only -3.1%. The maximum absolute deviation was limited to 13.4% and the average absolute deviation of all cases was 5.3% (Appendix 6.3).

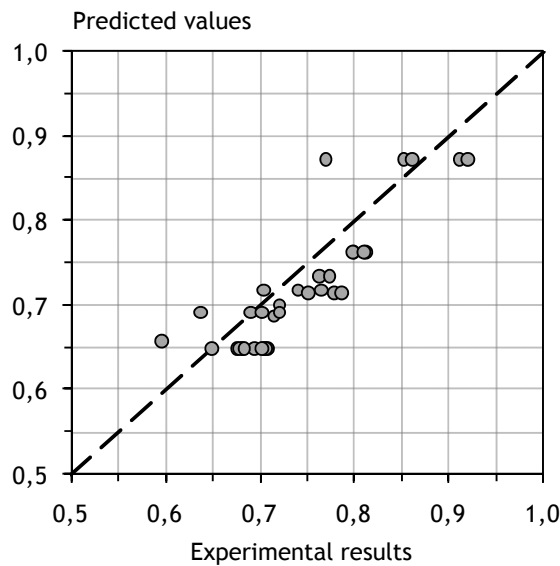


Fig.7.12 - Overall predictions for the orientation number in the hardened-state (η_θ).

7.7 CONCLUDING REMARKS

This chapter proposes an ambitious framework aiming to establish a link between fiber orientation and the properties of FRC, the structure to be built and its respective production process. In the first part, the motivations for this investigation were highlighted and the core concepts of this novel framework were advanced. In a second part, two major subjects that are unsolved up to the present were analyzed and approached from a theoretical perspective (fiber orientation in 3-D and the wall-effects in anisotropic conditions). Finally, in the last part, the proposed framework was explained in detail and validated with several results from literature.

The need of integrating material characteristics, production processes and the structure itself within a unique framework has never been as recognized as it is in the present. With this chapter, a first attempt to combine all these aspects within a comprehensive, straightforward and intuitive approach has been proposed. It has to be noted that, regarding the complexity of the subject, there are some aspects that still require further investigation in order to create a robust and general engineering toolbox to predict fiber orientation. Nonetheless, predictions provided by this framework are very promising and support the proposed approach as a breakthrough advance on the field of fiber reinforced concretes.

Chapter 8

New constitutive model

8.1 INTRODUCTION

In the previous chapters of this thesis, the single fiber pullout responses and the orientation of steel fibers were predicted with very reasonable agreements. The relevance of these studies would be significantly increased if their results could be applied to explain and characterize the tensile behavior of SFRC.

The chapter aims at describing, validating and discussing a direct approach to predict the post-cracking response of SFRC. It contains six core sections: First, the main conceptual basis and strategy of this approach are presented. Then, the analytical formulation of the model is described. Based on Parts III and IV, the individual performances of fibers are combined with their respective orientations through an additive approach. Afterwards, the new constitutive model is validated with the experimental uniaxial tensile test results reported in Part II. Insight on the most relevant parameters affecting the tensile response of SFRC can then be achieved through a parametric study. Subsequently, simplified analytical expressions are suggested in order to provide a more convenient tool for design and optimization purposes. The chapter ends with a practical example for the definition of the new constitutive model.

8.2 PHILOSOPHY OF THE APPROACH

8.2.1 Conceptual basis

According to what was mentioned in Chapter 1, the lack of knowledge on characterizing appropriately the tensile behavior of SFRC significantly hinders the quantity and diversity of its applications due to technical and economical reasons. Among engineers and structural designers, relevant and common sense questions are commonly raised: Are steel fibers able to bear tensile stresses the way conventional steel rebars do? If so, what is their relative efficiency? Can they somehow substitute conventional steel reinforcement?

More than providing the answers to these questions, one may focus as well on molding these same answers to the perspective of the recipient. In fact, great theories can only be classified as such if their implications can be perceived! Consequently, simple, intuitive and logical concepts should be used to support them.

The post-cracking strength of SFRC in uniaxial tension is, typically, much lower than the one provided by the same concrete matrix reinforced with the same amount of steel in the format of conventional rebars. Two main reasons may justify this relatively limited performance:

- The orientation of fibers with regard to the direction of tensile stresses. Steel rebars have always very high efficiency, provided that they are placed along with the direction of tensile stresses and have sufficient anchorage length. On the other side, the anchorage lengths of fibers are very small and their orientation is, typically, misaligned with respect to the direction of loading. According to Part III of this thesis, the strengthening contributions of fibers in such conditions may be significantly smaller.
- Different bond properties between fibers and the surrounding matrix. Given that the geometry of fibers is very different from the one of steel rebars, their pullout mechanisms turn out to be particularly complex and dissimilar.

From a conceptual point of view, steel fibers may be regarded as equivalent to a conventional steel rebar with smaller efficiency. In other words, the pullout response of all the steel fibers in a cracked section may be analogous to the one of a steel rebar with an inefficient orientation and weaker bond strength (Fig.8.1).

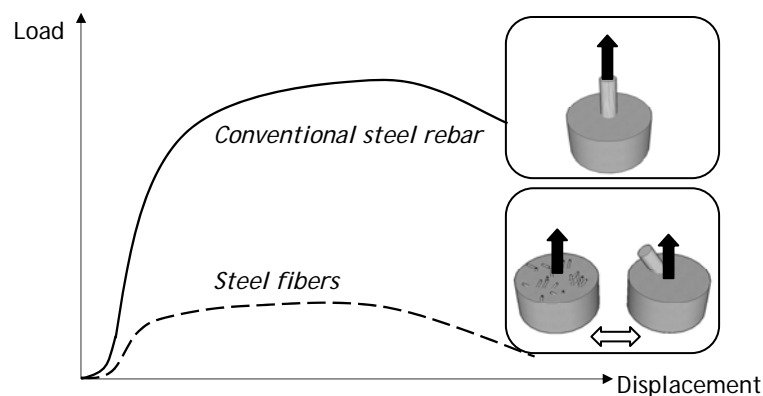


Fig.8.1 - Schematic analogy between conventional steel rebars and steel fibers.

Regarding the resemblance between steel fibers and conventional steel rebars, the tensile behavior of SFRC can be defined in terms of three main physical concepts:

1. Plain concrete
2. Equivalent steel rebar
3. Specific bond strength

Similarly to concrete with conventional reinforcement, the tensile behavior of SFRC is equivalent to the one exhibited by plain concrete during the uncracked range. At this stage there is no influence of the steel reinforcement in the matrix. However, once in the post-cracking range, plain concrete exhibits a softening behavior and the load-carrying capacity is gradually transferred to the steel elements (Fig.8.2). In case of SFRC, the latter are activated through the deflection of the major crack into smaller interfacial cracks along the fiber/matrix interface. During crack growth and under a scenario of perfect bond conditions, the strengthening contribution of all the fibers in the cross-section would be equal to the one of a steel rebar, increasing progressively until its tensile yield strength is achieved (Fig.8.2). However, in most of the situations fibers are pulled out from the cement matrix and, consequently, a specific bond strength law has to be considered to account for the pullout behavior of steel fibers (Fig.8.2).

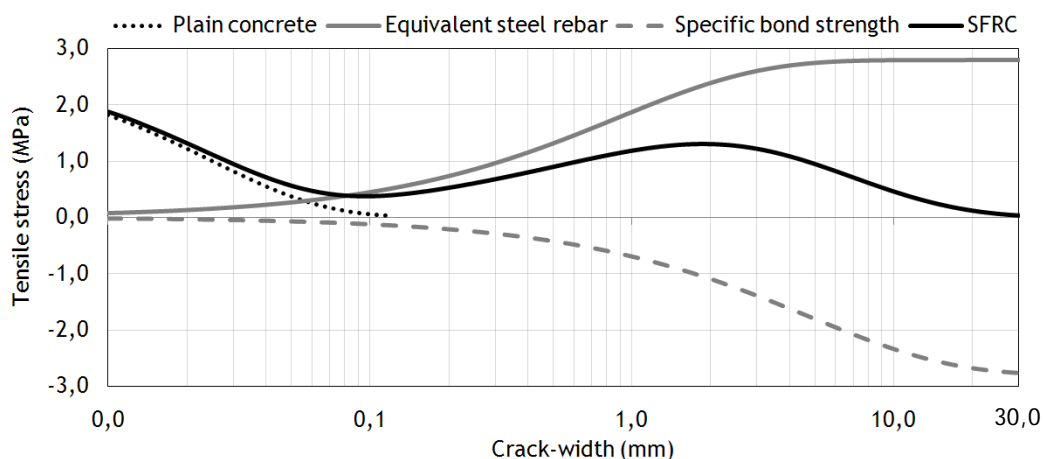


Fig.8.2 - Identification of the three physical concepts on the tensile response of SFRC.

8.2.2 Strategy

In this model SFRC is approached as a concrete with conventional steel reinforcement which has some particular characteristics. This is, undoubtedly, a relevant comparison that provides logical reasoning to this approach. However, according to the predefined demands, it is also necessary to guarantee that this constitutive model is based on physical concepts that can be gathered into a straightforward procedure.

In Chapter 2, a brief review of the existing constitutive models in literature was presented. Most of the approaches advanced up to the present, including European and National standards, are based on inverse analysis procedures. These approaches share the disadvantage of requiring

significant experimental characterization, thus turning the design of SFRC a tedious and inoperative practice. Furthermore, since they imply the pre-definition of a shape for the SFRC constitutive model, it is hard to gain insight on the actual mechanisms governing the tensile behavior.

To overcome the drawbacks of existing approaches the new constitutive model should follow the philosophy that resembles in larger degree the current practice of concrete with conventional reinforcement. For that purpose, this new constitutive model follows a direct approach. In other words, this means that an engineer may be able to define the stress-crack width relationship of SFRC based uniquely on physical input parameters with no need of performing inverse, fitting or iterative analyses.

The previous conceptual basis showed that the tensile behavior of SFRC can be assimilated to the one of concrete with conventional reinforcement in terms of three main physical concepts. By adding together the post-cracking strength from the plain concrete and steel fibers with a specific bond strength relationship, the entire tensile response can be captured. This way, the constitutive model of SFRC will be divided in two main contributions: (1) Plain concrete post-cracking strength; (2) Overall steel fiber pullout strength.

8.3 FORMULATION

In this constitutive model, the tensile stress sustained by steel fiber reinforced concrete as a function of the crack width, $\sigma_{\text{SFRC}}(w)$, will be obtained by assembling the stress exhibited by the respective plain concrete in tension, $\sigma_{\text{C}}(w)$, and the tensile stress provided by all the steel fibers in the cracked section, $\sigma_{\text{SF}}(w)$, according to Eq.8.1.

$$\sigma_{\text{SFRC}}(w) = \sigma_{\text{C}}(w) + \sigma_{\text{SF}}(w) \quad (8.1)$$

8.3.1 Plain concrete

Investigation on the tensile response of plain concrete was extensively carried out during last decades. However, in the present, this subject is no longer a matter of relevant discussion among researchers regarding that the behavior of plain concrete has been successfully characterized through experiments and modeling.

Plain concrete under tensile stresses exhibits an approximated linear response until a major crack is generated. Then, the material follows a softening behavior which resembles the one observed in compression tests. For design purposes, the post-cracking resistance of plain concrete is often not critical and, consequently, ignoring this strength mechanism is a reasonable assumption. However, neglecting the softening branch is not an acceptable approximation when crack widths or bond transfer mechanisms have to be predicted in concrete with conventional reinforcement. Consequently, the post-cracking strength of plain concrete has also to be taken into account to predict the σ - w relationship of SFRC.

Among the several works reported in literature, this constitutive model considers the analytical formulation advanced by Gopalaratnam and Shah (1985) to define $\sigma_c(w)$. The expression proposed by these authors (Eq.8.2) is uniquely defined by the maximum tensile strength of plain concrete (f_{ctm}) and by a constant value k which is approximately equal to 39.8mm^{-1} .

$$\sigma_c(w) = f_{ctm} \times e^{-kw} \quad (8.2)$$

Regarding that concretes are commonly classified in terms of their characteristic compressive strengths (f_{ck}) or average compressive strengths (f_{cm}), the expressions included in the Model Code (ENV 1992-1-1) may be used when f_{ctm} is not known in advance (Eq.8.3). With Eqs.8.2-8.3 the softening branch of plain concretes can be obtained for any case (Fig.8.3).

$$f_{ctm} = \begin{cases} 0.3 \times f_{ck}^{\frac{2}{3}} & \text{if } 12 \leq f_{ck} \leq 50 \text{ MPa} \\ 2.12 \times \ln\left(1 + \frac{(f_{ck} + 8)}{10}\right) & \text{if } 50 < f_{ck} \leq 90 \text{ MPa} \end{cases} \quad (8.3)$$

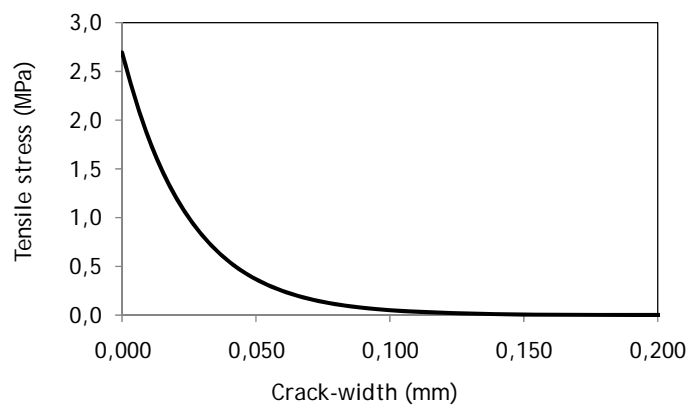


Fig.8.3 - Post-cracking response of a plain concrete with f_{ck} equal to 30MPa.

8.3.2 Steel fibers

The tensile stress provided by all the steel fibers in the cracked section (σ_{sf}) depends on a large variety of parameters and material properties. Three fundamental aspects govern this strengthening contribution:

- Number of fibers
- Orientation of fibers
- Pullout responses of fibers

It has been shown by several researchers (Krenchel, 1975; Dupont and Vandewalle, 2005) that the total number of fibers in a cross-section (N_f) can be approximated as follows:

$$N_f = \frac{A_{\text{sec}}}{A_f} \times V_f \times \eta_\theta \quad (8.4)$$

where A_{sec} is the SFRC cross-sectional area (mm^2), A_f is the fiber cross-sectional area (mm^2), V_f is volume fraction of fibers (%) and η_θ is the orientation number.

The pullout responses and the orientation of fibers were addressed in Parts III and IV of this thesis, respectively. Regarding that the fiber pullout responses were found to be significantly different depending on their inclination angles, it was concluded that a detailed investigation on the distribution of fiber orientation angles was required.

The characterization of the orientation profile of SFRC was performed in Chapter 6. Several statistical analyses were carried out in that study to evaluate the suitability of different statistical laws on describing the distribution of orientation angles measured experimentally. For analysis purposes, the data was grouped into a number i of discrete intervals defined as follows:

$$i = \frac{90}{\Delta\theta} \quad (8.5)$$

where $\Delta\theta$ is the amplitude of each interval in degrees. From the several analyses carried out it was concluded that the orientation profiles can be reasonably approximated by making use of $\Delta\theta$ up to 15° . Regarding that larger values of $\Delta\theta$ make the subsequent calculations easier to perform, this will be the value adopted for this constitutive model.

In Chapter 6 it was concluded that the frequency of occurrence of fiber orientation angles follows a Gaussian distribution. Moreover, it was also observed that the dispersion of the orientation angles is related with the average orientation of fibers. The frequency of occurrence of the orientation angles can then be predicted by taking as unique input parameter the orientation number (η_θ). Fig.8.4 shows the values of the orientation profile under isotropic conditions ($\eta_\theta=0.50$) on the basis of the six class marks (θ_i) defined by $\Delta\theta$ equal to 15° (7.5° ; 22.5° ; 37.5° ; 52.5° ; 67.5° ; 82.5°).

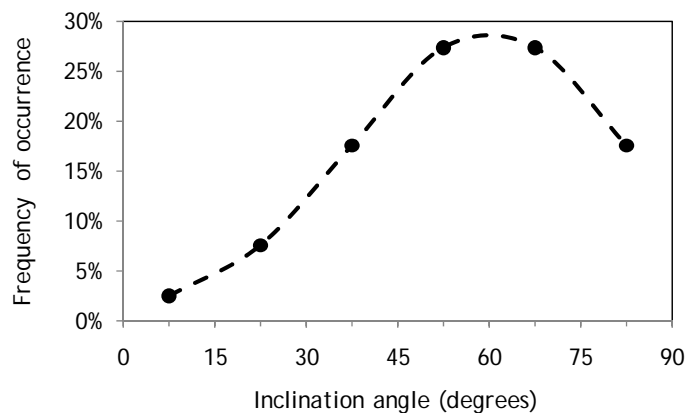


Fig.8.4 - Orientation profile of fibers under isotropic conditions.

From the previous it becomes obvious that, if η_θ could be somehow predicted, both the total number of fibers in a cross-section (N_f) and their respective orientation profile would be known. Because these are crucial parameters for the tensile behavior of SFRC, an innovative framework to predict the orientation number was advanced in Chapter 7.

Although the orientation of fibers is assumed to be of stochastic nature, it is of common-sense that depending on the fresh-state properties of concrete, the narrowness of the formwork, the casting procedure, among others... fibers may assume preferential alignments within the concrete. The work presented in Chapter 7 introduces a breakthrough philosophy due to the integration of materials, structure and production processes within a unique approach. Although further research is required to evaluate and/or corroborate some of its newest concepts, the framework proposed may be useful to predict appropriate orientation numbers rather than adopting the common and erroneous assumption of isotropy, i.e., that fibers are homogeneously oriented in all directions.

By assuming the average orientation of fibers in terms of the proposed framework, engineers would be performing the so-called integrated structural and material design (Li, 2007). This way, structures and materials could be linked together to pursue optimum performance-based structural designs. Although this concept is quite new respect to current procedures used on the design of concrete structures with conventional reinforcement, the importance of this new philosophy has been increasingly pointed out with the innovations on concrete technology that are currently taking place. Thereby, a suitable constitutive model for SFRC is not an outcome exclusive of concrete and fiber properties, but rather a characterization of the composite material which accounts as well for specific features of the production processes and the structure itself.

With an appropriate orientation number (η_θ) of the cross-section under analysis, the total number of fibers (N_f) and their respective orientation profile become known. Thereby, the number of fibers that have inclination angles within each of the intervals previously defined (N_{θ_i}) can be obtained (Eq.8.6):

$$N_{\theta_i} = P(\theta_i) \times N_f \quad (8.6)$$

The shape of the fibers is commonly assumed not to play a major influence on their distribution and orientation. Consequently, N_{θ_i} may be independent of the shape of steel fibers used. However, the load-crack width relationship provided by the respective amount of fibers ($P_{N,\theta_i}(w)$) does differ significantly with the geometry of the fiber.

Chapters 4 and 5 provided approaches to predict the pullout responses of straight and hooked fibers, respectively. Among the several material properties that influence the pullout behavior, two major boundary conditions are required to predict the pullout responses: (1) inclination angle; (2) fiber embedded length.

The influence of the inclination angles was extensively discussed in the proposed predictive pullout models. Fig.8.5 shows an example of such influence on hooked steel fibers with 2100MPa

tensile yield strength and a concrete matrix with f_{ck} of 30MPa. The remaining input parameters required to calculate Fig.8.5 are in accordance with the values presented in Section 5.5.2 for fibers with 20mm embedded length.

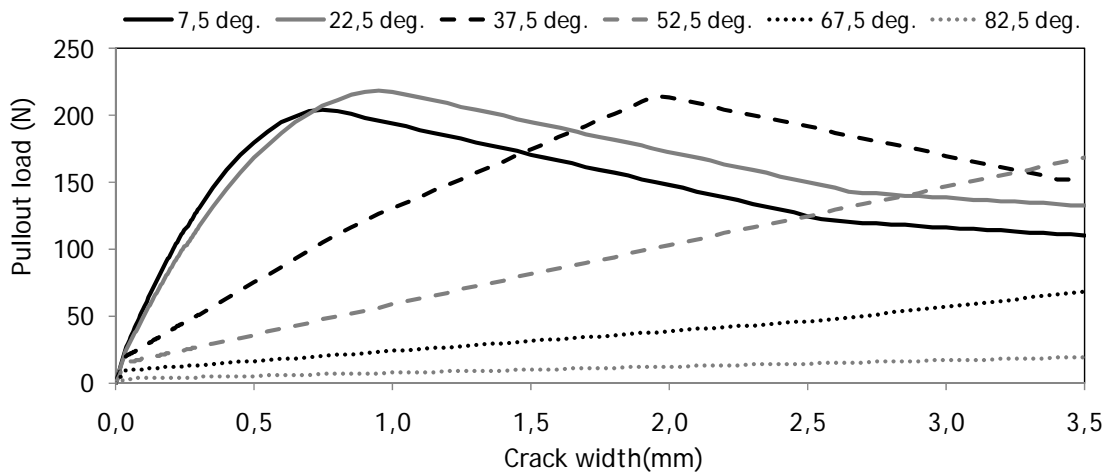


Fig.8.5 - Example of single fiber pullout responses of hooked fibers at different inclination angles.

The second major aspect required to calculate the strengthening contribution provided fibers is their embedded length. Fibers tend to be pulled out from the matrix at the side of the crack which has weaker bond strength. In such side, the embedded length of the fiber (L_e) may vary from zero up to a maximum length ($L_{e,max}$). Consequently, an average embedded length between these two extreme situations ($L_{e,average}$) may be considered to account for the pullout responses of all fibers in the constitutive model.

$L_{e,max}$ depends on the bond-strength mechanisms existing along the fiber/matrix interface. In the case of straight fibers, the latter are mainly dependent on the embedded length available to develop adhesion and friction processes. Therefore, fiber pullout tends to occur at the side of the crack having smaller embedded length and, consequently, $L_{e,max}$ may be equal to half the fiber length ($L/2$).

The major resisting mechanism occurring in hooked fibers is the mechanical anchorage provided by the hooked-ends. Provided that a critical embedded length for the straightening process of the hook is guaranteed, the pullout response of aligned fibers with different embedded lengths is very similar up to several millimeters (Robins et al., 2002). Consequently, fiber may be pulled out either from the side of the crack having a critical length ($L_{e,crit}$) or from the side having a maximum embedded length (equal to the total fiber length discounted by $L_{e,crit}$). According to results from literature (Robins et al., 2002), while embedded lengths of 5mm are not enough for the development of the straightening process of the hook, 10mm have proven to be a sufficient length for the occurrence of this phenomenon. In order to account for these evidences, a value of 7.5mm for $L_{e,crit}$ will be considered in this study. This is an important aspect which may play significant influence when hooked fibers with short lengths are applied.

A summary of the maximum embedded lengths ($L_{e,max}$) and the associated average values ($L_{e,average}$) considered in this constitutive model is provided in Table 8.1 for convenience.

Table 8.1 - Maximum and average fiber embedded lengths.

Geometry of the fiber	$L_{e,max}$	$L_{e,average}$
	[mm]	[mm]
Straight	$\frac{L}{2}$	$\frac{L}{4}$
Hooked	$L - 7.5$	$\frac{L - 7.5}{2}$

Regarding a given interval of inclination angles (θ_i), the number of fibers under such conditions (N_{θ_i}) and the respective single fiber pullout responses ($P_{\theta_i}(w)$) calculated with $L_{e,average}$, the contribution of these fibers to the total load-crack width response of the cross-section ($P_{N,\theta_i}(w)$) is given as follows:

$$P_{N,\theta_i} = P_{\theta_i} \times N_{\theta_i} \tag{8.7}$$

By applying Eq.8.7 to the values previously shown in Fig.8.4 and Fig.8.5 and assuming a cross-section in bulk with 150mm×150mm, fibers with 0.50mm diameter under isotropic conditions ($\eta_{\theta}=0.50$) and fiber content of 30.0kg/m³ ($N_f \approx 219$), the six $P_{N,\theta_i}(w)$ can be extracted (Fig.8.6).

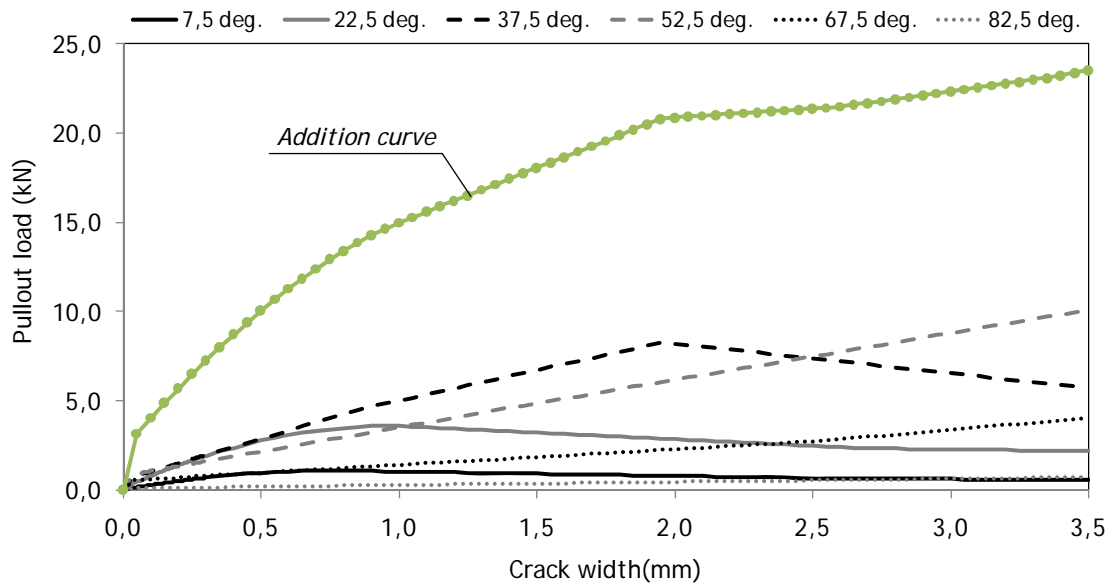


Fig.8.6 - Example of different contributions of pullout responses and curve resulting from their addition.

Once the contributions for the load-crack width relationship are known (Fig.8.6), the σ - w constitutive model for the SFRC can be extracted (Eq.8.8 and Fig.8.7).

$$\sigma_{SF}(w) = \frac{\sum P_{N,\theta_i}(w)}{A_{sec}} \tag{8.8}$$

which, based on $\Delta\theta=15^\circ$, accounts uniquely for six different contributions:

$$\sigma_{SF}(w) = \frac{P_{N,7.5}(w) + P_{N,22.5}(w) + P_{N,37.5}(w) + P_{N,52.5}(w) + P_{N,67.5}(w) + P_{N,82.5}(w)}{A_{sec}} \quad (8.9)$$

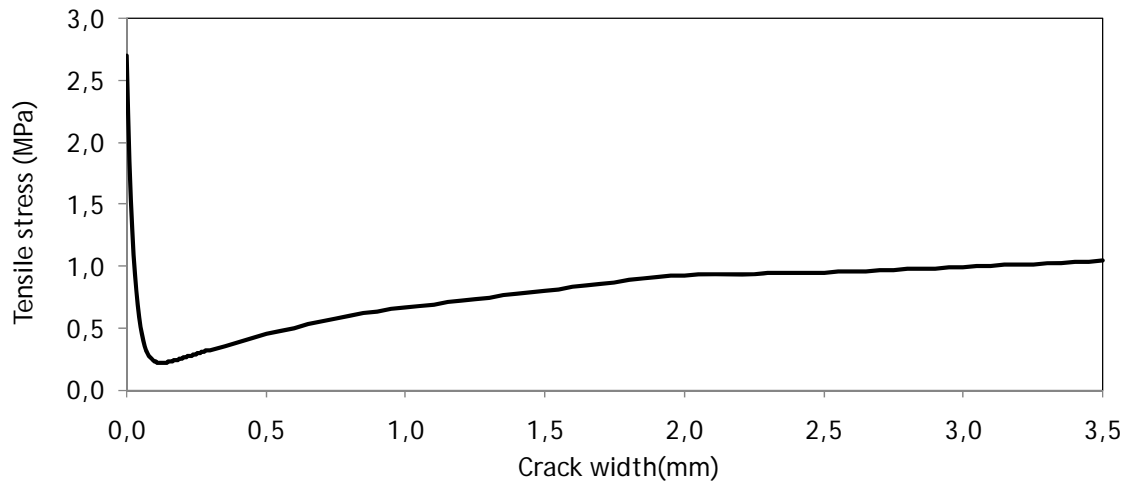


Fig. 8.7 - Example of constitutive model for hooked fibers under isotropic conditions.

8.3.3 Overview of the new constitutive model

The formulation previously described emphasizes the practical interest of Parts III and IV of this thesis on the definition of the new constitutive model. Thereby, it is worth to provide a general overview on how the foregoing expressions can be connected with the outputs extracted from Chapters 4, 5, 6 and 7 (Fig.8.8).

In Fig.8.8, it can be seen that the proposed constitutive model accomplishes what it was aimed for: provides a comprehensive theory within a straightforward procedure (by means of physical input parameters).

Note that the intrinsic bond strength between fibers and concrete cannot be generalized due to the innumerable possibilities of concrete compositions and types of steel fibers existing in the market. Nonetheless, apart from the experimental data obtained in the pullout tests of fibers aligned with the load direction, the proposed model only accounts for material properties such as the ones used in the design of concrete with conventional reinforcement.

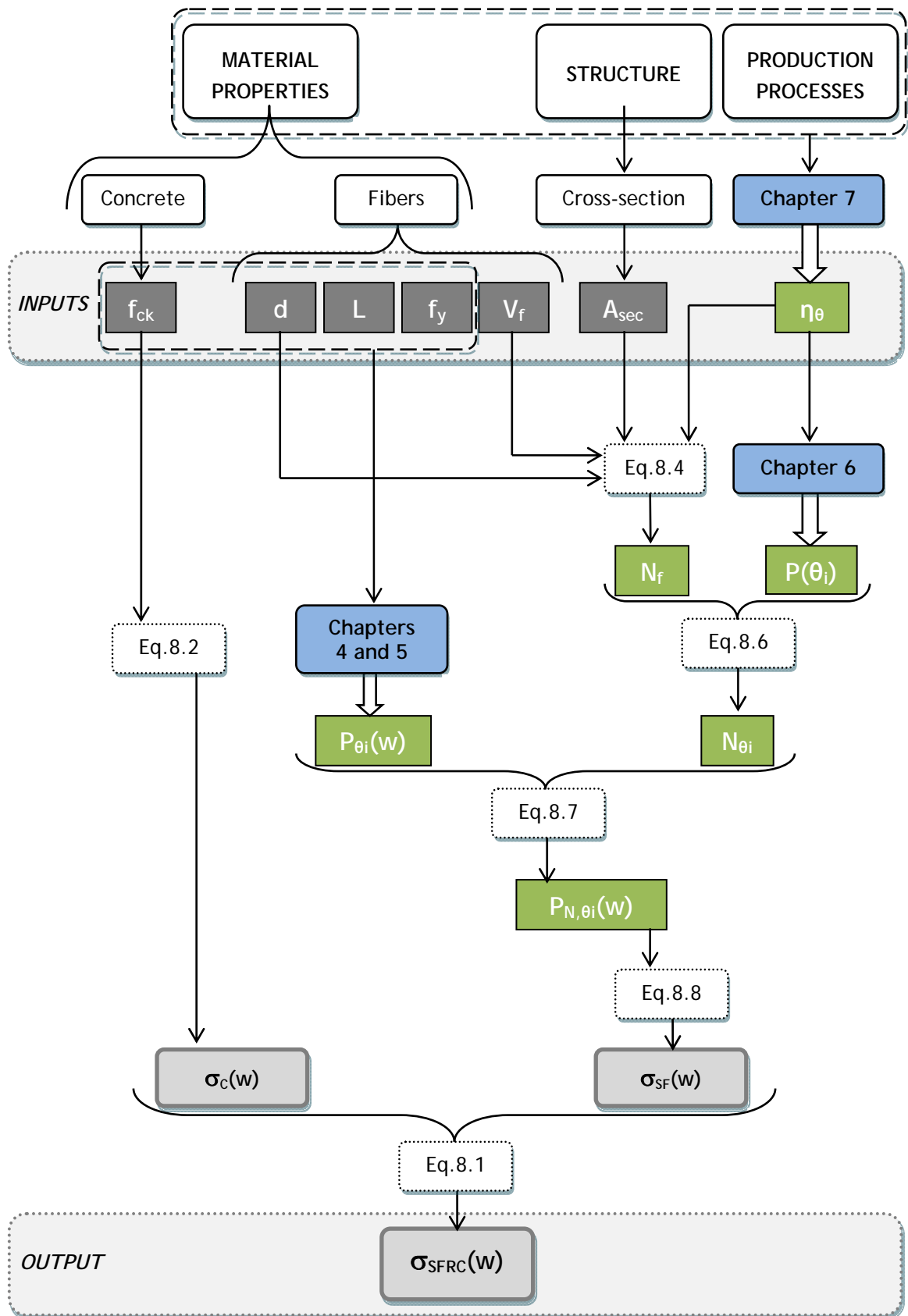


Fig. 8.8 - Strategy and formulation of the new constitutive model.

8.4 EXPERIMENTAL VALIDATION

The comparison between theory and experiments is a paramount requirement when proposing an innovative approach such as the one herein presented. In the following, the uniaxial tensile test results reported in Chapter 3 will be used to evaluate the suitability of the new constitutive model on describing the tensile behavior of SFRC. Regarding that the proposed approach intends to be used for design purposes, the range of crack widths covered should be in accordance with the ones measured in experiments. Thereby, the analysis of this model will be limited to crack widths up to 3.5mm as this refers to the maximum value measured on beam-bending tests, the experimental procedure in which existing guidelines and European standards are based in.

8.4.1 Identification of input parameters

In order to evaluate the capabilities of the model on reproducing the tensile responses shown in Chapter 3 it is necessary to obtain data from the plain concrete behavior and from the three fundamental aspects governing the contribution provided by steel fibers (number of fibers at the cracked section, their respective orientation and pullout responses). A brief explanation on how these inputs were defined is described in the following.

Plain concrete

According to what was discussed in Chapter 3, although uniaxial tensile tests provide reliable data on the post-cracking range of SFRC, this testing procedure is not the most indicated one to evaluate the tensile behavior of plain concrete. Consequently, the values of tensile strengths to be applied in Eq.8.2 will be the ones observed in the experimental results ($f_{ctm,A}=2.7$ MPa; $f_{ctm,B}=2.6$ MPa) in order to guarantee a reasonable reproduction of the post-cracking behavior.

Number of fibers

Predictions of the tensile behavior are based on the average number of fibers counted at the cracked sections of all the specimens that were considered for the average results. The total number of fibers (N_f) accounts for the two sides of the specimen after testing. This procedure was feasible regarding the small dimension of the cracked section and the geometry and content of the steel fibers used, such as illustrated in Fig.8.9.



Fig.8.9 - Counting of fibers at one side of the cracked section: a) 20 kg/m³; b) 40 kg/m³; c) 60 kg/m³.

Orientation of fibers

The framework presented in Chapter 7 was developed after the experimental work (Chapter 3) and, consequently, the production processes associated to the manufacturing of the specimens were not registered consistently. Alternatively, given that the number of fibers at the cracked sections was known, Eq.8.4 was used to provide approximations of the orientation numbers (η_{θ}). Then, based on these values, the orientation profiles were calculated according to the procedures described in Chapter 6.

Pullout responses of fibers

In order to apply the model to predict the pullout responses of inclined hooked steel fibers presented in Chapter 5, experimental data of the load crack width relationships of those fibers aligned with the load direction is required. This procedure is, for the reasons aforementioned, an irrevocable need of any rationale constitutive model. However, regarding that such requisite could limit the general application of this approach, an alternative option was investigated.

With the purpose of having a first order of magnitude for the key-points of the pullout responses of aligned fibers, a literature survey on experimental pullout test results of straight and hooked steel fibers was carried out (Appendix 7). Based on the compiled experimental data, Appendix 7 proposes simplified expressions to approximate the fundamental key-points of the pullout diagrams of aligned fibers. This way, provided that properties of steel fibers and concrete matrix do not differ substantially from the ones collected in Appendix 7, a first draft of the constitutive model can be traced.

According to the simplified version of the pullout model presented in Chapter 5, the post-peak branch of the pullout response of aligned fibers was approximated by a linear interpolation. This way, only the key-points S_{01} , H_{01} and H_{04} are required to characterize the bond-strength between aligned hooked fibers and the matrix.

The experimental characterization of the pullout response of aligned fibers used to validate this constitutive model was performed by Blázquez (2009). The fibers and matrix compositions applied in his work were the same as the ones used in the experimental campaign described in Chapter 3.

The crack-widths of the key-points were defined according to the main stages of the straightening process of the hooked-end defined in Fig.5.2. The respective pullout loads at key-points H_{01} and H_{04} were reported by Blázquez (2009) from a serie of pullout tests whose matrix was characterized through an average compressive strength of 53.5 MPa. No experimental data of the pullout response of straight fibers embedded in matrices with similar compressive strength were available. Consequently, an order of magnitude for P_{S01} was obtained through the expression suggested in Appendix 7.2 (Eq.A7.1).

Table 8.2 - Summary of the input values used to calculate the contribution provided by the steel fibers.

			Series					
			A20	A40	A60	B20	B40	B60
Fiber diameter	d	[mm]	0.75					
Fiber length	L	[mm]	60.0					
Fiber tensile yield strength	f_y	[MPa]	2000					
Average matrix compressive strength	f_{cm}	[MPa]	50.5		74.8			
Crack-width at key-point S_{01}	w_{S01}	[mm]	0.10					
Pullout load at key-point S_{01}	P_{S01}	[N]	146.0					
Crack-width at key-point H_{01}	w_{H01}	[mm]	0.60					
Pullout load at key-point H_{01}	P_{H01}	[N]	406.0					
Crack-width at key-point H_{04}	w_{H04}	[mm]	4.85					
Pullout load at key-point H_{04}	P_{H04}	[N]	241.0					
Number of fibers at cracked section	N_f	[-]	32	57	95	26	55	52
Area of the cracked section	A_{sec}	[mm ²]	11310					
Volume fraction of fibers	V_f	[%]	0.255	0.510	0.764	0.255	0.510	0.764
Orientation number	η_θ	[-]	0.491	0.437	0.486	0.399	0.422	0.266
Average fiber embedded lengths	$L_{e,average}$	[mm]	26.25					

Other parameters of interest:

$$\varepsilon_u = 35\% / E_f = 200Gpa / \mu = 0.60 / N = 2 / \Delta\theta = 15^\circ / L_{e,crit} = 7.5mm$$

8.4.2 Results and discussion

Chapter 3 discussed the influences of the fiber volume fraction and concrete strength on the average stress-crack width responses. Additional data from testing of each specimen was also provided in Appendix 1. In this section, those experimental results are now used to evaluate the suitability of the proposed constitutive model on describing appropriately the tensile behavior of SFRC. For the sake of clarity, the comparisons presented in the following (Fig.8.10 up to Fig.8.15) are based on the average experimental responses. The ranges of experimental values are also included in order to provide a magnitude of scattering on results.

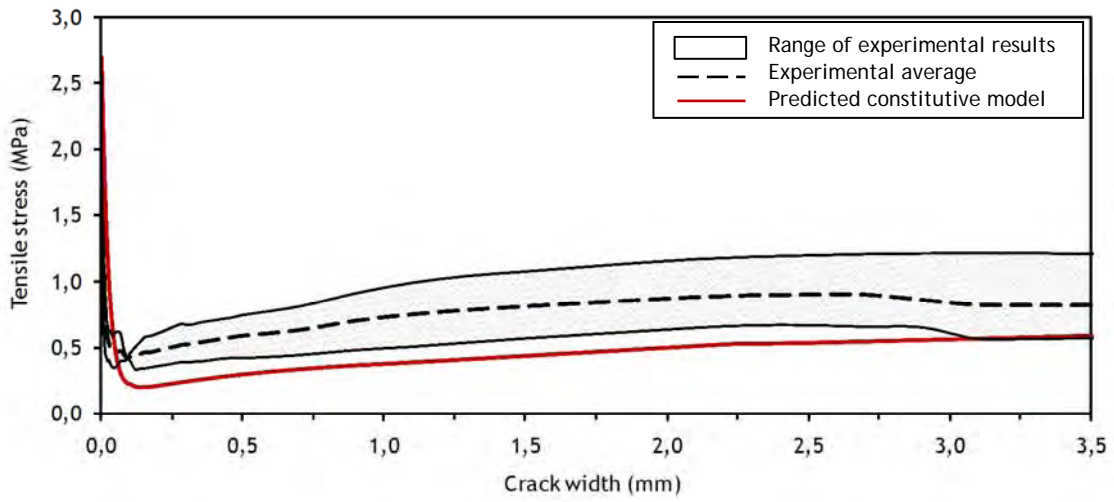


Fig.8.10 - Comparison of experimental and predicted σ -w curves for serie A20.

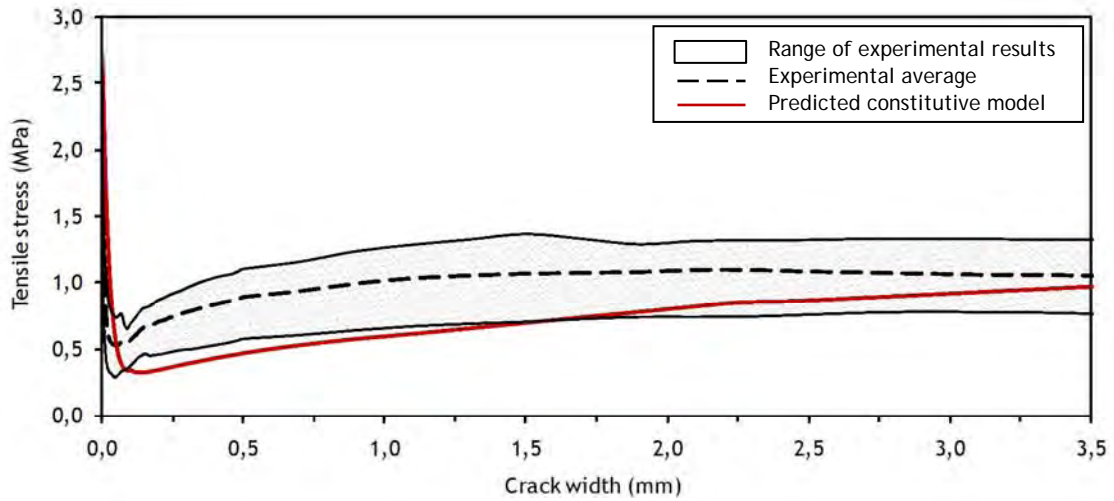


Fig.8.11 - Comparison of experimental and predicted σ -w curves for serie A40.

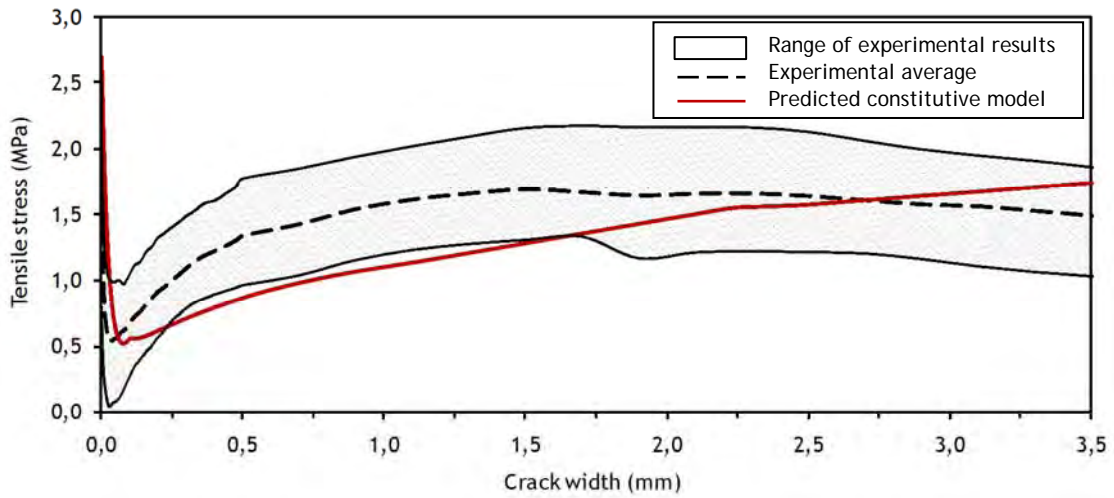


Fig.8.12 - Comparison of experimental and predicted σ -w curves for serie A60.

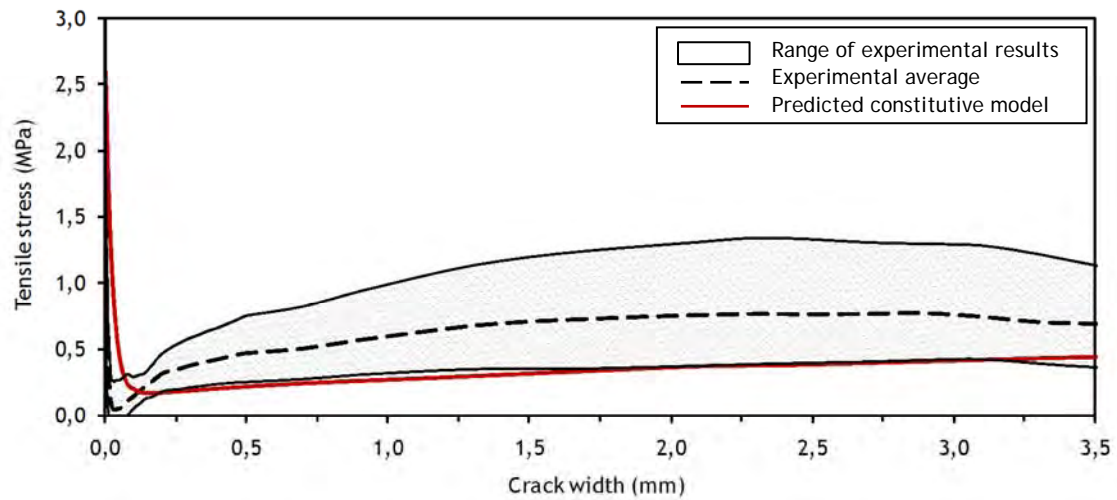


Fig. 8.13 - Comparison of experimental and predicted σ - w curves for serie B20.

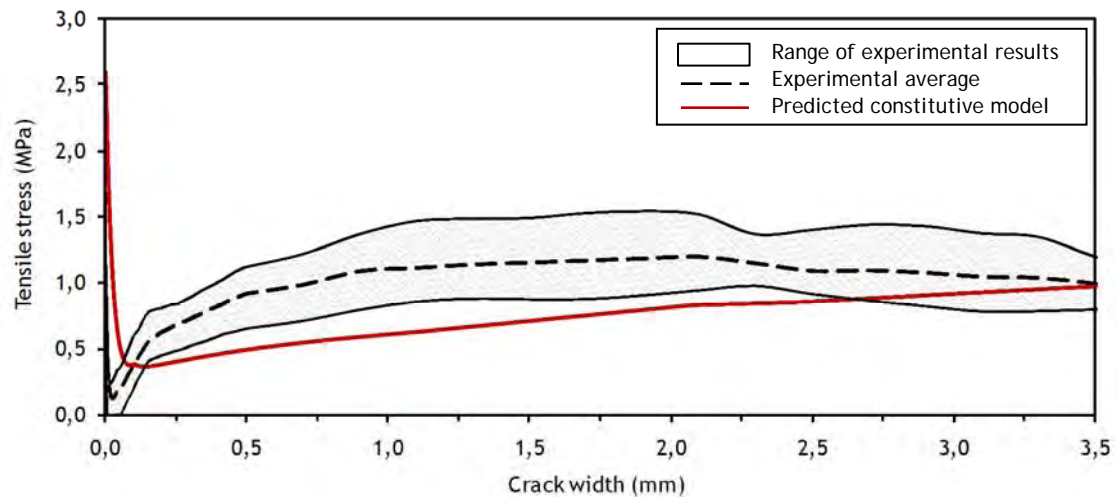


Fig. 8.14 - Comparison of experimental and predicted σ - w curves for serie B40.

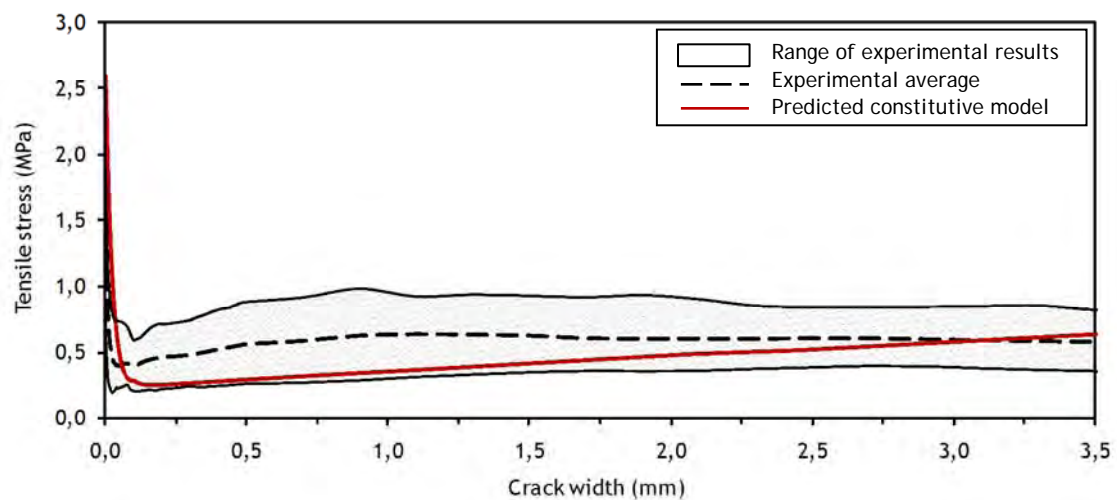


Fig. 8.15 - Comparison of experimental and predicted σ - w curves for serie B60.

Through the observation of Fig.8.9 up to Fig.8.15 it is possible to conclude that the new constitutive model herein proposed is capable of predicting the stress-crack width relationship of SFRC with hooked ends with reasonable agreement, at least for the fiber volume fractions and matrix strengths considered.

When comparing the average experimental curves with the predicted ones it is noticeable an underestimation of the model for small crack widths and a tendency for convergence of the stress values for larger crack widths. The reason for the uneven agreement along the crack width range may be due to the smaller η_θ assumed in the model.

In the expression used to infer the values of η_θ (Eq.8.4) there are four parameters: N_f , A_f , A_{sec} , and V_f . The number of fibers (N_f) used in the model was the same as the one in experiments. The actual cross-section of the fibers (A_f) was not measured but, typically, tolerances on fiber manufacturing are nowadays very strict. The area of the cracked section (A_{sec}) was also well controlled given the small tolerance applied when producing the notch of the specimen (1mm). However, the same may not be said with respect to the fiber volume fraction (V_f). In fact, in the short inspection carried out to the steel fiber content of two specimens of serie B60, differences were about 11% and 23% respect to theoretical values. Furthermore, the average coefficient of variation of the number of fibers in all series was about 20%. These two aspects indicate that the orientation number could vary within a similar order of magnitude uniquely due to such uneven distribution of fibers within the concrete.

As it will be shown in the parametric study presented in the following, the orientation number is the parameter that most affects the stress-crack width curves. The adoption of larger values of η_θ would increase the weight of the pullout responses of fibers at small inclination angles in the overall load-carrying capacity and, consequently, $\sigma_{SFRC}(w)$ would increase for small crack widths and slightly decrease for larger ones.

Taking into account the uncertainties associated to the assumption of the orientation number and the magnitude of scattering on experimental results, it can be concluded that the predictions of the average stress-crack width curves provided by this new constitutive model are very reasonable.

8.5 PARAMETRIC STUDY OF THE SFRC TENSILE BEHAVIOR

According to the analytical formulation presented in Section 8.3, this new constitutive model depends upon the strengthening contributions of plain concrete and steel fibers. While the former was already well characterized by previous works in literature, the contribution of fibers for the tensile behavior of SFRC was not so clear.

In Chapters 4 and 5, predictions of the pullout responses of inclined steel fibers were verified against experimental results. Then, the orientation profile was characterized by means of an extensive investigation of experimental data in Chapter 6. With these two premises validated, the thorough constitutive model could be developed and once more compared to results from experiments, such as shown in Section 8.4. Given the good agreement that was provided by the proposed approach, comprehensive insight on the σ - w relationship of SFRC can now be attained.

8.5.1 Focus of the constitutive model

Before performing the theoretical analysis of the tensile behavior of SFRC it is necessary to define the admissible ranges of input values for this constitutive model.

The predictions of the pullout responses of inclined steel fibers presented in Chapters 4 and 5 focused on common steel fiber geometries (from 30 to 60 mm length and diameters from 0.5 to 1.0 mm) whose aspect ratios vary from 40 to 100. The tensile yield strengths of current steel fibers are typically larger than 500 MPa and lower than 2500 MPa.

The model accounts for conventional concrete matrices whose characteristic compressive strengths vary between 12 and 90MPa and limits the fiber volume fraction up to 1.0%. Dosages higher than this value, typical of High Performance Fiber Reinforced Cementitious Composites (HPFRCC), are not the focus of this model since pullout mechanisms might be significantly influenced by small fiber spacing. Anyhow, the maximum fiber dosages should always be defined according to the fiber factor ($V_f \cdot L/d$) in order to avoid the formation of *clumps* or *balls* during the manufacturing process (Grünewald, 2004; Martinie et al., 2009).

Regarding the orientation of fibers, represented by means of the orientation number, the probabilistic interval advanced in Chapter 7 will be considered (0.26 up to 0.97). A summary of the ranges of variation of all the theoretical inputs of the model is presented (Table 8.3). From the experimental investigation of the pullout of aligned fibers with features according to Table 8.3, common orders of magnitude for the key-points of the pullout diagrams of straight and hooked fibers could be identified (Appendix 7). This way, absolute and relative orders of magnitude for the experimental data from aligned steel fibers are indicated in Table 8.4.

Table 8.3 - Ranges of the theoretical inputs covered by the model.

	d	L	L/d	f_y	f_{ck}	V_f	η_θ
	[mm]	[mm]	[-]	[MPa]	[MPa]	[%]	[-]
Minimum	0.5	30	40	500	15	0.0	0.26
Maximum	1.0	60	100	2500	90	1.0	0.97

Table 8.4 - Orders of magnitude of the experimental inputs covered by the model.

	w_{S01}	w_{S02}	w_{H01}	w_{H04}	P_{S01}	P_{S02}	P_{H01}	P_{H04}
	[mm]	[mm]	[mm]	[mm]	[N]	[N]	[N]	[N]
Minimum	0.005	w_{S01}	$w_{S01} + 0.40$	$w_{S01} + 4.5$	10	$0.2 \times P_{S01}$	60	0
Maximum	0.200	$5 \times w_{S01}$	$w_{S01} + 0.60$	$w_{S01} + 5.0$	240	P_{S01}	830	380

8.5.2 Case-studies

In order to understand how the input parameters of this constitutive model affect the tensile response of the material, this parametric study accounts for several case-studies whose input parameters are defined Table 8.5.

Table 8.5 - Input values for the case-studies considered.

Inputs	Cases												
	0	1	2	3	4	5	6	7	8	9	10	11	12
d [mm]	0.75	0.50	1.00	---	---	---	---	---	---	---	---	---	---
L [mm]	45	---	---	30	60	---	---	---	---	---	---	---	---
f _y [MPa]	1100	---	---	---	---	600	2100	---	---	---	---	---	---
f _{ck} [MPa]	30	---	---	---	---	---	---	45	60	---	---	---	---
V _f [%]	0.38	---	---	---	---	---	---	---	---	0.57	0.76	---	---
η _θ [-]	0.50	---	---	---	---	---	---	---	---	---	---	0.65	0.80
A _{sec} [cm ²]	225	---	---	---	---	---	---	---	---	---	---	---	---
P _{S01} [N]	39.2	26.1	52.2	26.1	52.2	---	---	51.3	58.9	---	---	---	---
P _{S02} [N]	19.6	13.1	26.1	13.1	26.1	---	---	25.7	29.4	---	---	---	---
w _{S01} [mm]	0.10	---	---	---	---	---	---	---	---	---	---	---	---
w _{S02} [mm]	0.20	---	---	---	---	---	---	---	---	---	---	---	---
w _{S03} [mm]	11.3	---	---	7.5	15.0	---	---	---	---	---	---	---	---
P _{H01} [N]	267.4	118.9	475.5	---	---	---	---	350.4	402.1	---	---	---	---
P _{H04} [N]	108.2	48.1	192.3	---	---	130.4	149.4	123.8	132.6	---	---	---	---
w _{H01} [mm]	0.60	---	---	---	---	---	---	---	---	---	---	---	---
w _{H04} [mm]	4.85	---	---	---	---	---	---	---	---	---	---	---	---

In Table 8.5, values in bold format represent the input parameters that differ with respect to the reference case (number 0). The inputs of cases 1-12 that do not change respect to case 0 were not displayed for clarity.

Changing the properties of the fibers and/or the concrete matrix influences the pullout behavior of aligned steel fibers. Therefore, in order to provide a more realistic evaluation of the tensile behavior, the values of Table 8.5 that characterize the key-points of the pullout responses of straight and hooked fibers were modified according to the approximations presented in Appendix 7.

8.5.3 Comparative analysis between straight and hooked fibers

The relative performance of straight and hooked fibers on the crack-bridging capacity of SFRC is commonly evaluated through the pullout tests of fibers aligned with the load direction. However, the latter are not representative of the pullout mechanisms existing in the material, where inclined fibers perform the most frequent situation. Moreover, even when the orientation effects are considered on the fiber pullout responses, the relative performance of SFRC cannot be evaluated without knowledge on the frequencies of occurrence associated to each orientation. Given that the present constitutive model accounts for both of these aspects, the actual differences on the residual strength of the composite due to fiber hooked-ends can be assessed.

For comparison purposes, Fig.8.16 presents the post-cracking tensile responses for the case-study of reference with straight and hooked fibers. It is evident that differences on the tensile behavior of the composite only occur after the activation of the hook ($w_{S01}=0.1\text{mm}$) and become progressively magnified with the straightening process of the hooked-ends. At a crack width of 3.5mm the residual strength provided by hooked fibers is about 6.5 times larger than the one of straight fibers.

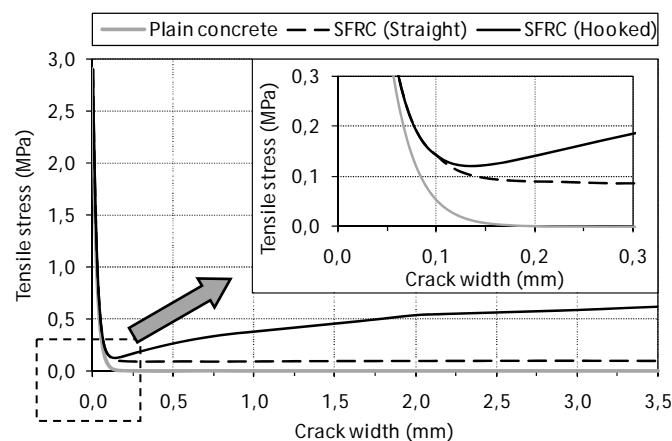


Fig.8.16 - Comparison of the σ - w response of SFRC with straight and hooked fibers for case No. 0.

This comparison between straight and hooked fibers is restricted to the specific input values that characterize case 0. In fact, if any other combination of inputs would have been chosen, both the relative and absolute differences on the σ - w curve would vary. This occurs because the inclined pullout responses of these types of fibers are differently influenced by the input parameters. For instance, the use of improved concrete strengths enhances both the maximum pullout loads of aligned fibers and the resistance against matrix spalling. However, because the pullout loads of hooked fibers are several times larger than the ones of straight fibers, the benefits from using high strength matrices in straight fibers is less significant regarding that spalling effects have less influence on the overall response. In order to understand how the major input parameters of the new constitutive model affect the tensile behavior of SFRC, a detailed analyses for both straight and hooked fibers is presented in the following.

8.5.4 Analysis for straight fibers

For SFRC with straight fibers and properties according to Table 8.3, the post-cracking strength is considerably smaller than the tensile strength of the concrete matrix (f_{ctm}), such as exemplified in Fig.8.16 for the case-study of reference. For this particular case, the post-cracking strength is approximately constant up to crack widths of 3.5mm with a value of 0.09MPa, a scanty 3% of the tensile strength of the concrete (2.90MPa).

Fig.8.17 shows a detail of the tensile behavior of the material under service conditions in which the load-carrying capacity is partially transferred to the fibers. It can be seen that the reinforcing action of the fibers starts when the plain concrete cracks ($w=0.0\text{mm}$) and increases progressively up to a value in accordance with the maximum pullout load of the aligned fibers ($w_{S01}=0.1\text{mm}$). Because this parametric study intends to evaluate the strengthening contribution provided by fibers in terms of the inputs of the model, the analysis presented in the following focus uniquely on the magnitude and variations of the residual strength of SFRC.

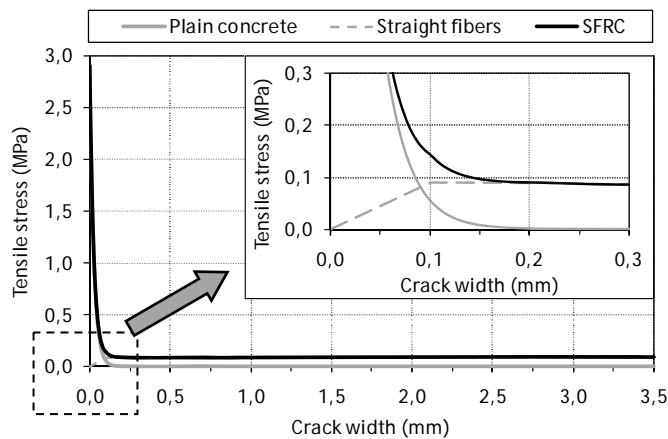


Fig.8.17 - σ - w response of SFRC with straight fibers for case No. 0.

The effect of the diameter of the fiber (d) on the residual strength of SFRC is shown in Fig.8.18a. Larger diameters increase the embedded surface of the fiber in the matrix and, consequently, also the maximum pullout load of aligned fibers (P_{S01}) increases. However, the increment of the diameter of the fibers under the same content of reinforcement significantly reduces the number of fibers at the cracked section (N_f). While P_{S01} increases linearly at increasing diameters (Eq.A8.1.1), N_f is inversely proportional to the squared diameter of the fiber (Eq.8.4). Thereby, the post-cracking strength is proportional to the ratio between the diameter of the reference case (0.75mm) and the ones from the case-studies considered (0.50mm and 1.0mm, respectively).

The influence of the fiber length (L) on the residual branch of the σ - w curve is presented in Fig.8.18b. As expected, the largest fibers (case 4) provide the higher strength because P_{S01} increases with the embedded surface of the fibers. Thereby, the residual strengths of cases 3 and 4 are proportional to the ratio between their average embedded lengths (7.5 and 15mm, respectively) and the one of the reference case (11.25mm).

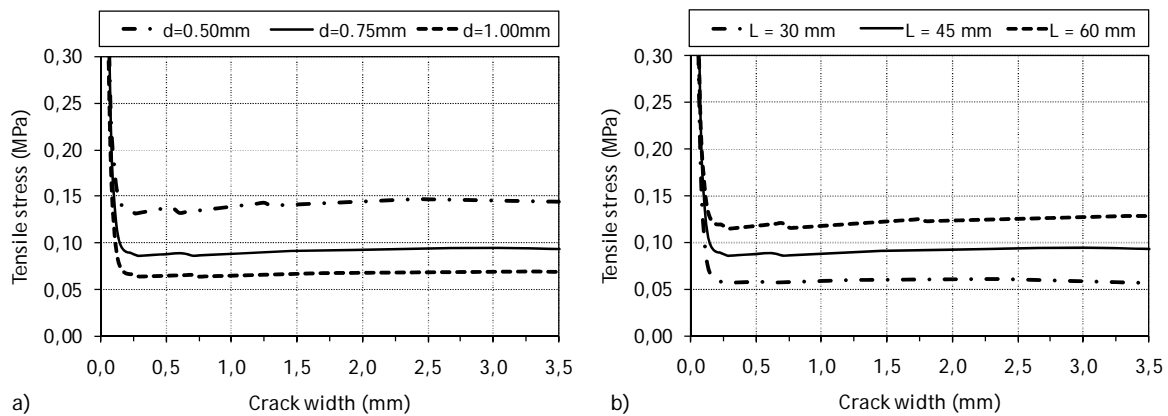


Fig.8.18 - σ - w responses of SFRC with straight fibers in terms of: a) fiber diameter; b) fiber length

The analyses of cases 1 to 4 corroborate the experimental evidences in literature that report improved performances of SFRC when using fibers with larger aspect ratios (L/d).

Considering the range of concrete strengths and properties of the fibers (Table 8.3), it was assumed in Chapter 4 that the pullout responses of straight steel fibers was not affected by their tensile yield strength (f_y). Such assumption is supported by the experimental data presented in Table A8.1.1. Consequently, the predicted tensile responses of SFRC with straight fibers provided by this constitutive model are the same irrespectively of f_y , such as shown in Fig.8.19a.

The effect of the characteristic compressive strength of the matrix (f_{ck}) on the residual strength of SFRC is shown in Fig.8.19b. The larger matrix strength (case 8) provides superior performance due to enhanced bond properties with fibers. Improved matrix strengths also counteract in higher degree the spalling phenomena occurring on the pullout of inclined fibers. Nonetheless, given that the maximum pullout loads of the fibers are reduced, spalling of the matrix is not significant and does not influence significantly the σ - w curve.

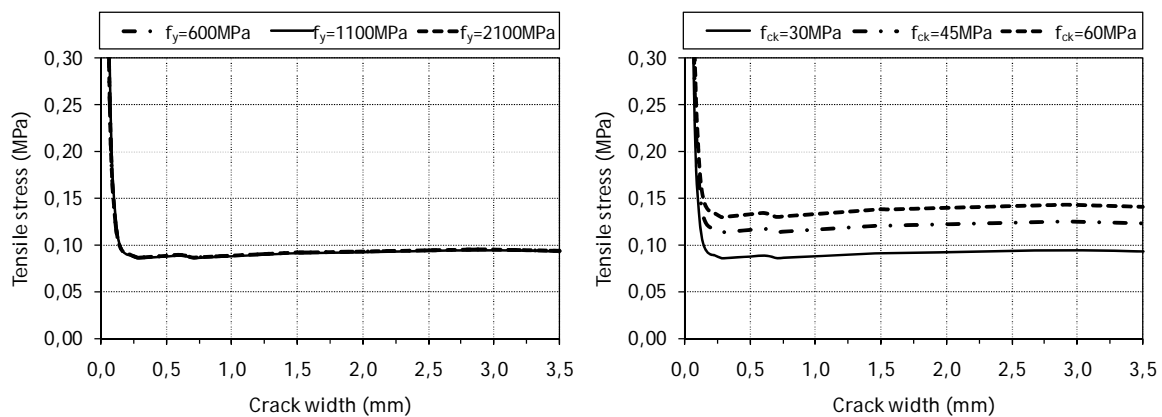


Fig.8.19 - σ - w responses of SFRC with straight fibers in terms of: a) fiber yield strength; b) matrix strength

From the previous, it can be concluded that the relative residual strengths of SFRC shown in Fig.8.19b derive from differences on their respective values of f_{ctm} . Cases 7 and 8 imply matrix

tensile strengths about 30 and 50% larger than the one of the reference case, which is in accordance with the increments of residual strengths observed.

Fig.8.20a presents the influence of the fiber volume fraction (V_f) on the reinforcing action of straight fibers. It is clear that the residual strengths of SFRC increase linearly with the number of fibers being pulled out from the matrix.

The effect of the orientation number (η_θ) on the residual strength of SFRC is shown in Fig.8.20b. Contrarily to the previous cases, the orientation of fibers not only influences the magnitude but also the shape of the σ - w curve. Larger orientation numbers induce overall strengthening contributions governed by fibers with smaller inclination angles whose maximum pullout loads occur for small crack widths. This way, it is not surprising why that the tensile strength of case 12 ($\eta_\theta=0.80$) is about twice the one of the reference case in the SLS and then progressively reduces its relative strength at larger crack widths.

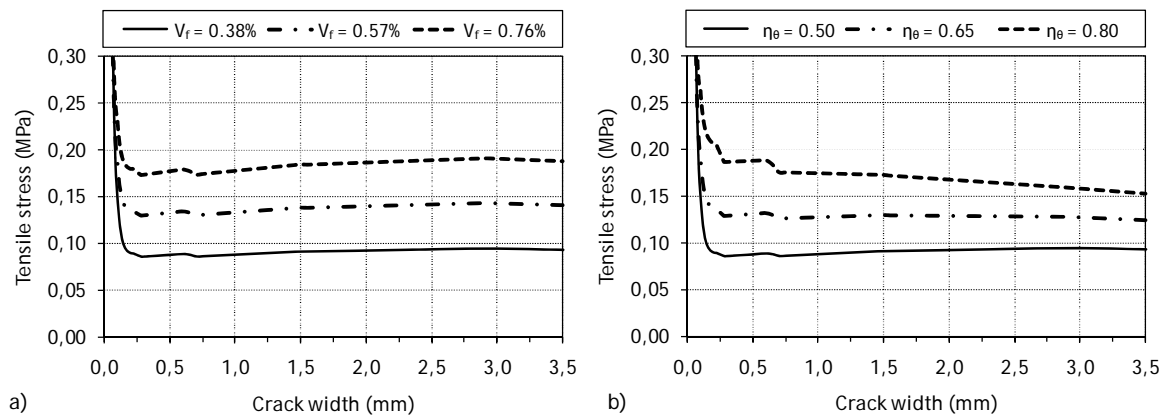


Fig.8.20 - σ - w responses of SFRC with straight fibers in terms of: a) fiber content; b) orientation number

8.5.5 Analysis for hooked fibers

The residual post-cracking strength of straight fibers for the case-study of reference is approximately constant up to crack widths of 3.5mm (Fig.8.17) due to the absence of a predominant alignment of fibers. However, having the same orientation pattern, the same could not be verified for SFRC with hooked fibers, such as presented in the previous comparative analysis (Fig.8.16). This occurs because the straightening process of inclined hooked fibers is delayed due to the occurrence of matrix spalling effects. Hooked fibers with large inclination angles are still being straightened at crack widths of 3.5mm and, consequently, the overall load-carrying capacity keeps increasing at this stage. The extent to what this tendency is prone to occur depends basically on the magnitude of the matrix spalling effects and on the orientation pattern of the fibers. However, such as described in the following, there are some other input parameters with major influence on the post-cracking strength of SFRC with hooked fibers.

The effect of the diameter of the fibers (d) on the residual strength of SFRC with hooked fibers is shown in Fig.8.21a. Similarly to what occurs in straight fibers, the total number of fibers in a

cross-section is inversely proportional to their squared diameter. However, in this case, the maximum pullout load of aligned fibers depends mainly on the plastic deformations at the hooked-end and, consequently, it is proportional to the cross-sectional area of the fiber. Since these two effects somehow compensate themselves, the influence of the diameter of the fibers is not as immediate and significant as in the case of straight fibers. Anyhow, the same trend can be identified in Fig.8.21a, where fibers with smaller diameters (case 2) perform better. This occurs because the fibers with small diameters carry smaller pullout loads and, consequently, imply smaller spalling effects on the surrounding matrix. Thereby, their maximum pullout loads are achieved at smaller crack widths than the ones of fibers with larger diameters.

Fig.8.21b shows the influence of the fiber length (L) on the tensile response of SFRC with hooked fibers. It can be seen that, while fibers with 45 and 60mm (case 0 and 4, respectively) have similar residual strengths, fibers with 30mm (case 3) have a slightly smaller performance. This occurs because their respective average embedded length ($L_{e,average}$), previously defined in Table 8.1, is only 11.25mm. Since the tensile strength of the concrete matrix is not very high ($f_{ctm}=2.90\text{MPa}$), the length of spalled matrix for fibers with large inclination angles approaches this value. Consequently, these fibers are removed from the matrix at crack widths smaller than 3.5mm, thus reducing the overall load-carrying capacity of the material.

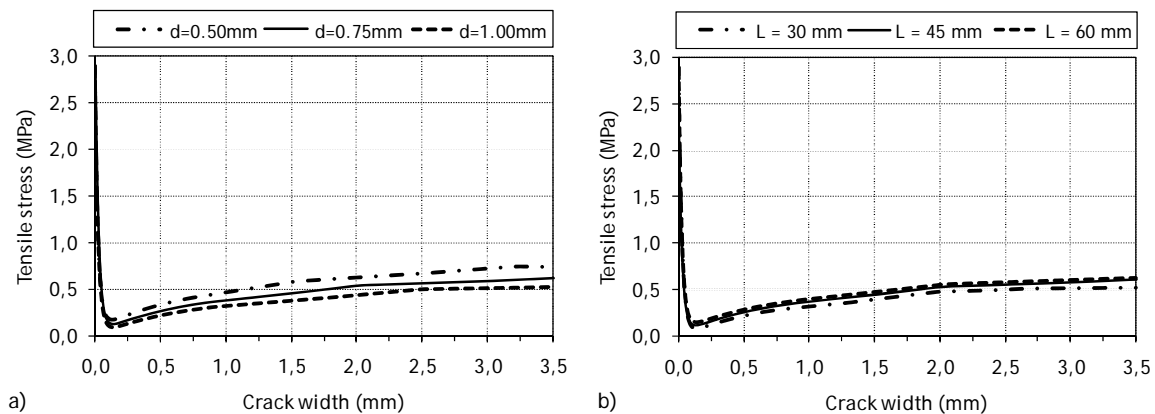


Fig.8.21 - σ - w responses of SFRC with hooked fibers in terms of: a) fiber diameter; b) fiber length

The influence of the tensile yield strength of the fibers (f_y) is shown in Fig.8.22a. Contrarily to straight fibers, this parameter does play an important role on the tensile response of SFRC. Due to the plastic deformations occurring at the hooked-ends, the normal stresses on these fibers may approach f_y even when they are aligned with the load direction. When fibers are inclined respect to the load direction, the deviation forces imposed by the matrix at the fiber exit point induce additional shear and bending stresses that may provoke rupture of the fibers and, consequently, significantly reduce the tensile strength of SFRC. This is what happens in case 5 (Fig.8.22a) whose small tensile yield strength of fibers (600MPa) implies their rupture with inclination angles smaller than 30° at about 0.6mm crack width and approximately at 1.5mm for fibers with inclination angles ranging from 30° to 45° . When rupture of fibers does not take place the tensile response of SFRC is roughly the same (cases 0 and 6 in Fig.8.22a).

Fig.8.22b shows the influence of the matrix strength. Larger matrix strengths avoid significant spalling effects and, consequently, make possible the occurrence of the maximum pullout loads at small crack widths, which is of particular interest for structural design. Furthermore, improved matrix strengths also potentiate the straightening process of the hooked-ends, thus increasing the maximum contribution that can be extracted from each single fiber. These two effects justify the enhanced post-cracking response of case 7 respect the case 0 (f_{ck} equal to 45 and 30MPa, respectively). On the other side, although case 8 is the one with largest matrix strength ($f_{ck}=60\text{MPa}$), its respective tensile response is rather poor. This occurs because the restraining action of the matrix was large enough to provoke plastic deformations on the fiber that could not be supported by its tensile yield strength. Thereby, this case emphasizes the relevance that this constitutive model may have on avoiding inappropriate combinations of fiber and matrix strengths.

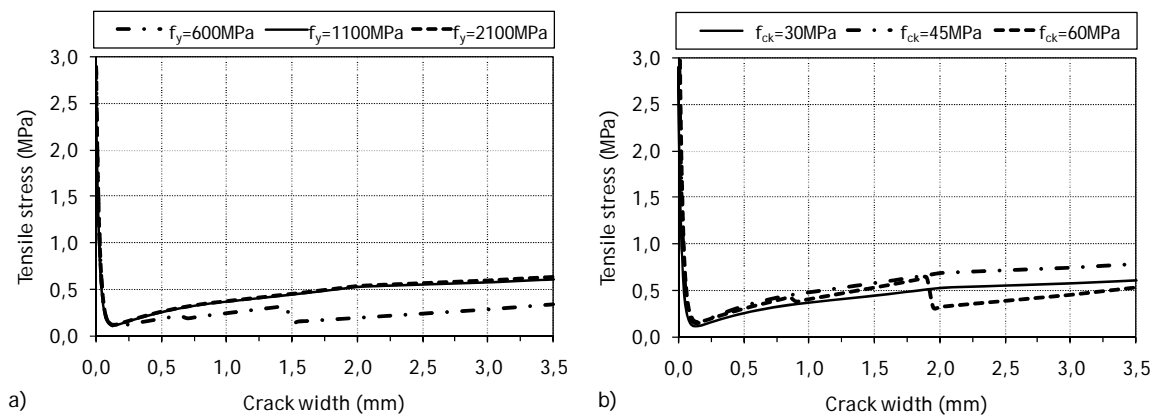


Fig.8.22 - σ - w responses of SFRC with hooked fibers in terms of: a) fiber yield strength; b) matrix strength

The effect of the fiber volume fraction (V_f) is shown in Fig.8.23a. Given the additive nature of the single fiber pullout contributions, it is evident that the post-cracking strength varies linearly with the amount of fibers in the cross-section.

Finally, Fig.8.23b shows the influence of the orientation number (η_θ). Given the characteristics of the orientation profile described in Chapter 6, large values of η_θ increase the frequency of occurrence of small inclination angles, thus bringing the peak of the post-cracking range towards smaller crack widths. This is noticeable in case 12 (Fig.8.23b) where the peak value occurs for a crack width of 2.0mm and the tensile stress at 0.3mm is more than thrice the one of case 0. Among all the input parameters previously analyzed, the orientation of fibers is probably the one with the strongest effect on the load-carrying capacity. Therefore, the inclusion of this parameter on the present constitutive model is of great relevance to explain the different tensile behaviors that can be exhibited by SFRC.

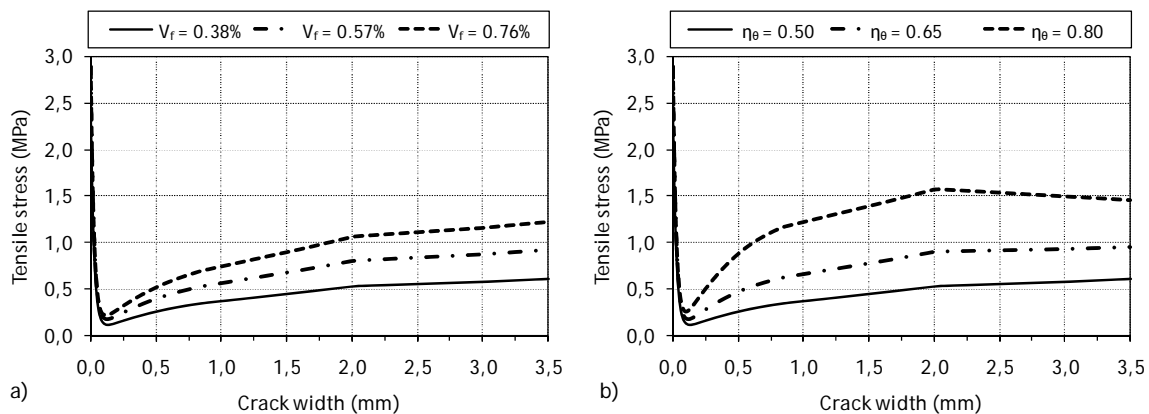


Fig.8.23 - σ - w responses of SFRC with hooked fibers in terms of: a) fiber content; b) orientation number

8.6 ENGINEERED EXPRESSIONS FOR DESIGN AND OPTIMIZATION OF SFRC

The present constitutive model accounts for the orientation and the pullout responses of fibers, complex phenomena which require many variables to be characterized. In order to avoid the development of a very complicated model, the prediction of each of its components was carried out by means of a reduced number of parameters. Thereby, the proposed approach can be easily introduced on a spreadsheet where the user can understand how the physical input parameters influence the tensile response of SFRC. Although this is an advance of great relevance, this section intends to go a step further and investigate whether simplified analytical expressions can be developed to provide similar results. Because these expressions would provide a very straightforward tool for structural design, they will be herein defined as the Engineered Expressions for Design and Optimization (EEDO).

8.6.1 Basic concepts and equations

In Section 8.2.1, an analogy between the pullout responses of the steel fibers and an equivalent steel rebar was advanced and the tensile behavior of SFRC was defined in terms of three physical concepts. Following the same conceptual basis, the EEDO are defined in terms of three contributions (Eq.8.10):

$$\sigma_{\text{SFRC}}(w) = \sigma_{\text{C}}(w) + \sigma_{\text{ER}}(w) + \sigma_{\text{B}}(w) \quad (8.10)$$

where $\sigma_{\text{SFRC}}(w)$ is the tensile stress of steel fiber reinforced concrete at crack width w ; σ_{C} is the respective post-cracking strength of the plain concrete; σ_{ER} is the contribution from the equivalent rebar at crack width w ; σ_{B} is the respective component accounting for bond between fibers and the matrix. In order to reproduce the shape of the tensile responses of SFRC based on these three components, their formulation should be able to provide individual contributions such as the ones previously identified in Fig.8.2.

Similarly to what was done in Section 8.3, the σ - w curve of plain concrete will be assumed from literature (Eq.8.2). Nonetheless, a more general form will be adapted to such expression (Eq.8.11):

$$\sigma_c(w) = B_c \times e^{-k_c \left(\frac{w}{c_c}\right)^{n_c}} \quad (8.11)$$

where B_c is the tensile strength of the concrete matrix (f_{ctm}); k_c is a constant equal to 39.8mm^{-1} ; c_c and n_c are equal to 1.0. Using the same mathematical identity, the contributions provided by the equivalent rebar (ER) and by the bond strength (B) can provide the shape exhibited in Fig.8.2 through the following expressions:

$$\sigma_{ER}(w) = B_{ER} \times \left[1 - e^{-k_{ER} \left(\frac{w}{c_{ER}}\right)^{n_{ER}}} \right] \quad (8.12)$$

$$\sigma_B(w) = -B_B \times \left[1 - e^{-k_B \left(\frac{w}{c_B}\right)^{n_B}} \right] \quad (8.13)$$

It is interesting to notice that, based on Eq.8.10-8.13, $\sigma_{SFRC}(w)$ becomes defined as the sum of three exponential curves which, in all cases, depend uniquely on four input parameters (B , c , k and n) whose values may be different according to the index associated to each of them. Because the use of these four parameters provides a large degree of freedom to the shape of the exponential curves, the influence of each of one of them is briefly described in the following.

8.6.2 Analysis of the parameters

Regarding the similar nature of Eq.8.11-8.13, the identification of their four defining parameters will be exemplified by means of Eq.8.12, depicted in Fig.8.24 for convenience:

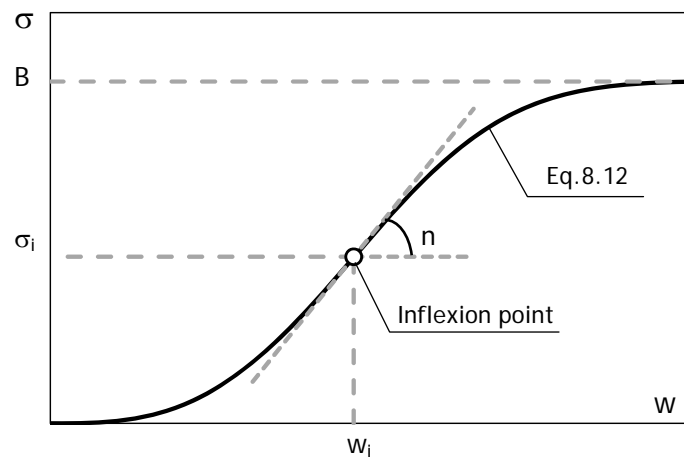


Fig.8.24 - Identification of the four parameters controlling the shape of the exponential functions.

From Fig.8.24 it becomes evident that parameter B is the asymptote of Eq.8.12 whereas parameter n controls the inclination of the curve at the inflexion point. The coordinates of the later (w_i, σ_i) are defined in Eq.8.14-8.15, where it can be seen that c is a parameter related to the location of the inflexion point whereas k is a parameter that, indirectly, controls the ordinates of the curve. Regarding that all the parameters will be taken as positive values, the condition for the existence of an inflexion point (Eq.8.14) implies that n is larger than 1.0. If n is positive and smaller than 1.0 there would be no inflexion point and the shape of the curve would be monotonically concave downwards.

$$w_i = c \times \left(\frac{n-1}{k \times n} \right)^{\frac{1}{n}} \quad \text{with} \quad \left(\frac{n-1}{k \times n} \right) > 0 \quad (8.14)$$

$$\sigma_i = B \times \left[1 - e^{\left(\frac{1-n}{n} \right)} \right] \quad (8.15)$$

Fig.8.25 shows the effects of varying independently each of the four parameters in one exponential curve of reference. By taking a parameter B , smaller than the one of reference, the magnitude of all the ordinates becomes diminished (Fig.8.25a). Decreasing parameters k and c introduces opposite effects on the curve: while the former smooths the curve and tends to reduce the ordinates (Fig.8.25b), the latter makes it steeper and increases all the values (Fig.8.25c). Finally, by decreasing parameter n the curve becomes smother and the ordinates increase for abscissas smaller than w_i and decrease for the ones larger than w_i (Fig.8.25d).

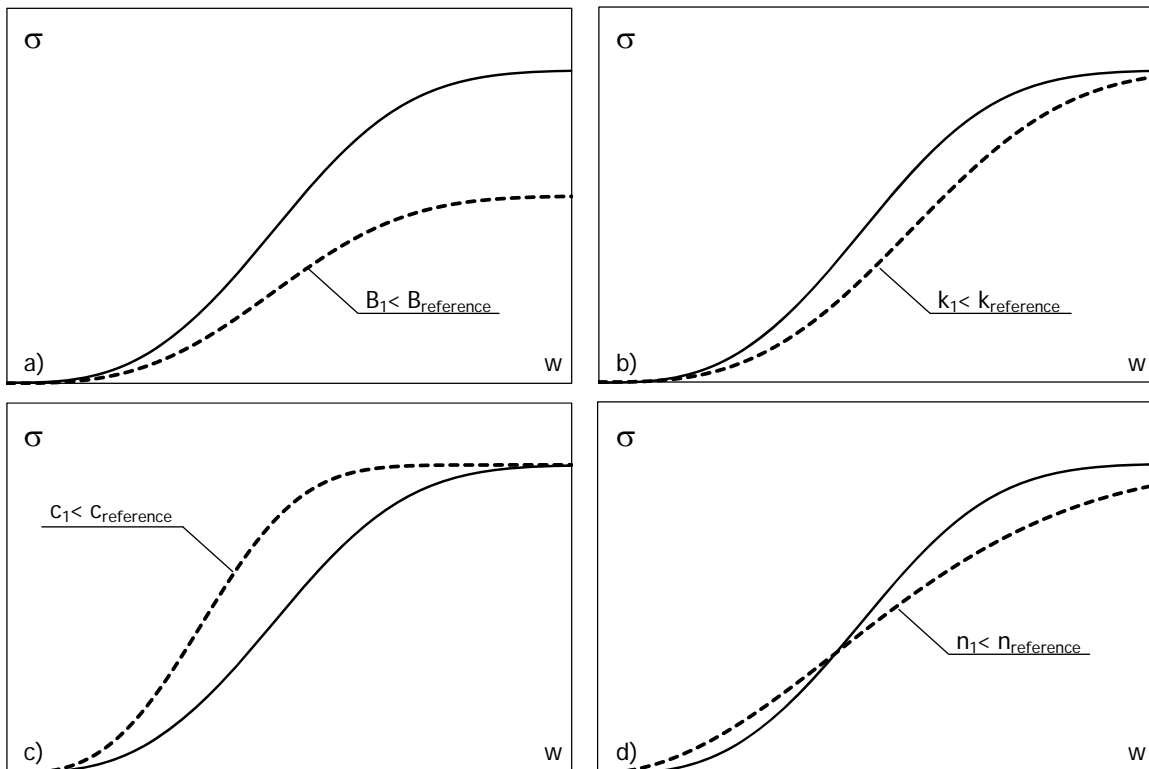


Fig.8.25 - Influence of each parameter on the shape of the exponential curve.

Given the previous description, it is now possible to make an interpretation of these parameters in terms of their phenomenology. For instance, given the analogy presented in Fig.8.1 and the asymptotic nature of parameter B_{ER} (Eq.8.12), the later can be interpreted as the tensile yield strength of the the cross-section. Similarly to what occurs in conventional reinforced concrete, B_{ER} would depend on the tensile yield strength of the fibers (f_y), on their relative percentage in the cross-section (V_f) and on a parameter accounting for the alignment with the orthogonal axis of the section (η_θ), such as defined in Eq.8.16. In practice, B_{ER} would be the maximum tensile strength provided by fibers under conditions of perfect bond with the surrounding matrix. However, regarding that fibers tend to be pulled out from the matrix and that their contribution after that process is null, the asymptote of the expression representing the bond-strength (Eq.8.13) has to present the same value (Eq.8.17).

$$B_{ER} = f_y \times V_f \times \eta_\theta \quad (8.16)$$

$$B_B = B_{ER} \quad (8.17)$$

With respect to the remaining parameters, some intuitive interpretations can also be advanced. In fact, given that n controls the inclination of the curve at the inflexion point, it can be interpreted as the equivalent elastic modulus of SFRC in Eq.8.12. Regarding the expression referring to bond (Eq.8.13), n would be a parameter accounting for the pace at which bond decreases up to the removal of the fiber. In Eq.8.12, parameter c determine the crack width at which fibers absorb tensile stresses at higher rate and k accounts for the level of load-carrying capacity that fibers are able to provide at such crack width. With respect to the expression referring to the bond strength (Eq.8.13), c establishes the slippage at which the average decrease on the pullout load of fibers is larger whereas k determines the percentage of bond with the matrix at that stage.

Although the meaning and the effect of parameters k , c and n on the tensile response of SFRC can be easily accepted, their general quantification is not as simple as it is for parameter B because they depend on the complex phenomena of orientation and pullout responses of all the fibers in the cross-section. Thereby, an investigation of the values that could define these parameters was carried out by following the methodology that is described in the next section.

8.6.3 Methodology

In order to examine the values of the six unknown parameters (k_{ER} , c_{ER} , n_{ER} , k_B , c_B and n_B) required to characterize $\sigma_{SFRC}(w)$, several case-studies were defined by attributing different values to the inputs of the constitutive model, according to the ranges defined in Tables 8.3-8.4. Then, the values of these six parameters that provided the best fitting to the solutions extracted from the analytical formulation were obtained for the several case-studies. The non lineal regressions of each case-study were performed with the software of statistical analysis *SPSS*. Once having the values of the parameters that provided the best approximation for each case-study, an investigation of their dependencies respect to the input values was carried out.

When trying to correlate the inputs of the constitutive model with the group of best-fitting values for each case-study it was possible to conclude that, in all cases, changing one input at a time always returned different values for all the six parameters. Given the innumerable combinations that can be arranged with the inputs of the model, it is easily perceived that such coupling does not allow an unequivocally definition of these parameters. Consequently, fitting procedures would always be required if this constitutive model is to be defined by the previous exponential expressions with high accuracy.

Some restraint conditions were considered in order to obtain the non-linear regressions of the σ - w curve provided by the analytical formulation. According to the physical interpretation previously mentioned all the six parameters have to be positive. Furthermore, the stresses provided by Eq.8.10 also have to remain equal or greater than zero along the entire crack width range. In order to guarantee this condition, the following additional restraints were considered:

$$k_{ER} \geq k_B \quad (8.19)$$

$$c_{ER} \leq c_B \quad (8.20)$$

$$n_{ER} \leq n_B \quad (8.21)$$

From the previous, it becomes obvious that the use of the proposed expressions with the parameters that provide the best fitting to the analytical formulation may be meaningless. Although it would have the advantage of providing a continuous and differentiable σ - w curve, it would be a time and effort-consuming task that would not bring other relevant benefits.

It has to be kept in mind that a straightforward tool was intended when developing simplified analytical expressions. This way, instead of approaching the values of the parameters through such an inverse analysis procedure, direct formulations were investigated. Although this is surely a roughly approach, it should be wise to assess how inaccurate these approximations could be on describing the tensile responses of SFRC in different scenarios. For this purpose, the following methodology was applied:

- Step 1: Definition of case-studies: 3 to 4 values were attributed to each input of the constitutive model, according to the ranges defined in Tables 8.3-8.4 (total of 36 case-studies).
- Step 2: The formulation of the new constitutive model was applied to each case-study and the software SPSS was used to extract the six parameters that provided the best fitting curve within a crack width range up to 3.5 mm.
- Step 3: The variation the parameters was analyzed for each range of input values. Then, the inputs that generated a large variation in each parameter were selected (the criteria applied was a coefficient of variation larger than 30%) and the regression curves that best fitted the variation of the parameters for each input were extracted.
- Step 4: Each parameter was defined through the regressions curves of the inputs that implied the larger variations. All these regression curves were added into a unique expression for the definition of each parameter by attributing similar weights to each input.

The formulation of simplified expressions was developed both for straight and hooked fibers. In the following, the expressions and results of this study are presented and discussed on the basis of several case-studies.

8.6.4 Straight fibers

The investigation on the constitutive model for SFRC with straight fibers returned the simplified formulation summarized in Table 8.6. By applying the expressions from Table 8.6 in Eq.8.10-8.13 the tensile responses of SFRC could be easily predicted.

Table 8.6 - Exponential functions for SFRC with straight steel fibers.

Physical contribution	Expressions
σ_C	$B_B = f_{ctm}$
	$k_C = 39.8$
	$c_C = 1.0$
	$n_C = 1.0$
σ_{ER}	$B_{ER} = \frac{M_f}{7850} \times \eta_\theta \times f_y$
	$k_{ER} = -0.595 + 0.65\eta_\theta + \frac{0.35f_y + 14.8M_f + L(140 - 1.7L)}{1000}$
	$c_{ER} = -0.85 + \frac{5}{3}\eta_\theta + d(3.06 - 2.58d) + \frac{0.7f_y + 3M_f + 6.9f_{ck} + L(53 - 0.6L)}{1000}$
	$n_{ER} = 0.6 - \frac{\eta_\theta}{1000} \left(175 + \frac{P_{S01}}{20 \times w_{S01}} \right)$
σ_B	$B_B = B_{ER}$
	$k_B = k_{ER} \left[1 - \eta_\theta \frac{P_{S01}}{P_U} (1 + 0.5 \times 10^{-3} f_y) \right]$
	$c_B = c_{ER} \left(1 + \eta_\theta \frac{P_{S01} + P_{S02}}{P_U} \right) + \frac{60 - L}{100}$
	$n_B = n_{ER}$

In order to evaluate whether the σ - w curves predicted through the exponential functions in Table 8.6 approximate the predictions obtained through the formulation of the constitutive model, several different scenarios of input parameters would have to be taken into account. For this purpose, the case-studies presented in Table 8.5 were taken into account. From the results

of this study, presented in Appendix 8.2, it is possible to conclude that the exponential functions shown in Table 8.6 cannot approximate the tensile responses of SFRC with straight fibers along the entire crack width range of interest, such as can be observed in Fig.8.26.

According to the results given by the formulation of the constitutive model, the residual tensile strength at crack widths of 3.5 mm is only about 6% of the maximum contribution that could be provided by fibers in the scenario of perfect bond conditions (B_{ER}). The load-carrying capacity of fibers significantly decreases due bond-effects at small crack widths and then remains approximately constant within the analyzed crack width.

Regarding the characteristics of the formulation adapted for bond (Eq.8.14), such exponential function implies a pronounced decrease of the predicted tensile stresses at increasing crack widths, justifying the divergence of results observed both in Fig.8.26 and Appendix 8.2 for large crack widths. However, despite these limitations, the approximations provided by the exponential functions with respect to the analytical formulation are very reasonable in all cases studies up to crack widths of 0.5 mm (Appendix 8.2).

Given the previous analysis, the Engineered Expressions for Design and Optimization of SFRC with straight fibers may be defined in two branches:

$$\left\{ \begin{array}{l} 0.0 < w \text{ (mm)} \leq 0.5 \quad \Rightarrow \quad \sigma_{SFRC}(w) \text{ is obtained through expressions from Table 8.6.} \\ 0.5 < w \text{ (mm)} \leq 3.5 \quad \Rightarrow \quad \sigma_{SFRC}(w) \text{ is equal to } \sigma_{SFRC}(0.5). \end{array} \right.$$

With these simplified expressions, a very good agreement with the formulation of the constitutive model can be obtained (Fig.8.26 and Appendix 8.2).

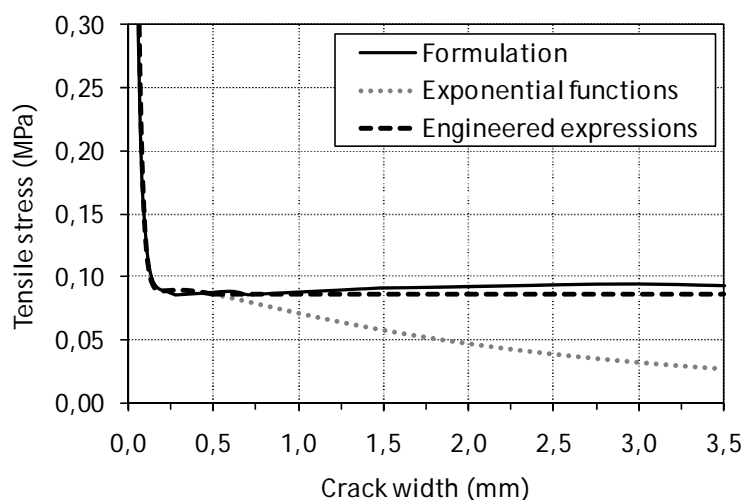


Fig.8.26 - Predicted constitutive model of SFRC with straight fibers for the case-study of reference.

8.6.5 Hooked fibers

The results from the investigation carried out on the constitutive model of SFRC with hooked fibers provided the expressions presented in Table 8.7. Similarly to the previous case, the tensile responses of SFRC were calculated by introducing these expressions into Eq.8.10-8.13. Once more, the suitability of this formulation was evaluated through comparison with the cases defined in the parametric study (Table 8.5). The results are presented in Fig.8.27 for the case-study of reference and in Appendix 8.3 for the remaining cases.

Table 8.7 - Engineered expressions for design and optimization (EEDO) of SFRC with hooked steel fibers.

Physical contribution	Expressions
σ_C	$B_B = f_{ctm}$
	$k_C = 39.8$
	$c_C = 1.0$
	$n_C = 1.0$
σ_{ER}	$B_{ER} = \frac{M_f}{7850} \times \eta_\theta \times f_y$
	$k_{ER} = 2 + \frac{f_{ck} - 12}{100} + 3 \times e^{\eta_\theta} - f_y \left(\frac{5 - 1.2 \times 10^{-3} f_y}{1000} \right)$
	$c_{ER} = 50 + 25d + 2.2 \times 10^{-3} f_y + \eta_\theta (30 - 25\eta_\theta) + 2.5 f_{ck} \left(\frac{f_{ck}}{100} - 1 \right)$
	$n_{ER} = 0.8 - 2.5 \times 10^{-3} L - \frac{\sqrt{\eta_\theta}}{10}$
σ_B	$B_B = B_{ER}$
	$k_B = 1.3 - e^{\eta_\theta} + \frac{(f_{ck} + 8)}{2.5 \times 10^6} \times f_y \times \eta_\theta \times \left(39 - \frac{f_{ck}}{2} \right) + k_{ER} \left[0.85 - 0.036 \times \left(\frac{P_{H01}}{P_U} \right) \left(1 + 20 \frac{P_{H01}}{P_U} \right) \right]$
	$c_B = \left(\frac{2500}{f_y} \right)^2 e^{\eta_\theta} + c_{ER} \left[1.32 + 0.36 \frac{P_{H01}}{P_U} \left(1 + 20 \frac{P_{H01}}{P_U} \right) \right]$
	$n_B = n_{ER}$

From the analysis of Fig.8.27 and the cases presented in Appendix 8.3, it can be concluded that the simplified expressions advanced for hooked fibers provide an encouraging agreement with the analytical formulation along the thorough crack width range analyzed.

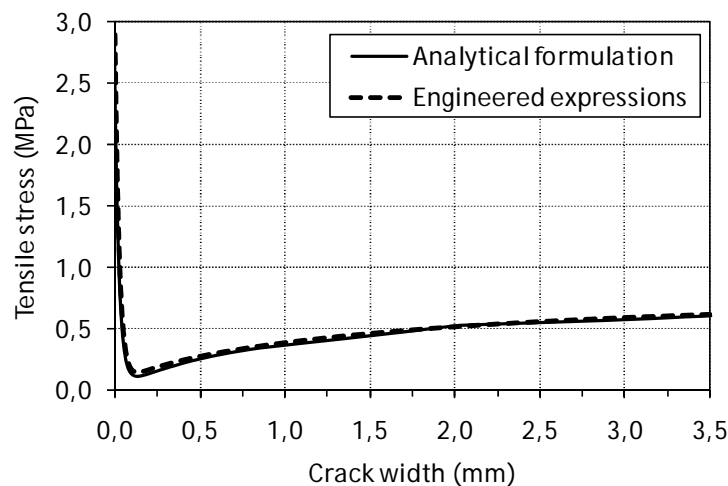


Fig. 8.27 - Predicted constitutive model of SFRC with hooked fibers for the case-study of reference.

The expressions advanced in Table 8.7 are valid whenever the input values are within the limits defined in Tables 8.3-8.4. However, regarding the simplicity of these expressions, they are only able to approach the tensile responses of SFRC whose failure mode is governed by fiber pullout. Therefore, undesirable failure modes such as fiber rupture were not taken into account, thus justifying the less good results observed in Appendix 8.3 for cases 5 and 8. In order to avoid poor predictions of the EEDO due to this reason, an additional restraint between the values of the fiber and matrix strengths is advanced hereafter.

Rupture of the fibers tends to occur whenever high strength matrices are combined with fibers with low tensile strengths. Typically, this undesirable failure mode is observed on inclined fibers, where the maximum pullout loads tend to be larger than the ones of aligned fibers.

In Fig. 5.14b it was shown that the maximum pullout loads tend to occur on fibers at inclination angles within the range of 25°-30° and are about 14% larger than the ones that are aligned with the load direction. Moreover, since rupture of the fibers tends to occur under pullout loads whose percentage relatively to the loads of aligned fibers decreases at increasing inclination angles, a larger fiber tensile strength was suggested in Fig. 5.14b in order to avoid fiber ruptures. The respective ratio between the pullout loads of aligned fibers and the ultimate load calculated with the suggested f_y was about 78%. This means that a minimum margin of 22% should exist in order to avoid fiber rupture for any inclination angle. This result is of great relevance for the design of SFRC and will be denominated in the following as the Margin to Avoid Rupture (MAR):

$$\text{MAR} = 1 - \frac{P_{H01}}{P_U} \quad (8.22)$$

For design purposes, a minimum MAR should always be guaranteed. However, large values of MAR may lead to conservative and anti-economic combinations of fibers and matrix properties. In order to have an order of magnitude on how the strengths of these two material properties should be combined, consider the approximated maximum pullout load of aligned fibers (P_{H01}) suggested in Eq. A8.1.2, which returns the following condition:

$$\frac{f_y}{f_{ctm}} \geq \frac{209}{1 - MAR} \tag{8.23}$$

With Eq.8.23 and the correlation between f_{ck} and f_{ctm} (Eq.8.3), maximum characteristic strengths of the concrete matrix that avoid rupture of the fibers for any orientation can be suggested. Fig.8.28 presents the results for two of the most common fiber tensile yield strengths existing in the market (1100MPa and 2100MPa).

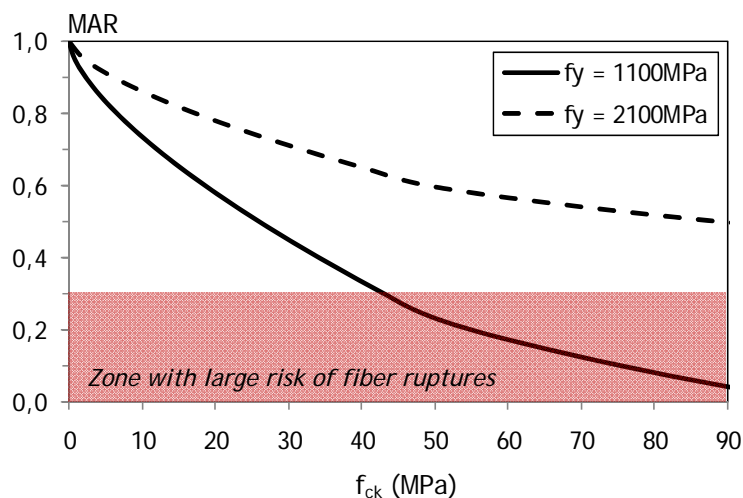


Fig.8.28 - Correlation between the concrete matrix strength and the safety factor for fiber rupture (MAR).

Fig.8.28 shows that, for the most common range of concrete matrices ($f_{ck}<90\text{MPa}$) the MAR provided by steel fibers with 2100MPa tensile yield strength is always greater than 0.50, which is probably too conservative. On the other side, for steel fibers with f_y equal to 1100MPa, the decrease of the MAR at increasing concrete strengths is much more pronounced, with values smaller than 30% for matrices with f_{ck} larger than 43MPa. These indicative values should be used as guidelines when defining the properties of matrix and fibers to be used on SFRC.

For design purposes, the author recommends that a minimum MAR of 30% should always be guaranteed (second term of Eq.8.23 around 300), such as pointed out in Fig.8.28. This will also be defined as the additional condition that establishes the range of application of the expressions presented in this section.

Regarding the good approximations with regard to the formulation of the new constitutive model provided by the EEDO, it can be concluded that these simplified expressions perform a valuable tool to be used for the design and optimization of SFRC both with straight and hooked steel fibers.

8.7 DESIGN-ORIENTED CONSTITUTIVE MODEL: A PRACTICAL EXAMPLE

With the purpose of demonstrating how straightforward and comprehensive the new constitutive model can be, this section presents an example of application of the proposed approach. The tensile response of the material will be obtained both through the analytical formulation (Section 8.3) and through the engineered expressions (Section 8.6) in order to clarify the procedures associated to each of these approaches.

8.7.1 Problem statement

Consider the production of a prismatic beam with 150×150×600mm by means of a self-compacting fiber reinforced concrete mixture with 0.57% (45kg/m³) reinforcement of hooked steel fibers and a characteristic compressive strength of 60MPa. Steel fibers have 60mm length, 0.50mm diameter and tensile yield strength of 2100MPa.

The tensile response of the SFRC is to be known at the square cross-section located at middle length of the beam. With respect to the orientation of fibers at this location, the influence of the manufacturing process was evaluated in detail in Section 7.6.2 (Table 7.4) and provided an average orientation number of 0.73.

In the absence of experimental data regarding the pullout response of these fibers aligned with the load direction, the associated input values are assumed to be within the orders of magnitude advanced in Table 8.4 and to follow the approximations advanced in Appendix 7. A summary of the inputs that will be considered in order to define the constitutive model for these particular conditions is provided in Table 8.8.

Table 8.8 - Summary of the input values.

d	L	f _y	f _{ck}	V _f	η _θ	w _{S01}	w _{S02}	w _{H01}	w _{H04}	P _{S01}	P _{S02}	P _{H01}	P _{H04}
[mm]	[mm]	[MPa]	[MPa]	[%]	[-]	[mm]	[mm]	[mm]	[mm]	[N]	[N]	[N]	[N]
0.64	41.2	2100	60	0.57	0.73	0.10	0.20	0.60	4.75	46	23	293	133

8.7.2 Resolution based on the analytical formulation

In order to easily follow the definition of the constitutive model through the analytical formulation, the reader is invited to go back to Fig.8.8 and observe the strategy of the approach. From the overview shown in Fig.8.8 the tensile response of the material, $\sigma_{\text{SFRC}}(w)$, can be obtained through 9 steps which will be described and quantified in the following.

Step 1: Define the strengthening contribution given by the plain concrete, $\sigma_c(w)$

$$f_{ctm} = 2.12 \times \ln\left(1 + \frac{(60 + 8)}{10}\right) = 4.35 \quad (\text{Eq. 8.3})$$

$$\sigma_c(w) = 4.35 \times e^{-39.8w} \quad (\text{Eq. 8.2})$$

Step 2: Predict the orientation number of fibers, η_θ

$$\eta_\theta = 0.734 \quad (\text{Tab. 7.4})$$

Step 3: Infer the approximate number of fibers in the cross-section, N_f

$$N_f = \frac{150 \times 150}{\pi \times 0.64^2} \times 0.0057 \times 0.734 = 293 \quad (\text{Eq. 8.4})$$

Step 4: Predict the orientation profile of the fibers, $P(\theta_i)$

$$\theta_m = \arccos(0.73) \times \frac{180}{\pi} = 43.1 \quad (\text{Eq. 6.2})$$

$$\sigma(\theta) = 90 \times 0.73 \times (1 - 0.73) = 17.7 \quad (\text{Eq. 6.8})$$

Table 8.9 - Calculation of the orientation profile.

θ_i	θ_{Si}	$F(\theta_{Si})$	$F(\theta_i)$	θ_i	$f(\theta_{ia})$	C_F	$P(\theta_i)$
(Eq. 6.10)				(Eq. 6.2)			
0	-2.43	49.3%	0.7%	7.5	5.0%	1.011	5.1%
15	-1.58	44.3%	5.7	22.5	17.3%	1.011	17.4%
30	-0.74	27.0%	23.0%	37.5	31.4	1.011	31.8%
45	0.11	4.4%	54.4%	52.5	28.5%	1.011	28.8%
60	0.95	32.9%	82.9%	67.5	13.5%	1.011	13.7%
75	1.80	46.4%	96.4%	82.5	3.2%	1.011	3.2%
90	2.64	49.6%	99.6%				

Step 5: Obtain the number of fibers at each group inclination angles, N_{θ_i}

Table 8.10 - Number of fibers at each group inclination angles, N_{θ_i}

θ_i	7.5	22.5	37.5	52.5	67.5	82.5
N_f	293					
$P(\theta_i)$	5.1%	17.4%	31.8%	28.8%	13.7%	3.2%
N_{θ_i}	14.8	51.1	93.1	84.5	40.1	9.4

(Eq. 8.6)

Step 6: Predict the pullout response of hooked fibers at each inclination angle, $P_{\theta_i}(w)$

Table 8.11 - Key-points of the pullout responses at inclinations θ_i (Table 5.1)

Key-points	θ_i						
	7.5	22.5	37.5	52.5	67.5	82.5	
H_1	w_{H1} [mm]	0.10	0.10	0.10	0.10	0.10	0.10
	P_{H1} [N]	45.6	42.5	36.5	28.0	17.6	6.0
H_2	w_{H2} [mm]	*	*	0.79	1.49	2.69	4.27
	P_{H2} [N]	*	*	170.1	109.4	62.1	30.5
H_3	w_{H3} [mm]	0.60	0.82	1.80	3.94	7.38	8.12
	P_{H3} [N]	312.4	332.4	327.0	295.9	241.2	99.7
H_4	w_{H4} [mm]	2.19	2.30	3.07	4.92	7.99	10.12
	P_{H4} [N]	248.7	275.5	282.6	268.1	232.5	0.0
H_5	w_{H5} [mm]	3.77	3.78	4.34	5.89	8.60	10.12
	P_{H5} [N]	184.6	215.5	230.4	227.0	205.1	0.0
H_6	w_{H6} [mm]	4.82	4.75	5.17	6.53	9.00	10.12
	P_{H6} [N]	125.8	161.2	183.3	189.1	177.7	0.0

* Branch between key-points 1 and 3 is parabolic.

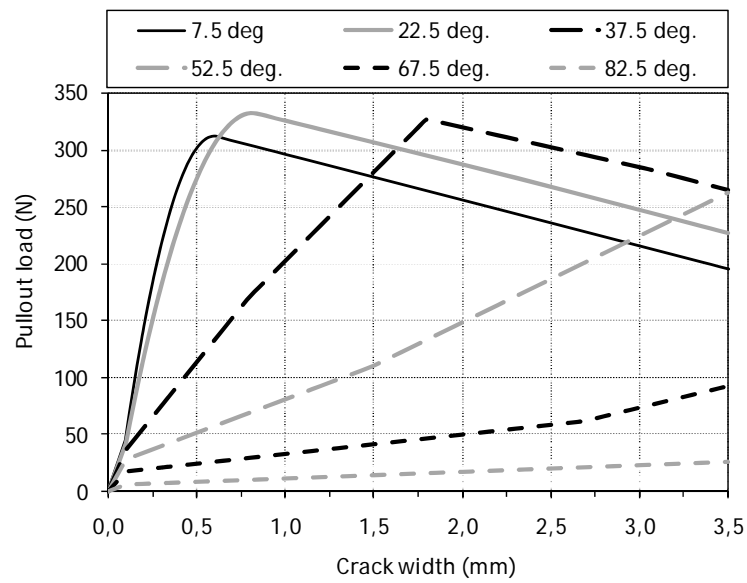


Fig. 8.29 - Single fiber pullout responses at different inclination angles.

Step 7: Quantify the contribution from each group of inclination angles, $P_{N,\theta_i}(w)$

$$P_{N,\theta_i}(w) = P_{\theta_i}(w) \times N_{\theta_i} \tag{Eq. 8.7}$$

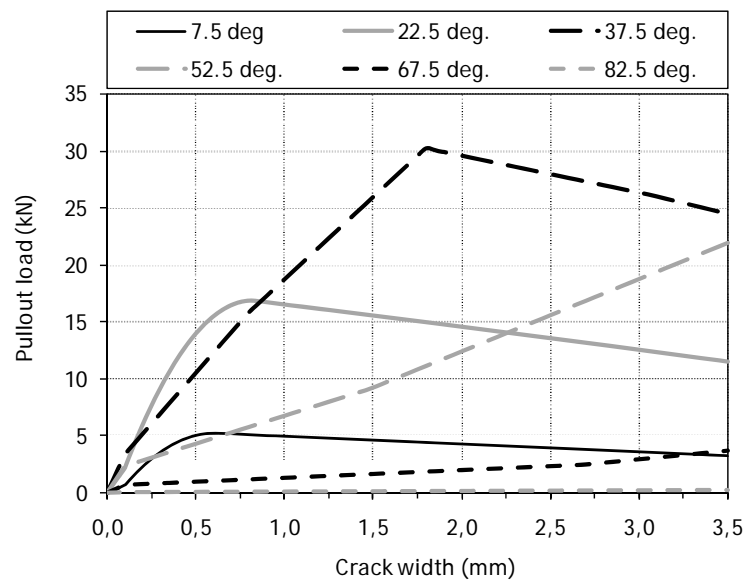


Fig. 8.30 - Contributions from each group of inclination angles

Step 8: Extract the overall strengthening contribution provided by steel fibers, $\sigma_{SF}(w)$

$$\sigma_{SF}(w) = \frac{P_{N,7.5}(w) + P_{N,22.5}(w) + P_{N,37.5}(w) + P_{N,52.5}(w) + P_{N,67.5}(w) + P_{N,82.5}(w)}{A_{sec}} \tag{Eq. 8.9}$$

Step 9: Obtain the stress-crack width relationship of SFRC, $\sigma_{SFRC}(w)$

$$\sigma_{SFRC}(w) = \sigma_c(w) + \sigma_{SF}(w) \quad (Eq. 8.1)$$

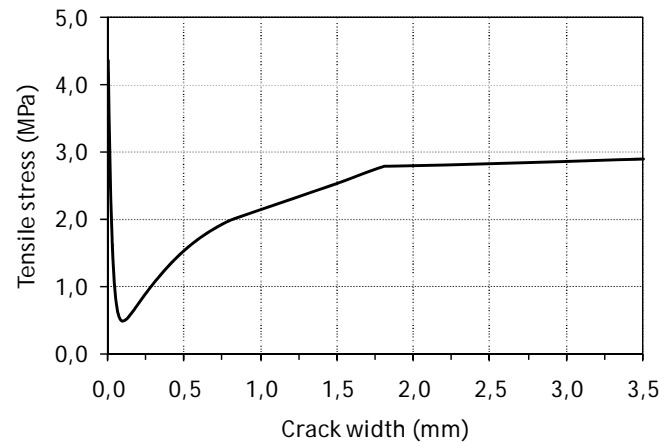


Fig.8.31 - Predicted constitutive model for SFRC.

8.7.3 Resolution based on the engineered expressions

From the inputs defined in Table 8.8 it can be concluded that the minimum MAR of 30% is guaranteed (Fig.8.28). Consequently, an alternative and straightforward procedure can be used to predict the constitutive model of SFRC. For that purpose, the values from Table 8.8 were introduced in the EEDO for hooked fibers (Table 8.7), leading to the results presented in Fig.8.32 and Table 8.12.

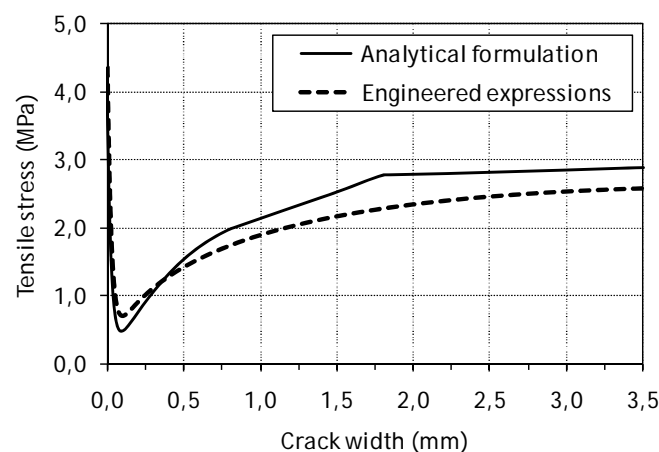


Fig.8.32 - Comparison of the predicted constitutive model for SFRC.

Table 8.12 - EEDO of SFRC with hooked steel fibers.

Physical contribution	Expressions
σ_C	$B_B = 4.35$
	$k_C = 39.80$
	$c_C = 1.0$
	$n_C = 1.0$
σ_{ER}	$B_{ER} = \frac{45}{7850} \times 0.73 \times 2100 = 8.79$
	$k_{ER} = 2 + \frac{60 - 12}{100} + 3 \times e^{0.73} - 2100 \left(\frac{5 - 1.2 \times 10^{-3} \times 2100}{1000} \right) = 3.50$
	$c_{ER} = 50 + 25 \times 0.64 + 2.2 \times 10^{-3} \times 2100 + 0.73 \times (30 - 25 \times 0.73) + 2.5 \times 60 \times \left(\frac{60}{100} - 1 \right) = 19.20$
	$n_{ER} = 0.8 - 2.5 \times 10^{-3} \times 41.2 - \frac{\sqrt{0.73}}{10} = 0.61$
σ_B	$B_B = 8.79$
	$k_B = 1.3 - e^{0.73} + \frac{(60 + 8)}{2.5 \times 10^6} \times 2100 \times 0.73 \times \left(39 - \frac{60}{2} \right) + 3.5 \times \left[0.85 - 0.036 \times \left(\frac{293}{676} \right) \times \left(1 + 20 \times \frac{293}{676} \right) \right] = 2.04$
	$c_B = \left(\frac{2500}{2100} \right)^2 e^{0.73} + 19.20 \times \left[1.32 + 0.36 \times \frac{293}{676} \times \left(1 + 20 \times \frac{293}{676} \right) \right] = 31.18$
	$n_B = 0.61$

8.8 CONCLUDING REMARKS

This chapter presented a new constitutive model for the design and optimization of SFRC by assembling Parts II, III and IV of this thesis.

The relevance of predicting single fiber orientations and the respective pullout responses were emphasized on the basis of a rational and comprehensive approach. Likewise, the analytical formulation of the new constitutive model was presented both for straight fibers and hooked fibers. Then, the data from the uniaxial tensile tests reported in Chapter 3 was considered for validation purposes and a reasonable agreement with the tensile behavior predicted by the new model was observed.

The fundamental causes for the differences on the magnitude and shape of the σ - w curves of SFRC were investigated through a parametric study that analyzed the influence of the inputs of the model. With the insight gained from this study, the possibility of reproducing the results provided by the analytical formulation through a direct and more straightforward procedure was investigated. The outcome of this analysis was the so-called engineered expressions for design and optimization. These expressions provided encouraging agreements with the tensile responses predicted by the analytical formulation for hooked fibers and, at smaller extent, for straight fibers. Finally, a practical example of the definition of the new constitutive model was presented for the two alternative approaches: the comprehensive one (based on the analytical formulation) and the straightforward one (based on the engineered expressions).

Chapter 9

Conclusions and future perspectives

9.1 CONCLUSIONS

SFRC is an interesting material which offers many advantages and that has been showing to be promising for structural applications. This thesis provides a novel approach for the structural design of SFRC elements. Its major contribution is a direct and rationale method to predict its post-cracking response in tension by considering design parameters physically meaningful and practical aspects associated to material properties, production processes and the structure to be built. The consecution of this work is divided into five main parts:

The first part (Chapter 2) provided a state of the art on constitutive models for SFRC and on several related subjects, namely: experimental methods to determine the material's tensile behavior, investigations on the pullout responses of steel fibers and on their orientation. From the literature survey carried out it was noticed that an unequivocal and widely assumed method to characterize SFRC tensile response is missing out. The evaluation of the existing constitutive laws concluded that an improved model should be based on physical concepts from a meso-scale level and account for a continuous diagram calculated through a direct approach. Few

experimental studies on the uniaxial tensile behavior of SFRC could be found in literature, emphasizing the need of further material characterization. The review of the major aspects governing the tensile response indicated that the most fundamental strengthening mechanism in SFRC - the pullout responses of inclined steel fibers - could not yet be accurately predicted. Furthermore, in spite of many studies and recent advances in testing methods, an efficient and reliable approach to characterize fiber orientation was found to be lacking.

The second part of this thesis (Chapter 3) aimed at understanding the uniaxial tensile behavior of SFRC with different fiber contents and matrix strengths. From the experimental work carried out the nature of the uniaxial stress-crack width curves could be identified. It was found that the number of fibers at the cracked sections and their performances at different concrete matrices and orientations were most affecting. A closer analysis of the results obtained revealed that the orientation of fibers influences the number of fibers at the cracked sections as well as their average pullout performance. In this regard, the fresh-state properties and the casting method were found to be paramount aspects governing the mechanical properties of SFRC.

In the third part of this dissertation the behavior of single fibers from cement matrices was analyzed and models to predict the pullout responses of inclined steel fibers were advanced for the most common geometries: straight fibers (Chapter 4) and with hooked-ends (Chapter 5). From these studies the following conclusions can be drawn:

- The matrix properties, fiber geometry (shape, length, diameter and aspect ratio) as well as the fiber embedded length and orientation with respect to the cracked section are the most important aspects governing the crack-bridging effect in SFRC. In the case of fibers with hooked-ends, the tensile strength of steel fibers also plays a relevant influence as it determines the type of failure mode occurring in the pullout process.
- The pullout responses of inclined steel fibers depend on two major mechanisms: 1) local friction at the zone where fiber exits the matrix; 2) debonding and friction in the direction of fiber embedded length and, in case of hooked fibers, straightening process of the hook. The first mechanism was accounted for in the models through the calculation of deviation forces and the respective portions of matrix spalled off. In the case of the second mechanism, given the large variety of influencing factors (matrix compositions, steel fiber properties, geometry, etc.), it was concluded that an experimental quantification by means of single fiber pullouts of aligned fibers was required in order to develop a general predictive tool.
- A clear link between the load-crack width responses of a single fiber and the physical phenomena associated to each stage of its pullout process could be identified. Consequently, simplified and comprehensive diagrams were advanced by defining the major key-points of the pullout behavior. In both cases (straight and hooked fibers), the pullout predictions provided an encouraging agreement with experimental data.
- In practical applications, most of the fibers are inclined with respect to the cracked surface. Consequently, the optimization of fiber/matrix bond strength by means of

pullout tests on aligned fibers may be meaningless. These new predictive models provide a more realistic procedure to tailor and optimize both fiber and matrix properties.

In the fourth part of this work the orientation of steel fibers was investigated at two different scales: single fiber orientations (Chapter 6) and the average orientation of fibers in an element cross-section (Chapter 7). The most relevant conclusions from these studies are the following:

- From the detailed analysis of single fiber orientations measured in specimens it was concluded that the distribution of the orientation angles in SFRC follows a Gaussian law and that the dispersion of orientation angles depends on the average fiber orientation. With these two findings, the new concept of orientation profile was advanced.
- Extensive validation of the orientation profile with measurements from literature provided a good agreement. Its complete characterization only requires the orientation number and the standardized Gaussian law to be defined. Thereby, more detailed information on fiber orientation can be obtained without introducing additional unknown parameters.
- The analytical and experimental investigation of fiber orientation in 3-D limited the theoretical interval of variation for the orientation number (0.0 to 1.0) into a smaller probabilistic range (0.26 to 0.97) when considering a 90% confidence interval.
- A novel philosophy was advanced to predict the orientation number of fibers in SFRC. In this new approach the several aspects influencing fiber orientation (fresh-state properties, casting method, flow, vibration and formwork geometry) are evaluated from an integrated and sequential perspective of the overall production process through a step-by-step procedure.
- The influence of the wall-effects on fiber orientation was analyzed in detail. So far, this phenomenon has only been approached by assuming non-preferential orientation of fibers in bulk conditions. However, because preferential fiber alignments tend to occur, such assumption is sometimes poor. Thereby, a proposal to quantify the increment of the orientation number due to wall-effects under anisotropic conditions is herein suggested for the first time. Then, based on such approach, simplified expressions to quantify generalized wall-effects for common cross-section geometries are advanced.
- The new approach to predict fiber orientation integrates material characteristics, production processes and the structure to be built within a unique framework. Regarding the large amount of phenomena involved and its wide range of application, further investigation is required to create a general engineering toolbox to predict fiber orientation. Nonetheless, the results obtained so far are by-and large encouraging and establish a new perspective to approach the most sensitive parameter affecting the tensile behavior of SFRC.

Finally, the last part of the thesis (Chapter 8) assembles the results from the previous chapters and presents the conceptual basis, strategy and formulation of the new constitutive model for SFRC. Several relevant conclusions can be drawn from this chapter:

- The new constitutive model provides a reasonable agreement of the stress-crack width curves obtained in the uniaxial tensile tests of SFRC with hooked fibers (Chapter 3).
- Given the capabilities of the new constitutive model, physical insight on the uniaxial tensile behavior of SFRC with straight and hooked fibers can be gained by means of a parametric study. While the post-peak range of SFRC up to crack widths of 3.5 mm was found to be approximately constant for straight fibers, increasing residual strengths after the post-peak value are expected for SFRC with hooked fibers. In both cases, the orientation number was found to be the most affecting parameter on the shape and magnitude of the post-cracking response.
- The formulation of the new constitutive model is very simple and intuitive. Each of its components was approached through a pragmatic perspective and, consequently, a simple spreadsheet is enough for its determination. With the aim of providing an even more straightforward approach which could return the same solutions given by the new constitutive model, the Engineered Expressions for Design and Optimization (EEDO) were formulated. The latter showed to be a suitable and reasonable alternative to predict the constitutive behavior of SFRC with straight and hooked fibers.

The design-oriented constitutive model presented in this dissertation differentiates itself from previous studies in multiple aspects and establishes a new philosophy for the design of SFRC elements. Four major differential abilities can be identified in this work:

- **Direct:** The new model does not require inverse analysis procedures. Design method resembles the one of concrete with conventional steel reinforcement: based on the properties of its constituent materials (concrete and steel components) and on specific boundary conditions (location of rebars/orientation of fibers).
- **Practical:** The complex behavior of SFRC is characterized through a straightforward (alternative) formulation: the Engineered Expressions for Design and Optimization (EEDO).
- **Comprehensive:** Post-cracking behavior is defined in terms of two clear concepts (fiber pullouts and orientations) by means of input parameters with physical meaning.
- **Innovative:** Intuitive and fundamental aspects that have never been introduced in previous constitutive models are finally included in this work: 1) distinct tensile responses are predicted depending on the specific combination of matrix and fiber properties; 2) practical aspects such as casting methods, fresh-state properties and formwork geometry are integrated within a unique framework that predicts the orientation of fibers to be included in the constitutive law.

9.2 FUTURE PERSPECTIVES

In this research, a design-oriented constitutive model for SFRC has been advanced. The proposed method provides a practical and comprehensive approach that may contribute to the continuous growth of SFRC structural applications that has been observed in the last years. However, there are several aspects that need to be further investigated in the future:

- A σ - ε constitutive law is more convenient for design than a σ - w curve because it can be easily combined with normal reinforcement. In this regard, the advanced constitutive model should be multiplied by a characteristic structural length. Because the latter does not only depends on material properties it has been controversial whether it should be included or not in the SFRC constitutive model. This thesis showed that material and structural designs influence each other mutually and cannot be dissociated. Consequently, the influence of the structural system, the load configuration and the geometry of the structure on the characteristic structural length should be further investigated in order to obtain reliable σ - ε diagrams.
- In spite of the reasonable agreement provided by the new constitutive model with the experimental σ - w curves, the reasons for the consistent underestimation at small crack widths should be further investigated.
- The Engineered Expressions for Design and Optimization (EEDO) should be optimized in order to evaluate whether further simplifications are possible or some physical meaning can be attributed to the variables involved.

This thesis corroborated that the uniaxial tensile behavior of SFRC can be characterized by means of single fiber pullouts and orientations. With regard to the study of the crack-bridging capacity of steel fibers there are many topics of interest:

- Insight on pullout behavior under different loading conditions needs to be enlarged. So far, studies on pullout tests at high-rate and impact loading denoted increased toughness comparatively to quasi-static tests. Similar conclusions were drawn on high temperature pullout tests. However, there are no studies reporting single fiber pullout behavior under fatigue and creep conditions. The correlation between the uniaxial stress-crack width curves and the pullout responses shown in this thesis should also be evaluated under such types of loading conditions.
- Recent studies combining SFRC with different types of steel fibers are very promising. While steel fibers covered in this thesis enlarge the post-cracking tensile strength, micro fibers bridge micro-cracks and enlarge the tensile strength of the matrix. In order to quantify these synergetic effects, the models to predict the pullout response of inclined steel fibers herein advanced should be improved to cover micro fibers. Particularly, group effects should be evaluated regarding that overlapping of tensile stresses at the cracked surface tend to occur in the presence of smaller fiber spacing (arising from smaller fiber unit volumes or larger fiber contents).

- The proposed constitutive model addresses steel fibers with straight and hooked geometries. Anyhow, the design philosophy advanced may be used for SFRC having steel fibers with different shapes. For that purpose, the inclined pullout responses of those types of fibers should be carefully evaluated.
- Standardization of test methods would be of great importance, particularly in the case of single fiber pullout test. The latter does not provide results at a macroscopic level and, consequently, has been depreciated when defining standards or guidelines that tend to focus on practical applications. However, this thesis pointed out the importance of the single fiber pullouts as a fundamental element to understand and quantify SFRC uniaxial tensile behavior. Regarding that some pullout test configurations existing in literature are not representative of the actual crack-bridging effects occurring in SFRC, the standardization of this test method for fibers at any inclination angle would be a great contribution for further studies.

In order to exploit the full potential of SFRC, the orientation of steel fibers has to be quantified. This thesis advanced a novel framework to predict the orientation of steel fibers by focusing on practical and intuitive aspects of the manufacturing process. However, regarding the complexity of the subject, there are some aspects that deserve further investigation:

- The influence of the casting method on fiber orientation depends on the cross-section's geometry of the pouring element and on the direction of casting relatively to the cross-section of the element under analysis. Extensive descriptions of these manufacturing procedures are very scarce in literature. The specific impact of the direction of casting on fiber orientation should be contrasted through experiments by varying both the horizontal and vertical pouring angles.
- Compaction processes tend to introduce preferential fiber alignments in the plane perpendicular to the gravity axis. However, although this has been largely observed in literature, conclusions are limited to particular experiments because details on power, frequency and durations of compaction are very limited. The influence of these aspects on the orientation of fibers should be quantified for mixtures with different slump values and fiber lengths.
- The flow of SCSFRC affects the orientation of the fibers. It has been reported in literature that, in the absence of wall-effects, flow orients fibers perpendicularly to flow direction and, under the influence of the sides of the mould, aligns fibers parallel to the mould surfaces. In order to dissociate the several influencing aspects, it would be interesting to evaluate the effect of the flow at the bulk of the cross-sections for different slump flows and casting rates.

A better understanding on how the fibers distribute and orient themselves would provide the basis for more economical SFRC.

Bibliography

Aguado A (2007) Tendencias del hormigón con fibras en construcciones subterráneas, *Cemento hormigón*, 904:44-54.

Alwan JM, Naaman AE, Guerrero P (1999) Effect of Mechanical Clamping on the Pull-Out Response of Hooked Steel Fibers Embedded in Cementitious Matrices, *Concrete Science and Engineering*, 1:15-25.

Armelin HS, Banthia N (1997) Predicting the Flexural Postcracking Performance of Steel Fiber Reinforced Concrete from the Pullout of Single Fibers, *ACI Materials Journal*, 94(1):18-31.

ASTM C-1550 (2003) Standard Test Method for Flexural Toughness of Fibre Reinforced Concrete (Using Centrally-Loaded Round Panel), West Conshohoken, American Society for Testing and Materials.

Banholzer B, Brameshuber W, Jung W (2005) Analytical simulation of pull-out test - the direct problem, *Cement and Concrete Composites*, 27:93-101.

Banholzer B, Brameshuber W, Jung W (2006) Analytical simulation of pull-out test - the inverse problem, *Cement and Concrete Composites*, 28:564-571.

Banthia N, Trottier J (1994) Concrete Reinforced with Deformed Steel Fibers, Part I: Bond-Slip Mechanisms, *ACI Materials Journal*, 91(5):435-446.

Barragán BE (2002) Failure and toughness of steel fiber reinforced concrete under tension and shear, PhD Thesis, Universitat Politècnica de Catalunya.

Barros JAO, Figueiras JA (1999) Flexural Behavior of SFRC: Testing and Modeling, *Journal of Materials in Civil Engineering*, 11(4):331-339.

Bartos PJM, Duris M (1994) Inclined tensile strength of steel fibres in a cement-based composite, *Composites*, 25(10):945-952.

Bazant ZP, Oh BH (1983) Crack band theory for fracture of concrete, *Materials and Structures*, 16:155-177.

Behloul M (1996) Analyse et Modelisation du Comportement d'un Materiau a Matrice Cimentaire Fibree a Ultra Hautes Performances (Beton des Poudres Reactives), PhD Thesis, Ecole Normale Supérieure du Cachan.

Bentur A, Alexander MG (2000) A review of the work of the RILEM TC 159-ETC: Engineering of the interfacial transition zone in cementitious composites, *Materials and Structures*, 33:82-87.

Bentur A, Diamond S, Mindess S (1985) Cracking processes in steel fiber reinforced cement paste, *Cement and Concrete Research*, 15(2):331-342.

Bentur A, Mindess S (1985) Cracking processes in steel fiber reinforced cement paste, *Cement and Concrete Research*, 15:331-342.

Bernard, ES (2000) Behavior of round steel fibre reinforced concrete panels under point loads, *Materials and Structures*, 33(3):181-188.

Bindiganavile V, Banthia N (2005) Impact response of the fiber-matrix bond in concrete, *Canadian J. Civ. Eng.*, 32: 924-933.

Blanco A, Pujadas P, de la Fuente A, Aguado A (2010) Análisis comparativo de los modelos constitutivos del hormigón reforzado con fibras (*submitted to Hormigón y Acero*).

Blázquez XB (2009) Caracterització experimental de l'arrencament de fibres d'acer en provetes de formigó, Minor Thesis (oriented by Climent Molins and Filipe Laranjeira), Universitat Politècnica de Catalunya.

Cailleux E, Cutard T, Bernhart G (2005) Pullout of steel fibres from a refractory castable: experiment and modeling, *Mechanics of Materials*, 37:427-445.

Cavalaro S (2009) Aspectos tecnológicos de túneles construidos con tuneladora y dovelas prefabricadas de hormigón, PhD Thesis, Universitat Politècnica de Catalunya.

CEB-FIP (1991) Model Code 1990, Comité Euro-International Du Béton - Fédération International de la Précontrainte, Paris.

CEB-FIP (1993) CEB-FIP Model Code 1990: Design code. Thomas Telford, Lausanne.

Chanvillard G (1999) Modeling the pullout of wire-drawn steel fibers, *Cement and Concrete Research*, 29:1027-1037.

CNR-DT 204 (2006) Istruzioni per la Progettazione, l'Esecuzione ed il Controllo di Strutture Fibrorinforzate, Consiglio Nazionale delle Ricerche, Italia.

Cunha VMCF, Barros JAO, Sena-Cruz JM (2007) Pullout behavior of hooked-end steel fibres in self-compacting concrete, Report 07-DEC/E06, University of Minho.

DBV (2001) Merkblatt Stahlfaserbeton, Deutsche Beton Vereins.

di Prisco M (2009) FRC: structural applications and standards, *Journal of Materials and Structures*, (available online: DOI 10.1617/s11527-009-9545-4).

di Prisco M, Ferrara L, Colombo M, Mauri M (2004) On the identification of SFRC constitutive law in uniaxial tension. Proceedings of Sixth RILEM Symposium on Fibre-Reinforced Concretes BEFIB 2004: 827-836.

Dozio D (2008) SFRC structures: Identification of the uniaxial tension characteristic constitutive law, PhD Thesis, Politecnico di Milano.

Dupont D (2003) Modelling and experimental validation of the constitutive law (σ - ϵ) and cracking behavior of steel fibre reinforced concrete, PhD Thesis, Katholieke Universiteit Leuven.

Dupont D, Vandewalle L (2002) Characterisation of steel fibre concrete with a σ - ϵ relation, Proceedings of the 4th International PhD Symposium in Civil Engineering, Munich, 19-21 September 2002, 108-114.

Dupont D, Vandewalle L (2005) Distribution of steel fibres in rectangular sections, Cement and Concrete Composites, 27:391-398.

Easley TC, Faber KT, Shah SP (1999) Use of a Crack-Bridging Single Fiber Pullout Test to Study Steel Fiber/Cementitious Matrix Composites, J. Am. Soc., 82(12):3513-3520.

Edington J, Hannant DJ (1972) Steel Fibre reinforced concrete. The effect on fibre orientation of compaction by vibration, Materials and Structures, 5(25):41-44.

EHE (2008) Instrucción del Hormigón Estructural, Comisión Permanente del Hormigón, Ministerio de Fomento.

EN 14651 (2005) Test method for metallic fibered concrete - Measuring the flexural tensile strength (limit of proportionality (LOP), residual), European Committee for Standardization, Brussels.

ENV 1992-1-1 (1992) Eurocode 2: Design of Concrete Structures - Part 1: General rules and rules for buildings, CEN.

Fantilli AP, Vallini P (2007) A cohesive interface model for the pullout of inclined steel fibers in cementitious matrices, Journal of Advanced Concrete Technology, 5(2):247-258.

Fantilli AP, Vallini P (2007) A Cohesive Interface Model for the Pullout of Inclined Steel Fibers in Cementitious Matrixes, Journal of Advanced Concrete Technology, 5(2):247-258.

Ferrara L, Park Y, Shah SP (2008) Correlation among fresh State Behavior, Fiber Dispersion and Toughness Properties of SFRCs, Journal of Materials in Civil Engineering, 20(7):493-501.

Ferrara L, Park YD, Shah SP (2007) A method for mix-design of fiber-reinforced self-compacting concrete, Cement and Concrete Research, 37(6):957-971.

FIB Model Code (2007) Fibre Reinforced Concrete. Draft version. Joint paper by Horst Falkner, Marco di Prisco and Giovanni Plizzari.

Gettu R, Gardner DR, Saldívar H, Barragán BE (2005) Study of the distribution and orientation of fibers in SFRC specimens, Materials and Structures, 38(1):31-37.

Gomes P (2002) Optimization and characterization of high strength self-compacting concrete, PhD Thesis, Universitat Politècnica de Catalunya.

Gopalaratnam VS, Shah, SP (1985) Softening Reponse of Plain Concrete in Direct Tension, ACI Journal, 82(3):310-323.

Groth P (2000) Steel Fibre Reinforced SCC, Final report of task 6, Brite Euram project (BE 96-3801) - Rational production and improved working environment through using SCC, Doc. No.: RT6-v1.doc.

Groth P, Nemegeer D (1999) The use of steel fibres in self-compacting concrete, Proceedings from the 1st International Symposium on SCC, RILEM publications PRO 7 (ed. By Skarendahl and Petersson), Cachan, Stockholm, 497-508.

Grünewald S (2004) Performance-based design of self-compacting fibre reinforced concrete, PhD Thesis, Delft University of Technology.

Grünewald S, Walraven JC (2002) Self-compacting fibre reinforced concrete - Orientation and distribution of steel fibres in beams, Report 24.5-02-3, Delft University of Technology.

Guàrdia J (2007) Caracterització del comportament a tracció de formigó d'alta treballabilitat reforçat amb fibres d'hacer mitjançant l'assaig Barcelona, Minor Thesis (oriented by Climent Molins), Universitat Politècnica de Catalunya.

Guerrero P, Naaman AE (2000) Effect of mortar fineness and adhesive agents on pullout response of steel fibers, ACI Materials Journal, 97(1):12-20.

Hillerborg A (1985) The theoretical basis of a method to determine the fracture energy G_F of concrete, Materials and Structures, 18(4):291-296.

Hillerborg A, Modéer M, Petersson P (1976) Analysis of crack formation and crack growth in concrete by means of fracture mechanics and finite elements, Cement and Concrete Research, 6:773-782.

Hordjik D (1991) Local approach to fatigue of concrete, PhD Thesis, Delft University of Technology.

Hoy CW (1998) Mixing and mix proportioning of fibre reinforced concrete, PhD Thesis, University of Paisley.

Jones PA, Austin SA, Robins PJ (2008) Predicting the flexural load-deflection response of steel fibre reinforced concrete from strain, crack-width, fibre pull-out and distribution data, Materials and Structures, 41:449-463.

Kameswara Rao CVS (1979) Effectiveness of random fibres in composites, Cement and Concrete Research, 9:685:693.

Karihaloo BL, Wang J (1997) Micromechanical modeling of strain hardening and tension softening in cementitious composites, *Computational Mechanics*, 19:453-462.

Katz A, Li VC (1995) Inclination angle effect of carbon fibers in cementitious composites, *Journal of Engineering Mechanics*, 121(12):1340-1348.

Kerans R, Parthasarathy T (1991) Theoretical analysis of the fiber pullout and pushout tests, *Journal of the American Ceramic Society*, 74(7):1585-1596.

König G, Kützing L (1999) Modelling the increase of ductility of HPC under compressive forces - a fracture mechanical approach, *Proceedings of the 3rd International RILEM Workshop of HPFRCC*, Mainz, Germany, 251-260.

Kooiman AG (2000) Modelling Steel Fibre Reinforced Concrete for Structural Design, PhD Thesis, Delft University of Technology.

Krenchel H (1975) Fibre spacing and specific fibre surface, In: Neville A, editor. *Fibre reinforced cement and concrete*, UK: The Construction Press, 69-79.

Kullaa J (1994) Fibre-reinforced concrete under uniaxial tension, *Nordic Concrete Research*, 14:77-90.

Lange-Kombak D, Karihaloo B (1998) Design of fiber-reinforced DSP mixes for minimum brittleness, *Advanced Cement Based Materials*, 7:89-101.

Lappa L (2007) High Strength Fibre Reinforced Concrete: Static and fatigue behavior in bending, PhD Thesis, Delft University of Technology.

Laranjeira F, Aguado A, Molins C (2007) Constitutive equations of fiber reinforced concrete, CD-ROM *Proceedings of the ECCOMAS Thematic Conference on Computational Methods in Tunneling (EURO:TUN 2007)*, August 27-29 2007, Vienna, Austria. Eds.: J. Eberhardsteiner, G. Beer, Ch. Hellmich, H.A. Mang, G. Meschke, W. Schubert. Publisher: Vienna University of Technology (ISBN: 978-3-9501554-7-1).

Laranjeira F, Aguado A, Molins C (2009) Predicting the pullout response of inclined straight steel fibers, *Materials and Structures* (available online: DOI 10.1617/s11527-009-9553-4).

Lataste JF, Behloul M, Breysse D (2008) Characterisation of fibres distribution in a steel fibre reinforced concrete with electrical resistivity measurements, *NDT&E International*, 41:638-647.

Lee MK, Barr BIG (2004) A four-exponential model to describe the behaviour of fibre reinforced concrete, *Materials and Structures*, 37:464-471.

Leung CKY, Li VC (1992) Effect of fiber inclination on crack bridging stress in brittle fiber reinforced brittle matrix composites, *Journal of the Mechanics and Physics of Solids*, 40(6):1333-1362.

- Leung CKY, Shapiro N (1999)** Optimal steel fiber strength for reinforcement of cementitious materials, *Journal of Materials in Civil Engineering*, 11(2):116-123.
- Leung CKY, Ybanez N (1997)** Pullout of inclined flexible fiber in cementitious composite, *Journal of Engineering Mechanics*, 123(3):239-246.
- Li VC (1992)** Post-crack scaling relations for fiber reinforced cementitious composites, *ASCE Journal of Materials in Civil Engineering*, 4(1):41-57.
- Li VC (2007)** Integrated structures and materials design, *Materials and Structures*, 40:387-396.
- Li VC, Stang H (1997)** Interface property characterization and strengthening mechanisms in fiber reinforced cement based composites, *Advanced Cement Based Composites*, 6(1):1-20.
- Li VC, Stang H, Krenchel H (1993)** Micromechanics of crack bridging in fiber reinforced concrete, *Materials and Structures*, 26(162):486-494.
- Li VC, Wang I, Backer S (1990)** Effect of inclining angle, bundling and surface treatment on synthetic fibre pullout from a cement matrix. *Composites*, 21(2):132-140.
- Lim TY, Paramasivam P, Lee SL (1987)** Analytical Model for Tensile Behavior of Steel-Fiber Concrete, *ACI Materials Journal*, 84(4):286-298.
- Lok TS, Xiao L (1998)** Tensile behavior and moment-curvature relationship of steel fibre reinforced concrete, *Magazine of Concrete Research*, 50(4):359-368.
- Maidl, BR (1995)** *Steel Fibre Reinforced Concrete*, Ernst and Sohn, Berlin (ISBN: 3433012881).
- Markovic I (2006)** *High-Performance Hybrid-Fibre Concrete: Development and Utilisation*, PhD Thesis, Delft University of Technology.
- Markovic I, van Mier JGM, Walraven JC (2003)** Experimental evaluation of fibre pullout from plain and fibre reinforced concrete, *Proceedings of the 4th International Workshop on HPRCC*, Ann Arbor, 419-436.
- Markovic I, Walraven JC, van Mier JGM (2004)** Tensile response of hybrid-fibre concrete. *Proceedings from the 6th RILEM Symposium on fibre-reinforced concretes (BEFIB 2004)*, Varenna, Italy, 1341-1352.
- Martinie L, Rossi P, Roussel N (2009)** Rheology of fiber reinforced cementitious materials: classification and prediction (available online: DOI: 10.1016/j.cemconres.2009.08.032).
- Molins C, Aguado A, Saludes S (2009)** Double Punch Test to control the energy dissipation in tension of FRC (Barcelona test), *Materials and Structures*, 42(4):415-425.

Molins C, Martinez J, Arnáiz N (2008) Distribución de fibras de acero en probetas prismáticas de hormigón, CD-ROM from the 4th International Structural Concrete Congress (ACHE), Valencia, Spain.

Mora F (2008) Distribución y orientación de fibras en dovelas aplicando el ensayo de Barcelona, PhD Thesis, Universitat Politècnica de Catalunya.

Morton J, Groves GW (1974) The cracking of composites consisting of discontinuous ductile fibres in brittle matrix - effect of fibre orientation, *Journal of Materials Science*, 9:1436-1445.

Mumm D, Faber KT (1995) Interfacial debonding and sliding in brittle matrix composites measured using an improved fiber pullout technique, *Acta Metall Mater*, 43(3):1259-1270.

Naaman AE (2003) Engineered Steel Fibers with Optimal Properties for Reinforcement of Cement Composites, *Journal of Advanced Concrete Technology*, 1(3):241-252.

Naaman AE, Najm H (1991) Bond-slip mechanisms of steel fibers in concrete, *ACI Materials Journal*, 88(2):135-145.

Naaman AE, Nammur G, Alwan J, Najm H (1991) Fiber pullout and bond slip. I: Analytical study, *Journal of Structural Engineering*, 117(9):2769-2790.

Naaman AE, Shah SP (1976) Pull-out mechanism in steel fiber-reinforced concrete, *Journal of the Structural Division, American Society for Civil Engineers*, 102:1537-1548.

NBN B 15-238 (1992) Test on fibre reinforced concrete - bending test on prismatic samples, Norme Belge, Institut Belge de Normalisation, Brussels.

Ouyang C, Pacios A, Shah SP (1994) Pullout of inclined fibers from cementitious matrix, *Journal of Engineering Mechanics*, 120(12):2641-2659.

Ozyurt N, Mason TO, Shah SP (2006) Non-destructive monitoring of fiber orientation using AC-*IS*: An industrial-scale application, *Cement and Concrete Research*, 36:1653-1660.

Ozyurt N, Mason TO, Shah SP (2007) Correlation of fiber dispersion, rheology and mechanical performance of FRCs, *Cement and Concrete Composites*, 29:70-79.

Pompo A, Stupak PR, Nicolais L, Marchese B (1996) Analysis of Steel Fibre Pull-Out from a Cement Matrix Using Video Photography, *Cement and Concrete Composites*, 18:3-8.

Prudencio Jr L, Austin S, Jones P, Armelin H, Robins P (2006) Prediction of steel fibre reinforced concrete under flexure from an inferred pull-out response, *Materials and Structures*, 39:601-610.

RILEM TC 162-TDF (2000) Test and design methods for steel fibre reinforced concrete: bending test, *Materials and Structures*, 33:3-5.

RILEM TC 162-TDF (2001) Test and design methods for steel fibre reinforced concrete: Uniaxial tension test for steel fibre reinforced concrete - Recommendations, Materials and Structures, 34:3-6.

RILEM TC 162-TDF (2002) Test and design methods for steel fibre reinforced concrete - Design of steel fibre reinforced concrete using the σ -w method: principles and applications, Materials and Structures, 35:262-278.

RILEM TC 162-TDF (2003) Test and design methods for steel fibre reinforced concrete - σ - ϵ design method: Final recommendations, Materials and Structures, 36:560-567.

RILEM TC 188-CSC (2006) Final Report of RILEM TC 188-CSC: Casting of self-compacting concrete, Materials and Structures, 39:937-954.

Robins P, Austin S, Jones P (2002) Pull-out behavior of hooked steel fibres, Materials and Structures, 35:434-442.

Robins PJ, Austin SA, Jones PA (2003) Spatial distribution of steel fibres in sprayed and cast concrete, Magazine of Concrete Research, 55(3):225-235.

Roelfstra PE, Wittmann FH (1986) Numerical method to link strain softening with failure of concrete, Fracture Toughness and Fracture Energy of Concrete, edited by Wittmann FH, Elsevier Science Publishers B.V., Amsterdam.

Romualdi JP, Mandel JA (1964) Tensile strength of concrete affected by uniformly distributed and closely spaced short lengths of wire reinforcement, ACI Journal, 61(6):27-37.

Roqueta G, Romeu J, Jofre L, Aguado A (2009) Microwave Non-Destructive Fiber Content Imaging of Steel Fiber Reinforced Concrete (submitted to Advanced in Civil Engineering, Hindawi Publishing Corporation)

Roussel N (2007) Rheology of fresh concrete: from measurements to predictions of casting processes, Materials and Structures, 40:1001-1012.

Sato Y, van Mier JGM, Walraven JC (2000) Mechanical characteristics of multi-modal fibre-reinforced cement based composites, Proceedings of the 5th RILEM Symposium on fibre reinforced concretes (BEFIB 2000), 791-800.

Schönlin K (1988) Determination of the orientation, the content and the distribution of the fibres in fibre reinforced concrete, Beton- und Stahlbetonbau, 6:168-171.

Schumacher P (2006) Rotation Capacity of Self-Compacting Steel Fiber Reinforced Concrete, PhD Thesis, Delft University of Technology.

Sedran T, de Larrard F (1999) Optimization of Self-compacting Concrete thanks to Packing Model, Proceedings from the 1st International Symposium on SCC, RILEM publications PRO 7 (ed. By Skarendahl and Petersson), Cachan, Stockholm, 321-332.

- Serna P, Arango S, Ribeiro T, Núñez AM, Garcia-Taengua E (2009)** Structural cast-in-place SFRC: technology, control criteria and recent applications in Spain, *Materials and Structures* (available online: DOI: 10.1617/s11527-009-9540-9).
- Shah SP (1991)** Do fibers increase the tensile strength of cement-based matrixes?, *ACI Materials Journal*, 88(6):595-602.
- Shah SP, Li Z (1995)** Fracture Mechanism of Fiber Reinforced Quasi Brittle Matrix Composites, *Fracture of Brittle Disordered Materials: Concrete, Rocks and Ceramics* (eds. G Baker, BL Karihaloo), E & FN Spon, London, 83-100.
- Shah SP, Ouyang C (1991)** Mechanical behavior of fiber-reinforced cement-based composites, *Journal of the American Ceramic Society*, 74:2727-2738.
- Shannag M, Brincker R, Hansen W (1997)** Pullout behavior of steel fibers from cement-based composites, *Cement and Concrete Research*, 27(6):925-936.
- Soroushian P, Lee C (1990)** Distribution and orientation of fibers in steel fiber reinforced concrete, *ACI Materials Journal*, 87(5):433-439.
- Sousa JLAO, Gettu R (2006)** Determining the Tensile Stress-Crack Opening Curve of Concrete by Inverse Analysis, *Journal of Materials in Civil Engineering*, 132(2):141-148.
- Stälhi P (2008)** Ultra-Fluid, Oriented Hybrid-Fibre-Concrete, PhD Thesis, Institute for Building Materials ETH Zürich.
- Stälhi P, Custer R, van Mier JGM (2008)** On flow properties, fibre distribution, fibre orientation and flexural behaviour of FRC, *Materials and Structures*, 41:189-196.
- Stälhi P, van Mier JGM (2007)** Manufacturing, fibre anisotropy and fracture of hybrid fibre concrete, *Engineering Fracture Mechanics*, 74:223-242.
- Stroeven P (1999)** Steel fibre reinforcement at boundaries in concrete elements, *Proceedings of the 3rd International Workshop on High Performance Fiber Reinforced Cement Composites (HPFRCC3)*, Mainz, Germany, 413-421.
- Sujivorakul C, Waas AM, Naaman AE (2000)** Pullout Response of a Smooth Fiber with an End Anchorage, *Journal of Engineering Mechanics*, 126(9):986-993.
- Taerwe L, Van Gysel A (1996)** Influence of steel fibres on the design stress-strain curve for high-strength concrete, *Journal of Engineering Mechanics*, 122(8):695-704.
- Torrents JM, Juan-García P, Patau O (2007)** Control de calidad del hormigón con fibras, *Proceedings from Conference in Structural Applications of Fiber Reinforced Concretes* (www.bmbupc.org), Barcelona, Spain, 87-96.

Torrijos MC, Tobes JM, Barragán BE, Zerbino RL (2008) Orientation and Distribution of Steel Fibres in Self-Compacting Concrete, Proceedings of the 7th RILEM Symposium on Fibre Reinforced Concrete: Design and Applications (BEFIB 2008), Chennai, India, 729-738.

Toujanji H, Bayasi Z (1998) Effects of manufacturing techniques on the flexural behavior of steel fiber-reinforced concrete, *Cement and Concrete Research*, 28(1):115-124.

Tschegg EK, Linsbauer HN (1986) Testing procedure for determination of fracture mechanics parameters, Patentschrift no. A-233/86, Österreichisches Patentamt.

UNE 83316 (1996) Determinación del modulo de elasticidad del hormigón in compresión, Spanish Association for Standardisation and Certification.

UNE 83507 (2004) Rotura por compression de probetas de hormigón reforzado con fibras, Spanish Association for Standardisation and Certification.

UNI 11039 (2003) Calcestruzzo rinforzato con fibre d'acciaio; Parte I: Definizioni, classificazione e designazione; Parte II Metodo di prova per la determinazione della resistenza di prima fessurazione e degle indici di duttilità.

Van Gysel A (2000) Studie van het uittrekgedrag van staalvezels ingebed in een cementgebonden matrix met toepassing op staalvezelbeton onderworpen aan buiging, PhD Thesis, Gent University.

Van Mier JGM, Van Vliet MRA (2002) Uniaxial tension test for the determination of fracture parameters of concrete: state of the art, *Engineering Fracture Mechanics*, 69:235-247.

Vandewalle L, Heirman G, van Rickstal F (2008) Fibre orientation in self-compacting fibre reinforced concrete, Proceedings of the 7th RILEM Symposium on Fibre Reinforced Concrete: Design and Applications (BEFIB 2008), Chennai, India, 719-728.

Walraven JC (2007) Fibre reinforced concrete: a material in development, Proceedings from Conference in Structural Applications of Fiber Reinforced Concretes (www.bmbupc.org), Barcelona, Spain, 199-213.

Wei S, Mandel JA, Said S (1986) Study of the Interface Strength of Steel Fibre Reinforced Cement Based Composites, *ACI Journal*, 83:597-605.

Appendices: overview

Appendix 1 Uniaxial tensile test reports

A1.1	Introduction.....	201
A1.2	Serie A0.....	202
A1.3	Serie A20	209
A1.4	Serie A40	217
A1.5	Serie A60	225
A1.6	Serie B0.....	233
A1.7	Serie B20	240
A1.8	Serie B40	248
A1.9	Serie B60	256

Appendix 2 Definition of the matrix spalled lengths

A2.1	Introduction.....	265
A2.2	Definition of L_{SP1}	266
A2.3	Definition of L_{SP2}	268

Appendix 3 Inclined tensile strength and data for validation of the pullout model

A3.1	Introduction.....	271
A3.2	Predicting $f_u(\theta)$	272
A3.3	Input values used for model validation	274

Appendix 4 Statistical analyses of the orientation profile

A4.1	Introduction.....	275
A4.2	Features of the experimental data	276
A4.3	Results from the non-parametric tests	277
A4.4	Coefficients of determination (R^2).....	278
A4.5	Statistical orientation laws ($\Delta\theta=10^\circ$)	279

Appendix 5 Wall-effects on fiber orientation

A5.1	Introduction.....	283
A5.2	Wall-effects under isotropic conditions	284
A5.2.1	Orientation number of a fiber with one boundary condition.....	284
A5.2.2	Orientation number of a fiber with two boundary conditions	285
A5.3	Generalized wall-effects for common cross-section geometries.....	289
A5.3.1	Rectangular cross-section	289
A5.3.2	Circular cross-section	290
A5.3.3	Hollow-circular cross-section	291
A5.3.4	Summary.....	293

<u>Appendix 6</u>	Experimental validation of the framework to predict fiber orientation	
A6.1	Introduction.....	295
A6.2	Input data for experimental validation	296
A6.3	Results from experimental validation.....	297
<u>Appendix 7</u>	Literature survey on pullout test results of aligned fibers	
A7.1	Introduction.....	299
A7.2	Straight steel fibers	300
A7.3	Hooked steel fibers.....	302
<u>Appendix 8</u>	Application of the engineered expressions on several case-studies	
A8.1	Introduction.....	305
A8.2	Straight steel fibers	306
A8.3	Hooked steel fibers.....	309